Numerical Study of Pulsatile Blood Flow in Arteries

By

Akbar Zaman

Department of Mathematics and Statistics
Faculty of Basic and Applied Sciences
International Islamic University, Islamabad, Pakistan
2016

Numerical Study of Pulsatile Blood Flow in Arteries

By

Akbar Zaman

Supervised by

Dr. Nasir Ali

Co-Supervised by

Dr. Muhammad Sajid

Department of Mathematics and Statistics
Faculty of Basic and Applied Sciences
International Islamic University, Islamabad, Pakistan
2016

Numerical Study of Pulsatile Blood Flow in Arteries

By

Akbar Zaman

A Dissertation

Submitted in the partial fulfillment of the

requirements for the degree of

DOCTOR OF PHILOSOPHY

IN

MATHEMATICS

Supervised by

Dr. Nasir Ali

Co Supervised by

Dr. Muhammad Sajid

Department of Mathematics and Statistics
Faculty of Basic and Applied Sciences
International Islamic University, Islamabad, Pakistan
2016

<u>Certificate</u>

Numerical Study of Pulsatile Blood Flow in Arteries

By

Akbar Zaman

A THESIS SUBMITTED IN THE PARTIAL FULFILLMENT OF THE REQUIREMENTS
FOR THE DEGREE OF THE *DOCTOR OF PHILOSOPHY IN MATHEMATICS*

We accept this thesis as conforming to the required standard

1. _____   2. _____

   Dr. Nasir ali   Dr. Muhammad Sajid
   (Supervisor)   (Co-Supervisor)

3. _____   4. _____

   (External Examiner)   (External Examiner)

5. _____   6. _____

   (Internal Examiner)   (Chairman)

Department of Mathematics and Statistics
Faculty of Basic and Applied Sciences
International Islamic University, Islamabad, Pakistan
2016

<u>Declaration</u>

I hereby declare and affirm that this research work neither as a whole nor as a part has been copied out from any source. It is further declared that I have developed this research work entirely on the basis of my personal efforts. If any part of this thesis is proven to be copied out or found to be a reproduction of some other, I shall stand by the consequences.

Moreover, no portion of the work presented in this thesis has been submitted in support of an application for other degree or qualification in this or any other university or institute of learning.

Name and signature of student: .

Akbar Zaman

PhD (Mathematics)

Acknowledgements

First of all, I pay my special thanks to the creator of mankind, the everlasting Allah, who gave us this life, taught us everything we did not know, granted us health, knowledge and intelligence to extract the hidden realities in the universe through scientific and critical approach. I just want to add this verse, start learning with the name of Almighty Allah and you will find the right way you even never expected. I thank the lord Almighty with whose kindness I have achieved this very important goal in my life. I offer salutations upon the Holy Prophet, Hazrat Muhammad (*PBUH)* who has lightened the life of all mankind with His guidance. He is a source of knowledge and blessings for the entire creations. His teachings make us to ponder and to explore this world with directions of Islam.

I express my profound gratitude to my respectable supervisor **Dr. Nasir Ali** and co-supervisor **Dr. Muhammad Sajid,** who helped me throughout my PhD studies to complete my thesis. Their many valuable comments and suggestions put me on the straight path when I was led astray. I also pay my regards to all my teachers who always directed me to right dimensions and made it possible for me to achieve an attractive goal.

I would like to thank all my friends specially Mr. Khurram Javid, Mr. Sami ullah khan, Mr Zeeshan Asghar, Mr. Aamir abaasi, Mr. Muhammad Asif Javed who always helped me during my studies in all respects.

I extend my gratitude to my family for encouragement and support, even in the gloomiest of times. Their prayers have always been my driving source and whose sustained hope led me to where I am today.

I am very thankful to Higher Education Commission, Pakistan for providing me scholarship, Indigenous 5000 PhD Fellowship Program.

Akbar Zaman

Preface

Pulsatile accounts for pumping produced by heart that deals with the propagation of sinusoidal waves which enforces the blood to flow through vessels. In the cardiovascular system, pulsatile procedure occurs due to contractions and relaxation of heart which pumps blood from heart to different part of the body. The pulsatile procedure is also responsible for general propulsive and mixing movements and it also involves in pumping the blood against pressure rise. The mathematical models for pulsatile flow of blood through arteries are of major significance because they provide non-invasive mean to estimates various important hemodynamical variables. The utility of these models further increase when the arteries under consideration have localized narrowing called stenosis. These localized narrowing are due to fat deposition, abnormal internal growth and proliferation of convective tissue in the arterial lumen. It is generally accepted that the development and progression of stenosis is intimately linked to the fluid dynamics of the post-stenotic blood flow. Although experimental estimates to quantify the role of blood fluid dynamics on the formation of stenosis and its progression are clinically more acceptable. Nevertheless, the mathematical models of blood flow constitute an alternative and useful tool for supporting experiments and detect mildly constricted phenomena and the local features which are not always obvious by experiments. Motivated by the above facts, the present thesis focuses on development and simulation of mathematical models of pulsatile flow in rigid constricted/ normal arteries. The developed models explore the effects of rheology of the blood, geometrical parameters of the stenosis and catheter radius on unsteady characteristics of the blood. The thesis is structured in the following manner.

The preliminary information regarding blood and its rheological behavior and some basic definition equations are included in chapter one. A review of literature on pulsatile flow of blood in arteries is provided. The numerical scheme used for simulations is also explained in this chapter.

Chapter 2 deals with two-layered pulsatile blood flow through a circular tube. The Sisko non-Newtonian model is integrated in the analysis to capture the rheological behavior of the blood in the core region. The blood in the peripheral region is modeled as Newtonian fluid. The equations governing the flow in each

region are derived assuming the flow to be uni-directional and one-dimensional. An explicit finite difference scheme is employed to solve these nonlinear equations. The behavior of various flow quantities is analyzed through a parametric study. The contents of these chapter are published online in **Engineering Science and Technology, an International Journal, (2015) Doi.org/10.1016/j.jestch.2015.09.013.**

The mathematical model presented in chapter 2 is modified to take into account the viscoelastic nature of the blood in chapter 3. In this chapter Oldroyd-B model is used instead of Sisko model to characterize the rheology of the core region. The equations governing the flow in both core and peripheral regions are modeled and solved numerically with appropriate boundary/initial conditions. The results are graphically displayed and analyzed for several values of pertinent parameters. The analysis presented in this chapter is published in **International Journal of nonlinear Sciences and Numerical simulation 16 (2015) 5.**

Chapter 4 provides an analysis of pulsatile flow of blood through a porous-saturated overlapping stenotic artery under the effects of magnetic field and body acceleration. The power-law model is used to capture the hemo-rheological characteristics of blood. The equations governing the flow is modeled under the assumption of mild stenosis. An explicit finite difference scheme is employed for solution of these equation. An extensive quantitative analysis is carried out to investigate effects of various involved parameters on axial velocity, flow rate, resistance impedance and wall shear stress. The instantaneous patterns of streamlines are also displayed. The findings of this chapter are published in **Journal of Mechanics in Medicine and Biology 16 (2015) 2.**

The pulsatile flow of blood in a catheterized overlapping stenosed vessel is analyzed in this chapter 5. The streaming blood in the artery is assumed to obey Carreau constitutive law. Employing the mild stenosis condition, the equation governing the flow is derived and solved numerically using an explicit finite difference scheme. The blood velocity, flow rate, arterial wall shear stress and resistance impedance are computed and shown graphically for several values of involved parameters. The bolus dynamics is also studied qualitatively. The material presented in this chapter is published in **Mathematical Biosciences 269 (2015) 94-103.**

Chapter 6 is devoted to analyze unsteady flow characteristics of blood through a catheterized artery with a combination of stenosis and aneurysm. The Eringen's micropolar model is used to capture the rheological characteristics of the streaming blood. The two-dimensional flow equations are reduced to one-dimensional equations under mild stenosis assumption. The numerical computations carried out using finite difference method and validated against finite element simulations. The important hemodynamical variables are qualitatively analyzed for geometrical and rheological parameters of the model. The streamline of the flow indicating the effects of various involved parameter are also shown graphically. The material of this chapter is published online in **Medical & Biological Engineering & Computing DOI 10.1007/s11517-015-1415-3.**

In chapter seven, the effects of unsteadiness and non-Newtonian rheology on blood flow through a tapered time-variant stenotic artery are examined through numerical method. A two-dimensional model is used to analyze the unsteady pulsatile flow of blood through a tapered artery with stenosis. The problems under consideration is made dimensionless and solved numerically using finite difference method. The axial and radial velocities, flow rate, wall shear stress and resistance impedance are analyzed graphically for several values of the involved parameters. The results presented in this chapter are published in **AIP Advances 5, (2015) 037129.**

The theoretical analysis regarding the effects of peripheral thickness on pulsatile flow of blood through a stenotic artery is carried out in chapter 8. A two-fluid model consisting of core region as a Herschel-Bulkley material and a plasma layer as a Newtonian fluid is employed. The equations governing the flow in both core and peripheral regions are setup and solved numerically using explicit finite difference scheme which is forward in time and central in space. The results obtained through the numerical computations are compared with existing experimental and theoretical results. The important flow quantities are analyzed graphically for different values of the emerging parameters. The contents of this chapter are submitted for publication in **Canadian Journal of Physics.**

A two-dimensional model of blood flow through a time variant stenotic artery is investigated using Sisko model in chapter nine. The continuity and momentum equations along with expression of stresses are

numerically solved for axial and radial velocity components. The important hemodynamical variables based on physiologically relevant data are graphically shown and discussed in detail. The significance of Sisko model over power-law in context of problem under consideration is highlighted. The results presented in this chapter are published in **Computers & Fluids 101 (2014) 42–49.**

Contents

Nomenclature

Greek Symbol

a	Radius of the artery
A_0	Amplitude of the pressure gradient
A_1	Amplitude of the pulsatile component
A_g	Amplitude of the body acceleration
b	Radius of the core region
$\boldsymbol{B}$	Total magnetic field
B_1	Dimensionless pulsatile constant
B_2	Dimensionless body acceleration constant
d	Length of non-stenotic arterial segment
e	Ratio of the systolic to diastolic pressure
f_p	Heart pulse frequency
$G(t)$	Body acceleration
k	Radius ratio
k'	Permeability of the porous medium
l_0	Length of the stenotic region
n	Power law constant
p	Pressure
Q	Volumetric flow rate
r	Radial coordinate

t	Time
u_1	Velocity component in core region
u_2	Velocity component in periphery region
U_0	Average velocity
V	Velocity vector
We	Weisenberg number
z	Axial coordinate

Greek Symbol

Π	The second invariant of strain-rate tensor
A_1^*	First Rivilin-Ericksen tensor
μ_1	Viscosity of the non-Newtonian fluid
μ_2	Viscosity of the Newtonian fluid
ρ_1	Density of the core fluid
ρ_2	Density of the Plasma fluid
ϕ	Phase angle
ω_p	Circular frequency
ε_1	Asymptotic value of viscosity at very high shear rates
ε_2	Consistency index
α	Womersley number in the core region

γ	Womersley number in the peripheral region
τ_s	Wall shear stress
$\mu*$	Dimensionless viscosity
$\rho*$	Dimensionless density
τ_1	Relaxation time
τ_2	Retardation time
ξ	Tapering parameter
ϕ	Tapering angle
δ	Height of the stenosis
Γ	Time sonstant
μ_{eff}	Effective viscosity parameter

Chapter 1

Introduction and some basic definitions

In this chapter, we introduce the reader with basic terminology about pulsatile blood flow in arteries. The fundamental equations used in blood flow modeling are given. A review of literature on pulsatile flow of blood in arteries is presented. The explicit finite difference method is also illustrated with example. Basic definitions given here are based on internet resources.

1.1 Some basic definitions

1.1.1 Blood

Blood is a heterogeneous multi-phase mixture of solid corpuscles (red blood cells, white blood cells and platelets) suspended in liquid plasma which is an aqueous solution of proteins, organic molecules and minerals.

1.1.2 Pulsatile Flow

In fluid dynamics, a flow with periodic variations is known as pulsatile flow. The cyclic nature of heart pumping creates pulsatile flow of blood in arteries. These phenomena in medical science are called systolic and diastolic. In systolic, the blood is pumped out, while in diastolic, the blood is pumped into the heart. The cardiovascular system of chordate animals is very good example where pulsatile flow is found.

Pulsatile flow is also observed in engines and hydraulic systems as a result of rotating mechanisms belonging to them.

1.1.3 Atherosclerosis

Atherosclerosis is a disease in which plaque builds up inside your arteries. Plaque is made up of fat, cholesterol, calcium, and other substances found in the blood. Over time, plaque hardens and narrows your arteries. This limits the flow of oxygen-rich blood to your organs and other parts of your body. Atherosclerosis can lead to serious problems, including heart attack, stroke, or even death.

1.1.4 Stenosis

A stenosis is an abnormal narrowing in a blood vessel or other tubular organ or structure. It is also sometimes called a stricture. Stricture as a term is usually used when narrowing is caused by contraction of smooth muscle. Stenosis is usually used when narrowing is caused by lesion that reduces the space of lumen.

1.1.5 Aneurysm

An aneurysm or aneurism is a localized, blood-filled balloon-like bulge in the wall of a blood vessel. Aneurysms can occur in any blood vessel, with examples including aneurysms of the circle of Willis in the brain, aortic aneurysms affecting the thoracic aorta, and abdominal aortic aneurysms. Aneurysms can also occur within the heart itself. As an aneurysm increases in size, the risk of rupture increases. A ruptured aneurysm can lead to bleeding and subsequent hypovolemic shock, leading to death. Aneurysms are a result of a weakened blood vessel wall, and can be a result of a hereditary condition or an acquired disease.

Atherosclerosis
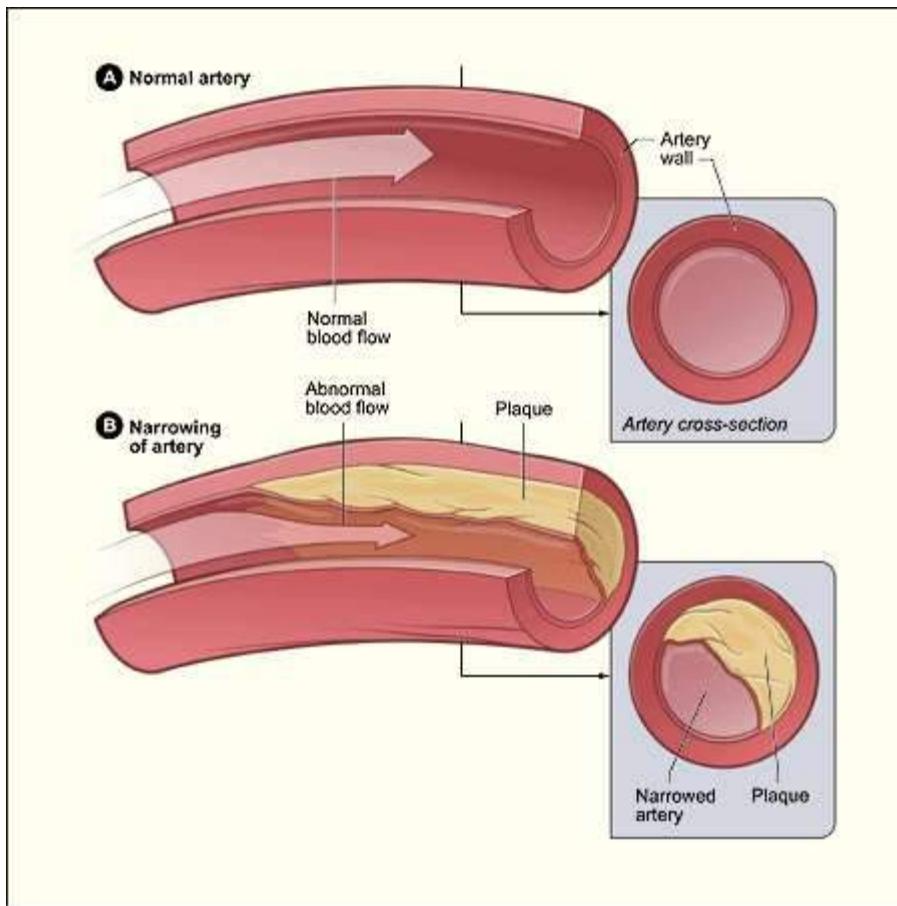
Fig. 1. 1. Shows a normal artery with normal blood flow. The inset image shows a cross-section of a normal artery.

Figure B shows an artery with plaque buildup. The inset image shows a cross-section of an artery with plaque buildup.

Figure is taken from the website http://www.nhlbi.nih.gov/ (National Heart, Lungs, and Blood institute).

1.1.6   Catheterization

Catheterization is the insertion of a catheter into a chamber or vessel of the heart. Catheters are commonly used for the diagnosis and treatment of diseases like atherosclerosis. Subsets of this technique are mainly coronary catheterization, involving the catheterization of the coronary arteries, and catheterization of cardiac chambers and valves of the cardiac system.

1.1.7   Externally imposed Body acceleration

The human body may experience body acceleration in many situations e.g. helicopter crew members, flying in an aircraft, astronauts, jet pilots, athletes and sportsmen for their sudden movements. In such situation, a human body may be subjected to vibratory or acceleratory motion. Such acceleratory motion is known as the imposed body acceleration. There are evidences that, prolonged exposures to the body acceleration may bring some serious physiological effects, e.g. headache, abdominal pain and loss of vision.

1.1.8   Womersley number

The Womersley number is a dimensionless number in bio-fluid mechanics. It is a dimensionless expression of the pulsatile flow frequency in relation to viscous effects. The Womersley number is also important in determining the thickness of the boundary layer to see if entrance effects can be ignored.

1.1.9   Reynolds number

The Reynolds number is defined as the ratio of momentum forces to viscous forces. In fluid mechanics, the Reynolds number is a dimensionless quantity that is used to help predict similar flow patterns in different fluid flow situations. Reynolds numbers frequently arise when performing scaling of fluid dynamics problems.

1.1.10   Fahraeus-Lindqvist (F-L) effect

The Fahraeus–Lindqvist (F-L) effect is an effect where the viscosity of a fluid, in this case blood, changes with the diameter of the tube it travels through. It is clear that red blood cells cannot pass through the capillary wall, which implies that the centers of red blood cells must lie at least one red blood cell half-thickness away from the wall. This means that, on average, there will be more red blood cells near the center of the capillary than very near the wall.

1.2   Literature Review

Though non-Newtonian in nature in diseased arteries, blood is also treated as Newtonian fluid by various researchers in stenotic arteries. Young et al. [1] undertaken a study to investigate the pressure loss across the arterial stenosis of varying severities at elevated flow rates and the corresponding effects of the stenosis on the vascular bed reserve. A technique for the solution of the approximate equations governing steady flow through models of mild axisymmetric arterial stenosis was presented by MacDonald [2]. Yongchareon and Young [3] studied experimentally the development of turbulence under both steady and pulsatile flow through models of arterial stenosis. Doffin and Chagnaeu [4] carried out a study to understand the special flow conditions which may be produced by a clot of blood in the vessel. A modified MAC-SOLA method was implemented by Liou et al. [5] to compute numerically the steady non-uniform viscous flow part a partial stenosis in a circular vessel. Pollard [6] investigated numerically the laminar flow in axisymmetric sudden expansions using three diameter ratios and up to four inlet velocity profiles. The pulsatile flow of blood with periodic body acceleration was investigated with the help of finite Hankel and Laplace transforms by Chaturani and Palanisamy [7]. Chakravarty et al. [8] studied pulsatile flow characteristics of blood in a distensible bifurcated artery having a stenosis when it is subjected to whole body acceleration. Two-dimensional blood flow through tapered arteries under stenotic conditions was numerically simulated by Chakravarty and Mandal [9]. Pulsatile flow of blood through stenotic artery using finite Hankel and Laplace transforms was studied by El-Shahed [10]. The application of Adomian decomposition method to blood flow through stenotic arteries in the presence of a magnetic field was presented by Halder [11]. A mathematical model based on the principles of Ferrohydrodynamics (FHD) and Magneto-hydrodynamics for bio-magnetic flow of blood in a stenotic channel was developed and simulated by Tzirtzilakis [12]. Mehmood et al [13] employed MAC method to understand the flow characteristics of an unsteady axi-symmetric two-dimensional blood flow in a diseased arterial segment with flexible wall. Sharma et al. [14] investigated uni-directional model of pulsatile flow of blood through a porous-saturated stenotic artery under the influence of transverse magnetic field. Eldesokyet al. [15] employed the differential quadrature

11

method (DQM) to study the unsteady pulsatile flow of blood through an artery filled with porous medium. A time-variant overlapping stenosis model was incorporated by Haghighi et al. [16] to simulate the pulsatile flow of blood through elastic tapered artery. Srivastava presented an analytical investigation of magneto-hydrodynamic blood flow in a porous inclined stenotic artery.

Recently, it is also observed through experiments that the rheological behavior of blood does not obey the Newtonian postulate, which linearly relates shear stress to the rate of deformation, and therefore cannot be modeled through Newtonian fluid. Blood exhibits non-Newtonian effects such as shear thinning, Thixotropy, Visco-elasticity and Yield Stress. It is pointed out by Cho and Kensey [17] that in large arteries the instantaneous shear rate over a cardiac cycle ranges from 0 to approximately 1000 s^{-1}. Therefore, over the whole cardiac cycle there exists a time span when the shear rate (σ) is low $\left(\sigma < 10^{-2} \, sec^{-1}\right)$, medium $\left(10^{-2} < \sigma < 10^{3} \, sec^{-1}\right)$ and high $\left(\sigma > 10^{3} \, sec^{-1}\right)$. Further observations reveal that shear rate is low in some regions for instance near bifurcations, grafts anastomoses, stenosis and aneurysms [18]. Blood being concentrated suspension of cells displays both thixotropic and visco-elastic behavior. However, thixotropy and visco-elasticity are exhibited by blood at low shear rates and they diminish as it rises. Blood behaves like a Newtonian fluid when shear rate exceeds over a critical value. Its critical value is 50 s^{-1} [19], 100 s^{-1} [20] or from 100 s^{-1} to 300 s^{-1} [21]. The shear thinning behavior is exhibited by normal blood at low and medium rates. Shear thinning is generally perceived as a decrease in the blood viscosity with increase in the shear rate. For instance the general shape of the curve of shear rate of blood flow indicates three distinct regions: a lower Newtonian region (low shear rate constant viscosity), an upper Newtonian region (high shear rate constant viscosity), and a middle region where apparent viscosity decreases with increasing shear rate. The choice of appropriate model to represent shear thinning effects should encompass all the above mentioned requirements. A critical review of blood flow in large arteries with relevance to blood rheology and physiological conditions is presented by Yilmaz and Gundogdu [22]. Studies pertaining to blood flow in stenotic arteries using different non-Newtonian models will be reviewed in the following paragraph.

Srivastava [23] examined the non-Newtonian effects of blood using couple stress model to study blood flow through mild stenotic artery. He concluded that the magnitude of resistance to flow and wall shear stress is greater in couple stress model as compared to the Newtonian model. The pulsatile flow of blood under body acceleration is studied by Majhi and Nair [24] using third grade fluid model. The Laplace transform technique was used by Misra and Pal [25] to obtained analytical solution for pulsatile flow of blood under externally imposed body acceleration. They have constructed a mathematical model by treating blood as a non-Newtonian fluid, using a biviscosity model for blood. Mandal [26] carried out a study using power-law model to investigate the effects of the non-Newtonian rheology of blood, the vessel tapering, the severity of stenosis and the wall deformability on pulsatile blood flow through stenotic arteries. A two-dimensional power law model for blood through an elastic stenosed artery in the presence of periodic body acceleration was presented by Mandal *et al.* [27]. The Power law model has been implemented successfully by Ismail et al. [28] to represent haemo-rheological transport phenomena through overlapping stenotic artery. The micropolar fluid model is a common choice to account for the suspension nature of blood in fluid dynamical studies on blood flow through stenotic arteries. The Eringen micropolar fluid model has been successfully applied to blood flow through stenotic arteries by Makheimer and Elkot [29]. Mathematical modelling of pulsatile flow of Casson's fluid in arterial stenosis is investigated by Siddique et al. [30]. Srivastava and Mishra [31] used the Casson fluid model for blood flow through overlapping stenotic artery. The Erigen micropolar fluid model has been used by Abdullah and Amin [32] and Abdullah et al. [33] to investigate the characteristics of blood through a tapered stenotic artery. Unsteady Analysis of viscoelastic blood flow through arterial Stenosis is examined by Ikal et al. [34]. Makheimer and Elkot [35] investigated mathematical modelling of unsteady flow of a Sisko fluid through an anisotropically tapered elastic arteries with time-variant overlapping stenosis. Numerical simulation of Casson fluid flow through differently shaped arterial stenosis are carried out by Sarifuddin et al. [36]. Akbar and Nadeem [37] analyzed steady flow of Carreau fluid in an artery under the assumption of mild stenosis using perturbation technique.

It has been observed through clinical studies that the stenosis may develop in series and may not be regular in shape. According to Moore [38] multiple stenosis and post-stenotic dilatations are common in the coronary arteries. Therefore investigations of hemodynamics in an artery with post-stenotic dilation is of major clinical significance. Very few studies in the literature deal with the simultaneous effects of stenosis and dilatation on flow through small arteries. Mention may be made of the work of Pincombe and Mazumdar [39], Pincombe et al. [40] and Wong et al. [41]. In the above studies Casson, Bingham and Ostwald-DeWaele power law models were used to characterize the rheology of blood. Supplementary to the above-mentioned studies, more sophisticated investigations addressing blood flow in three-dimensional models of human thoracic aorta at different stages of atherosclerotic lesion growth (using computed tomography images and a mathematical model of biological structures in relation to coronary arteries with atherosclerosis) have been presented by Dabagh et al. [42] and Wang et al. [43], respectively.

Medical catheters are commonly used for the diagnosis and treatment of diseases like atherosclerosis. The technique used for diagnosis of stenosis in coronary arteries is usually known as angiography while treatment procedure of such arteries is called as angioplasty. In diagnostic procedure, such as angiography, small catheters are inserted under X-ray guidance to the opening of coronary arteries in order to get information about location and severity of stenotic arterial segment. Once the location of the stenosis is identified, the next procedure is to treat the diseased segment through angioplasty. In angioplasty two types of Catheters namely, guided catheter and Doppler catheter are commonly used. Doppler catheters are used to monitor the changes in proximal and distal flow velocity during coronary angioplasty while guided catheters with a small balloon at their tips are inserted into the artery and advanced to the stenotic region of the coronary artery. The balloon is then inflated to enlarge the stenotic segment. When inserted in arteries, these catheters will significantly alter the flow patterns of blood. It has been shown by Kanai et al. [44] that apart from other factors, the error in the measurement of blood pressure by catheter-insertion may also be due to reflection of pressure wave at the tip of the catheter. Back and Denton [45] and Back [46] provided estimates of wall shear stress and mean flow resistance due to the insertion of a catheter in a stenosed artery. The influence of the presence and size of a catheter on mean pressure gradient across human coronary

stenosed artery was also examined by Back et al. [47]. The study of Sarkar and Jayaraman [48] revealed that pressure drop, shear stress and impendence vary markedly in the presence of catheter. Dash et al. [49] performed the analysis of blood in a curved catheterized stenosed artery and found that increase in catheter size leads to a considerable increase in pressure drop, impendence and wall shear stress. Apart from the attempts reported above, some other hemo-dynamical studies encompassing formation and progression of plaque in coronary artery, analysis in an intracranial aneurysm and mathematical analysis of differential models of circulatory system can be found in refs. [50-54]. For example, Dash et al. [55] carried out a study to estimate the increase in flow resistance in a narrow catheterized artery using a Casson model to account for blood rheology. A mathematical model of pulsatile flow of blood in a catheterized artery using Herschel-Bulkley constitutive equation is studied analytically by Sankar and Hemalatha [56]. Reddy et al. [57] utilized the constitutive equation of couple stress fluid and investigated the effect of tapering angle and slip velocity on unsteady blood flow through a catheterized stenosed artery. Two-phase model of blood flow through a catheterized stenosed artery is analyzed by Srivastava and Rastogi [58]. Nadeem and Ijaz [59] investigated the effects of nanoparticles on blood flow through a catheterized artery using regular perturbation method. Steady flow of a Herschel-Bulkley fluid in a catheterized artery is analyzed by Sankar and Hemalatha [60].

Hemodynamical studies reveal that blood shows anomalous behavior while flowing through large vessel (femoral artery) because its viscosity varies along the diameter of vessel which depicts Fahraeus-Lindqvist (F-L) effect. The definition of F-L effect is given in the literature as, a phenomena in which the viscosity of a fluid/blood changes with the diameter of the vessel. This effect is observed due to migration of suspended cells in the radial direction which is due to variation of composition of blood [61-63]. In order to capture the F-L effect, the blood flow in arteries is treated as two-phase. The core layer is treated as a non-Newtonian while peripheral layer is modeled as a Newtonian fluid. Since the flow of blood in arteries is generated by pulsatile pressure gradient produced by the pumping action of the heart, therefore several authors examined the F-L effects by considering the flow to be unsteady. For instance, Majhi and Usha [64]

have examined the F-L effect by considering third grade non-Newtonian fluid in the core. In another study, Majhi and Nair [65] followed the same study in the presence of body acceleration. Halder and Anderson [66] investigated the two-layer blood flow in a cosine shape artery considering Casson model for blood. The pulsatile flow of blood in the presence of body acceleration was examined by Usha and Prema [67] by considering blood as Newtonian fluid. Pulsatile flow of blood using a generalized second grade fluid model in the core region was investigated by Massoudi and Phouc [68]. Recently Sankar [69] carried out a perturbative analysis to discuss the one dimensional flow of blood through stenosed artery by taking Herschel–Bulkley fluid in the core. An unsteady analysis of blood flow through a stenotic artery using two-fluid model, consisting of Erigen's micropolar fluid in the core region was presented by Ikbal et al. [70].

1.3   Fundamental Equations

The analysis of blood flow is based on mass and momentum conservation equations. In this section, we shall give vectorial form of these equations.

1.3.1   Mass conservation/continuity equation

This equation relates the density at a point inside the fluid with the velocity at that point. In mathematical form, it reads

$$\frac{\partial \rho}{\partial t} + \nabla \cdot \left(\rho \, V \right) = 0, \tag{1.1}$$

where ρ is the fluid velocity and V is the velocity. For incompressible fluid, Eq. (1.1) reduces to continuity equation

$$\nabla \cdot V = 0, \tag{1.2}$$

1.3.2   The momentum equation

The momentum equation is based on law conservation of momentum. For a fluid flowing through a porous medium and subjected to magnetic field, the momentum equation reads

$$\rho \frac{dV}{dt} = \nabla \cdot T + \rho G(t) + J \times B + + \frac{\mu_{eff} V}{k'}, \tag{1.3}$$

where k' is the permeability of the porous medium, μ_{eff} is the effective viscosity of the porous medium, $G(t)$ is body acceleration vector, T is the Cauchy stress tensor, J is the current density, $B = B_0 + B_1$ is the total magnetic field, B_0 is the constant applied a magnetic field and B_1 is the induced magnetic field and d/dt is the material time derivative given by:

$$\frac{d(\bullet)}{dt} = \frac{\partial(\bullet)}{\partial t} + (V \cdot \nabla). \tag{1.4}$$

The expression of Cauchy stress tensor T is based on the choice of fluid model used to represent the rheology of blood.

1.3.3   Generalized Ohm's law

The current density J in Eq. (1.3) is given by

$$J = \sigma(E + V \times B), \tag{1.6}$$

where σ is the electrical conductivity of blood and E is the total electric field. In the present thesis, it is assumed that the induced magnetic field is negligible in comparison with constant applied magnetic field. Moreover, the imposed and induced electrical fields are also assumed to be negligible. Thus

$$J \times B = -\sigma \times B_0^{\,2} V. \tag{1.7}$$

1.3.4   Explicit Finite Difference Method

The finite difference approximations for derivatives are one of the simplest and the oldest methods to solve differential equations. The advent of finite difference techniques in numerical applications began in the early 1950s and their development was stimulated with the emergence of computers that offered a convenient framework for dealing with complex problems of science and technology.

An example of typical second order parabolic partial differential equation is taken to explain the forward time/ central space *(FTCS)* method [71].The model equation under consideration has the following form

$$\frac{\partial u}{\partial t} = \eta \frac{\partial^2 u}{\partial x^2},$$

(1.8)

where η is assumed as a constant. Let $\partial u / \partial t$ be represented by a forward difference approximation of order Δt:

$$\frac{\partial u}{\partial t} = \frac{u_i^{n+1} - u_i^n}{\Delta t} + O(\Delta t).$$

(1.9)

Similarly, the space derivative is represent by a central difference approximation formula:

$$\frac{\partial^2 u}{\partial x^2} = \frac{u_{i+1}^n - 2u_i^n + u_{i-1}^n}{(\Delta x)^2} + O(\Delta x^2).$$

(1.10)

In view of Eqs. (1.8) and (1.9), Eq. (1.1) can be approximated by the following difference equation:

$$\frac{u_i^{n+1} - u_i^n}{\Delta t} = \eta \frac{u_{i+1}^n - 2u_i^n + u_{i-1}^n}{(\Delta x)^2}.$$

(1.11)

In Eq. (1.8), u_i^{n+1} is the only unknown and, therefore, it can be computed in the following form

$$u_i^{n+1} = u_i^n + \frac{\Delta t \eta}{(\Delta x)^2} \left(u_{i+1}^n - 2u_i^n + u_{i-1}^n \right).$$

(1.12)

Now with suitably defined time and space step sizes Eq. (1.12) can be used along with initial/boundary conditions to compute u_i^{n+1}. It can been shown that the solution obtained via above expression is stable for $\Delta t \eta / (\Delta x)^2 \leq 0.5$.

Chapter 2

Numerical study of unsteady blood flow through a vessel using Sisko model

In this chapter, an analysis is carried out to study two-phase blood flow through an artery under the influence of pulsatile pressure gradient and externally imposed body acceleration. It is assumed that the blood in the core region obeys the Sisko constitutive equation whilst it behaves as a Newtonian liquid in the peripheral region. The mass and momentum conservation laws are used to model the proposed problem in terms of nonlinear partial differential equations. These equations along with initial and boundary conditions are made dimensionless and then solved numerically. The behavior of various flow quantitates is analyzed through a parametric study.

2.1   Mathematical formulation

For the present analysis, the artery is assumed to be a circular tube of radius a and a cylindrical co-ordinates (r, θ, z) system is employed. Following [68], a periodic forcing term due externally imposed body acceleration is also included in the force balance. The geometry of the flow configuration is presented in **Fig. 2.1**. Here it is shown that blood flow in the vessel is divided into two regions, a core region $0 \le r \le b$ and a periphery region $b \le r \le a$.
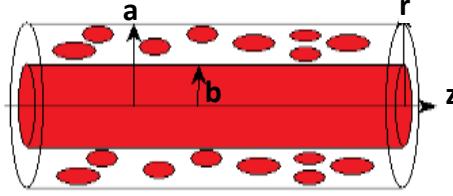
Fig. 2.1. Schematic diagram of flow in vessel.

For the subsequent analysis, it is assumed the Reynolds number associated with the flow is small. As an implication of this assumption the radial velocity can be neglected in comparison to the axial velocity. Thus for the present case the velocity field is taken as

$$V_i = [0, \ 0, \ u_i(r,t)], i = 1,2. \tag{2.1}$$

Where u_1 and u_2 are the axial velocities in core and periphery regions, respectively. Using Eq. (2.1) in Eq. (1.2), continuity equation is identically satisfied and z-component of equation of motion gives (in absence of magnetic field and porous medium)

$$\rho \frac{\partial u_i}{\partial t} = -\frac{\partial p}{\partial z} + \rho G(t) + \frac{1}{r} \frac{\partial}{\partial r} (r S_{rz}), i = 1,2. \tag{2.2}$$

where it is assumed that $G(t) = (0, 0, G(t))$. It is assumed that the fluid in the core is a Sisko fluid and in the periphery a Newtonian fluid. The Cauchy stress tensor for a Sisko fluid is given by [72]

$$T = -pI + S, \tag{2.3}$$

in which p is the pressure, I is the identity tensor and S is the extra stress tensor defined by

$$S = \left[\varepsilon_1 + \varepsilon_2 \left| \sqrt{\Pi} \right|^{n-1} \right] A_1^*, \tag{2.4}$$

where n, ε_1 and ε_2 are the material parameters of the Sisko fluid. The Sisko model include Newtonian and generalized power law models for $n = 1$ (or $\varepsilon_2 = 0$) and $\varepsilon_1 = 0$, respectively. The first Rivilin-Ericksen tensor A_1^* is defined by

20

$$A_1^* = L + L^T \tag{2.5}$$

in which
$$L = \nabla V \tag{2.6}$$

and
$$\Pi = \frac{1}{2} \, \mathrm{tr}\left(A_1^{*2}\right). \tag{2.7}$$

For a Newtonian fluid, the extra stress tensor is

$$S = \mu_2 A_1^*, \tag{2.8}$$

where μ_2 is the dynamic viscosity. In view of Eqs. (2.1), (2.4) and (2.8), the shear stress in core and periphery region is given by

$$S_{rz} = \begin{cases} \left[\varepsilon_1 + \varepsilon_2 \left|\dfrac{\partial u_1}{\partial r}\right|^{n-1}\right]\left(\dfrac{\partial u_1}{\partial r}\right), & 0 \le r \le b, \\[4mm] \mu_2 \dfrac{\partial u_2}{\partial r}, & b \le r \le a, \end{cases} \tag{2.9}$$

Following Burton [99], we choose

$$-\frac{\partial p}{\partial z} = A_0 + A_1 \cos \omega_p t, \tag{2.10}$$

where $\partial p / \partial z$ is the driving pressure gradient due to the contraction and expansion of the heart, A_0 and A_1 are the systolic and diastolic components of the pressure gradient, respectively, $\omega_p = 2\pi f_p$ is the circular frequency and f_p is the pulse rate frequency. Further, we assume $G(t)$ as follows:

$$G(t) = A_g \cos\left(\omega_b t + \phi\right). \tag{2.11}$$

In Eq. (2.11) A_g is the amplitude, f_b is the frequency $[\omega_b = 2\pi f_b]$ and ϕ is the lead angle of $G(t)$ with respect to the heart action. Eliminating S_{rz} between (2.7) and (2.8), the equation in the core region. i.e $0 \le r \le b$ is obtained as

$$\rho \frac{\partial u_1}{\partial t} = A_0 \left(1 + \frac{A_1}{A_0} \cos(\omega_p t) \right) + \rho A_g \cos\left(\omega_b t + \phi\right) + \frac{1}{r} \frac{\partial}{\partial r} \left\{ r \left[\varepsilon_1 + \varepsilon_2 \left| \left(\frac{\partial u_1}{\partial r} \right) \right|^{n-1} \right] \left(\frac{\partial u_1}{\partial r} \right) \right\}. \tag{2.12}$$

Similarly, for the periphery region i.e $b \leq r \leq a,$ we get

$$\rho \frac{\partial u_2}{\partial t} = A_0 \left(1 + \frac{A_1}{A_0} \cos(\omega_p t) \right) + \rho A_g \cos\left(\omega_b t + \phi\right) + \frac{\mu_2}{r} \frac{\partial u_2}{\partial r} + \mu_2 \frac{\partial^2 u_2}{\partial r^2}. \tag{2.13}$$

The boundary and initial conditions for the present flow configuration are

$$\left. \begin{array}{ll}
\left. \dfrac{\partial u_1(r,t)}{\partial r} \right|_{r=0} = 0, & \left(\text{Symmetry condition}\right) \\[2mm]
\left. u_2(r,t) \right|_{r=a} = 0, & \left(\text{No} - \text{slip condition}\right) \\[2mm]
\left. u_1(r,t) \right|_{r=b} = \left. u_2(r,t) \right|_{r=b}, & \\[2mm]
\left. \left[\varepsilon_1 + \varepsilon_2 \left| \left(\dfrac{\partial u_1}{\partial r} \right) \right|^{n-1} \right] \left(\dfrac{\partial u_1}{\partial r} \right) \right|_{r=b} = \left. \mu_2 \dfrac{\partial u_2}{\partial r} \right|_{r=b}, &
\end{array} \right\} \tag{2.14}$$

$$u_1(r,t) = u_2(r,t) = 0, \quad at \ t = 0. \quad \text{(Initial conditions)} \tag{2.15}$$

The last two boundary conditions in (2.14) represent the continuity of velocities and stresses at the interface.

The expressions of flow rate and wall shear stress are respectively given by

$$Q = 2\pi \int_0^b u_1 r \, dr + 2\pi \int_b^a u_2 r \, dr, \tag{2.15}$$

$$\tau_s = -\mu_2 \left(\frac{\partial u_2}{\partial r} \right)_{r=a}. \tag{2.16}$$

2.2   Dimensionless formulation of the problem

Introducing the dimensionless variables [68]

$$\bar{r} = \frac{r}{a}, \ \bar{u} = \frac{u}{U_0}, \ \bar{t} = \frac{\omega_p}{2\pi} t, \tag{2.17}$$

Where U_0 and ω_p are average velocity and angular frequency, respectively. Eqs. (2.12) - (2.13) may be

casted as (after dropping bars)

$$\alpha\left[\frac{\partial u_1}{\partial t}\right] = B_1\left(1+e\,cos(2\pi t)\right) + B_2\left(\cos\left(2\pi\omega_r t + \phi\right)\right) + \frac{1}{r}\left\{\left[\varepsilon + \left|\left(\frac{\partial u_1}{\partial r}\right)\right|^{n-1}\right]\left(\frac{\partial u_1}{\partial r}\right)\right\} +$$

$$+ \left\{\left[\varepsilon + \left|\left(\frac{\partial u_1}{\partial r}\right)\right|^{n-1}\right]\frac{\partial^2 u_1}{\partial r^2}\right\} + \left(\frac{\partial u_1}{\partial r}\right)\left\{\frac{\partial}{\partial r}\left(\left|\left(\frac{\partial u_1}{\partial r}\right)\right|^{n-1}\right)\right\},$$

(2.18)

$$\gamma\frac{\partial u_2}{\partial t} = \hat{B}_1\left(1+e\,cos(2\pi t)\right) + \hat{B}_2\left(\cos\left(2\pi\omega_r t + \phi\right)\right) + \frac{1}{r}\left[\frac{\partial u_2}{\partial r}\right] + \frac{\partial^2 u_2}{\partial r^2}.$$

(2.19)

Where α and γ are the Womersley numbers. The other parameters appearing in Eqs. (2.18) and (2.19) are

$$U_0 = \left(\frac{A_0 b^2}{\mu_2}\right), \omega_r = \frac{\omega_b}{\omega_p}, \rho^* = \frac{\rho_2}{\rho_1}, \mu^* = \frac{\mu_2}{\bar{\varepsilon}}, \quad \bar{\varepsilon} = \varepsilon_2\left(\frac{U_0}{a}\right)^{n-1}, \varepsilon = \frac{\varepsilon_1}{\bar{\varepsilon}}, e = \frac{A_1}{A_0},$$

$$B_1 = \frac{A_0 b^2}{\bar{\varepsilon}U_0}, B_2 = \rho_1 A_g\frac{b^2}{\bar{\varepsilon}U_0} = \frac{\rho_1 A_g}{A_0}B_1, \alpha = \frac{\rho_1\omega_p b^2}{2\pi\bar{\varepsilon}}, \gamma = \frac{\rho_2\omega_p b^2}{2\pi\bar{\varepsilon}\mu^*} = \frac{\rho_1\omega_p b^2}{2\pi\mu^*}\frac{\rho_2}{\rho_1} = \alpha\frac{\rho^*}{\mu^*},$$

$$\hat{B}_1 = \frac{A_0 b^2}{\bar{\varepsilon}U_0\mu^*} = \frac{B_1}{\mu^*}; \hat{B}_2 = \frac{\rho_2 A_g b^2}{\bar{\varepsilon}U_0\mu^*} = \rho_1 A_g\frac{b^2}{\bar{\varepsilon}U_0}\frac{\rho_2}{\rho_1\mu^*} = B_2\frac{\rho^*}{\mu^*}.$$

(2.20)

The dimensionless boundary conditions becomes

$$\left.\frac{\partial u_1}{\partial r}\right|_{r=0} = 0,$$

$$u_2\big|_{r=1} = 0,$$

$$u_1\big|_{r_0} = u_2\big|_{r_0},$$

$$\left[\varepsilon + \left|\left(\frac{\partial u_1}{\partial r}\right)\right|^{n-1}\right]\left(\frac{\partial u_1}{\partial r}\right)\bigg|_{r=r_0} = \mu^*\frac{\partial u_2}{\partial r}\bigg|_{r=r_0},$$

(2.21)

where $r_0 = b/a$. It is pointed out that Eq. (2.18) reduces to the corresponding equation of Massoudi and

Phuoc [68] when $\varepsilon \to 0$. In dimensionless variables, volume flow rate and wall shear stress become

$$Q = 2\pi\left(\int_0^{r_0} u_1 r dr + \int_{r_0}^1 u_2 r dr\right),$$

(2.22)

$$\tau_s = \left(\frac{\partial u_2}{\partial r}\right)_{r=1}.$$

(2.23)

2.3   Numerical solution

We have integrated the Eqs. (2.18) - (2.19) with the initial and boundary data given in Eq. (2.21) numerically by using a finite difference method which is forward in time and central in space. Let us denote $u_1\left(r_i, t_j\right)$ as u_{1i}^j and approximate various partial derivatives as

$$\frac{\partial u_1}{\partial r} \cong \frac{u_{1i+1}^j - u_{1i-1}^j}{2\Delta r} = u_{1r},$$

$$\frac{\partial^2 u_1}{\partial r^2} \cong \frac{u_{1i+1}^j - 2u_{1i}^j + u_{1i-1}^j}{\left(\Delta r\right)^2} = u_{1r^2},$$

$$\frac{\partial}{\partial r}\left(\left|\frac{\partial u_1}{\partial r}\right|^{n-1}\right) \cong \frac{\left(\left|\frac{u_{1i+1}^j - u_{1i-1}^j}{2\Delta r}\right|^{n-1}\right)_{i+1}^j - \left(\left|\frac{u_{1i+1}^j - u_{1i-1}^j}{2\Delta r}\right|^{n-1}\right)_{i-1}^j}{2\Delta r} = abs\left(u_{1r}\right), \tag{2.24}$$

Similarly, for the time derivative we define the approximation:

$$\frac{\partial u_1}{\partial t} \cong \frac{u_{1i}^{j+1} - u_{1i}^j}{\Delta t} = u_{1t}. \tag{2.25}$$

The partial derivative of axial velocity computed u_2 are approximated in a similar manner. Using (2.24) and (2.25), Eqs. (2.18) and (2.19) take the following discretized form

$$u_{1i}^{k+1} = u_{1i}^k + \frac{\Delta t}{\alpha}\left[B_1\left(1 + e\ cos(2\pi t^k)\right) + B_2\left(\cos\left(2\pi\omega_r t^k + \phi\right)\right) + \right.$$
$$\left. \left\{\left(\varepsilon + \left|u_{1r}\right|^{n-1}\right)u_{1r^2} + \left(u_{1r}\right)abs\left(u_{1r}\right) + \frac{1}{r}\left(\varepsilon + \left|u_{1r}\right|^{n-1}\right)u_{1r}\right\}\right], \tag{2.26}$$

$$u_{2i}^{k+1} = u_{2i}^k + \left(\frac{\Delta t}{\gamma}\right)\left[B_1\left(1 + e\ cos\left(2\pi t^k\right)\right) + B_2\left(\cos\left(2\pi\omega_r t^k + \phi\right)\right) + \frac{1}{r}\left[u_{2r}\right] + u_{2r^2}\right]. \tag{2.27}$$

For the solution of present problem we have discretized the radius by using the formula $r_i = (i-1)\Delta r,$

$\left(i = 1, 2, ..., N_c + 1\right)$ such that $r_{(N_c+1)} = r_{core}$ and $r_i = \left(i - \left(N_c + 1\right)\right)\Delta r, \ i = \left(N_c + 1, N_c + 2, \ ......, N + 1\right)$ with

$r_{N+1} = 1,$ where Δr is the increment in the radial direction. Similarly for discretization of time, we have use

the following discretization formula $t_j = (j-1)\,\Delta t,\ (i = 1,2,.....)$, where Δt is the small time increment. For the present computations, we have chosen $\Delta r = 0.025$ and $\Delta t = 0.00001$, so that the results are accurate up to $\sim 10^{-7}$.

2.4   Results and discussion

To observe the quantitative effects of the Sisko material parameter, computer code is developed for the numerical simulations in Matlab. In this study, generally we have taken $\phi = 0$ and assume the core radius to be 60% of the tube radius. Our results are based on the data of two different arteries (radius): Smaller vessel, coronary artery, the data is chosen as ($A_0 = 698.65\ dyne/cm^3$, $a = 0.15\ cm$) and for larger vessel, femoral artery, the data is chosen as ($A_0 = 32\ dyne/cm^3$, $a = 0.5\ cm$) [68] and value of *Womersley number* is chosen as 2. Moreover, in all the simulations we have assumed $\hat{B}_1 = B_1$, $\hat{B}_2 = B_2$ and $\alpha = \gamma$.

$$B_1 = 1.41, \quad B_2 = 21.67, \quad n = 0.635$$
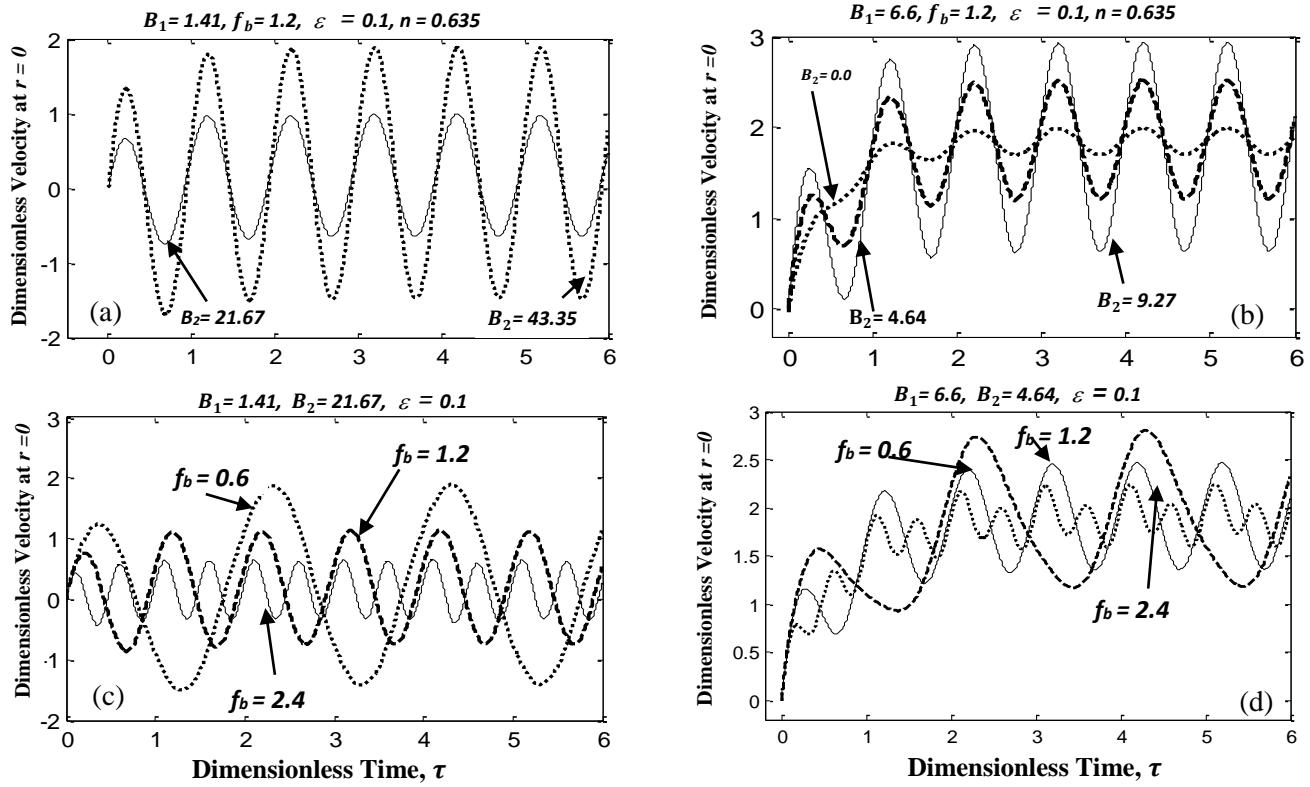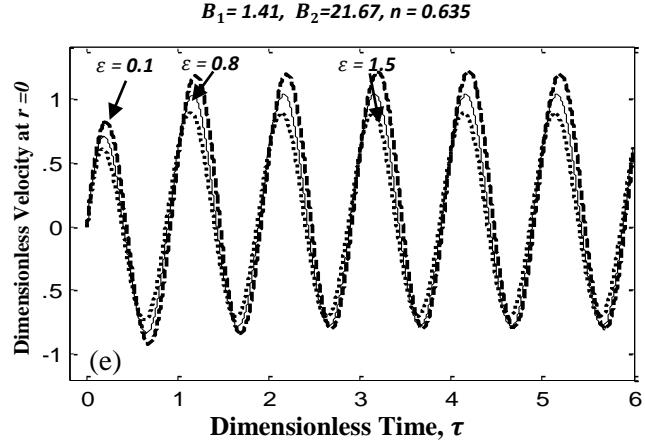
Fig. 2.2. Time -series of velocity at $a = 0$ for flow in two arteries, where Figs. 2.2 a, c and e are for larger *artery (a = 0.5 cm, A_0 = 32 dyne/cm^3)* and Figs. 2.2 b and d are for smaller *artery (a = 0.15 cm, A_0 = 698.65 dyne/cm^3)*. Velocity graphs for different values of B_2 (varying A_g) are shown in Fig. 2.2 (a, b); Velocity graphs for different values of f_b are shown in the Fig. 2.2(c and d); velocity graphs for different values of ε are shown in Fig. 2.2 (e).

The time-series of velocity at the central plane are shown in **Fig. 2.2** for both femoral and coronary arteries. These graphs shows that irrespective of the artery type, the velocity at the centre fluctuates around its mean value, increases and eventually attains the steady state condition as the time increases (here we define τ_s is the dimensionless steady state time where the maximum velocity distribution is obtained). Fig. 2.2 (a) and (b) show that the amplitude of the velocity increases by increasing the amplitude of the body acceleration while it shows decreasing trend by increasing the pulse frequency f_b (Fig. 2.2 (c) and (d)) and material parameter of the Sisko model (Fig. 2.2(e)).
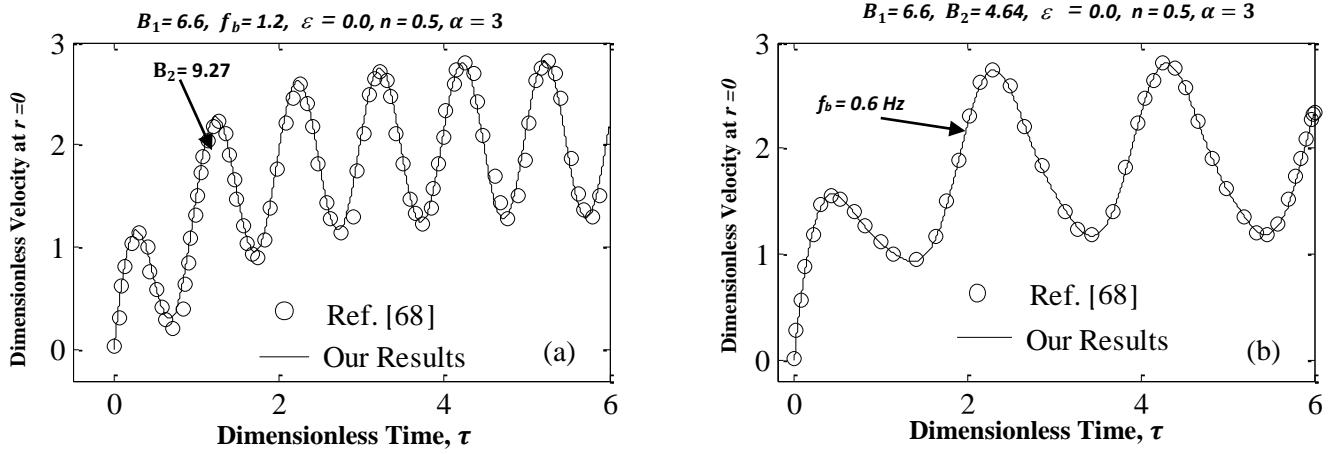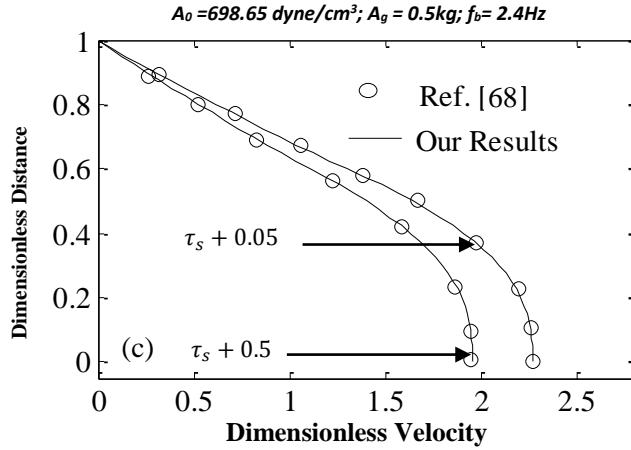
Fig. 2.3: Comparison of our results with Massoudi and Phuoc results for coronary artery.

A comparison of our numerical results in the limiting case when $\varepsilon \to 0$ with that of Massoudi and Phuoc [68] is presented in **Fig. 2.3**. Here radial and time evolutions of axial velocity for coronary artery are compared. It is observed that our results are in pleasing agreement with the existing results of Massoudi and Phuoc [68]. This obviously corroborates the validity of our model and further strengthen our faith on results obtained through it.

f_b = 1.2 Hz; B_1=0.25; B_2 = 3.83; ε = 0, n = 1

(e)

$\tau_s + 0.0$

$\tau_s + 0.1$

$\tau_s + 0.3$

$\tau_s + 0.2$

$\tau_s + 0.5$

f_b = 1.2 Hz; B_1=1.41; B_2 = 21.67; ε = 0.1

(f)

$\tau_s + 0.2$

$\tau_s + 0.1$

$\tau_s + 0.0$

$\tau_s + 0.3$

$\tau_s + 0.5$
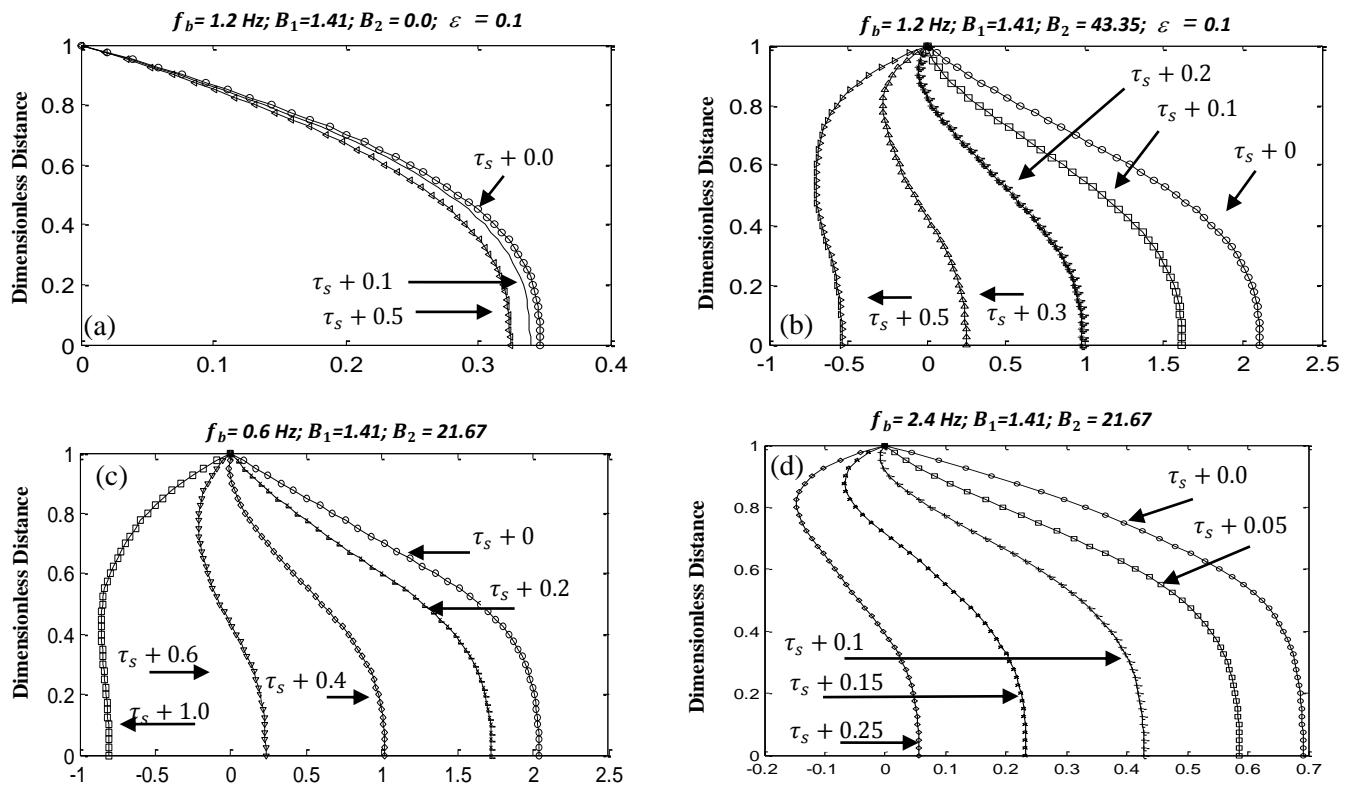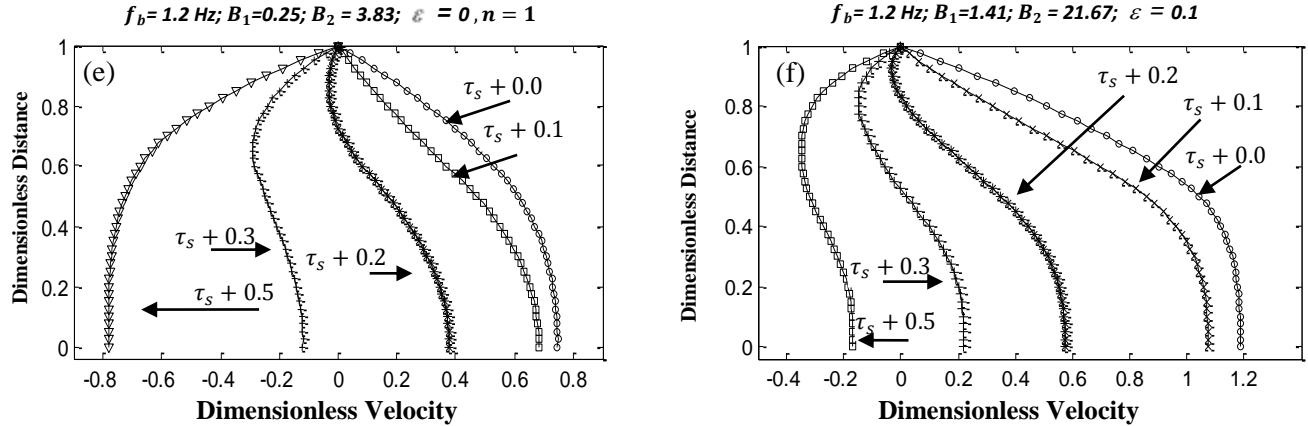
Fig. 2.4: Radial distribution of axial velocity graphs for larger artery *(a = 0.5 cm, A₀ = 32 dyne/cm³)*. Velocity Graphs for different values of B_2 (varying A_g) are shown in Fig. 2.4 (a and b); Graphs for different values of f_b are shown in Fig. 2.4(c and d); Graphs for different values of B_1 and B_2 are shown in Fig. 2.4 (e and f).

The velocity profiles at different time instants for femoral artery are shown in **Fig. 2.4**. It is generally observed from these plots that the body acceleration increases the magnitude of velocity while an increase in pulse frequency f_b decreases its magnitude. There are inflection points within time cycle of the velocity profile where the shapes of velocity changes from convex to concave. It is observed from Fig. 2.4 (a) that the shape of the velocity profile is parabolic in the absence of body acceleration at the beginning of the fluctuation cycle or $t = \tau_s$ as evident in Fig. 2.4 (b). Figs. 2.4 (c) and (d) indicate that the maximum velocity shifts from the centre of an artery toward the wall during the first half of fluctuation cycle and then moving back to the centre of an artery during the second half of fluctuation cycle. The core region is taken as Newtonian and the effects of body acceleration are minimized in comparison with other panels in Fig. 2.4 (e). It is noted from this figure that the velocity profile returns to its parabolic shape and the curve becomes concave at $t = \tau_s + t_{half}$. In Fig. 2.4(f) the core region is assumed as non-Newtonian fluid and effect of body acceleration is increased. This results in the forward shift of the fluctuation cycle.

The velocity profile for smaller artery, coronary artery, is shown in **Fig. 2.5**. Figs. 2.5 (a)-(b) show that the velocity profiles follow the same pattern as shown in Fig. 2.4. A Comparison of the velocity profiles in Figs. (2.4) and (2.5) for two arteries reveals that the velocity is faster in larger artery as compare to smaller

artery while its grows significantly slowly for Newtonian case as compared to the non-Newtonian case. Fig. 2.5 (g) shows the effect of material parameter of Sisko model. It is found that the magnitude of velocity increases by decreasing ε which ultimately shows that velocity profile is a decreasing function of material parameter. Fig. 2.5(h) show a decrease in velocity by increasing the thickness of the peripheral layer.
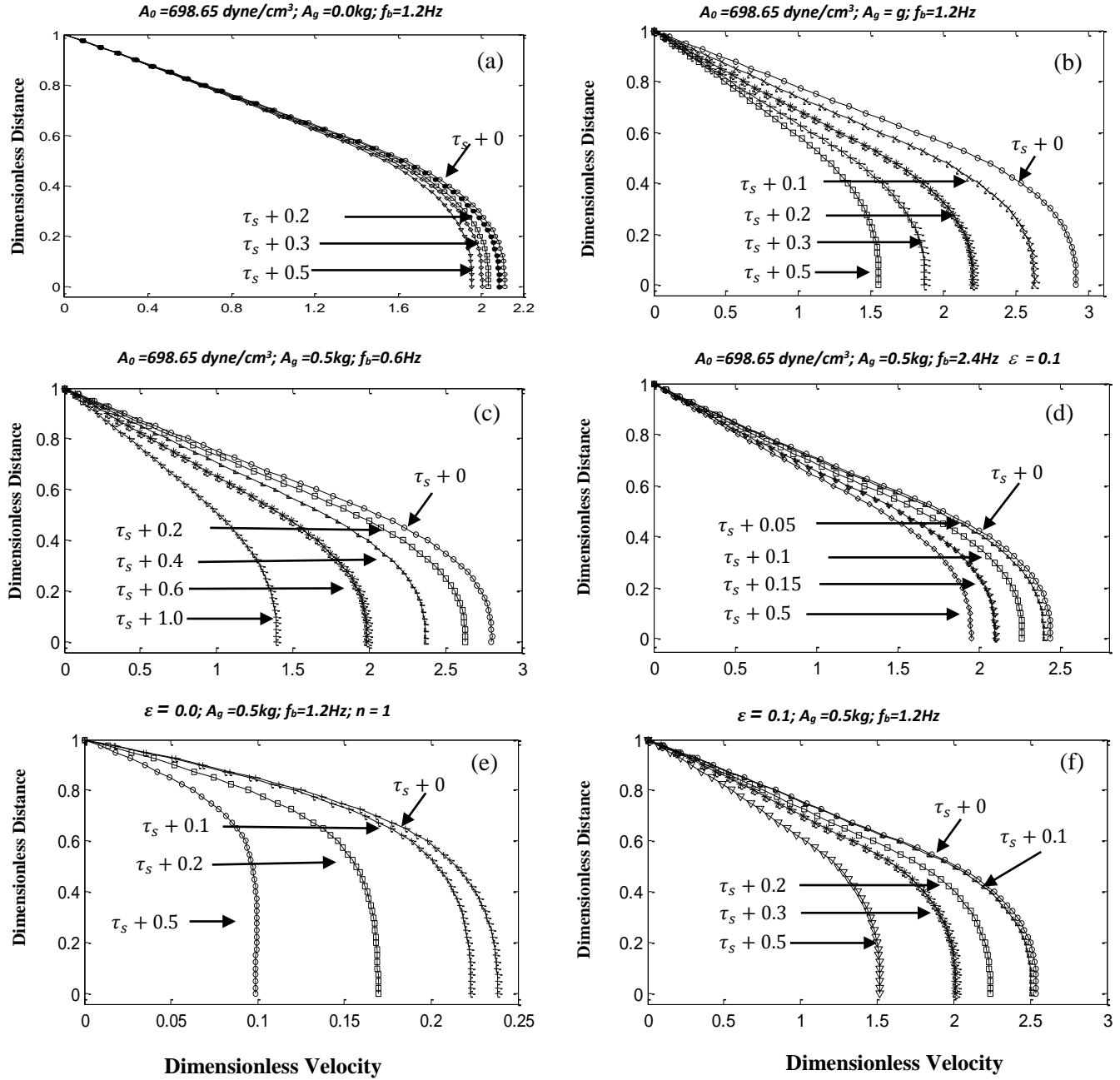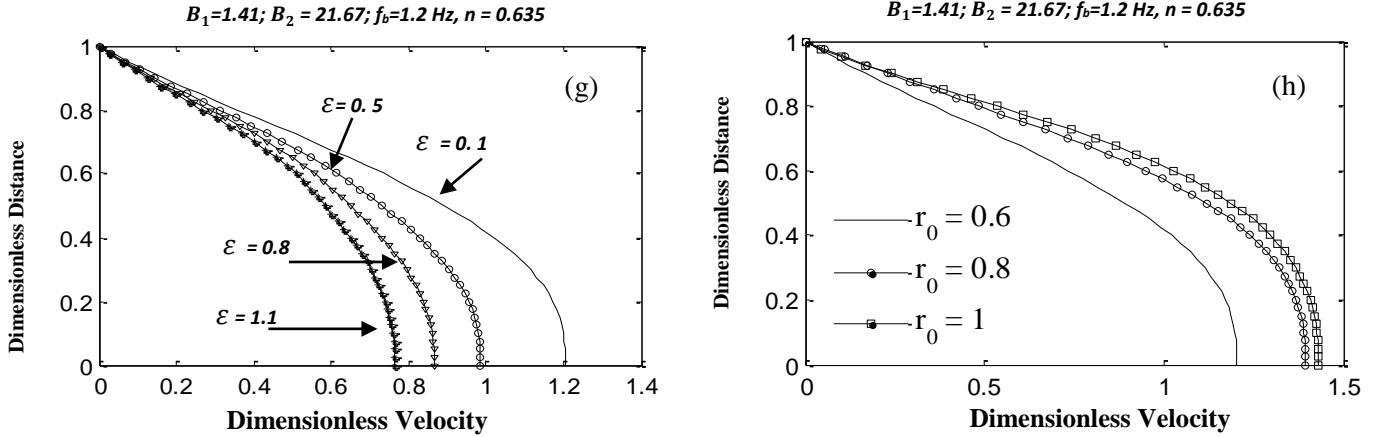
Fig. 2.5. Dimensionless Velocity graphs for smaller artery *(a = 0.15 cm, A_0 = 698.65 dyne/cm³)*. The Effects of B_2 (varying A_g) are shown in Fig. 2.5 (a & b); Velocity graphs for different values of f_b are shown in Fig. 2.5 (c & d); Graphs for different values of ε are shown in Fig. 2.5 (e, f and g); Graphs for different peripheral thickness are shown in Fig. 2.5 (h).

Figs. 2.6 and 2.7 present the effects of body acceleration A_g, body force f_b, shear-thinning and material parameter on the dimensionless wall shear stress and flow rate. The profiles indicate that the flow rate and the wall shear stress fluctuate around mean values and these mean values become constant values when steady state conditions are achieved. It is also observed that the amplitude of fluctuation increase with an increase in the amplitude of body acceleration while it shows converse behavior with increasing the material constant of the Sisko model. The fluctuation of these profile is always between a positive and a negative value in the time cycle for the larger artery, while for the small artery such fluctuation of wall shear stress in the smaller artery are significantly higher (about three to five times) than those obtained for the larger artery.

Now in the end, we would like to comment on significance of Sisko model in the light of above discussion. It has been pointed by Yilmaz and Gundogdu [22] that all the generalized Newtonian fluid models of (blood) viscosity show shear-thinning behavior and must meet the following requirements. They must effectively fit the viscosity shear rate data of blood at all shear rates, whether high, medium or low. Power-law model is suitable for blood at medium shear rates. However, it does not represent the blood rheology at low and high shear rates. In fact power-law equation predicts infinite viscosity at low shear rate and zero

viscosity as shear rate approaches to infinity. Sisko model extends the power-law model to include a finite value of viscosity as shear rates approaches infinity. In this sense, Sisko model is better capable of predicting the blood rheology at high shear rates. Graphical illustrations show that the additional constant μ_∞ (ε in dimensionless form) in Sisko equation significantly alters the flow characteristics of blood. It is observed that the power-law model predicts higher value of the amplitude of dimensionless velocity at $r = 0$ than the Sisko model. Similar is the case with dimensionless radial velocity. This significant effect of ε on velocity is later transmitted in other variables such as flow rate and wall shear stress. It is found that flow rate through artery decreases whilst wall shear stress increases in going from power-law to Sisko model. For instance, keeping the other parameters fixed, a decrease of 20 % is noted in the flow rate as ε changes from *0 to 1.5*.

The above discussion clearly shows that inclusion of ε in the power law equation brings significant qualitative changes in the results.
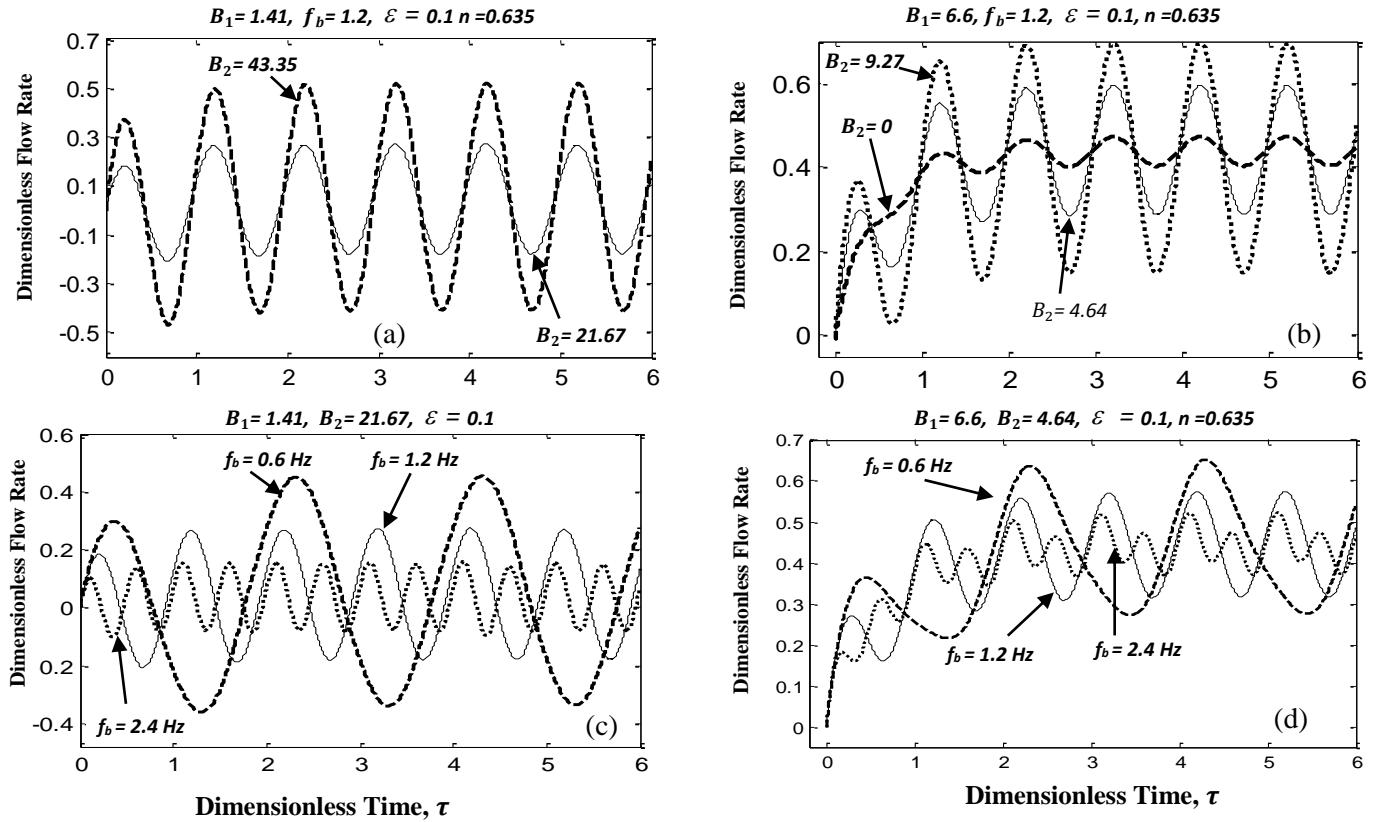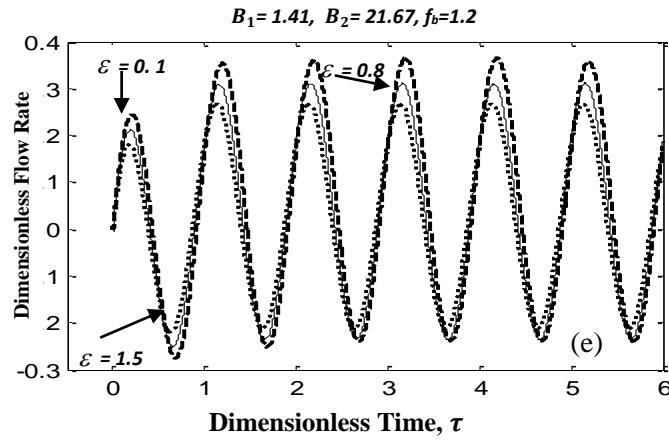
Fig. 2.6. Flow rate graphs in two different artery for different values of emerging parameters. Figs.2.6 a, c and e are for larger artery and Figs.5 b and d are for smaller artery. Fig.2.6 (a and b) demonstrate the effects of varying B_2; Graphs for different values of f_b are shown in Fig.2.6 (g and h) and Fig.2.6 (e) shows the effects of varying ε.

2.5   Concluding Remarks

A mathematical model for two-layer unsteady pulsatile flow in the presence of body acceleration is developed using the constitutive equation of a Sisko model. The important phenomena associated with the flow under consideration are discussed in detail and their interaction with pulsatile pressure gradient and body acceleration is analyzed. Following points are concluded from this study.

➤ The magnitude of blood velocity in the femoral artery is greater than in the coronary artery.

➤ Body acceleration increases the amplitude of the flow velocity.

➤ The material parameter of Sisko has greater influence on blood flow in coronary artery as compared to the femoral artery.

➤ This study also demonstrate the potential of rheological properties of the blood to control the important variables associated with the blood flow.

➤ The results obtained here show pleasing agreement with the existing results of Massoudi and Phuoc [68].

32
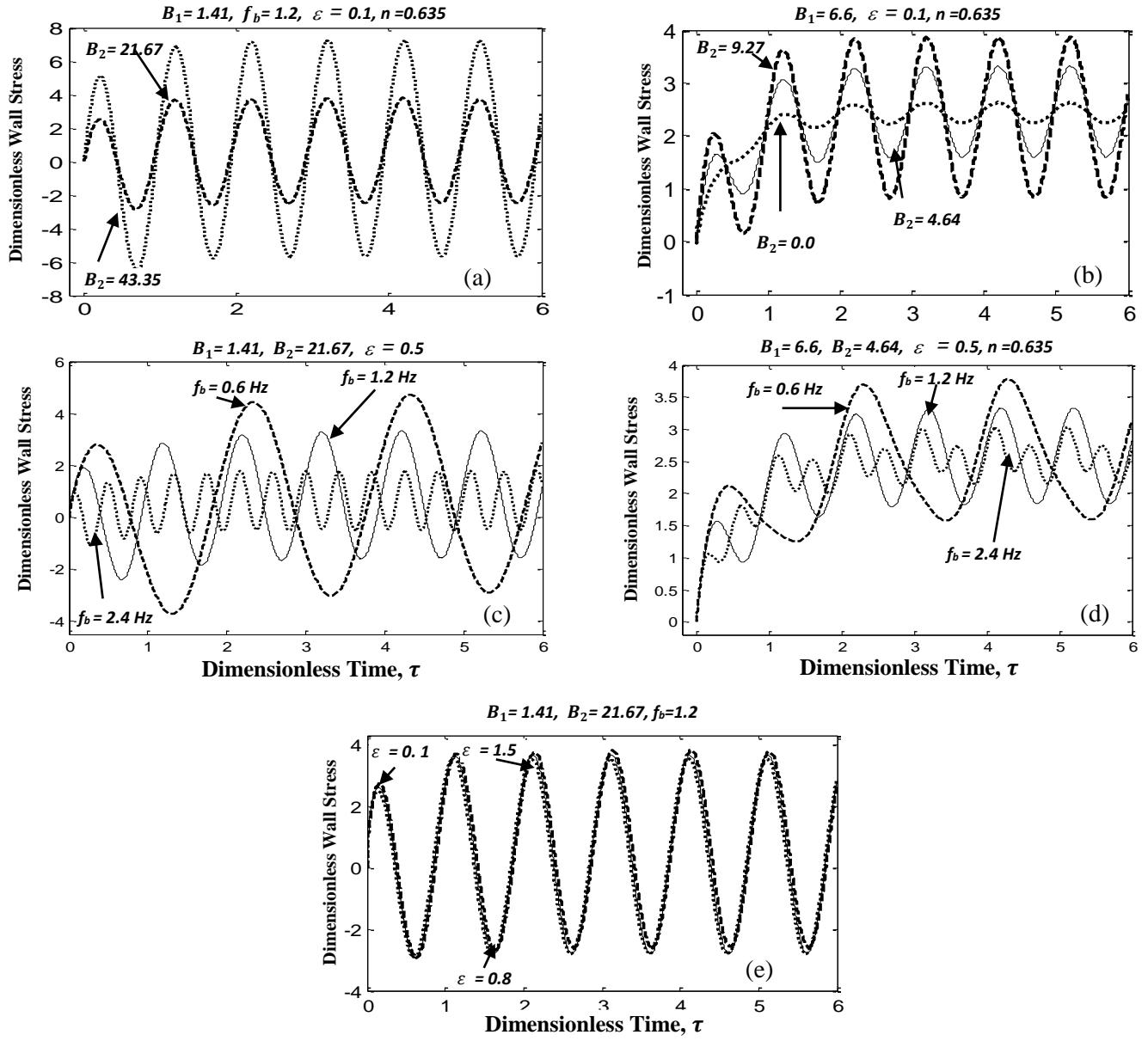
Fig. 2.7. Wall shear stress graphs in two different arteries for different values of emerging parameters. Figs. 2.7 a, c and e are for larger artery and Figs. 2.7 b and d are for smaller artery. Fig.2.7 (a and b) demonstrates the effects of varying B_2 $(A_g = 0,5g)$; Fig.2.7 (c and d) shows the effects of varying f_b $(A_g=0,5g)$ and Fig.2.7 (e) demonstrates the effects of varying ε.

Chapter 3

Computations of pulsatile blood flow in a tube for an Oldroyd-B fluid

This chapter investigates the effects of body acceleration on unsteady pulsatile flow of blood in a vessel. The non-Newtonian behavior of blood in the core region is modeled by the constitutive equation of an Oldroyd-B fluid. The peripheral region is assumed to obey Newtonian constitutive law. Our interest lies in investigating the effects of stress relaxation and retardation on various hemodynamical variables associated with the unsteady blood flow. The modeled equations are normalized and solved numerically using finite difference method. The results are graphically displayed and impact of various parameters on physical quantities of interest is analyzed.

3.1   Problem formulation

The flow geometry and the underlying assumptions are same as described in the previous chapter. However, the rheological behavior of streaming blood in the core region, in this chapter, is characterized by an Oldroyd-B fluid model.

The extra stress tensor of an Oldroyd-B fluid is given by [73]

$$ \mathbf{S} + \tau_1 \overset{\triangledown}{\mathbf{S}} = \mu_1 \left[\mathbf{A}_1^* + \tau_2 \overset{\triangledown}{\mathbf{A}_1^*} \right], \tag{3.1} $$

34

where τ_1, τ_2 are the relaxation and retardation times respectively, μ_1 is the viscosity of the blood in core region. $\overset{\nabla}{S}$ is the upper convected time derivative (a materially objective time derivative)

$$\overset{\nabla}{S} = \frac{\partial S}{\partial t} + V \cdot \nabla S - \left((\nabla V) \cdot \nabla S + S \cdot (\nabla V) \right) \tag{3.2}$$

In view of Eq. (3.1), the shear stress in the core region $(0 \leq r \leq b)$ satisfies

$$\left(1 + \tau_1 \frac{\partial}{\partial t} \right) S_{rz} = \mu_1 \left(1 + \tau_2 \frac{\partial}{\partial t} \right) \frac{\partial u_1}{\partial r}. \tag{3.3}$$

The shear stress in the periphery region $(b \leq r \leq a)$ is already defined in Eq. (2.8). Eliminating S_{rz} between Eqs. (3.3) and (2.7), we get the governing equation for flow in the core region:

$$\rho \left[\frac{\partial u_1}{\partial t} + \tau_1 \frac{\partial^2 u_1}{\partial t^2} \right] = A_0 \left(1 + \frac{A_1}{A_0} \cos(\omega_p t) \right) - \frac{A_1}{A_0} \tau_1 \omega_p \sin(\omega_p t) + \rho A_g \cos(\omega_p t + \phi)$$

$$- \rho A_g \tau_1 \omega_p \sin(\omega_p t) + \mu_1 \left[\frac{\partial^2 u_1}{\partial r^2} + \tau_2 \frac{\partial}{\partial t} \left(\frac{\partial^2 u_1}{\partial r^2} \right) \right] + \frac{\mu_1}{r} \left(\frac{\partial u_1}{\partial r} + \tau_2 \frac{\partial}{\partial t} \left(\frac{\partial u_1}{\partial r} \right) \right). \tag{3.4}$$

The flow in periphery region is governed by Eq. (2.12). Eqs. (3.4) and (2.12) are subject to same boundary and initial conditions as defined in (2.13) and (2.14) except at the interface $r = b$. At the interface $r = b$, we shall only employ the condition of continuity of the velocities.

3.2 Dimensionless analysis

To this end, we first normalize these equations by using the new variables as defined in Eqns. (2.17). In terms of new variables Eqns. (3.4) and (2.12) after dropping the bars yield

$$\alpha \left[\frac{\partial u_1}{\partial t} + \lambda_1 \frac{\partial^2 u_1}{\partial t^2} \right] = B_1 \left(1 + e \cos(2\pi t) \right) - \left(2\lambda_1 e B_1 \pi \right) \sin(2\pi t) + B_2 \left(\cos(2\pi \omega_r t + \phi) \right)$$

$$- \left(2\pi \omega_r B_2 \lambda_1 \right) \sin(2\pi \omega_r t) + \left\{ \frac{\partial^2 u_1}{\partial r^2} + \lambda_2 \frac{\partial}{\partial t} \left(\frac{\partial^2 u_1}{\partial r^2} \right) \right\}$$

$$+ \left\{ \frac{1}{r} \left(\frac{\partial u_1}{\partial r} \right) + \frac{\lambda_2}{r} \frac{\partial}{\partial t} \left(\frac{\partial u_1}{\partial r} \right) \right\}, \tag{3.5}$$

$$\gamma \frac{\partial u_2}{\partial \bar{t}} = B_1\left(1 + ecos(2\pi t)\right) + B_2\left(cos\left(2\pi \omega_r t + \phi\right)\right) + \frac{1}{r}\left[\frac{\partial u_2}{\partial r}\right] + \frac{\partial^2 u_1}{\partial r^2}, \tag{3.6}$$

where $\lambda_1 = \tau_1 \omega_p / 2\pi,\ \lambda_2 = \tau_2 / \mu^*$.

The dimensionless boundary and initial conditions become

$$\left.\frac{\partial u_1}{\partial r}\right|_{\bar{r}=0} = 0,\ \ u_2\big|_{r=1} = 0,\ \ u_1\big|_{r_0} = u_2\big|_{r_0}. \tag{3.7}$$

The volume flow rate and the shear stress at the wall are defined through expressions (2.21) and (2.22), respectively.

$$Q = 2\pi\left(\int_0^{r_0} u_1 r dr + \int_{r_0}^1 u_2 r dr\right), \tag{3.8}$$

$$\tau_s = \left(\frac{\partial u_2}{\partial r}\right)_{r=1}.$$

The various dimensionless variables appearing in Eqs. (3.5) and (3.6) are already defined in previous chapter through Eq. (2.23). The reader is only cautioned to use $\bar{\mu}$ instead of $\bar{\varepsilon}$ in Eq. (2.23) for the definitions of dimensionless variables appearing in this chapter.

3.3   Numerical solution using finite difference method

The methodology to obtain the solution of Eqs. (3.5) and (3.6) with corresponding initial and boundary conditions is same in described in the previous chapter. The formulae used to approximate the space derivatives are already given in previous chapter. However, in contrast to Eqs. (2.12), Eq. (3.5) involve mixed and second order derivatives. These derivatives are approximated as

$$\frac{\partial u_1}{\partial t} = \frac{u_{1i}^{j+1} - u_{1i}^{j}}{\Delta t} = u_{1t},$$

$$\frac{\partial^2 u_1}{\partial t^2} = \frac{u_{1i}^{j+1} - 2u_{1i}^{j} + u_{1i}^{j-1}}{\left(\Delta t\right)^2} = u_{1t^2},$$

36

$$\frac{\partial}{\partial t}\left(\frac{\partial u_1}{\partial r}\right) = \frac{u_{1i+1}^{j+1} - u_{1i+1}^{j} - u_{1i-1}^{j+1} + u_{1i-1}^{j}}{2\Delta r \Delta t} = u_{1tr},$$

$$\frac{\partial}{\partial t}\left(\frac{\partial^2 u_1}{\partial r^2}\right) = \frac{u_{1i+1}^{j+1} - 2u_{1i}^{j+1} + u_{1i-1}^{j+1} - u_{1i+1}^{j} + 2u_{1i}^{j} - u_{1i-1}^{j}}{\left(\Delta r\right)^2 \Delta t} = u_{1tr^2}, \qquad (3.8)$$

Using (2.24) and (3.8), Eqns. (3.5) and (3.6) may be transformed to the following difference equation

$$u_{1i}^{k+1} = \frac{1}{\left(\alpha + \dfrac{\lambda_1}{\Delta t}\right)}\left[u_{1i}^{k}\left(\alpha - \frac{2\lambda_1}{\Delta t}\right) + \frac{\lambda_1}{\Delta t}u_{1i}^{k-1}\right] + B_1\left(1 + e\cos(2\pi t^k)\right) - \left(2\lambda_1 e B_1 \pi\right)\sin\left(2\pi t^k\right)$$

$$+ B_2\left(\cos\left(2\pi\omega_r t^k + \phi\right)\right) - \left(2\pi\omega_r B_2 \lambda_1\right)\sin\left(2\pi\omega_r t^k\right) + \left\{u_{1r^2} + \lambda_2 u_{1tr^2}\right\}$$

$$+ \left\{\frac{1}{r}\left(u_{1r}\right) + \frac{\lambda_2}{r}u_{1tr}\right\}, \qquad (3.9)$$

$$u_{2i}^{k+1} = u_{2i}^{k} + \left(\frac{\Delta t}{\gamma}\right)\left[B_1\left(1 + e\cos\left(2\pi t^k\right)\right) + B_2\left(\cos\left(2\pi\omega_r t^k + \phi\right)\right) + \frac{1}{r}\left(u_{2r}\right) + u_{2r^2}\right]. \qquad (3.10)$$

The temporal and spatial discretizations are also carried out in a similar manner as done in chapter 2. Moreover, the choice of temporal and spatial time steps sizes is also the same as given in the previous chapter.

3.4   Results and Discussion

In simulation we have assumed that $\phi = 0$ and the core diameter is assumed to be *60%* of the tube diameter. In addition, the effect of the non-Newtonian nature of the blood is studied using Oldroyd-B fluid for different values of λ_1 and λ_2. Following [68], we have performed two simulations having radius size and systolic component of the pressure gradient. The set with $A_0 = 698.65$ *dyne/cm³*, *r = 0.15 cm* represents the values the constant pressure gradient inside the coronary artery whilst the other one with ($A_0 = 32$ *dyne/cm³*, *r = 0.5 cm*) representing the corresponding variables for femoral artery. The effect of the body acceleration on the flow field are shown for different values of A_g = *(0, 0.5g, g)* and pulse frequency f_b (= *0.6, 1.2* and *2.4).*
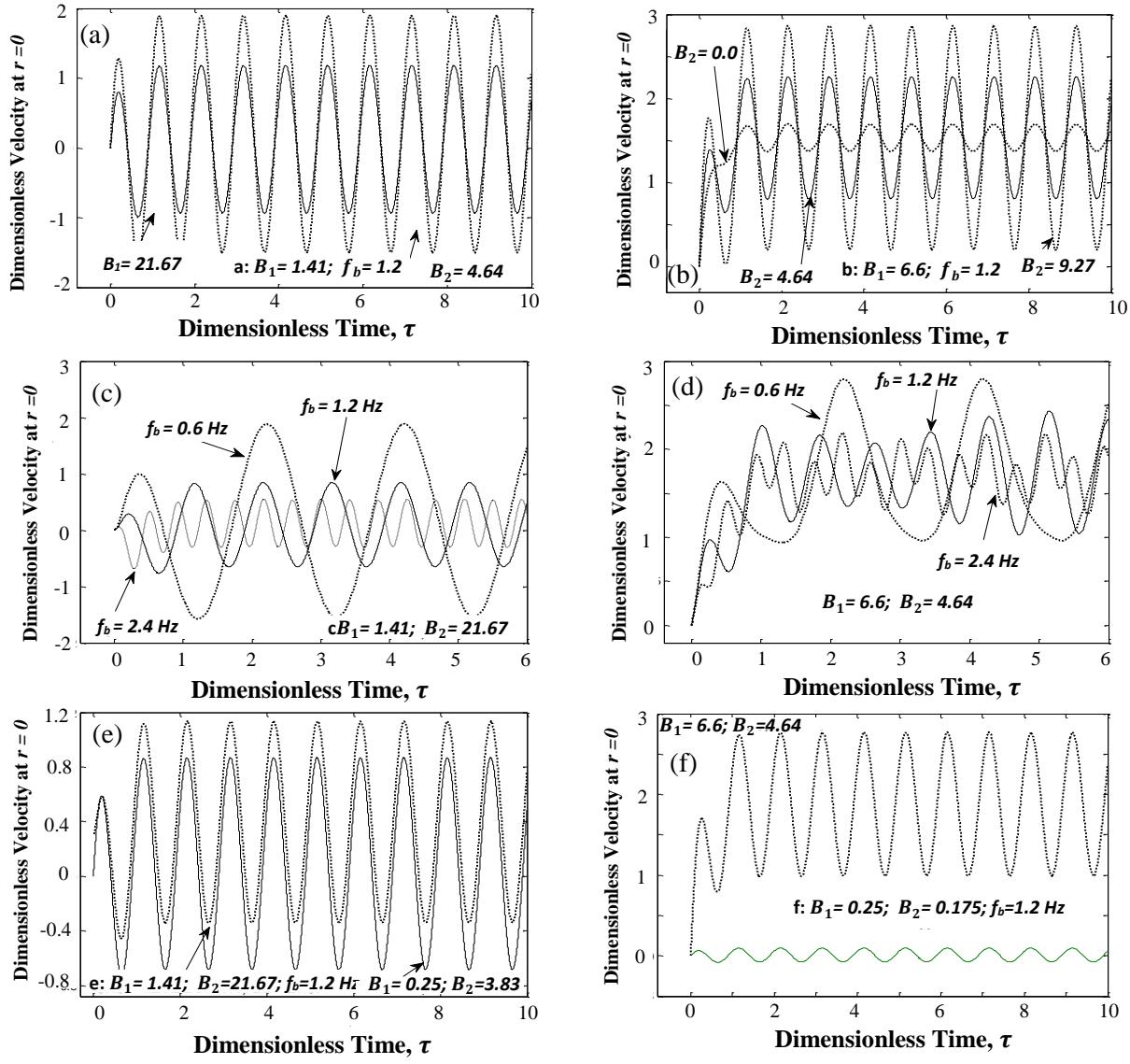
Fig. 3.1. Unsteady Dimensionless velocity at the centre of the tube for flow: Results in the larger artery (*r = 0.5 cm, A_0 =32 dyne/cm³*) are shown in Fig. 3.1 (a, c, and e); Results in the smaller artery *(r= 0.15, A_0 = 698.65 dyne/cm³)* are shown in Fig.3.1 (b, d and f). Velocity graph for different values of B_2 (varying A_g) are shown in Fig.3.1 (a and b); Velocity graph for different values of f_b are shown in the Fig.3.1(c and d); Velocity graph for different values of B_2 are shown in Fig.3.1 (e and f).

It is observed that due to the pulsating pressure and the body acceleration the velocity at the centre fluctuates, increases and finally attains the steady state as time increases (τ_s is the dimensionless steady state time where the maximum velocity distribution is obtained). Such behavior of velocity is shown in **Fig.**

3.1. The effects of the amplitude of the pressure gradient A_0, the body acceleration in term of the amplitude A_g, and the frequency f_b are also shown in Fig. 3.1 in the core of the artery for non-zero values of λ_1 and λ_2. Fig. 3.1a and 3.1b shows that the velocity fluctuates around its mean value with constant frequency and amplitude after achieving the steady state. Moreover, the amplitude of velocity increases by increasing the amplitude of body acceleration. However, it decreases by increasing the frequency of body acceleration as evident Fig. 3.1c and 3.1d. One may also conclude from the velocity plots that the mean value of the velocity fluctuation in absence of body acceleration is significantly higher than mean value of velocity fluctuation in presence of body acceleration.

Fig. 3.2 illustrates the velocity profiles for steady state condition in femoral artery. Hence t_s is the dimensionless steady state time where the maximum velocity distribution is obtained. Therefore, t_s is the starting time of the first half of one fluctuation cycle. In general, it is observed that if A_g is larger or f_b is smaller, the value of velocity grow faster. Same behavior is also observed when fluid is taken in the core region non-Newtonian. There are inflection points within cycle of the velocity profile where the shapes changes from being convex to concave.
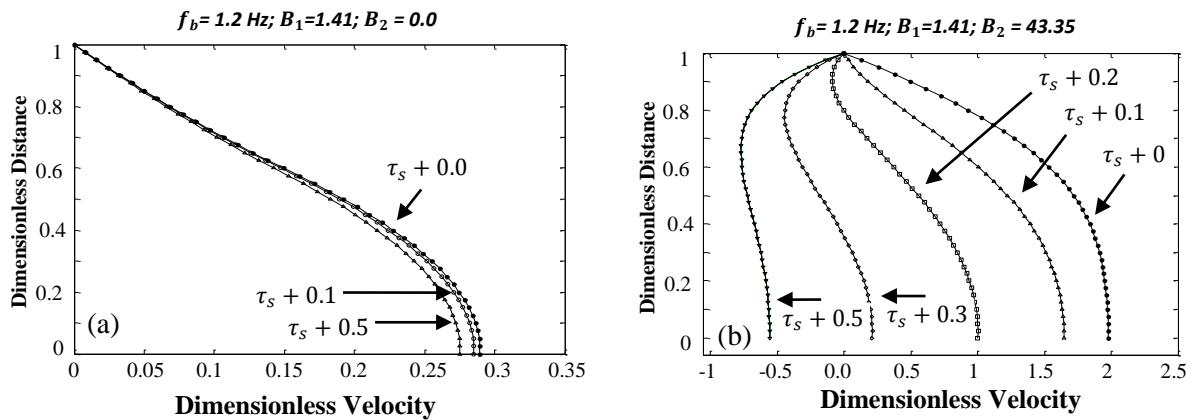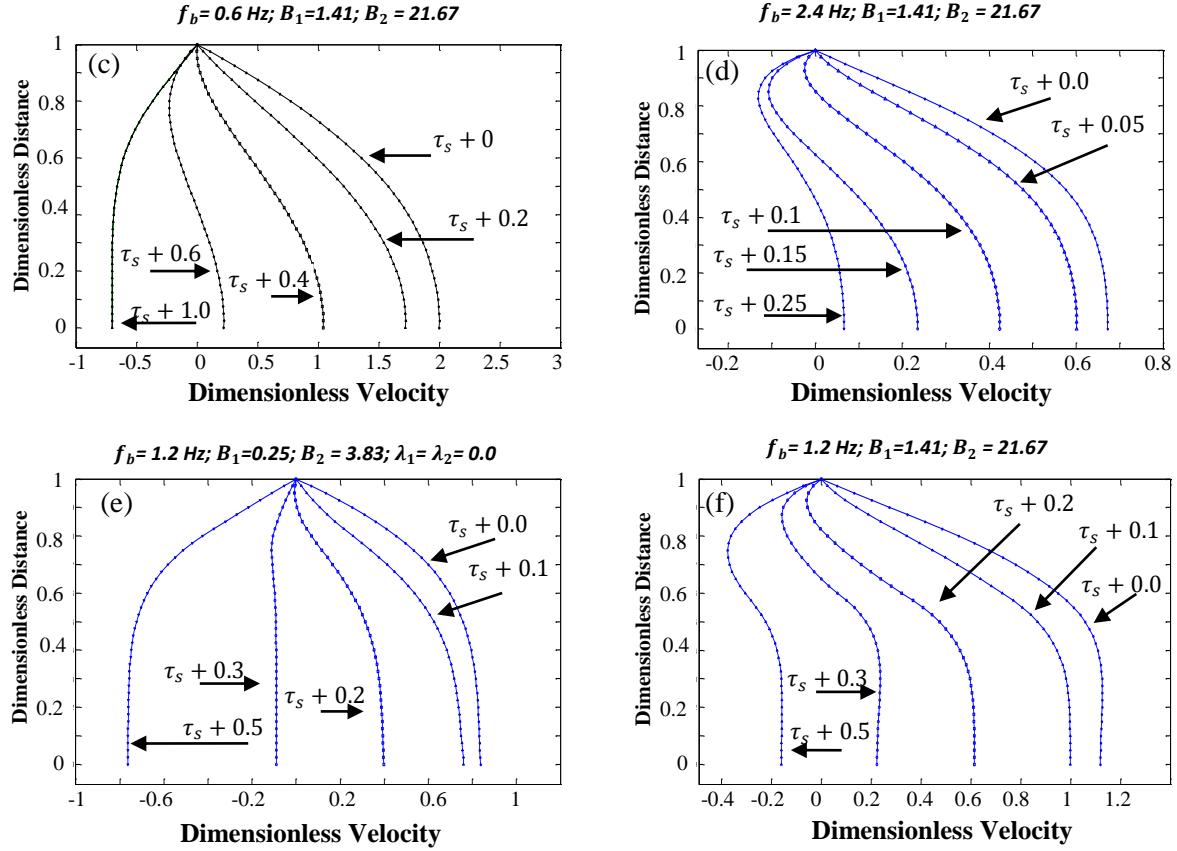
Fig. 3.2. Dimensionless velocity profile in the larger artery*(r=0.5cm,A_0=32 dyne/cm^3)*; Graphs for different values of B_2 (varying A_g) are shown in Fig. 3.2 (a and b); Graphs for different values of f_b are shown in Fig.3.2(c and d); Graphs for different values of λ_1 and λ_2 are shown in Fig.3.2 (e and f).

From Fig.3.2a, it is observed that when $A_g = 0$ the shape of the velocity profile is parabolic. Similar behavior is also found in Fig.3.2b at the start of the fluctuation cycle or $t = \tau_s$. From Figs. 3.2c and 3.2d one can observe that the velocity does not achieve maximum at the centre of the artery. Moreover, maximum in velocity is moving from the centre toward the arterial wall during the first half and moving back to the centre during the second half of the fluctuation cycle. Moreover, for the femoral artery when the velocity profile becomes negative, the maximum velocity can be seen near the wall beyond the core region.

$A_0 =698.65$ dyne/cm³; $A_g =0.0$kg; $f_b=1.2$Hz (a)

$A_0 =698.65$ dyne/cm³; $A_g = g$; $f_b=1.2$Hz (b)

$A_0 =698.65$ dyne/cm³; $A_g =0.5$kg; $f_b=0.6$Hz (c)

$A_0 =698.65$ dyne/cm³; $A_g =0.5$kg; $f_b=2.4$Hz (d)

$\lambda_1= \lambda_2= 0.0$; $A_g =0.5$kg; $f_b=1.2$Hz (e)

$A_0 =698.65$ dyne/cm³; $A_g =0.5$kg; $f_b=1.2$Hz (f)

$\lambda_2= 0.1$; $B_1=1.41$; $B_2 = 21.67$; $f_b=1.2$ Hz (g)

$\lambda_1= 0.5$; $B_1=1.41$; $B_2 = 21.67$; $f_b=1.2$ Hz (h)

41
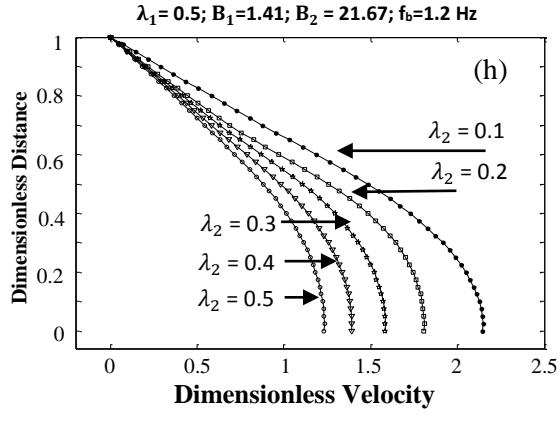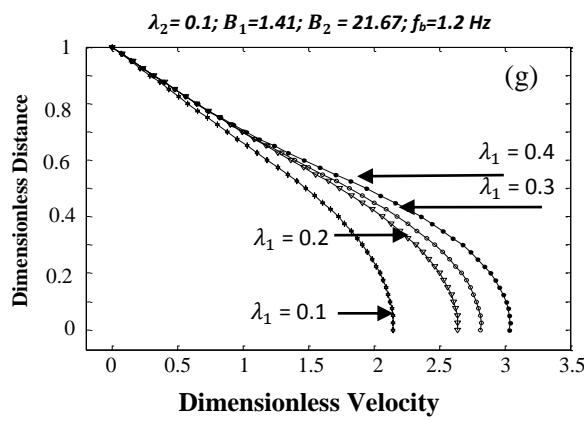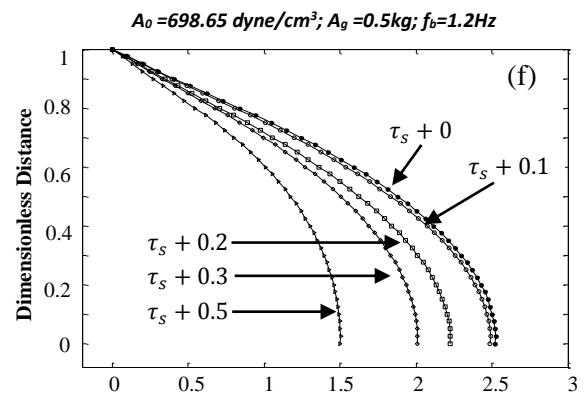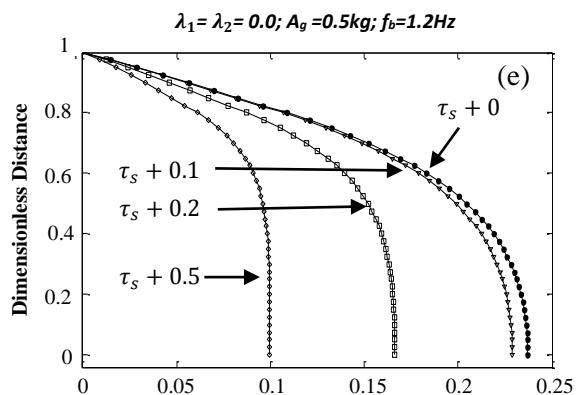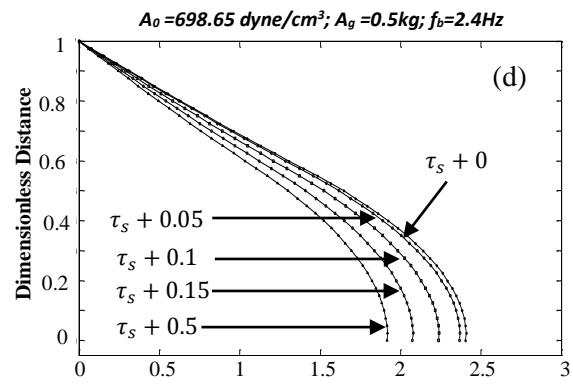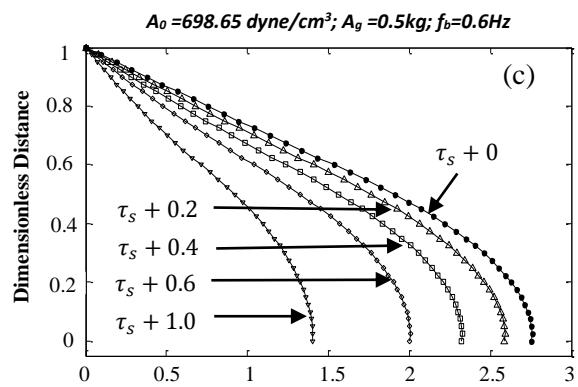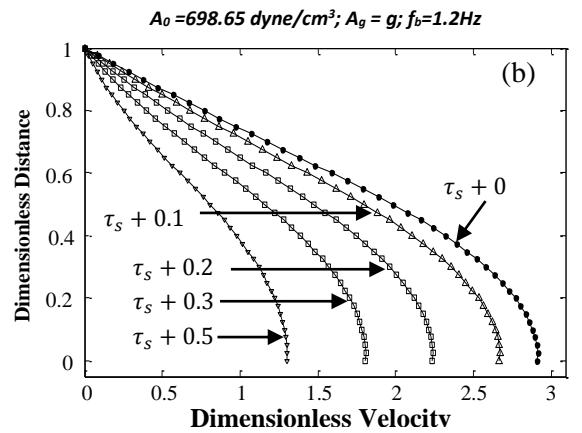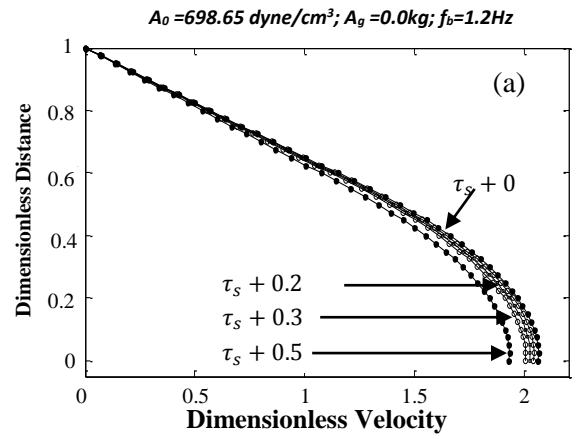
**Fig. 3.3.** Dimensionless velocity graphs in the smaller artery$(r=0.15cm, A_0=32\ dyne/cm^3)$: Fig. 3.3 (a & b): The Effects of B_2(varying A_g);Fig(c & d): The effects of varying f_b; Graphs for different values of λ_1 and λ_2 are shown in Fig. 3.3 (g and h)

In Fig. 3.2e, the core region is taken Newtonian and body acceleration is assumed minimum. It is found that the velocity profile to return to its parabolic shape and the curve becomes concave at $t = \tau_s + t_{half}$. Fig. 3.2f is shown for non-zero values of λ_1 and λ_2. This figure indicates shift in fluctuation cycle in time.

42
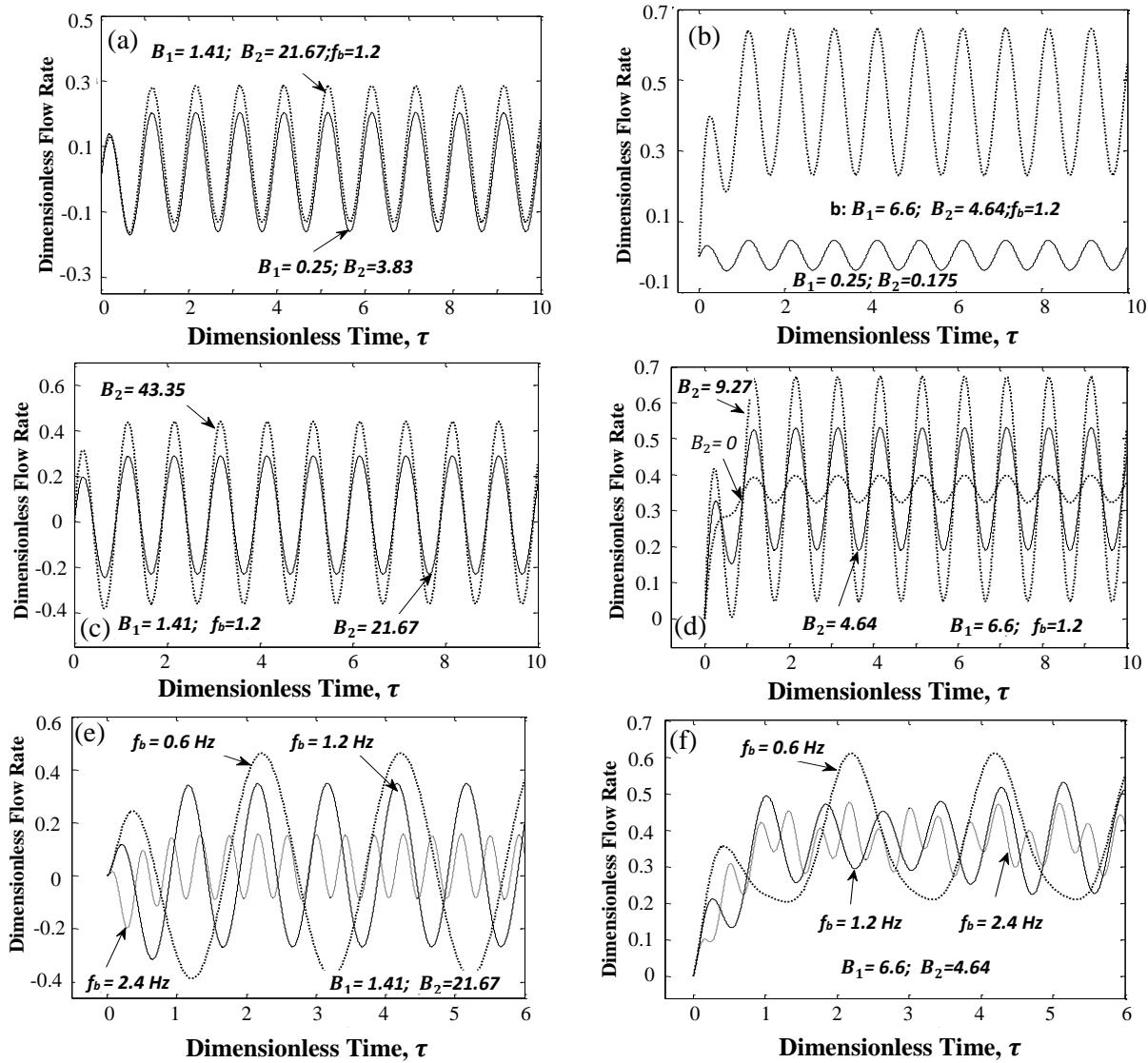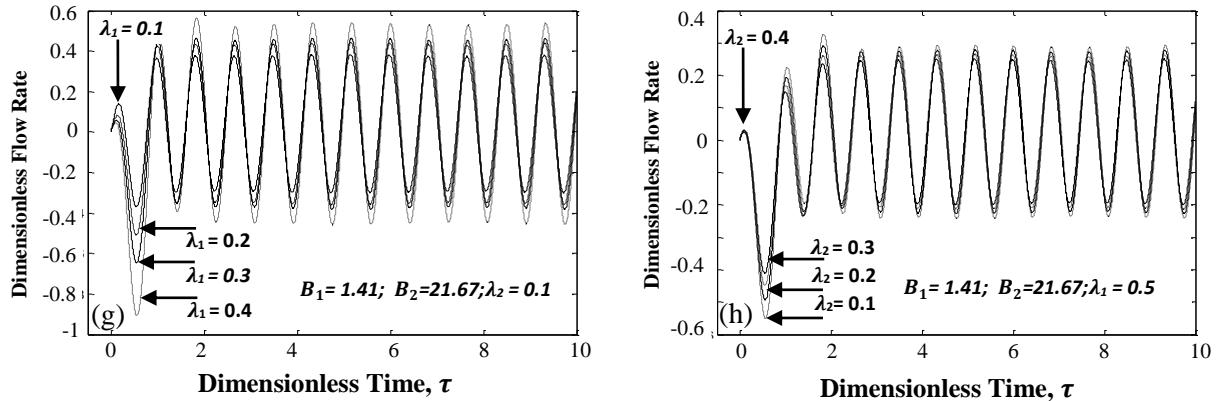
**Fig. 3.4.** Unsteady Dimensionless flow rate in two different arteries: Fig. 3.4 (a, c, and e) results for the larger artery($r = 0.5$ cm, $A0 = 32$ dyne/cm^3); Fig. 3.4 (b, d and f) results for the smaller artery $(r= 0.15, A0 = 698.65$ dyne/cm$^3)$. Fig. 3.4 (a and b) Effects of varying B2 (varying Ag); Fig. 3.4(c and d): the effects of varying f_b ($Ag=0.5g$); Graphs for different values of $\lambda_1 \ and \ \lambda_2$ are shown in Fig. 3.4 (g and h).

The variation in velocity with time after achieving steady state for coronary artery is shown in **Fig. 3.3**. It is evident from Figs. 3.3a and b that the profiles of velocity show increasing trend by increasing A_g. It is interesting to note that the shape of velocity profile is parabolic at all time. Figs. 3.3c and d indicate a decreasing trend in velocity by increasing f_b. The velocity in coronary artery when fluid in the core region is Newtonian is shown in Fig. 3.3e. The velocity with same set of values bit with non-zeros values of λ_1 and λ_2 is shown in Fig. 3.3f. A comparison of Figs. 3.3e and f indicates a faster decrease in velocity with time when fluid in the core region is non-Newtonian Oldroyd-B fluid. The effects of λ_1 and λ_2 on velocity at $t = t_s$ are shown in Figs. 3.3g and h respectively. These figures show that the effect of λ_1 on velocity is quite opposite to the effect of λ_2.

The effects of A_g, f_b, λ_1 and λ_2 on the non-dimensional wall shear stress and flow rate are shown through **Figs. 3.4 and 3.5.** It is observed that both flow rate and wall shear stress fluctuate with time around some mean value after steady state has been reached. The profiles further indicate that the amplitude of fluctuation increases by increasing A_g (the parameter controlling the amplitude of body acceleration). The effects of f_b on these profiles are quite opposite to the effects of A_g.

Moreover, the amplitude of fluctuate in flow rate and shear stress increases in going from Newtonian to Oldroyd-B fluid. Another interesting observation is that for the larger artery both flow rate and shear stress fluctuates between positive and negative value whilst for smaller artery such fluctuation is always between positive values. As an implication of the mean values flow rate and shear stress in the coronary artery are in excess of those in the femoral artery.

3.5   Conclusion

A mathematical model based on Oldroyd-B constitutive equation is developed for pulsatile flow of blood subject to body acceleration. The model bears the potential to explore the effects of stress relaxation and retardation effects. The analysis presented here is general and includes the results of Newtonian and Maxwell fluids as special cases. The important hemodynamical variables in pulsatile flow with superimposed body acceleration are analyzed for several values of relaxation and retardation parameters. The present analysis is general and even such an analysis with Fahraeus-Lindqvist effect in Oldroyd B-fluid is yet not available in the literature.
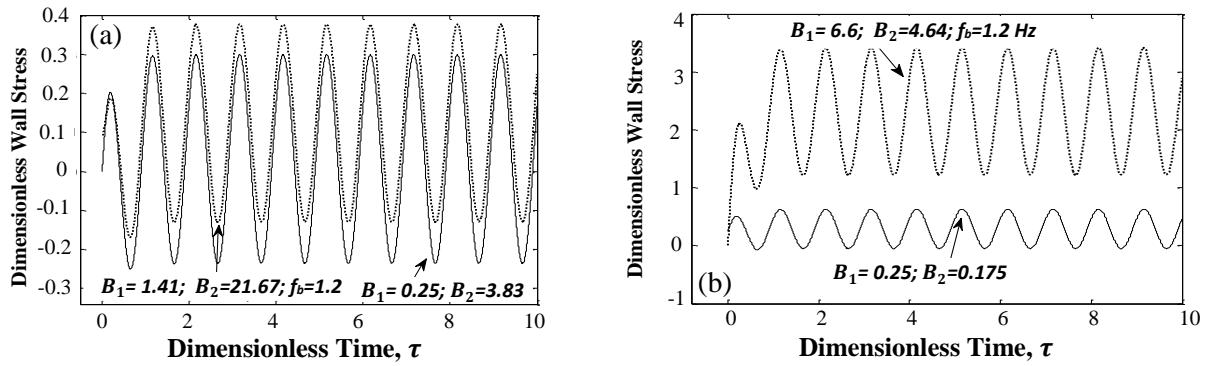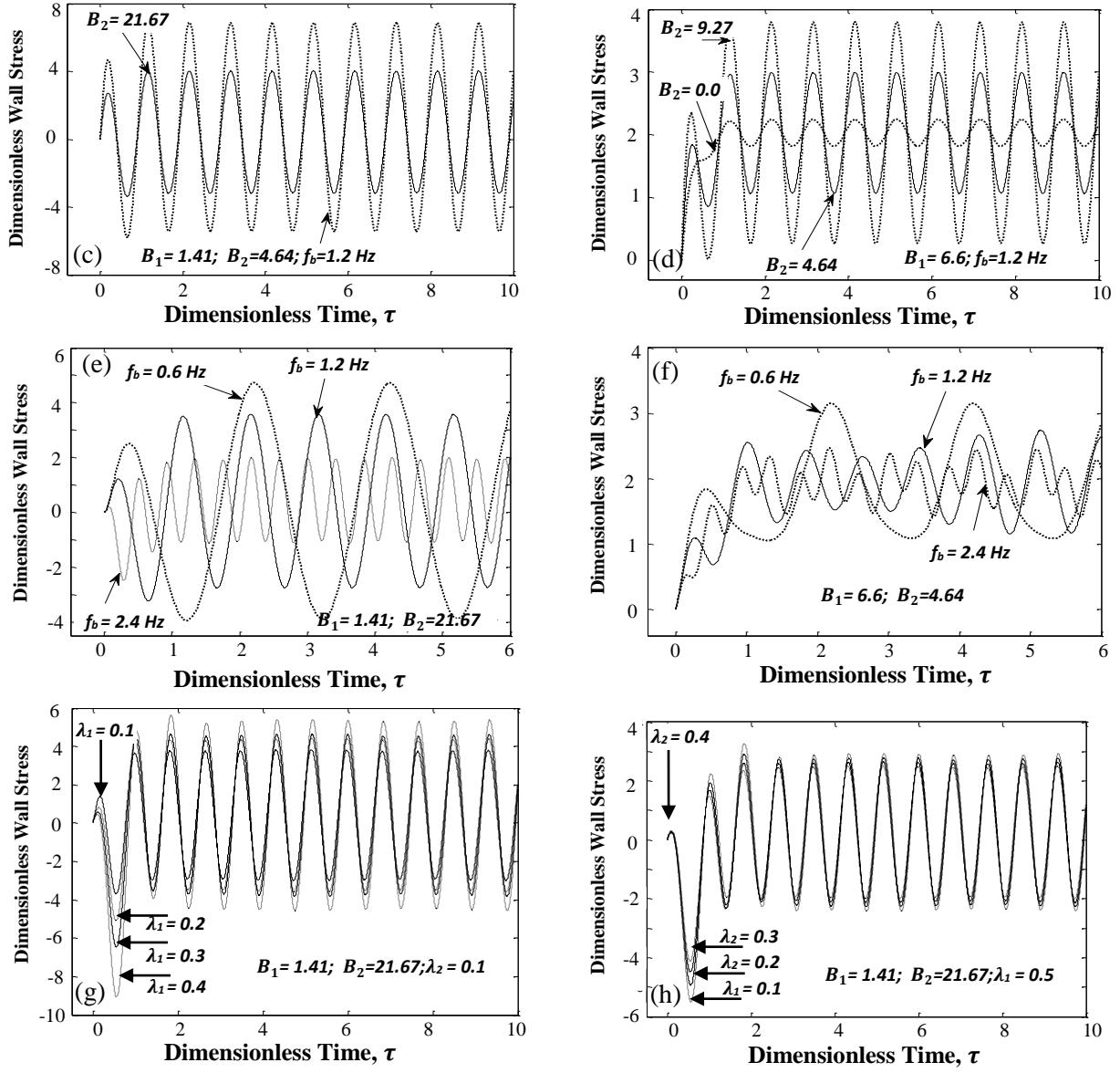
Fig.3.5. Dimensionless wall shear stress for flow in two different arteries as a function of the dimensionless time: Fig.3.5 (a, c, and e) results for the larger artery *(r = 0.5 cm, A₀ =32 dyne/cm³)*; Fig. 3.5 (b, d and f) results for the smaller artery *(r= 0.15, A₀ = 698.65 dyne/cm³)*. Fig. 3.5 (a and b) Effects of varying B_2 *(varying A_g)*; Fig. 3.5 (c and d): the effects of varying f_b *(A_g=0,5g)*; Fig. 3.5 (g and h): the effects of varying λ_1 *and* λ_2.

Chapter 4

Unsteady magnetohydrodynamic blood flow in a porous-saturated overlapping stenotic artery

Unsteady pulsatile flow of blood through a porous-saturated, tapered and overlapping stenotic artery in the presence of magnetic field is examined theoretically and computationally in this chapter. The power law constitutive model is employed to simulate haemo-rheological characteristics. The governing equation is derived assuming the flow to be unsteady, laminar and two-dimensional. A robust, finite difference method is employed for the solution of the governing equation, subject to appropriate boundary conditions. Based on this solution, an extensive quantitative analysis is performed to analyze the effects of blood rheology, body acceleration, magneto-hydrodynamic parameter, permeability parameter and arterial geometrical parameters of stenosis on various quantities of interest such as axial velocity, flow rate, resistance impedance and wall shear stress. The computations demonstrate that velocity, flow rate and shear stress increase while resistance to flow decreases with greater permeability parameter. Additionally, the effects of magnetic field are observed to be converse to those of permeability i.e. flow is decelerated and resistance is increased, demonstrating the powerful utility of exploiting magnetic fields in haemo-dynamic flow control (e.g. intra-corporeal surgical procedures). Furthermore, the size of trapped bolus of fluid is also found to be reduced for large values of the permeability parameter indicating that progressively more porous media circumvent bolus growth.

4.1   Mathematical Model

Let us consider incompressible power-law blood flow through a tapered artery of length L with a overlapping stenosis subject to periodic body acceleration. We employ a cylindrical coordinate system (r, θ, z) with r directed along the radial direction and z along the axis of the tube (artery). The geometry of the overlapping stenosed arterial segment is simulated according to (see **Fig. 4.1(a)**):

$$R(z) = \begin{cases} (\xi'z+a)\left(1-\dfrac{64}{10}\eta\left(\dfrac{11}{32}l_0^3(z-d)-\dfrac{47}{48}l_0^2(z-d)^2+l_0(z-d)^3-\dfrac{1}{3}(z-d)^4\right)\right), & d \le z \le d + \dfrac{3}{2}l_0, \\ (\xi'z+a), & otherwise, \end{cases}$$

(4.1)

where a is the radius of the non-tapered artery in the non-stenotic region, l_0 is the length of stenosis, d is the length of non-stenotic region, $\xi'\,(=\tan\phi)$ is the tapering parameter and ϕ is called taper angle. The cases $\phi > 0$, $\phi = 0$, $\phi < 0$ correspond to converging, non-tapered and diverging tapering artery respectively. These cases are depicted in **Fig. 4.1 (b).**

(*a*)   (*b*)
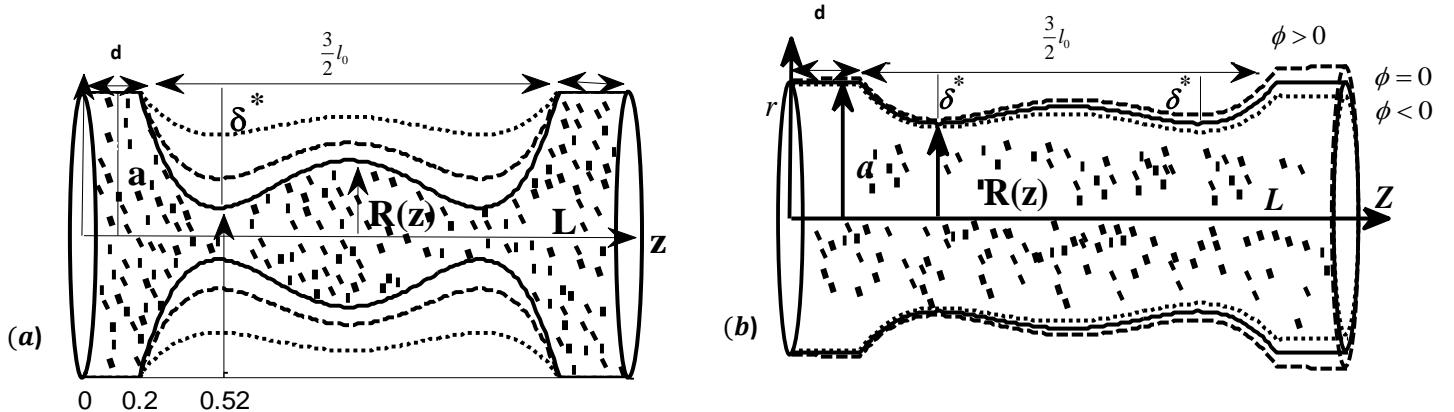
**Fig. 4.1**. Geometry of the stenosed arterial segment.

The parameter η is defined as

$$\eta = \frac{4\delta^*}{al_0^4},$$

(4.2)

in which δ^* denotes the maximum height of the stenosis located at

$$z = d + \frac{8l_0}{25}.$$

(4.3)

Since the flow under consideration is unsteady two-dimensional and axisymmetric, therefore we define

$$V = \left[u(r,z,t),\ 0,\ w(r,z,t)\right]. \tag{4.4}$$

The Cauchy stress tensor of power law fluid is given by [22]

$$S = \mu \Pi^{n-1} A_1^*, \tag{4.5}$$

where Π is the second invariant of rate of deformation tensor A_1^* and n is the power law index. According to the effective viscosity of the porous medium for a power law fluid is [74]

$$\mu_{eff} = -\mu \left|\bar{V}\right|^{n-1}, \tag{4.6}$$

where μ is the blood dynamic viscosity.

In view of (4.4), the continuity equation (1.2) reduces to

$$\frac{\partial u}{\partial r} + \frac{u}{r} + \frac{\partial w}{\partial z} = 0. \tag{4.7}$$

Similarly, the momentum equation (1.3) in the presence of magnetic field and component of extra stress S take the following form:

$$\rho\left(\frac{\partial u}{\partial t} + u\frac{\partial u}{\partial r} + w\frac{\partial u}{\partial z}\right) = -\frac{\partial p}{\partial r} + \left(\frac{1}{r}\frac{\partial}{\partial r}(rS_{rr}) + \frac{\partial}{\partial z}(S_{rz})\right) - \left(\mu|u|^{n-1}\right)\frac{u}{k'}, \tag{4.8}$$

$$\rho\left(\frac{\partial w}{\partial t} + u\frac{\partial w}{\partial r} + w\frac{\partial w}{\partial z}\right) = -\frac{\partial p}{\partial z} + \rho G(t) + \left(\frac{1}{r}\frac{\partial}{\partial r}(rS_{rz}) + \frac{\partial}{\partial z}(S_{zz})\right) - \sigma B_0^2 w - \left(\mu|w|^{n-1}\right)\frac{w}{k'}, \tag{4.9}$$

$$S_{rr} = 2\left[\mu\left\{\left[2\left(\left(\frac{\partial u}{\partial r}\right)^2 + \left(\frac{u}{r}\right)^2 + \left(\frac{\partial w}{\partial z}\right)^2\right) + \left(\frac{\partial u}{\partial z} + \frac{\partial w}{\partial r}\right)^2\right]^{\frac{n-1}{2}}\right\}\left(\frac{\partial u}{\partial r}\right)\right], \tag{4.10}$$

$$S_{zz} = 2\left[\mu\left\{\left[2\left(\left(\frac{\partial u}{\partial r}\right)^2 + \left(\frac{u}{r}\right)^2 + \left(\frac{\partial w}{\partial z}\right)^2\right) + \left(\frac{\partial u}{\partial z} + \frac{\partial w}{\partial r}\right)^2\right]^{\frac{n-1}{2}}\right\}\left(\frac{\partial w}{\partial z}\right)\right], \tag{4.11}$$

$$S_{rz} = \left[\mu \left\{ \left[\left[2\left(\left(\frac{\partial u}{\partial r} \right)^2 + \left(\frac{u}{r} \right)^2 + \left(\frac{\partial w}{\partial z} \right)^2 \right) + \left(\frac{\partial u}{\partial z} + \frac{\partial w}{\partial r} \right)^2 \right] \right]^{\frac{n-1}{2}} \right\} \right] \left(\frac{\partial w}{\partial r} + \frac{\partial u}{\partial z} \right). \tag{4.12}$$

In Eq. (4.9) $G(t)$ represents the body acceleration acting on stenosed arterial flow in axial direction. The above equation can be made dimensionless by defining

$$\bar{r} = \frac{r}{a}, \ \bar{w} = \frac{w}{U_0}, \ \bar{u} = \frac{l_0 u}{\delta^* U_0}, \ \bar{t} = \frac{\omega_p}{2\pi} t, \ \bar{z} = \frac{z}{l_0}, \ \bar{R} = \frac{R}{a}, \bar{p} = \frac{a^2 p}{U_0 l_0 \mu'}, \bar{S}_{rz} = \frac{a}{U_0 \mu'} S_{rz},$$

$$\bar{S}_{rr} = \frac{l_0}{U_0 \mu'} S_{rr}, \ \bar{S}_{zz} = \frac{l_0}{U_0 \mu'} S_{zz}, \ \mu' = \mu \left(\frac{U_0}{a} \right)^{n-1}. \tag{4.13}$$

Making use of these variables Eqns. (4.7) - (4.12) after dropping bars can be casted as

$$\delta \left(\frac{\partial u}{\partial r} + \frac{u}{r} \right) + \frac{\partial w}{\partial z} = 0, \tag{4.14}$$

$$\alpha \delta \varepsilon^2 \left(\frac{\partial u}{\partial t} + \varepsilon Re \left(\delta u \frac{\partial u}{\partial r} + w \frac{\partial u}{\partial z} \right) \right) = -\frac{\partial p}{\partial r} + \varepsilon^2 \left(\frac{1}{r} \frac{\partial}{\partial r} (r S_{rr}) + \frac{\partial}{\partial z} (S_{rz}) \right) - \left(\delta^n |u|^{n-1} \right) \frac{u}{k}, \tag{4.15}$$

$$\alpha \left[\frac{\partial w}{\partial t} \right] + Re \left(\delta \varepsilon u \frac{\partial w}{\partial r} + \varepsilon^2 w \frac{\partial w}{\partial z} \right) = -\frac{\partial p}{\partial z} + B_2 \left(\cos \left(2\pi \omega_r t + \theta \right) \right)$$

$$+ \left(\frac{1}{r} \frac{\partial}{\partial r} (r S_{rz}) + \varepsilon^2 \frac{\partial}{\partial z} (S_{zz}) \right) - M^2 w - |w|^{n-1} \left(\frac{w}{k} \right), \tag{4.16}$$

$$S_{rz} = \left\{ \left[\left[\delta \varepsilon \left(\left(\frac{\partial u}{\partial r} \right)^2 + \left(\frac{u}{r} \right)^2 \right) + \varepsilon \left(\frac{\partial w}{\partial z} \right)^2 \right] + \left(\delta \frac{\partial u}{\partial z} + \frac{\partial w}{\partial r} \right)^2 \right] \right\}^{\frac{n-1}{2}} \left(\frac{\partial w}{\partial r} + \delta \frac{\partial u}{\partial z} \right),$$

$$S_{rr} = \left\{ \left[\left[2 \left(\delta \varepsilon \left(\left(\frac{\partial u}{\partial r} \right)^2 + \left(\frac{u}{r} \right)^2 \right) + \varepsilon \left(\frac{\partial w}{\partial z} \right)^2 \right) + \left(\delta \frac{\partial u}{\partial z} + \frac{\partial w}{\partial r} \right)^2 \right] \right]^{\frac{n-1}{2}} \right\} \left(\varepsilon \delta \frac{\partial u}{\partial r} \right),$$

$$S_{zz} = \left\{ \left[\left[2 \left(\delta \varepsilon \left(\left(\frac{\partial u}{\partial r} \right)^2 + \left(\frac{u}{r} \right)^2 \right) + \varepsilon \left(\frac{\partial w}{\partial z} \right)^2 \right) + \left(\delta \frac{\partial u}{\partial z} + \frac{\partial w}{\partial r} \right)^2 \right] \right]^{\frac{n-1}{2}} \right\} \left(\varepsilon \frac{\partial w}{\partial z} \right). \tag{4.17}$$

For the subsequent analysis, we assume that the stenosis is mild $\left(\delta = \delta^*/a \ll 1\right)$, and the ratio $\varepsilon = a/l_0 \approx O(1)$. In view of above assumptions, Eqns. (4.15) - (4.16) reduce to

$$\frac{\partial p}{\partial r} = 0,$$ (4.18)

$$\alpha\left[\frac{\partial w}{\partial t}\right] = -\frac{\partial p}{\partial z} + B_2\left(\cos\left(2\pi\omega_r t + \theta\right)\right) + \frac{1}{r}\frac{\partial}{\partial r}\left[r\left|\frac{\partial w}{\partial r}\right|^{n-1}\frac{\partial w}{\partial r}\right] - M^2 w - |w|^{n-1}\left(\frac{w}{k}\right).$$ (4.19)

Moreover, the pressure gradient is assumed to be of the form defined in Eq. (2.9). In dimensionless form it becomes

$$-\frac{\partial p}{\partial z} = B_1\left(1 + ecos(2\pi t)\right).$$ (4.20)

In Eqs. (4.14) - (4.17), $Re = \rho U_0 a / \mu'$ is the Reynolds number, $k = k' / a^{n+1}$ is the modified permeability, and $M = B_0 a\left(\sigma / \mu'\right)^{1/2}$ is the Hartmann number.

Inserting value of $-\partial p/\partial z$ in axial momentum equation (4.19), we get

$$\alpha\left[\frac{\partial w}{\partial t}\right] = B_1\left(1 + ecos(2\pi t)\right) + B_2\left(\cos\left(2\pi\omega_r t + \theta\right)\right) + \frac{1}{r}\frac{\partial}{\partial r}\left[r\left|\frac{\partial w}{\partial r}\right|^{n-1}\frac{\partial w}{\partial r}\right] - M^2 - |u|^{n-1}\left(\frac{u}{k}\right).$$ (4.21)

The appropriate boundary and initial conditions for the problem under consideration are [26]

$$\frac{\partial w(r,t)}{\partial r} = 0, \qquad\qquad at\ r = 0,$$ (4.22)

$$w(r,t) = 0, \qquad\qquad at\ r = R(z),$$ (4.23)

$$w(r,0) = 0, \qquad\qquad at\ \ t = 0.$$ (4.24)

The physical quantities of interest such as volumetric flow rate, the shear stress at the wall and resistance impendence in terms of the new variables become:

$$Q = 2\pi \int_0^R wr\,dr, \tag{4.25}$$

$$\tau_s = \left(\left| \frac{\partial w}{\partial r} \right|^{n-1} \frac{\partial w}{\partial r} \right)_{r=R}, \tag{4.26}$$

$$\lambda = \frac{L\left(\dfrac{\partial p}{\partial z} \right)}{Q}. \tag{4.27}$$

The dimensionless expression of geometry of stenosis is given by:

$$R(z) = (1+\xi z)\left[1 - \frac{64}{10}\eta_1\left(\frac{11}{32}(z-\sigma) - \frac{47}{48}(z-\sigma)^2 + (z-\sigma)^3 - \frac{1}{3}(z-\sigma)^4 \right) \right], \quad \sigma \le z \le \sigma + \frac{3}{2},$$

where $\quad \eta_1 = 4\delta, \ \delta = \dfrac{\delta^*}{a}, \ \sigma = \dfrac{d}{l_0}, \ \xi = \dfrac{\xi' l_0}{a}.$ \hfill (4.28)

Employing the radial coordinate transformation [75]

$$x = \frac{r}{R(z)}, \tag{4.29}$$

Eq. (4.21) can be cast as

$$\alpha\left[\frac{\partial w}{\partial t} \right] = B_1\left(1 + ecos(2\pi t)\right) + B_2\left(\cos\left(2\pi\omega_r t + \theta\right)\right) + \frac{1}{xR^{n+1}}\frac{\partial}{\partial x}\left[x\left| \frac{\partial w}{\partial x} \right|^{n-1} \frac{\partial w}{\partial x} \right] - M^2 w - |w|^{n-1}\left(\frac{w}{k} \right). \tag{4.30}$$

The dimensionless boundary conditions assume the form:

$$\left. \frac{\partial w(x,t)}{\partial x} \right|_{x=0} = 0, \ \ w(x,t)\big|_{x=1} = 0. \tag{4.31}$$

Similarly the volumetric flow rate, the shear stress at the wall and resistance impendence respectively takes

the form:

$$Q = 2\pi R^2 \left(\int_0^1 w\,x\,dx \right), \tag{4.32}$$

$$\tau_w = \frac{1}{R^n}\left(\left| \frac{\partial w}{\partial x} \right|^{n-1} \frac{\partial w}{\partial x} \right)_{x=1}, \tag{4.33}$$

$$\lambda = \frac{\frac{L}{l_0}\left(\frac{\partial p}{\partial z}\right)}{Q}, \tag{4.34}$$

substituting the value dimensionless form of pressure gradient in Eq. (4.24), we can write,

$$\lambda = \frac{L}{l_0}\frac{B_1\left(1+ecos(2\pi t)\right)}{\left(\int_0^1 u\,xdx\right)R(z)}. \tag{4.35}$$

4.2   Numerical solution

Employing the finite difference formulas of various partial derivatives appearing in Eq. (4.30), we get the following difference equation.

$$w_i^{j+1} = w_i^j + \frac{dt}{\alpha}\left[\left(B_1\left(1+ecos(2\pi t^j)\right)+B_2\cos\left(2\pi\omega_r t^j+\theta\right)+\frac{1}{xR^{n+1}}\left|w_x\right|^{n-1}w_x\right)+\right.$$

$$\left.+\frac{w_x}{R^{n+1}}\frac{\partial}{\partial x}\left(\left|w_x\right|^{n-1}\right)+\frac{1}{R^{n+1}}\left|w_x\right|^{n-1}w_{xx}-M^2u_i^j-\left(\left|w_i^j\right|^{n-1}\right)\frac{w_i^j}{k}\right]. \tag{4.39}$$

The finite difference representation of the prescribed conditions is given by

$$\begin{aligned}
w_i^1 &= 0, & at\ t &= 0, \\
w_{N+1}^j &= 0, & at\ x &= 1, \\
w_1^j &= w_2^j & at\ x &= 0.
\end{aligned} \tag{4.40}$$

The numerical solution is sought for $N+1$ uniformly discrete points $x_i,\left(i=1,2,\ldots.N+1\right)$ with a grid size

$\Delta x = \frac{1}{N+1}$ at the time levels $t_j=(j-1)\Delta t$, where Δt is the small increment in time. To obtain the

accuracy of the order $\sim 10^{-7}$, we have taken the following step sizes: $\Delta x = 0.025$ and $\Delta t = 0.00001$.

4.3   Results and Discussion

The   following   default   parameters   are   used   in   the   simulations: $d=0.2, l_0=1,\ L=2.0,$

$\omega_p=2\pi f_p, f_p=1.2,\ \omega_b=2\pi f_b,\ f_b=1.2,\ \theta=0.0,\ \sigma=0.2.$

Fig. 4.2 (a), illustrates the variation of dimensionless velocity profiles with permeability parameter at a time instant at which the maximum velocity is obtained. A decrease in axial velocity is noted from this figure with increasing *k*. Greater permeability diminishes the porous matrix resistance which serves to accelerate the blood flow.
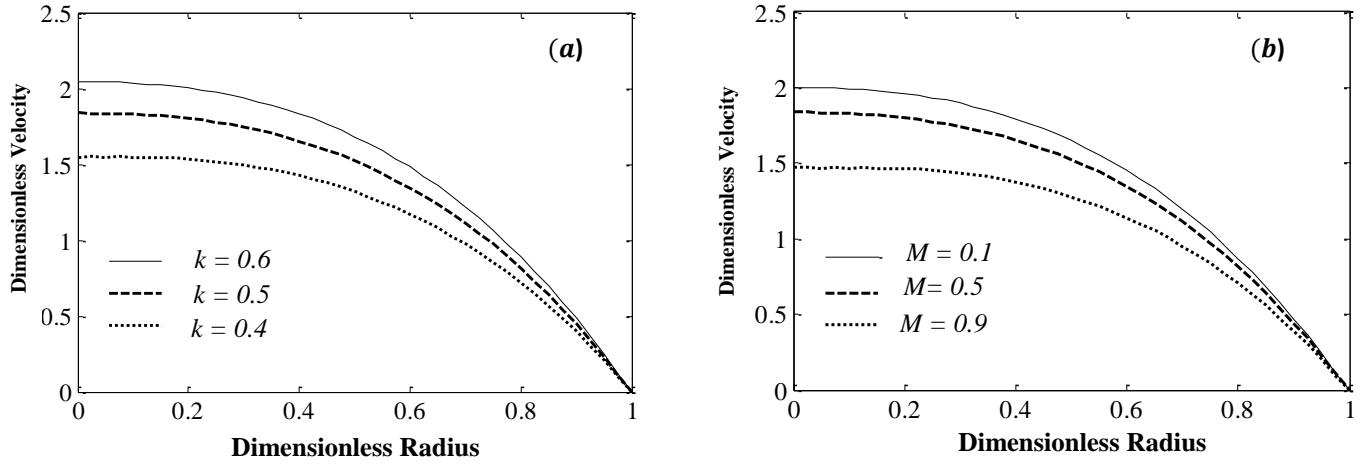

Fig. 4.2. Velocity profile for different values of permeability parameter k and Hartmann number *M* with the following data: $t = \tau_s$, $z = 0.52$, $\delta = 0.2$, $n = 0.8, M = 0.5$.

The dimensionless velocity profiles for different values magnetic field parameter Hartmann number, *M,* are shown in **Fig. 4.2 (b)**. It is observed that magnitude of velocity decreases by increasing the value of the Hartmann number, since greater hydro magnetic body force acts to retard the flow i.e. induces deceleration in the blood flow.
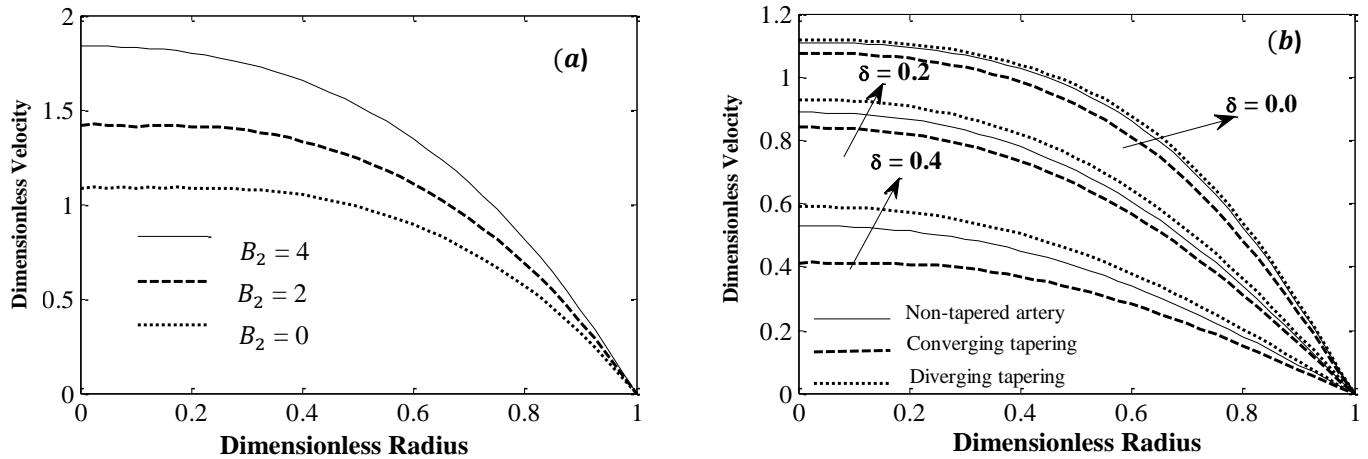
Fig. 4.3. Velocity profile for different values of dimensionless amplitude body acceleration and δ with the following data: $t = \tau_s$, $z = 0.52$, $\delta = 0.2$, $n = 0.8$, $k = 0.5$.

The variation in axial velocity for various values of dimensionless amplitude of body acceleration is shown in **Fig. 4.3(a)**. As expected the magnitude of axial velocity increases with increasing the amplitude of the body acceleration. **Fig. 4.3(b)** shows the non-dimensional axial velocity in the stenotic region for different values of δ and tapering parameter in the absence of magnetic field and porous medium. It is observed that an increase in δ decreases the velocity. i.e., magnitude of velocity in stenotic artery is less than that in normal artery, a physically realistic trend.
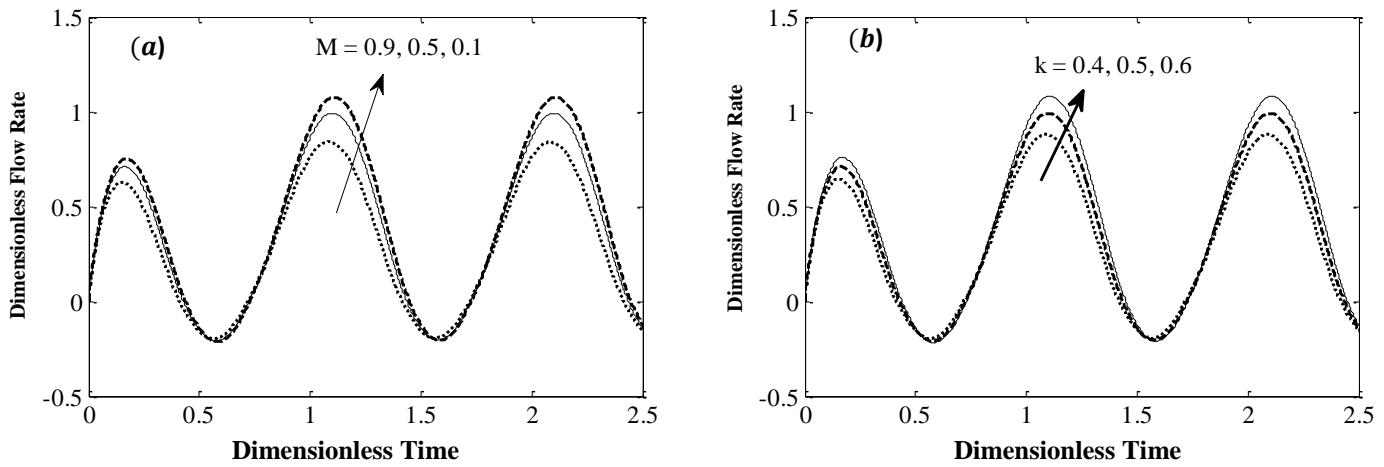

Fig. 4.4. Flow rate for different values of Hartmann number, M and k with the following data: $B_2 = 4$, $z = 0.52$, $n = 0.8$, $k = 0.5$.
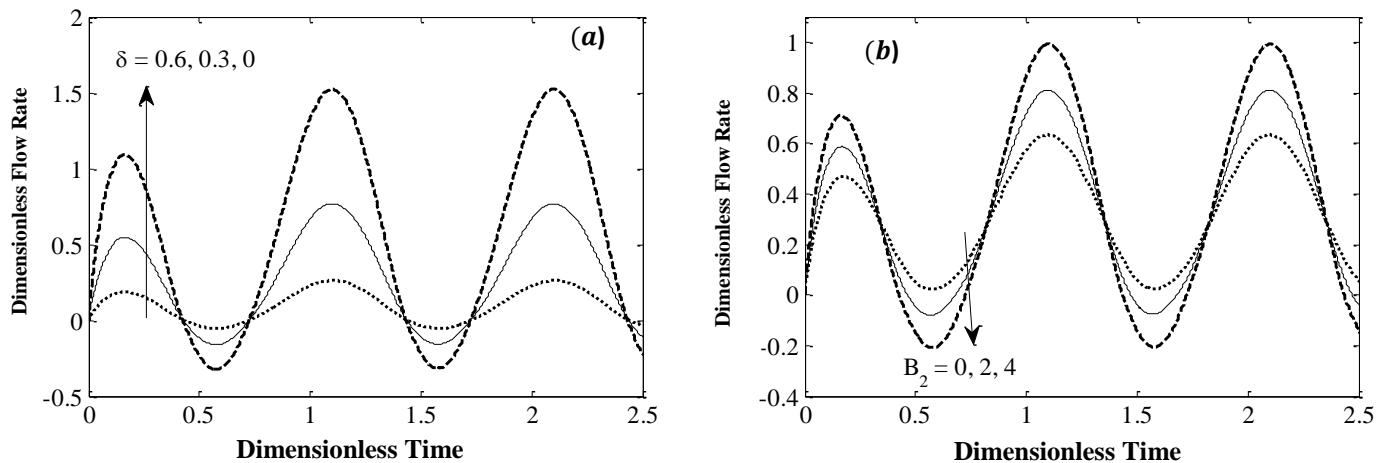
Fig. 4.5. Flow rate for different values of δ and B_2 with the following data: $B_2 = 4$, $z = 0.52$, $n = 0.8$, $k = 0.5$, $M = 0.5$.

Moreover, the diverging tapering accelerates the flow in the stenotic region in comparison with the converging tapering. Divergence in geometry enhances momentum flux and accelerates the flow. The converse behavior is induced with a convergence in taper.

The velocity curve for artery without tapering lies in between the corresponding profiles of converging and diverging arteries. **Fig. 4.4 (a)** shows the influence of M on dimensionless flow rate in the stenotic region. It is observed that an increase in the magnitude of M reduces the magnitude of flow rate i.e. impedes arterial flow. Further, it can be seen through **Fig. 4.4 (a)** that the flow rate fluctuates around its mean value after the achievement of steady state time which is observed to be approximately 1.3 in this case.
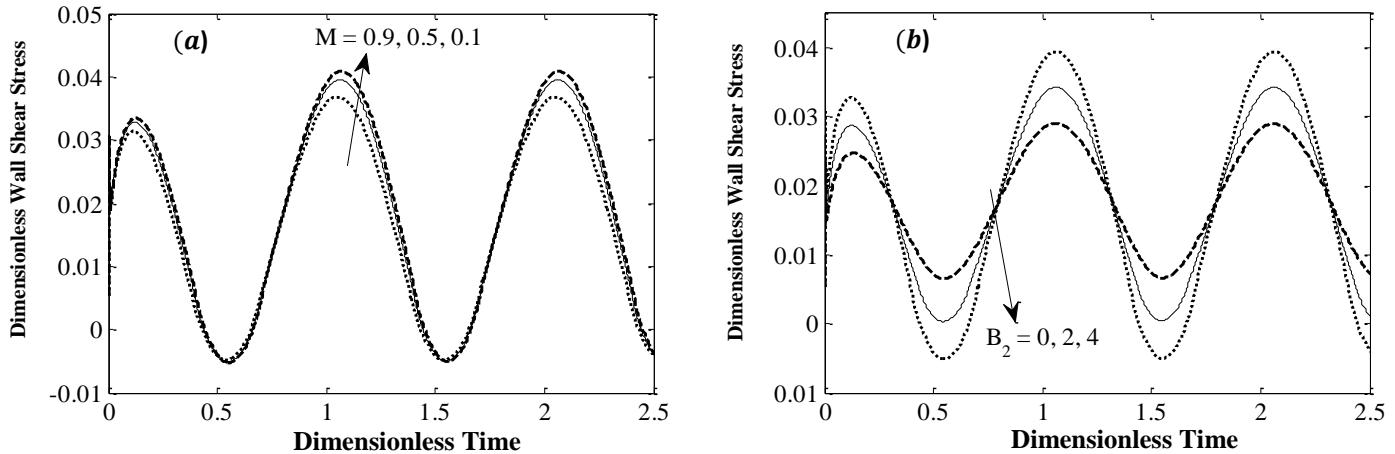
Fig. 4.6. Dimensionless wall shear stress for different values of Hartmann number, M and B_2 with the following data: $\delta = 0.2, B_2 = 4, z = 0.52, n = 0.8, k = 0.5$.

The plots of dimensionless flow rate for different values of k in the stenotic region are shown in **Fig. 4.4 (b)**. This figure reveals that flow rate increases by increasing the permeability of the porous medium, which is again attributable to the reduction in Darcian drag force (lesser fibers are present to resist the flow with greater permeability).
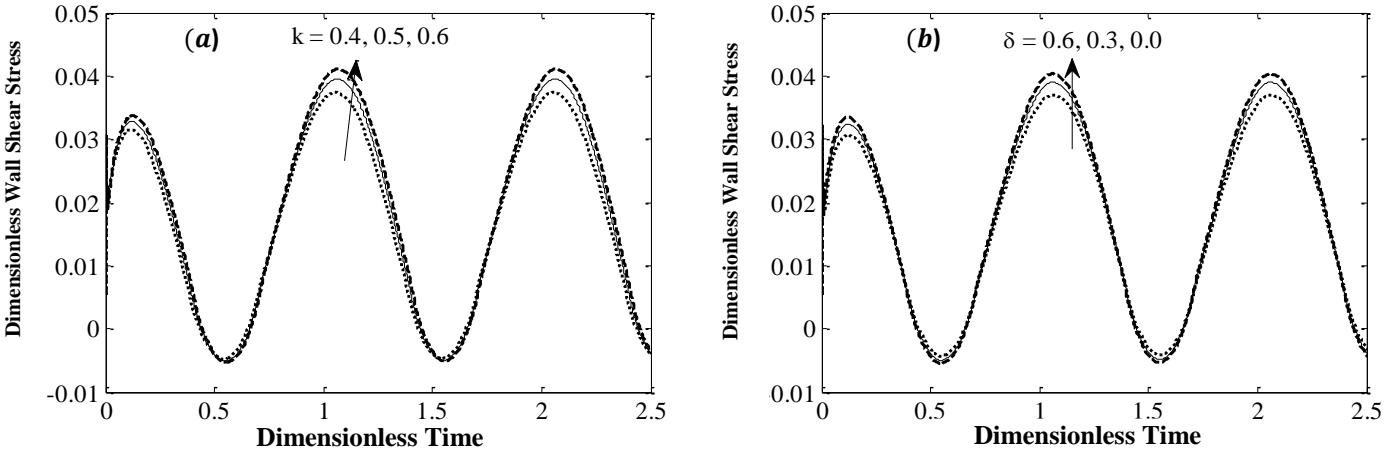
**Fig.4.7**. Wall shear stress for different values of k and δ with the following data: $\delta = 0.2, B_2 = 4,\ z = 0.52,$

$n = 0.8, M = 0.5.$

The variation of dimensionless flow rate with δ in the stenotic region is illustrated through **Fig. 4.5 (a)**. This figure indicates a decrease in the flow rate with an increase in the size of stenosis. Contrary to the observation made in **Fig. 4.5(a), Fig. 4.5(b)** shows that the flow rate increases by increasing the dimensionless amplitude of body acceleration.

The profiles of wall shear stress for different values of Hartmann number, M, and shape parameter, B_2 are shown in **Fig. 4.6 (a) and (b)**, respectively. **Fig. 4.6 (a)** indicates that wall shear stress decreases from the purely hydrodynamic (non-magnetic) to the magneto hydrodynamic case, since the presence of magnetic field decelerates the flow and reduces wall stress. **Fig. 4.6 (b)** indicates that wall shear stress increases with increase of amplitude of body acceleration.

The time evolution of non-dimensional wall shear stress for different values of permeability parameter k is shown in **Fig. 4.7 (a)**. It is evident from inspection of Fig. 4.7 (a) that an increase in the permeability parameter k increases the magnitude of the wall shear stress. The influence of δ on dimensionless wall shear stress at a specific location $z = 0.52$ is shown in **Fig. 4.7(b)**. It is interesting to note that shear stress decreases by increasing δ. The time series of dimensionless resistance to flow of various values of

permeability parameter is plotted in **Fig. 4.8**. This figure depicts that resistance to flow decreases with the permeability parameter k.
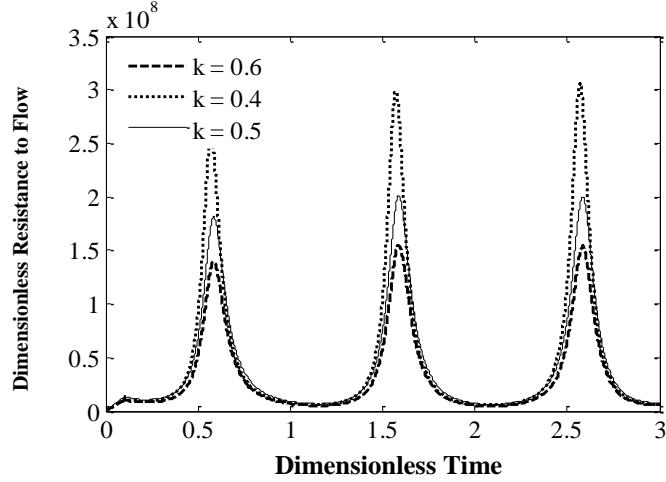

Fig. 4.8. Resistance to flow for different values of permeability parameter k with the following data: $\delta = 0.2, B_2 = 0,\ z = 0.52, n = 0.8,\ M = 0.5$.

Blood flow patterns over for the whole arterial segment at time instant $t = 0.3$ (which belongs to systolic phase) are shown in **Fig. 4.9** (Panels (a)-(f)). Panel (a) is considered as standard and rest of the panels are compared with it in order to illustrate the effects of various parameters on bolus pattern. Panels (a) and (b) illustrate streamlines for $k = 0.5$ and ∞ (purely blood flow i.e. vanishing porous medium), respectively. Both panels indicate a circulating bolus of fluid and their comparison reveals a decrease in the size of bolus by increasing the permeability of the porous medium. The effect of Hartmann number on streamlines pattern can be observed through the comparison of Panels (a) and (c). It is observed that an increase in the strength of magnetic field increases the size of the circulating bolus. This is perhaps due to the decelerating effect of magnetic on the flow velocity. A comparison of Panels (a) and (d) illustrate the effects of power law index n on streamlines pattern. It clear that size and circulation of trapped bolus increases when n approaches unity. In other words the size and circulation of trapped bolus increases from the shear-thinning blood scenario to the Newtonian blood scenario.
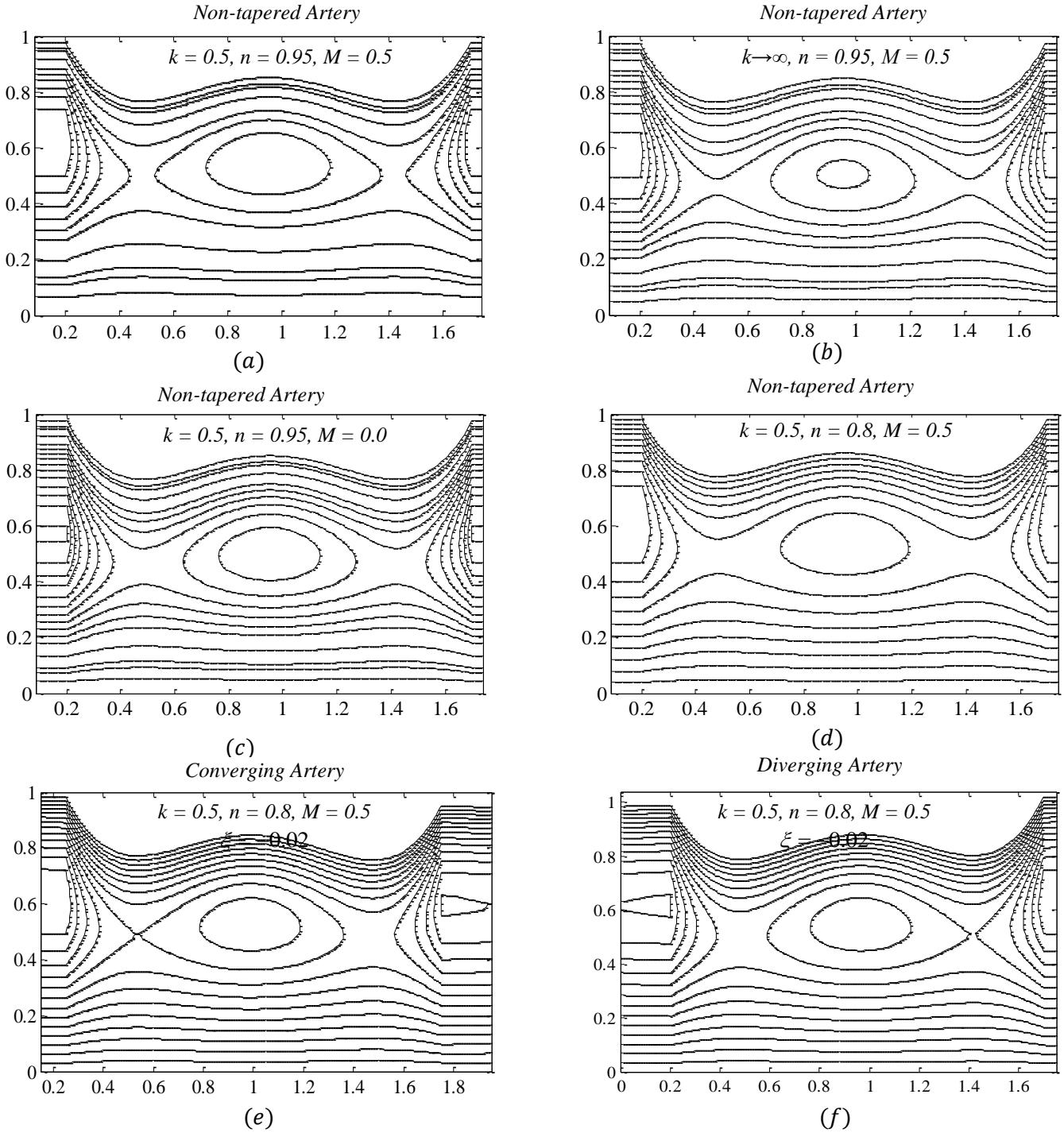
**Fig. 4.9**. Blood flow patterns for: $\delta = 0.2$, $B_1 = 2$, $B_2 = 2$, $t = 0.3$.

Streamlines patterns for converging and diverging arteries are shown in Panels (e) and (f) respectively. It is interesting to note that the outer streamline of the *eddying region* has a sharp edge on the upstream side for a converging artery while this sharp edge appears on the downstream side for a diverging artery. A close

examination of panels (e) and (f) also indicate the formation of a small eddy in the *downstream* zone for a *converging* artery and in the *upstream* region for a *diverging* artery.

4.4 Conclusions

A mathematical model for magneto-hydrodynamic pulsatile flow of blood through a porous saturated artery incorporating the effect of body acceleration and asymmetric shape of stenosis is presented. A power-law constitutive model is used to account for the blood rheology. The unsteady flow regime is shown to be governed by a nonlinear partial differential equation which is solved numerically using finite difference technique. The physical quantities of interest are plotted for various values of the emerging fluid dynamic and geometric parameters. The present computations have shown that:

- Dimensionless velocity in the stenotic region increases by increasing amplitude of the body acceleration and permeability parameter. However, it decreases when tapering parameter changes from positive to negative or when the height of the stenosis increases.

- A reduction in the magnitude of velocity accompanies increasing Hartmann number.

- The dimensionless flow rate in the stenotic region decreases by increasing the height of the stenosis while the converse response is computed by increasing permeability.

- Wall shear stress increases by increasing the permeability of the porous medium.

- The resistance to flow is a decreasing function of the permeability of the porous medium.

- The size of trapped bolus of fluid decreases by increasing the permeability of the porous medium. However bolus size is amplified as we progress from the shear-thinning to Newtonian blood scenarios.

Chapter 5

Unsteady non-Newtonian blood flow through a tapered overlapping stenosed catheterized vessel

This chapter investigates the unsteady flow characteristics of blood in a catheterized overlapping stenosed artery in presence of body acceleration and magnetic field. The stenosed arterial segment is modeled as a rigid constricted tube. An improved shape of stenosis in the realm of the formulation of the arterial narrowing caused by atheroma is integrated in the present study. The catheter inside the artery is approximated by a thin rigid tube of small radius while the streaming blood in the artery is characterized by the Carreau model. Employing mild stenosis condition, the governing equation of the flow is derived which is then solving numerically using finite difference scheme. The variation of axial velocity, flow rate, resistance impendence and wall shear stress is shown graphically for various parameters of interest. The flow patterns illustrating the global behavior of blood are also presented.

5.1 Geometry of the problem

A homogenous incompressible Carreau fluid is assumed to be flowing in a catheterized tapered stenosed artery of length L. The flow is subject to a constant applied radial magnetic field and periodic body acceleration. The flow analysis will be carried out in a cylindrical co-ordinate system (r, θ, z), where r

and z axes are along the radial and axial directions of the artery. It is assumed that the stenosed arterial segment is composed of two overlapping bell shaped curves whose equation is

$$R(z) = \begin{cases} \left(\xi^* z + a\right)\left(1 - \dfrac{64}{10}\eta\left(\dfrac{11}{32}l_0^3(z-d) - \dfrac{47}{48}l_0^2(z-d)^2 + l_0(z-d)^3 - \dfrac{1}{3}(z-d)^4\right)\right), & d \le z \le d + 1.5l_0, \\ \left(\xi^* z + a\right), & otherwise, \end{cases}$$

(5.1)

In above expression d represents the length of non-stenotic arterial region, a is the radius of undisturbed non-tapered part of the artery, l_0 the length of stenotic region, k is a parameter such that $0 < k < 1$ and $\xi^* \left(= \tan\phi\right)$ the parameter controlling the convergence $\left(\phi < 0\right)$ or divergence $\left(\phi > 0\right)$ of post-stenotic region. The case $\left(\phi = 0\right)$ corresponds to non-tapered artery. A schematic diagram of the both non-tapered and tapered catheterized arteries are shown in **Fig. 5.1(a) and (b)**.
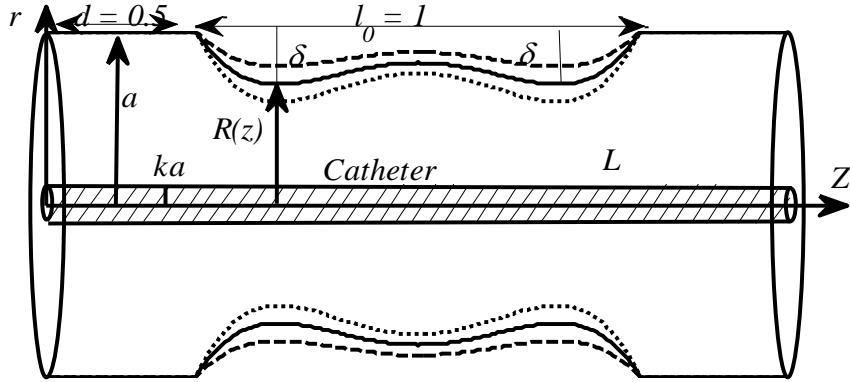
**Fig. 5.1(a)**. Geometry of the overlapping stenotic artery with a catheter.

5.2   Flow equations

The appropriate velocity field for two-dimensional and axi-symmeteric flow under consideration is defined in Eq. (4.4). The constitutive equation for Carreau fluid model is [22]

$$S = \left(\mu_\infty + \left(\mu_0 - \mu_\infty\right)\left[1 + \Gamma^2\Pi^2\right]^{\frac{n-1}{2}}\right)A_1^*.$$

(5.2)

In Eq. (5.2), μ_0 and μ_∞ are zero-shear-rate and infinite-shear-rate viscosities, respectively and Γ is the time constant.

In view of (4.4), the continuity equation (1.2) reduces to

$$\frac{\partial u}{\partial r} + \frac{u}{r} + \frac{\partial w}{\partial z} = 0. \tag{5.3}$$

Similarly, the momentum equation (1.3) in the presence of magnetic field and component of extra stress S take the following form:

$$\rho\left(\frac{\partial u}{\partial t} + u\frac{\partial u}{\partial r} + w\frac{\partial w}{\partial z}\right) = -\frac{\partial p}{\partial r} + \left(\frac{1}{r}\frac{\partial}{\partial r}(rS_{rr}) + \frac{\partial}{\partial z}(S_{rz})\right), \tag{5.4}$$

$$\rho\left(\frac{\partial w}{\partial t} + u\frac{\partial w}{\partial r} + w\frac{\partial w}{\partial z}\right) = -\frac{\partial p}{\partial z} + \rho G(t) + \left(\frac{1}{r}\frac{\partial}{\partial r}(rS_{rz}) + \frac{\partial}{\partial z}(S_{zz})\right) - \sigma B_0^2 w, \tag{5.5}$$

$$S_{rr} = 2\left[\mu_\infty + (\mu_0 - \mu_\infty)\left\{1 + \Gamma^2\left[2\left(\left(\frac{\partial u}{\partial r}\right)^2 + \left(\frac{u}{r}\right)^2 + \left(\frac{\partial w}{\partial z}\right)^2\right) + \left(\frac{\partial u}{\partial z} + \frac{\partial w}{\partial r}\right)^2\right]\right\}^{\frac{n-1}{2}}\right]\left(\frac{\partial u}{\partial r}\right), \tag{5.6}$$

$$S_{zz} = 2\left[\mu_\infty + (\mu_0 - \mu_\infty)\left\{1 + \Gamma^2\left[2\left(\left(\frac{\partial u}{\partial r}\right)^2 + \left(\frac{u}{r}\right)^2 + \left(\frac{\partial w}{\partial z}\right)^2\right) + \left(\frac{\partial u}{\partial z} + \frac{\partial w}{\partial r}\right)^2\right]\right\}^{\frac{n-1}{2}}\right]\left(\frac{\partial w}{\partial z}\right), \tag{5.7}$$

$$S_{rz} = \left[\mu_\infty + (\mu_0 - \mu_\infty)\left\{1 + \Gamma^2\left[2\left(\left(\frac{\partial u}{\partial r}\right)^2 + \left(\frac{u}{r}\right)^2 + \left(\frac{\partial w}{\partial z}\right)^2\right) + \left(\frac{\partial u}{\partial z} + \frac{\partial w}{\partial r}\right)^2\right]\right\}^{\frac{n-1}{2}}\right]\left(\frac{\partial w}{\partial r} + \frac{\partial u}{\partial z}\right). \tag{5.8}$$

Making use of dimensionless variables defined through Eqs. (4.13), (5.4) - (5.8) after dropping bars can be casted as

$$\delta\left(\frac{\partial u}{\partial r}+\frac{u}{r}\right)+\frac{\partial w}{\partial z}=0, \tag{5.9}$$

$$\alpha\delta\varepsilon^2\left(\frac{\partial u}{\partial t}+\varepsilon Re\left(\delta u\frac{\partial u}{\partial r}+w\frac{\partial u}{\partial z}\right)\right)=-\frac{\partial p}{\partial r}+\varepsilon^2\left(\frac{1}{r}\frac{\partial}{\partial r}(rS_{rr})+\frac{\partial}{\partial z}(S_{rz})\right), \tag{5.10}$$

$$\alpha\left[\frac{\partial w}{\partial t}\right]+Re\left(\delta\varepsilon u\frac{\partial w}{\partial r}+\varepsilon^2 w\frac{\partial w}{\partial z}\right)=-\frac{\partial p}{\partial z}+B_2\left(\cos\left(c_2 t+\phi\right)\right)+\left(\frac{1}{r}\frac{\partial}{\partial r}(rS_{rz})+\varepsilon^2\frac{\partial}{\partial z}(S_{zz})\right)-M^2 w, \tag{5.11}$$

$$S_{rz}=\left[m+(1-m)\left\{1+We^2\left[\left[2\left(\delta\varepsilon\left(\left(\frac{\partial u}{\partial r}\right)^2+\left(\frac{u}{r}\right)^2\right)+\varepsilon\left(\frac{\partial w}{\partial z}\right)^2\right)+\left(\delta\frac{\partial u}{\partial z}+\frac{\partial w}{\partial r}\right)^2\right]\right]^{\frac{n-1}{2}}\right\}\right]\left(\frac{\partial w}{\partial r}+\delta\frac{\partial u}{\partial z}\right),$$

$$S_{rr}=\left[m+(1-m)\left\{1+We^2\left[\left[\delta\varepsilon\left(\left(\frac{\partial u}{\partial r}\right)^2+\left(\frac{u}{r}\right)^2\right)+\varepsilon\left(\frac{\partial w}{\partial z}\right)^2\right)+\left(\delta\frac{\partial u}{\partial z}+\frac{\partial w}{\partial r}\right)^2\right]\right]^{\frac{n-1}{2}}\right]\left(\varepsilon\delta\frac{\partial u}{\partial r}\right),$$

$$S_{zz}=\left[m+(1-m)\left\{1+We^2\left[\left[2\left(\delta\varepsilon\left(\left(\frac{\partial u}{\partial r}\right)^2+\left(\frac{u}{r}\right)^2\right)+\varepsilon\left(\frac{\partial w}{\partial z}\right)^2\right)+\left(\delta\frac{\partial u}{\partial z}+\frac{\partial w}{\partial r}\right)^2\right]\right]^{\frac{n-1}{2}}\right]\left(\varepsilon\frac{\partial w}{\partial z}\right). \tag{5.12}$$

Employing mild stenosis assumption. i. e. $\left(\delta=\delta^*/a<<1\right)$, and further assuming that $\varepsilon=a/l_0\approx O(1)$, the above equations take the following form

$$\frac{\partial p}{\partial r}=0, \tag{5.13}$$

$$\alpha\left[\frac{\partial w}{\partial t}\right]=-\frac{\partial p}{\partial z}+B_2\left(\cos\left(c_2 t+\phi\right)\right)+\frac{1}{r}\frac{\partial}{\partial r}\left[r\left\{m+(1-m)\left(1+We^2\left|\frac{\partial w}{\partial r}\right|^2\right)^{\frac{n-1}{2}}\right\}\frac{\partial w}{\partial r}\right]-M^2 w. \tag{5.14}$$

Note that Eq. (5.9) does not need to be considered further because in view of the mild stenosis assumption the information given by it i.e. $\frac{\partial w}{\partial z}=0$ is already integrated in Eq. (5.14). Following Burton [99], we take

$$-\frac{\partial p}{\partial z} = A_0 + A_1 Re\left\{e^{2\pi i \omega_p t}\right\}, \qquad t > 0, \tag{5.15}$$

where A_0 is the mean pressure gradient and A_1 is the amplitude of the pulsatile component which is responsible for systolic and diastolic pressures. In dimensionless form (5.15) becomes

$$-\frac{\partial p}{\partial z} = B_1\left(1 + ecos(c_1 t)\right). \tag{5.16}$$

It is pointed out that expression (5.16) slightly differs from its counterpart given in previous chapters because of the use of ω as normalization frequency instead of ω_p. In Eqs. (5.9) - (5.12), $We = \Gamma U_0 / a$ is the *Weissenberg number* and $M = B_0 a \left(\sigma / \mu_0\right)^{1/2}$ is the Hartmann number and

$$c_1 = \frac{\omega_p}{\omega}, \ c_2 = \frac{\omega_b}{\omega}, \ m = \frac{\mu_\infty}{\mu_0}. \tag{5.17}$$

Inserting value of $-\partial p / \partial z$ in axial momentum equation (5.16), we get

$$\alpha\left[\frac{\partial w}{\partial t}\right] = B_1\left(1 + ecos(c_1 t)\right) + B_2\left(\cos\left(c_2 t + \phi\right)\right) + \frac{1}{r}\frac{\partial}{\partial r}\left[r\left\{m + (1-m)\left(1 + We^2\left|\frac{\partial w}{\partial r}\right|^2\right)^{\frac{n-1}{2}}\right\}\frac{\partial w}{\partial r}\right] - M^2 w. \tag{5.18}$$

The above equation is subject to following boundary and initial conditions

$$w(r,t)\Big|_{r=k} = 0, w(r,t)\Big|_{r=R} = 0, \ w(r,0) = 0, \tag{5.19}$$

The formulas of *volume flow rate*, *wall shear stress (WSS)* and *resistance impendence* in new variables read

$$Q = \int_k^R wr dr, \tag{5.20}$$

$$\tau_s = \left(\left\{m + (1-m)\left(1 + We^2\left|\frac{\partial w}{\partial r}\right|^2\right)^{\frac{n-1}{2}}\right\}\frac{\partial w}{\partial r}\right)_{r=R}, \tag{5.21}$$

$$\lambda = \frac{L\left(\dfrac{\partial p}{\partial z}\right)}{Q}, \tag{5.22}$$

where

$$R(z) = (1 + \xi z)\left[1 - \frac{64}{10}\eta_1\left(\frac{11}{32}(z-d) - \frac{47}{48}(z-d)^2 + (z-d)^3 - \frac{1}{3}(z-d)^4\right)\right], \quad \sigma \le z \le \sigma + 1.5, \tag{5.23}$$

with $\quad \eta_1 = 4\delta, \ \delta = \dfrac{\delta^*}{a}, \ \sigma = \dfrac{d}{l_0}, \ \xi = \dfrac{\xi^* l_0}{a}.$

The formula (5.21) actually represents the magnitude of generalized wall shear stress given in [76] under mild stenotic assumption. According to [76]

$$\tau_s = \sqrt{w \cdot w}, \tag{5.24}$$

where $w = Tn - (Tn.n)n$, T is the stress tensor given through Eq. (2.2) and n is outward normal to the wall surface.
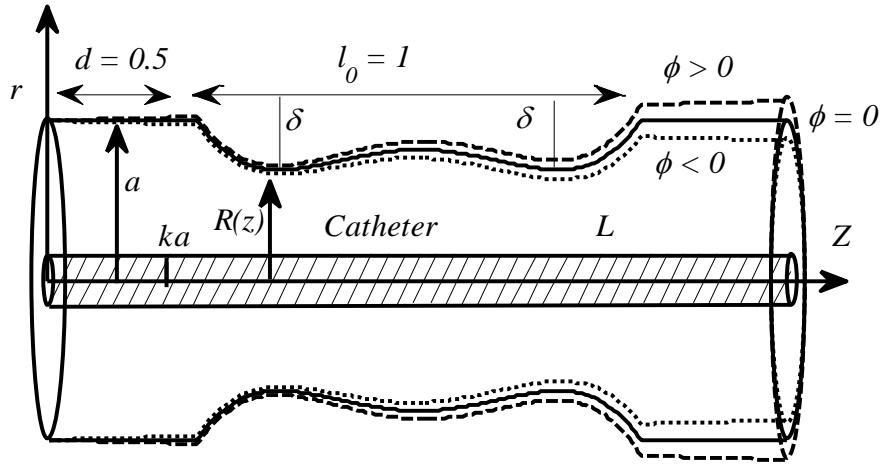

Fig. 5.1(b). Geometry of the stenotic artery with different tapering angles.

Employing the radial coordinate transformation [75]

$$x = \frac{r}{R(z)}, \tag{5.25}$$

Eq. (5.18) can be transformed as

$$\alpha\left[\frac{\partial w}{\partial t}\right] = B_1\left(1+ecos(c_1 t)\right) + B_2\left(cos\left(c_2 t+\phi\right)\right) + \frac{1}{xR^2}\frac{\partial}{\partial x}\left[x\left\{m+\left(1-m\right)\left(1+\left(\frac{We}{R}\right)^2\left|\frac{\partial w}{\partial x}\right|^2\right)^{\frac{n-1}{2}}\right\}\frac{\partial w}{\partial x}\right] - M^2 w,$$

(5.26)

and the dimensionless boundary conditions becomes

$$w\big|_{x=k} = 0, w\big|_{x=1} = 0, \; w\big|_{t=0} = 0.$$

(5.27)

Similarly the volume flow rate, the shear stress at the wall and resistance impendence, respectively takes

the form

$$Q = R^2\left(\int_k^1 w\,xdx\right),$$

(5.28)

$$\tau_s = \frac{1}{R}\left(\left\{m+\left(1-m\right)\left(1+\left(\frac{We}{R}\right)^2\left|\frac{\partial w}{\partial x}\right|^2\right)^{\frac{n-1}{2}}\right\}\frac{\partial w}{\partial x}\right)_{x=1},$$

(5.29)

$$\lambda = \frac{\dfrac{L}{l_0}\left(\dfrac{\partial p}{\partial z}\right)}{Q}.$$

(5.30)

Substituting the dimensionless form of pressure gradient in Eq. (5.30), we can write

$$\lambda = \frac{L}{l_0}\frac{B_1\left(1+ecos(2\pi t)\right)}{\left(\int_0^1 w\,xdx\right)R^2(z)}.$$

(5.31)

5.3   Solution methodology

Due to nonlinear nature of Eq. (5.26), an exact solution is difficult to find. Therefore, a numerical solution

is inevitable for further discussion. Now, employing a similar procedure to approximate the various partial

derivatives appearing in Eq. (5.26), we get the following discretized version of Eqs. (5.26):

$$w_i^{k+1} = w_i^k + \frac{\Delta t}{\alpha}\left[\left\{B_1\left(1+ecos(c_1 t^k)\right) + B_2\cos\left(c_2 t^k+\phi\right) + \frac{w_x}{xR^2}\left(m+\left(1-m\right)\left(1+\left(\frac{We}{R}\right)^2|w_x|^2\right)^{\frac{n-1}{2}}\right)\right\}+\right.$$

$$+\frac{(1-m)w_x}{R^2}\frac{\partial}{\partial x}\left[\left(1+\left(\frac{We}{R}\right)^2|w_x|^2\right)^{\frac{n-1}{2}}\right]+\frac{1}{R^2}\left[m+(1-m)\left(1+\left(\frac{We}{R}\right)^2|w_x|^2\right)^{\frac{n-1}{2}}\right]w_{xx}-M^2w_i^k\right].\quad (5.32)$$

The finite difference representation of prescribed conditions is given by

$$
\begin{aligned}
w_i^1 &= 0, & & at\ t=0, \\
w_{N+1}^k &= 0, & & at\ x=1, \\
w_1^k &= 0 & & at\ x=k\ (catheterered\ radius).
\end{aligned}
\qquad (5.33)
$$

Eq. (5.32) is used to compute the value of w at $N+1$ uniformly discrete points $x_i, (i=1,2,\ldots N+1)$ with

a space grid size $\Delta x = \frac{1}{N+1}$ at the time levels $t_k = (k-1)\Delta t$, where Δt is the small increment in time. To

obtain the accuracy of the order $\sim 10^{-7}$, we have taken the following step sizes: $\Delta x = 0.025$ and

$\Delta t = 0.00001$.

5.4   Results and discussion

The computation are carried out for the following set of parameters: $d=0.5, l_0=1.0,\ L=2.7, \alpha=0.8,\ \mu_0=0.56,\ \mu_\infty=0.0345, \phi=0.0, \omega_p=2\pi f_p,\ \sigma=0.25,\ k=0.1.$

Fig. 5.2 demonstrates the dimensionless velocity profiles of blood at different locations of the arterial segment. Panel (a) is plotted for a specific set of parameters. Each parameter of this specific set is varied to produce plots in panels ((b)-(h)) at the same cross-sections as taken in panel (a). In this way panel (a) is considered as standard and other panels are compared with it in order to observe the effects of various parameters. In panel (b) the velocity profiles are shown by changing the radius of the catheter. This panel when compared with panel (a) indicates that the effect of increasing catheter radius is to decrease the magnitude of velocity significantly at each cross-section. Panel (c) illustrates the effects of increasing critical stenotic height on velocity profile. It is evident from the comparison of panel (c) and panel (a) that blood flow velocity decreases by increasing the critical height of the stenosis. The effects of power law index n on velocity profile at various location of the artery are shown in panel (d). It is seen that an increase in n decreases the flow velocity of blood. The parameter We which control the viscoelastic behavior of

blood also bears the potential to significantly affect the velocity profile at each cross –section. It is observed through comparison of panel (a) and panel (e) that velocity profile of blood is an increasing function of *Weissenberg number* (*We*). In panel (a) the profiles are shown at the time instant *t =0.3* which belongs to systolic phase. For a time instant which belong to diastolic phase i.e. *t =0.45* the velocity profile are shown in panel (f). In diastolic phase pressure gradient fall down and as a result of that the magnitude of velocity at each cross-section reduces. The velocity profiles at different cross-sections of the artery also show decreasing behavior by increasing the strength of the magnetic field. This behavior of velocity can be readily observed by a comparison of panel (a) with panel (h). The effects of amplitude of body acceleration on velocity profiles at various cross-sections can be observed by comparing panels (a) and (h). The comparison shows that an increase in amplitude of body acceleration increases the magnitude of velocity. A general observation from Fig.5.2 is that the rheological parameters of blood, the catheter radius, the amplitude of body acceleration, the magnetic field alter the magnitude of velocity in both stenotic and non-stenotic region. However, the geometric parameter of stenosis δ effects the velocity profile only in the stenotic region. The decrease in the magnitude of velocity by inserting a catheter is of major concern to the clinicians. This may result in some complications during the treatment/diagnostic procedure. However, the non-Newtonian rheology of the blood could be exploited to tune the velocity profile in a manner so that the effects of catheter on flow velocity are minimum. Indeed, in case of Newtonian fluid, the flow velocity is only function of geometrical parameters of the stenosis. The only way to modify, for example, the flow velocity is to change the geometrical parameters of the stenosis which is of course not possible. However, for a non-Newtonian fluid the velocity in addition to the geometrical parameters of fluid is controlled by the mechanical properties of the blood. Thus the non-Newtonian feature of blood allows the flow velocity to be tuned without modification of geometrical parameters of the stenosis. It is worth mentioning that our approach basically follows the approach of Mandal [26] and that is why our results are in accordance with his results. In fact it is shown by Mandal [26] that axial velocity get reduced to a considerable extent in case of a steeper stenosis. Thus following Mandal [26], we have prescribed the pressure gradient of sinusoidal type instead of prescribing the flow rate. In this way flow rate in our study is unknown. Since pulsatile

pressure gradient is the main source of flow in our case therefore no flow velocity is imposed at the inlet. On the contrary, Tzirtzilakis [77] has prescribed the flow rate at inlet and calculated the stream function (consequently the velocity). His study shows different flow jets and downstream recirculation zones. Similar results are reported by Lee et al [78] by prescribing the Poiseuille type flow at the inlet, where apart from different flow jets and downstream recirculation it is also shown that axial velocity increases in the case of narrowing of stenosis. From the above discussion it concluded that increase of axial velocity in the stenotic region is attributed to the prescription of flow rate at the inlet. On the other hand, the decrease of axial velocity in the stenotic region is attributed to the prescription of pressure gradient. It is remarked here that fixing the correct boundary conditions at inlet and outlet in term of flow rate or velocity is an active subject of research. We refer the reader to recent articles by Guerra et al. [79] and Elia et al. [80] where data assimilation techniques based on variational approach are used to address the issue.

The time series of flow rate at $z = 0.77$ (where the maximum height of the stenosis is observed) for various values of emerging parameters is shown in **Fig. 5.3**. The solid line curve corresponds to a specific set of parameters i.e. $We = 1.8, n = 0.8, M = 0.5, k = 0.1, \delta = 0.1, B_2 = 2.$ Each parameter from this set except B_2 is varied to produce all the other curves in Fig. 5.3. For instance the dashed curve is generated by changing δ. It is noticed that due to pulsatile nature of flow, the flow rate also oscillates with time. For initial times its behavior is not periodic. However, it achieves periodicity after $t = 2.3sec$. The amplitude of oscillations shows quantitative variations by changing n, We, δ and M. In fact it is seen by examining the other curves that flow rate decreases by increasing n, M, δ and k, while it exhibits opposite trend by increasing We.

The time series of WSS at stenotic throat for some specific values of We, n, M, k and δ is shown through **Fig. 5.4**. Various curves in Fig. 5.4 are compared according to the rule as used in Fig. 5.3. It is observed from this figure that WSS is found to decrease by increasing critical height of stenosis, strength of magnetic field, radius of catheter and Weissenberg number. However, it magnitude increases by increasing amplitude of body acceleration.

The time series of resistive impedance at $z = 0.77$ corresponding to the critical height of stenosis is calculated using Eq. (5.33) and shown in **Fig. 5.5** for various parameters. A quantitative comparison of solid line curves with other curves indicates that impedance increases by increasing magnetic field strength, catheter radius, critical height of stenosis and power-law index. However, it follows opposite trend by increasing Weissenberg number. It is also observed during simulations that the magnitude of impedance at a location in overlapping region of stenosis ($z = 1.26$) is less than its magnitude at stenotic throat ($z = 0.77$).

The blood flow patterns for different values of involved parameters are shown in **Fig. 5.6**. Panel (*a*) shows the flow pattern for specific values of *We*, *n*, *M*, δ, and *t*. This panel confirms the appearance of circulating bolus of fluid in the stenotic region. By increasing *n* from *0.8* to *0.9*, the size and circulation of bolus increases as evident from panel (*b*). A comparison of panel (*a*) and panel (*c*) discloses the potential of applied magnetic field to reduce the strength of the circulating region. The effects of Weissenberg number on circulating bolus of fluid can be observed by comparing panel (*a*) and panel (*d*). It is noted that the strength of circulation region increases by increasing Weissenberg number. A comparison of flow patterns of panel (*a*) and panel (*e*) indicates that the outer most streamline of circulating region in non-tapered artery splits in case of converging artery. Moreover, there is an appearance of small eddy in the downstream region for converging artery. Panel (*f*) shows flow pattern for a diverging artery. When compared with panel (*a*), this panel also indicates the splitting of the outer most streamline and small eddy in upstream region. The effects of critical height of stenosis on flow pattern can be understood from a comparison of panel (*a*) and panel (*g*). It is seen that strength of circulating region increases by increasing the stenotic height. The strength of circulation bolus of fluid also varies with the passage of time. In fact the bolus size decreases in systolic phase while in diastolic its behavior is reversed panel (*h*). The effect of catheter radius on blood flow pattern can be well understood by comparing Figs. 5.6(*a*) and 5.6(*i*). It is interesting to note that the size and circulation of bolus increases by increasing the catheter radius.

5.5   Concluding remarks

A mathematical model for unsteady magneto-hydrodynamics blood flow through a catheterized stenotic vessel is analyzed. The constitutive equation of Carreau model is used to represent blood rheology. A numerical solution of the governing initial-boundary value problem is obtained employing the finite difference method. The velocity and volumetric flow rate of blood, arterial wall shear stress, impedance and streamlines of flow are analyzed quantitatively for geometrical parameter of stenosis, rheological parameters of blood, catheter radius and magnetic field. It is found that blood velocity and flow rate decrease with increasing the catheter radius. On the contrary, the impedance increases with increasing the catheter radius. Moreover, the strength of recirculating zones appearing in the stenotic region is also an increasing function of catheter radius. These observations may have certain clinical implications. In fact it is desired in any clinical procedure regarding treatment/diagnosis of atherosclerosis to avoid the reduction of flow rate and to decrease the impedance (resistance to flow) due to insertion of a catheter. The present study discloses two remedies to avoid such effects. One remedy, of course, is to manufacture the catheters of very thin radius and the other remedy is to tune the rheology of the blood. The later cannot be proposed by incorporating Newtonian fluid in the flow analysis. Moreover, power-law model gives the choice to tune the velocity of blood only by exploiting the shear-thinning nature of the blood. However, the Carreau model gives additional solution i.e., to use the viscoelastic nature of blood to tune the velocity of blood. In the end we would like to mention that the present analysis has certain limitations. In fact a more detailed analysis, without using mild stenosis condition, which encompasses wall properties, two- or three-dimensional aspects of the flow etc. may be more helpful in bringing out the realistic results.
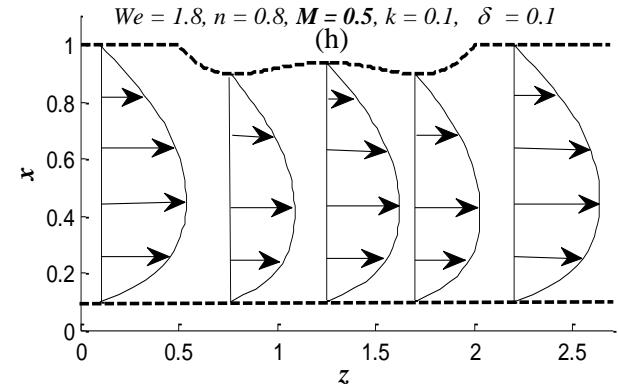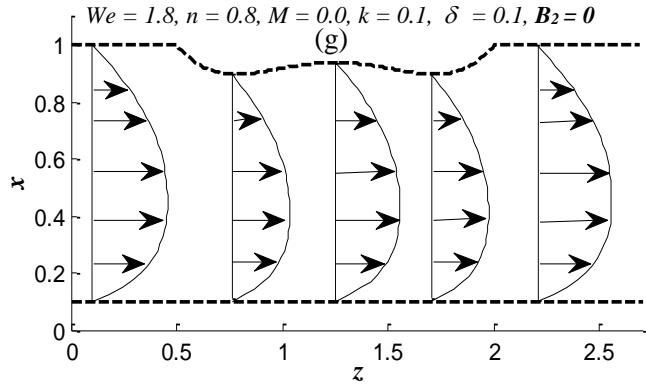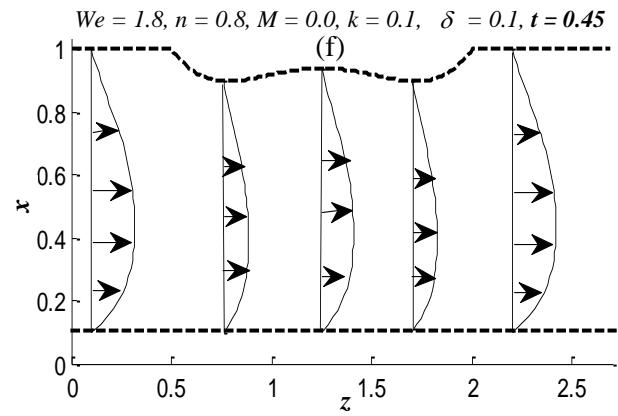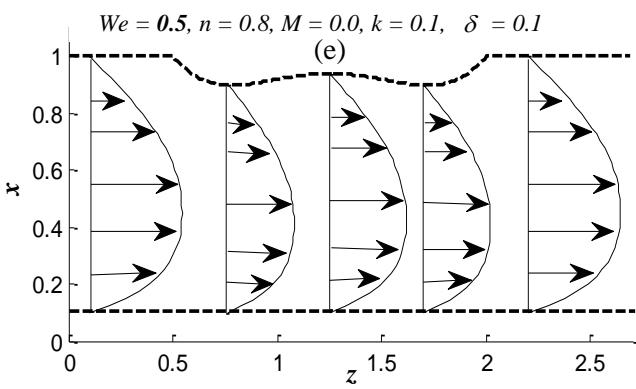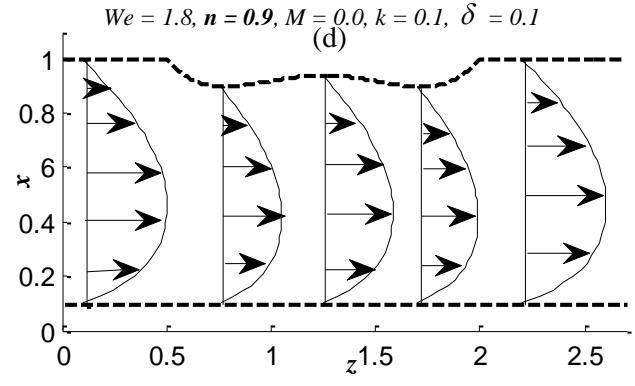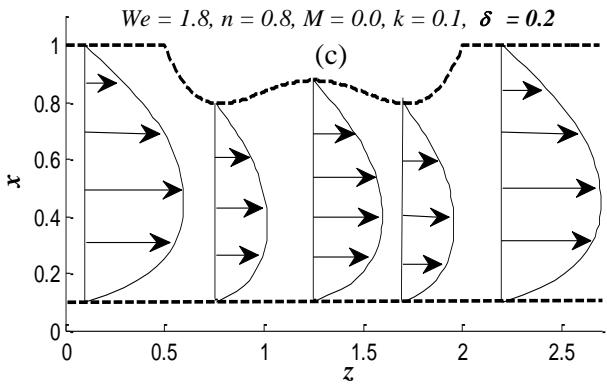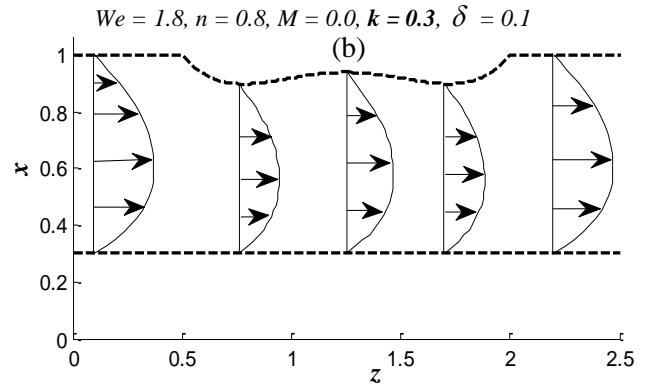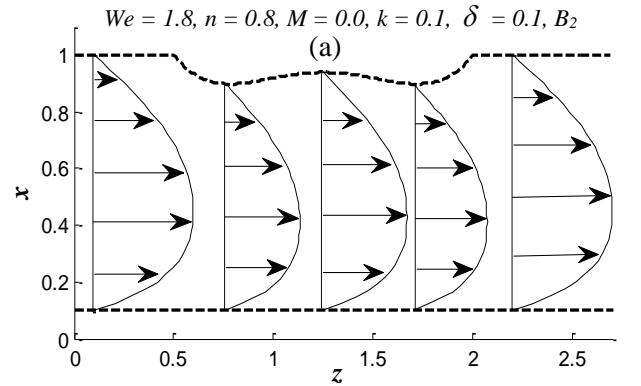
**Fig. 5.2**. Velocity profile at different cross sections of the artery.

72
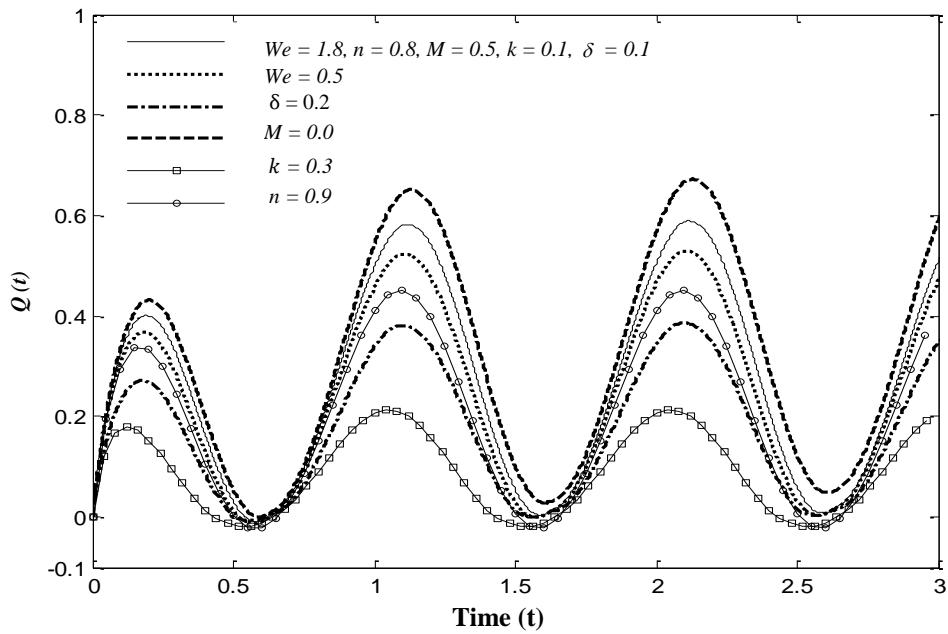
Fig. 5.3. Dimensionless flow rate profiles for: $B_1 = 2$, $B_2 = 2$.
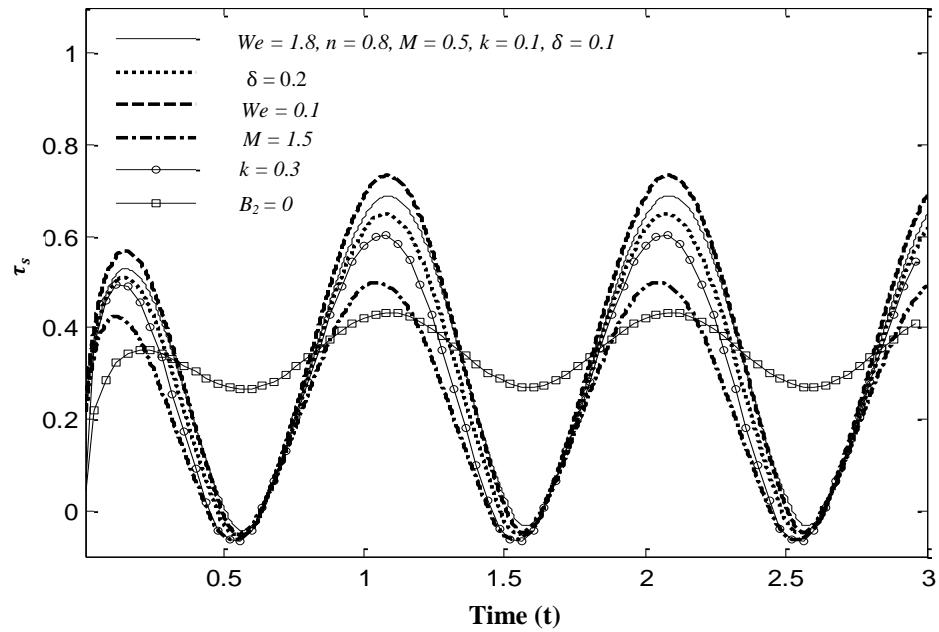

Fig. 5.4. Dimensionless shear stress profiles for: $B_1 = 2$, $B_2 = 2$.
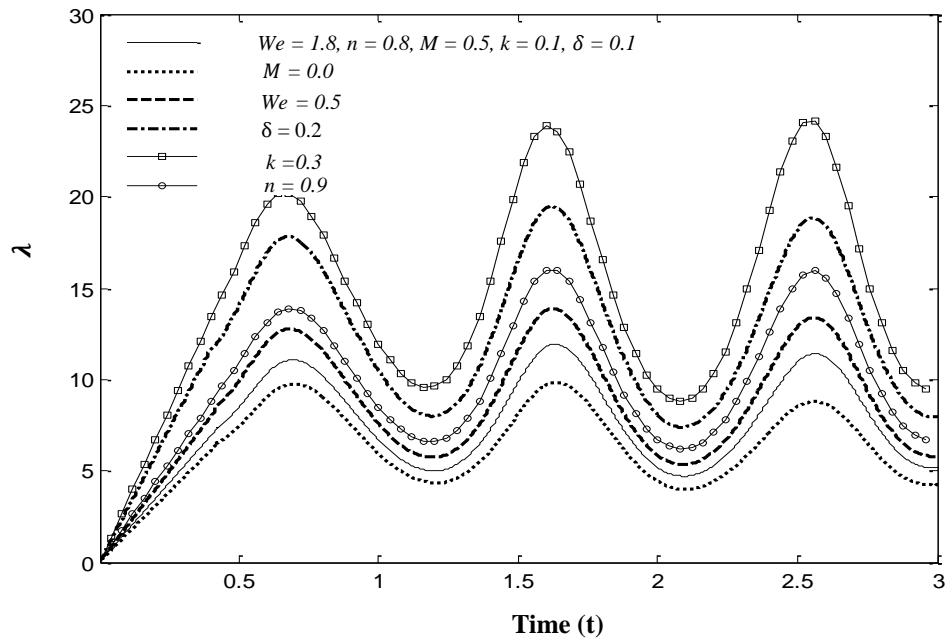
Fig. 5.5. Dimensionless resistance to flow profiles for: $B_1 = 2$, $B_2 = 0$.

(a) We = 1.8, n = 0.8, M = 0.5, δ = 0.1, t = 0.3

*(b) We = 1.8, **n = 0.9**, M = 0.5, δ = 0.1, t = 0.3*

*(c) We = 1.8, n = 0.8, **M = 0.0**, δ = 0.1, t = 0.3*

*(d) **We = 0.5**, n = 0.8, M = 0.5, δ = 0.1, t = 0.3*

(*e*) *We = 1.8, n = 0.8, M = 0.0, δ = 0.1, ξ = -0.05*   (*f*) *We = 1.8, n = 0.8, M = 0.0, δ = 0.1, ξ = 0.05*
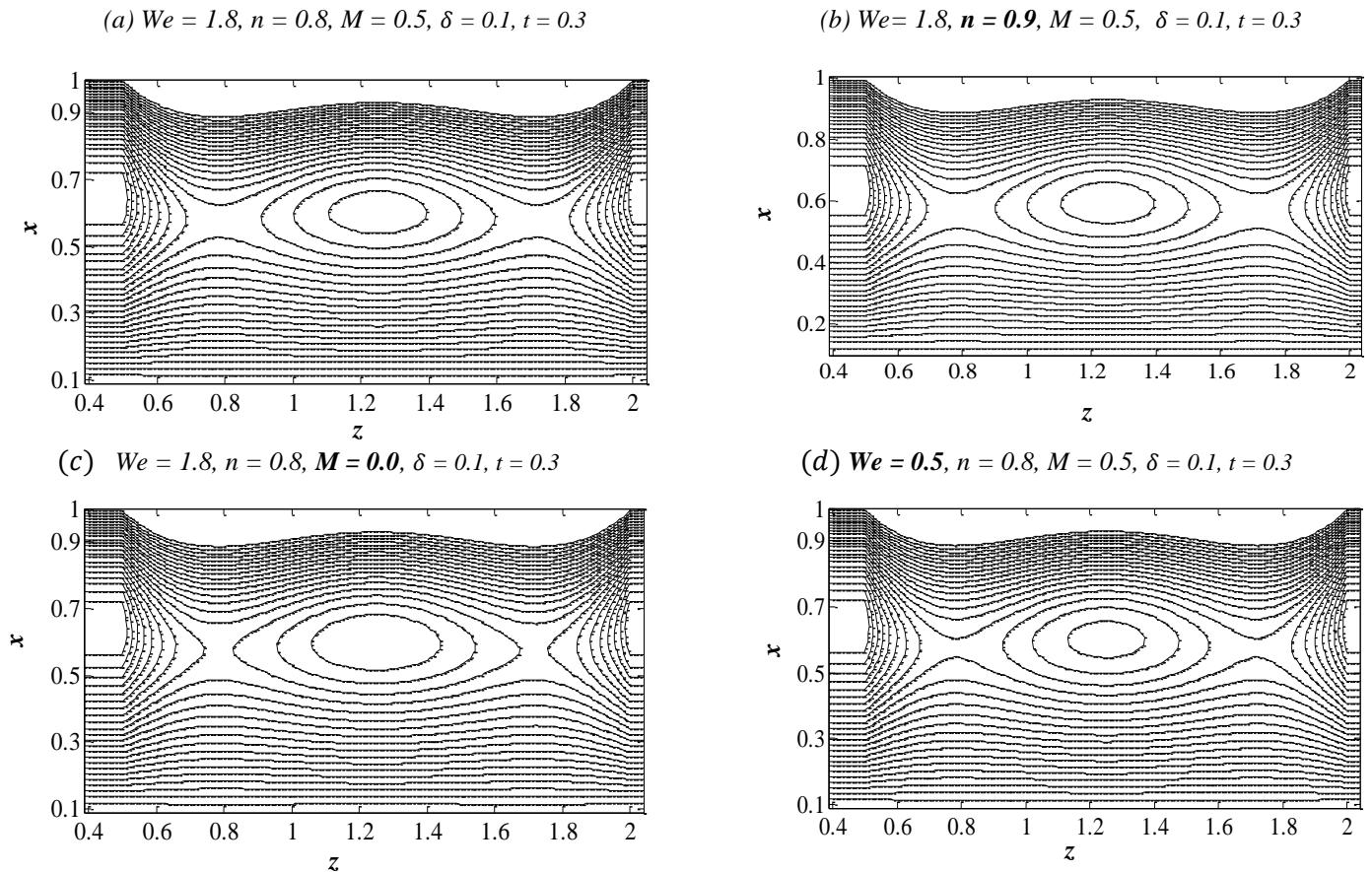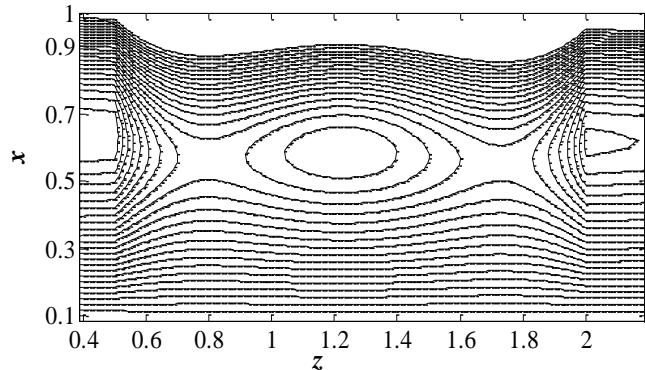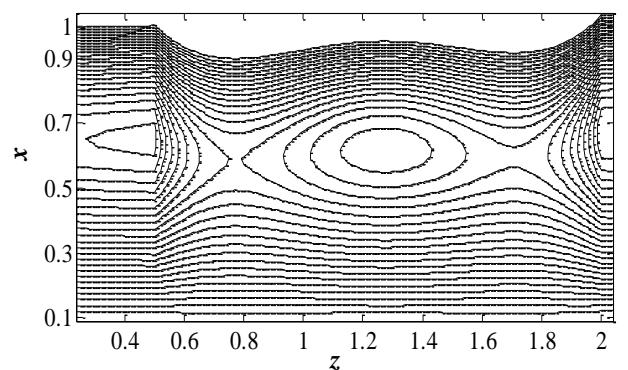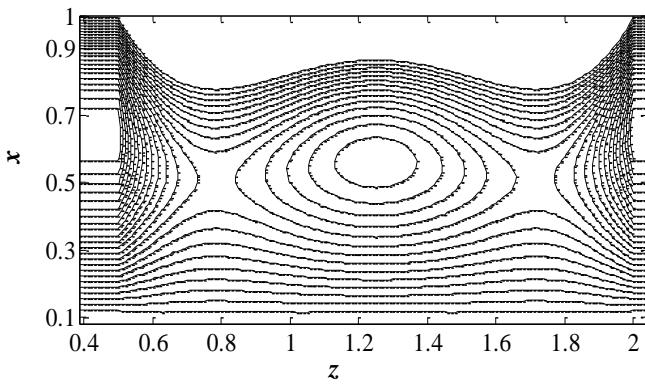
(*g*) *We = 1.8, n = 0.8, M = 0.0, δ = 0.2, t = 0.3*   (*h*) *We = 0.5, n = 0.8, M = 0.5, δ = 0.1, t = 0.45*
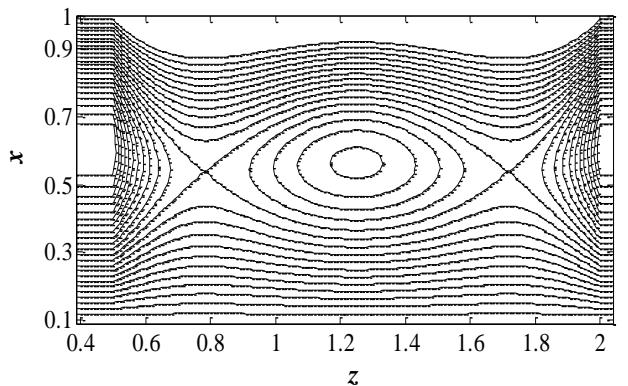
(*i*) *We = 1.8, n = 0.8, M = 0.0, k = 0.3, t = 0.3*
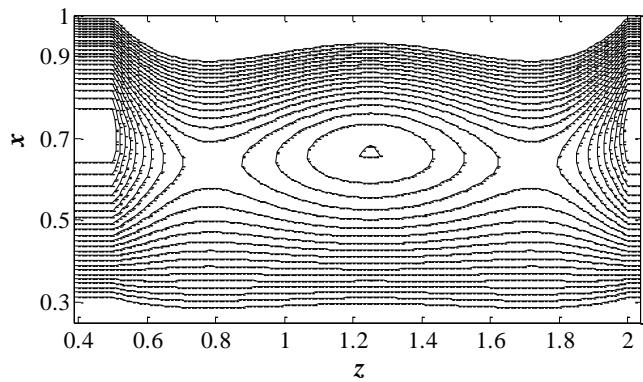
Fig. 5.6. Blood flow patterns for: $B_1 = 2$, $B_2 = 2$.

Chapter 6

Unsteady micropolar hemodynamics in a tapered catheterized artery with a combination of stenosis and aneurysm

In this chapter, the unsteady flow characteristics of blood are analyzed through a catheterized stenotic artery with post-stenotic dilatation. A rigid tube with a pair of abnormal wall segments in close proximity to each other is employed to geometrically simulate the diseased artery. A micropolar fluid model is used to capture the rheological characteristics of the streaming blood in the annulus. The mild stenosis approximation is employed to derive the governing flow equation which is then solved using a robust finite difference method. Particular attention is paid to the effects of geometrical parameters of the arterial wall and rheological parameters of the blood on axial velocity, flow rate, resistance impedance and wall shear stress. The global behavior of blood is also analyzed through instantaneous pattern of streamlines.

6.1   Geometric Model

Consider the unsteady two-dimensional and incompressible flow of non-Newtonian blood in a straight, rigid and axisymmetric catheterized artery of length L that contains two diseased segments. A cylindrical coordinate system (r, θ, z) has been utilized for the analysis of the current problem, in which r and z

axes are along the radial and axial directions of the artery respectively. The equation describing the geometry of wall is given by:

$$R(z) = \begin{cases} \left(\xi^* z + a\right)\left[1 - \left(\dfrac{\delta^*}{2a}\left(1 + \cos\dfrac{2\pi}{l_i}\left(z - \beta_i - \dfrac{l_i}{2}\right)\right)\right)\right], & \beta_i \leq z \leq \beta_i + l_i, i = 1, 2. \\ \left(\xi^* z + a\right), & \text{otherwise.} \end{cases}$$
(6.1)

In the above expression, β_i represents the length of ith abnormal segment from the origin, a denotes radius of the undisturbed *non-tapered* component of the artery, l_i is the length of abnormal segment and $\xi^* \left(= \tan\phi\right)$ the parameter controlling the convergence or divergence of an artery. A schematic diagram of the *non-tapered* artery is shown in **Fig. 6.1 (a)**, in which δ_i^* denotes the critical height of the ith abnormal segment appearing at two specific locations respectively i.e.

$$z = \beta_1 + \frac{l_0}{2}, \ and \ z = \beta_2 + \frac{l_0}{2}.$$
(6.2)

The cases $\phi < 0,\ \phi = 0,\ \phi > 0$ corresponding to converging, non-tapered and diverging artery scenario's, respectively are displayed in **Fig. 6.1 (b)**. It is emphasized that δ_i^* is *positive for stenosis* and *negative for aneurysms*. The radius of the catheter inserted in the diseased artery is *ka (k << 1)*.
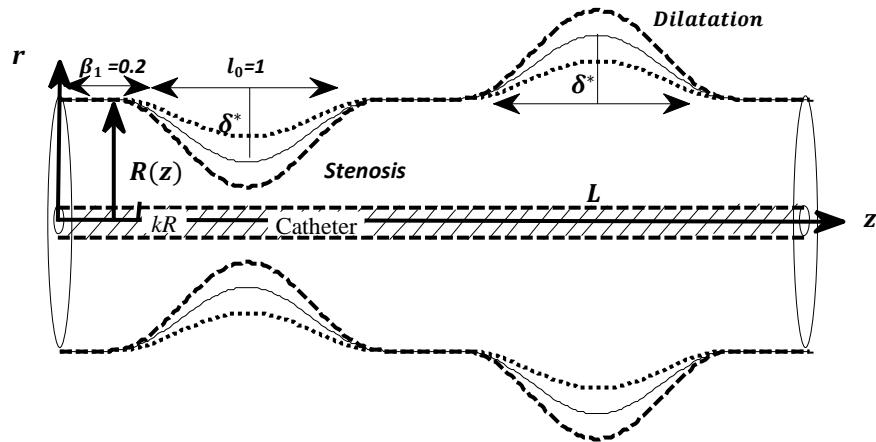

Fig. 6.1(a). Geometry of the arterial segment in pulsatile rheo-hemodynamic model.

For the problem under consideration we have assumed $l_1 = l_2 = l_0$, $\delta_1^* = \delta^*$ and $\delta_2^* = -\delta^*$ for simplicity.

6.2 Flow equations

The equations that govern the unsteady flow of an incompressible micropolar fluid are [81]:

$$\rho\left(\frac{\partial \mathbf{V}}{\partial t} + \mathbf{V} \cdot \nabla \mathbf{V}\right) = -\nabla p + m_1 \nabla \times \mathbf{V} + (\mu + m_1)\nabla^2 \mathbf{V}, \tag{6.3}$$

$$\rho j\left(\frac{\partial \mathbf{v}}{\partial t} + \mathbf{V} \cdot \nabla \mathbf{v}\right) = -2m_1 \mathbf{v} + m_1 \nabla \times \mathbf{V} - \gamma(\nabla \times \nabla \times \mathbf{v}) + (\eta + \chi + \gamma)\nabla(\nabla \cdot \mathbf{v}), \tag{6.4}$$

where $\mathbf{V}$ is the velocity vector, $\mathbf{v}$ is the micro-rotation vector, ρ is the fluid density, j is the micro-gyration parameter, p is the fluid pressure, γ, χ, η are the coefficients of the viscosities and m_1, μ are coefficients of the vortex and shear viscosity, respectively. Moreover, the parameters μ, m_1, γ, χ and η are subject to the following constraints [29]:

$$2\mu + m_1 \geq 0, \ m_1 \geq 0, \ 3\eta + \gamma + \chi \geq 0, \quad \gamma \geq |\chi|. \tag{6.5}$$

Since the flow under consideration is unsteady, two-dimensional and axisymmetric, therefore, we define the vectors:

$$\mathbf{V} = \left[u(r,z,t), \ 0, \ w(r,z,t)\right], \tag{6.6}$$

$$\mathbf{v} = \left[0, \ v(r,z,t), \ 0\right]. \tag{6.7}$$

In view of (6.6)-(6.7), the continuity equation (1.2) reduces to

$$\frac{\partial u}{\partial r} + \frac{u}{r} + \frac{\partial w}{\partial z} = 0. \tag{6.8}$$

Similarly, the balances of linear and angular momenta given through Eqs. (6.3) and (6.4) take the following form:

$$\rho\left(\frac{\partial u}{\partial t} + u\frac{\partial u}{\partial r} + w\frac{\partial u}{\partial z}\right) = -\frac{\partial p}{\partial r} + (\mu + m_1)\left(\frac{\partial^2 u}{\partial r^2} + \frac{1}{r}\frac{\partial u}{\partial r} - \frac{u}{r^2}\right) - m_1\frac{\partial v}{\partial z}, \tag{6.9}$$

$$\rho\left(\frac{\partial w}{\partial t}+u\frac{\partial w}{\partial r}+w\frac{\partial w}{\partial z}\right)=-\frac{\partial p}{\partial z}+\left(\mu+m_1\right)\left(\frac{\partial^2 w}{\partial r^2}+\frac{1}{r}\frac{\partial w}{\partial r}+\frac{\partial^2 w}{\partial z^2}\right)+\frac{m_1}{r}\frac{\partial(rv)}{\partial r},\tag{6.10}$$

$$\rho J\left(\frac{\partial v}{\partial t}+u\frac{\partial v}{\partial r}+w\frac{\partial v}{\partial z}\right)=-2m_1\,v-m_1\left(\frac{\partial w}{\partial r}-\frac{\partial u}{\partial z}\right)+\gamma\left(\frac{\partial}{\partial r}\left(\frac{1}{r}\frac{\partial(rv)}{\partial r}\right)+\frac{\partial^2 v}{\partial z^2}\right).\tag{6.11}$$

Let us scale the variables *r, z, w, u, t and p* in a similar fashion as done in previous chapter and write Eqs. (6.1), (6.9)–(6.11) as follows:

$$\delta\left(\frac{\partial u}{\partial r}+\frac{u}{r}\right)+\frac{\partial w}{\partial z}=0,\tag{6.12}$$

$$\alpha\delta\varepsilon^2\left(\frac{\partial u}{\partial t}+\varepsilon Re\left(\delta u\frac{\partial u}{\partial r}+w\frac{\partial u}{\partial z}\right)\right)=-\frac{\partial p}{\partial r}+\varepsilon^2\delta^2\left(\frac{\partial^2 u}{\partial^2 r}+\frac{1}{r}\frac{\partial u}{\partial r}-\frac{u}{r^2}\right)-M\varepsilon^2\frac{\partial v}{\partial z},\tag{6.13}$$

$$\alpha\left[\frac{\partial w}{\partial t}\right]+Re\left(\delta\varepsilon u\frac{\partial w}{\partial r}+\varepsilon^2 w\frac{\partial w}{\partial z}\right)=-\frac{\partial p}{\partial z}+\left(1+K\right)\left(\frac{\partial^2 w}{\partial^2 r}+\frac{1}{r}\frac{\partial w}{\partial r}+\varepsilon^2\frac{\partial^2 w}{\partial z^2}\right)+\frac{M}{r}\frac{\partial(rv)}{\partial r},\tag{6.14}$$

$$\alpha J\frac{\partial v}{\partial t}+Re\,J\,\varepsilon\,\delta\,u\frac{\partial v}{\partial r}+Re\,J\,\varepsilon\,w\frac{\partial v}{\partial z}=-2\,M\,v-M\left(\frac{\partial w}{\partial r}-\varepsilon^2\delta\frac{\partial u}{\partial z}\right)+K\left(\frac{\partial}{\partial r}\left(\frac{1}{r}\frac{\partial(rv)}{\partial r}\right)+\varepsilon^2\frac{\partial^2 v}{\partial z^2}\right),\tag{6.15}$$

where $\bar{v}=\dfrac{av}{U_0}$, $\bar{J}=\dfrac{J}{a^2}$, $\bar{\beta}_i=\dfrac{\beta_i}{l_0}$, $\mathrm{M}=\dfrac{m_1}{\mu}$, $K=\dfrac{\gamma}{\mu a^2}$, $\delta=\dfrac{\delta^*}{a}$, $\bar{R}=\dfrac{R}{a}$, $\bar{p}=\dfrac{a^2 p}{U_0 l_i \mu}$.

For the subsequent analysis, we assume that the stenosis/aneurysm is *mild* $\left(\delta=\delta^*/a\ll1\right)$, and the ratio $\varepsilon=a/l_0\approx O(1)$ [57]. As an implication of these assumptions, Eqs. (6.13)-(6.15) reduce to:

$$\frac{\partial p}{\partial r}=0,\tag{6.16}$$

$$\alpha\left[\frac{\partial w}{\partial t}\right]=-\frac{\partial p}{\partial z}+\left(1+M\right)\left[\frac{\partial^2 w}{\partial r^2}+\frac{1}{r}\frac{\partial w}{\partial r}\right]+M\left(\frac{1}{r}\frac{\partial(rv)}{\partial r}\right),\tag{6.17}$$

$$\alpha J\left[\frac{\partial v}{\partial t}\right]=-M\left(2v+\frac{\partial w}{\partial r}\right)+K\frac{\partial}{\partial r}\left(\frac{1}{r}\frac{\partial(rv)}{\partial r}\right).\tag{6.18}$$

Inserting the value of $-\partial p / \partial z$ from Eq. (5.16) in the axial momentum equation (6.17), we get:

$$\alpha\left[\frac{\partial w}{\partial t}\right] = B\left(1 + e\cos(ct)\right) + \left(1 + M\right)\left[\frac{\partial^2 w}{\partial r^2} + \frac{1}{r}\frac{\partial w}{\partial r}\right] + M\left(\frac{1}{r}\frac{\partial(rv)}{\partial r}\right).$$

(6.19)

Eqs. (6.18) and (6.19) are subject to following boundary and initial conditions:

$$w(r,t)\big|_{r=ka} = 0, w(r,t)\big|_{r=R} = 0, \ w(r,0) = 0,$$
$$v(r,t)\big|_{r=ka} = 0, v(r,t)\big|_{r=R} = 0, \ v(r,0) = 0,$$

(6.20)

The appropriate expressions for wall shear stress (*WSS*) may be defined as:

$$\tau_w = \left(\frac{1+M}{\alpha^2}\right)\left(\frac{\partial w}{\partial r}\right) + \left(\frac{M}{\alpha^2}\right)v,$$

(6.21)

where

$$R(z) = \left(1 + \xi z\right)\left(1 - \left(\frac{\delta}{2}\left(1 + \cos 2\pi\left(z - \beta_i - \frac{1}{2}\right)\right)\right)\right), \quad \sigma \le z \le \sigma + 1,$$

$$\text{with} \quad \sigma = \frac{\beta_i}{l_i}, \ \xi = \frac{\xi^* l_i}{a}.$$

(6.22)
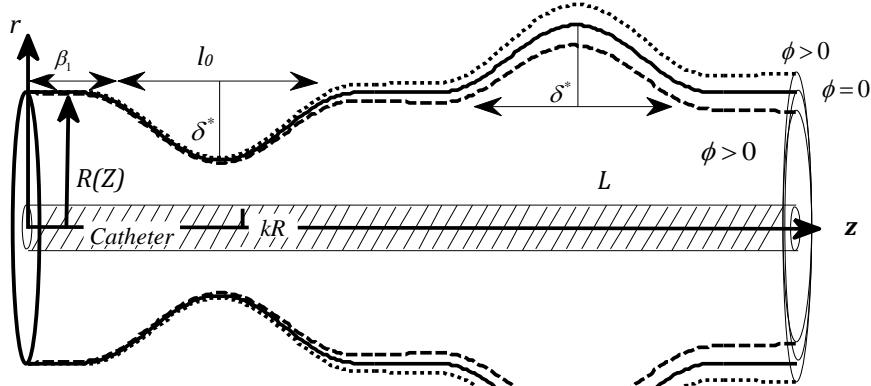
Fig. 6.1 (b). Geometry of the diseased artery with tapering.

Employing a radial coordinate transformation [75]:

$$x = \frac{r}{R(z)} \ .$$

(6.23)

Eqns. (6.18) and (6.19) now assume the form:

$$\alpha\left[\frac{\partial w}{\partial t}\right] = B(1+ecos(ct)) + \left(\frac{1+M}{R^2}\right)\left[\frac{\partial^2 w}{\partial x^2} + \frac{1}{x}\frac{\partial w}{\partial x}\right] + \frac{M}{R^2}\left(\frac{1}{x}\frac{\partial(rv)}{\partial x}\right),$$
(6.24)

$$\alpha J\left[\frac{\partial v}{\partial t}\right] = -M\left(2v + \frac{1}{R}\frac{\partial w}{\partial x}\right) + \frac{K}{R^2}\frac{\partial}{\partial x}\left(\frac{1}{x}\frac{\partial(xv)}{\partial x}\right).$$
(6.25)

The dimensionless boundary conditions become:

$$w\big|_{x=k/R} = 0, w\big|_{x=1} = 0, \ w\big|_{t=0} = 0,$$
(6.26)

$$v\big|_{x=k/R} = 0, v\big|_{x=1} = 0, \ v\big|_{t=0} = 0.$$
(6.27)

Similarly the volumetric flow rate, shear stress at the wall and resistance impedance, respectively, take the form:

$$\tau_s = \left(\frac{1+M}{R\alpha}\right)\left(\frac{\partial w}{\partial r}\right) + \left(\frac{M}{\alpha}\right)v.$$
(6.28)

6.3   Numerical method

Although Eqns. (6.24) and (6.25) are *linear* partial differential equations, their analytical solutions are still difficult to obtain. In these circumstances it is judicious to employ an approximate numerical technique. The finite difference scheme employed in the previous chapter is also implemented here to obtain the numerical solution of Eqs. (6.24) and (6.25). Inserting the finite difference approximations of various partial derivatives, Eqs. (6.24) and (6.25) may be transformed to the following form:

$$w_i^{k+1} = w_i^k + \frac{\Delta t}{\alpha}\left[B(1+ecos(ct^k)) + \frac{1+M}{R^2}\left(\left(w_{xx} + \frac{1}{x}w_x\right) + \frac{M}{R^2}\left(v_x + \frac{v}{x}\right)\right)\right],$$
(6.29)

$$v_i^{k+1} = v_i^k + \frac{\Delta t}{\alpha J}\left[-M\left(\left(2v + \frac{1}{R}w_x\right) + \frac{K}{R^2}\left(v_{xx} + \frac{v_x}{x} - \frac{v}{x^2}\right)\right)\right].$$
(6.30)

Where w_i^k and v_i^k are the corresponding values of w and v at node x_i and at time instant t_k. The boundary conditions in discretized form read

$$
\begin{aligned}
w_i^1 &= 0, \ v_i^1 = 0, & at \ t = 0, \\
w_{N+1}^k &= 0, \ v_{N+1}^k = 0, & at \ x = 1, \\
w_1^k &= 0, \ v_1^k = 0, & at \ x = k \ (catheter ed \ radius).
\end{aligned}
\tag{6.31}
$$

With the help of Eqns. (6.29) - (6.30), the numerical solution over *each* arterial cross-section can be easily obtained for *(N+1)* uniformly discretized points $x_i, (i = 1, 2, \dots N + 1)$ with a space grid size $\Delta x = \dfrac{1}{N+1}$ and at time levels $t_k = (k-1)\Delta t$, ($k = 1, 2, \dots$ and Δt is the time step size). Test computations have shown that for the present case, a stable solution with an accuracy of 10^{-7} is achievable by taking $\Delta x = 0.025$ and $\Delta t = 0.00001$. Validation of the present numerical solutions with another computational method (Nakamura's tridiagonal method), is provided in the next section. Excellent correlation is achieved.

6.4 Validation

The explicit numerical scheme which is forward in time and central in space [71] is validated using a variational finite element method (**FEM**). The FEM is found to be a powerful tool for solving partial differential equations as well as integral equations and utilizes *numerical integration*, rather than *differentiation* as with difference methods. The whole domain is delineated into smaller elements (sub-domains) of finite dimensions called "finite elements". The finite element mesh or grid refers to the collection of elements. By choosing a typical element from the mesh, the *variational* formulation of the given problem over the typical element is constructed. An approximate solution of the variational problem is assumed and the element equations are derived by substituting this solution in the governing differential equations. This process generates an element matrix, referred as *stiffness matrix*, is constructed by using *element interpolation functions*. The algebraic equations so obtained are assembled by imposing the inter-element continuity conditions. This yields a large number of algebraic equations defining the *global finite element model*, which governs the whole domain. The essential and natural boundary conditions are

82

imposed on the assembled equations. The assembled equations so obtained can be solved by any "matrix" numerical technique e.g. Gaussian elimination method, Householder's approach, LU Decomposition method etc as elaborated by Bathe [82]. Numerous nonlinear micro- and nano-scale biofluid mechanics problems have been successfully addressed in recent years with variational FEM including biomagnetic micropolar convection flow in tissue [83], deoxygenated blood flows [84], pulsating drug dispersion [85], nano-bio-polymer manufacture [86] and nano-pharmaco-dynamics [87]. In the present transient problem, the linear momentum eqn. (6.24) and angular momentum eqn. (6.25) contain the two dependent variables, w and v, and the independent variables, x and t. *Discretization* is performed *separately* in the time domain (t) and in the spatial domain (x). Quadratic elements are used. The variational form associated with equations (6.24)-(6.25) over a typical quadratic element is constructed and arbitrary test functions invoked. Interpolation functions are applied for the dependent variables in the form:

$$w = \sum_{j=1}^{2} w_j \Psi_j \text{ and } v = \sum_{j=1}^{2} v_j \Psi_j. \tag{6.32}$$

With $w_1 = w_2 = \Psi_i$, $i = 1, 2$. The *shape elements* for a typical quadratic element (x_e, x_{e+1}) in the *space variable*, take the form [71]:

$$\Psi_1^e = \frac{[x_{e+1} - x_e - 2x][x_{e+1} - x]}{[x_{e+1} - x_e]^2}, \tag{6.33}$$

$$\Psi_2^e = \frac{4[x - x_e][x_{e+1} - x]}{[x_{e+1} - x_e]^2}, \tag{6.34}$$

$$\Psi_3^e = \frac{[x_{e+1} - x_e - 2x][x - x_e]}{[x_{e+1} - x_e]^2}. \tag{6.35}$$

Valid for $x_e \leq x \leq x_{e+1}$. A similar procedure is used for the time-domain. The finite element model of the equations thus formed is given in matrix-vector form by;

$$\begin{bmatrix} [K^{11}] & [K^{12}] \\ [K^{21}] & [K^{22}] \end{bmatrix} \begin{bmatrix} \{w\} \\ \{v\} \end{bmatrix} = \begin{bmatrix} \{\delta_1\} \\ \{\delta_2\} \end{bmatrix}. \tag{6.36}$$

Here $[K^{mn}]$ and $[\delta^n]$ (m, n =1, 2) are the components of the stiffness matrix and displacement vector, and are lengthy integral expressions, which are omitted for conservation of space here. Further details are readily available in the articles of Bég and co-workers [82-87]. The entire flow domain is divided into 600 quadratic elements. Approximately 1800 linear equations are generated. Following the assembly of all element equations, a large order matrix is generated. The non-linear algebraic system of equations is solved iteratively. The process is terminated when the relative difference between the current and previous iterations is less than 0.00001. The integrations are carried out using two point Gaussian formula. The FEM code is developed in **MATLAB** running on an Octane SGI desktop workstation and takes 25 seconds on average. Comparisons of the FEM and FDM solutions are documented in **Tables 6.1, 6.2 and 6.3** for *axial velocity at two different locations*, for both diverging and converging arteries in *micropolar* blood flow ($M \neq 0$). Excellent correlation is obtained testifying to the validity of the FDM computations, the latter which are used in all graphical illustrations.

R	Numerical values of axial velocity						
	Non-tapered artery ($\xi = 0.0$)			$M = 0.1$			
	$M = 0.1$	$M = 0.8$ FDM	$M = 0.8$ FEM	Diverging artery ($\xi = 0.1$) FDM	Diverging artery ($\xi = 0.1$) FEM	Converging artery. ($\xi = -0.1$) FDM	Converging artery. ($\xi = -0.1$) FEM
0.1000	0	0	0	0	0	0	0
0.1889	0.0958	0.0669	0.0670	0.1065	0.1063	0.0846	0.0845
0.2779	0.1409	0.0992	0.0994	0.1567	0.1568	0.1246	0.1245
0.3668	0.1606	0.1138	0.1137	0.1786	0.1785	0.1420	0.1421
0.4557	0.1628	0.1157	0.1159	0.1812	0.1813	0.1438	0.1437
0.5447	0.1512	0.1076	0.1074	0.1684	0.1682	0.1334	0.1335
0.6336	0.1277	0.0908	0.0910	0.1425	0.1427	0.1126	0.1128
0.7225	0.0939	0.0666	0.0668	0.1050	0.1049	0.0826	0.0827
0.8115	0.0509	0.0360	0.0361	0.0570	0.0571	0.0447	0.0448
0.9000	0	0	0	0	0	0	0

Table 6.1: Numerical values of axial velocity at a cross-section $z = 0.7$ corresponding to the critical height of the stenosis for $k = 0.1,\ \delta = 0.1,\ t=0.3$.

r	Numerical values of axial velocity			
	Non-tapered artery ($\xi = 0.0$)		$M = 0.1$	
	$M = 0.1$ FDM	$M = 0.8$ FDM	Diverging artery ($\xi = 0.1$) FDM	Converging artery. ($\xi = -0.1$)FDM
0.1000	0	0	0	0
0.2111	0.1287	0.0969	0.1572	0.0923
0.3222	0.1891	0.1446	0.2302	0.1358
0.4333	0.2157	0.1665	0.2626	0.1548
0.5444	0.2193	0.1701	0.2681	0.1569
0.6555	0.2046	0.1587	0.2522	0.1456
0.7666	0.1741	0.1345	0.2170	0.1229
0.8777	0.1290	0.0990	0.1631	0.0903
0.9888	0.0706	0.0537	0.0905	0.0490
1.0999	0	0	0	0

Table 6.2: FDM numerical values of axial velocity at a cross-section $z = 2$ corresponding to the critical height of the post-stenotic dilated region (aneurysm) for $k = 0.1,\ \delta = 0.1,\ t=0.3$.

r	Numerical values of axial velocity			
	Non-tapered artery ($\xi = 0.0$)		$M = 0.1$	
	$M = 0.1$ FEM	$M = 0.8$ FEM	Diverging artery ($\xi = 0.1$) FEM	Converging artery. ($\xi = -0.1$) FEM
0.1000	0	0	0	0
0.2111	0.1288	0.0970	0.1573	0.0924
0.3222	0.1893	0.1445	0.2303	0.1359
0.4333	0.2155	0.1666	0.2625	0.1547
0.5444	0.2191	0.1702	0.2681	0.1568
0.6555	0.2047	0.1588	0.2523	0.1455
0.7666	0.1742	0.1346	0.2172	0.1228

0.8777	0.1289	0.0991	0.1630	0.0904
0.9888	0.0704	0.0538	0.0907	0.0491
1.0999	0	0	0	0

Table 6.3: FEM computations for axial velocity at a cross-section $z = 2$ corresponding to the critical height of the post-stenotic dilated region (aneurysm) for $k = 0.1$, $\delta = 0.1$, $t=0.3$.

6.5   Results

In this section, the axial velocity of flowing blood obtained through numerical simulations is plotted over the whole arterial segment for various values of the geometrical parameter of the stenosis/aneurysm and rheological blood parameters. Also volumetric flow rate, wall shear stress, resistive impedance and instantaneous streamlines of the blood flow are also visualized graphically. The following parameters are kept constant throughout the simulations: $l_0 = 1$, $L = 2.8$, $\alpha = 2$, $e = 0.5$, $J = 0.1$, $K = 0.1$, $B = 2$. It is pointed out that values of J and K are chosen in accordance with the available theoretical studies [35-36].

The axial velocity of blood in the systolic phase $(t = 0.3)$ over the whole arterial segment is plotted for $M = 0.1$, $k = 0.1$, $\delta = 0.1$ and $\xi = 0$ in panel (a) of **Fig. 6.2**. The remaining panels in Fig. 6.2 illustrate the axial velocity profiles over the whole arterial segment by changing either of the parameters used in panel (a). This makes it possible to observe the quantitative variations in axial velocity due to pertinent parameters associated with the blood rheology and geometry of the arterial segment. Panel (b) of Fig. 6.2 is prepared by changing the radius of the catheter. A comparison of panel (b) with panel (a) clearly indicates a *significant decrease* in axial velocity due to a corresponding increase in catheter radius. The effects of increasing the critical height of stenosis/aneurysm (δ) can be observed by comparing panel (c) with panel (a). It is quite apparent from the comparison of both panels that blood velocity is *substantially reduced* in the stenotic region whereas the converse behavior i.e. *acceleration* is observed in the post-stenotic dilated region by increasing δ.
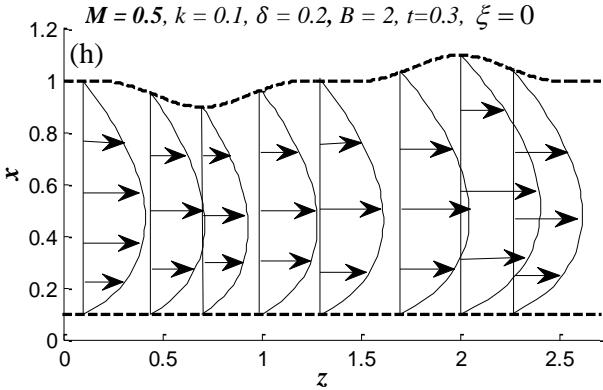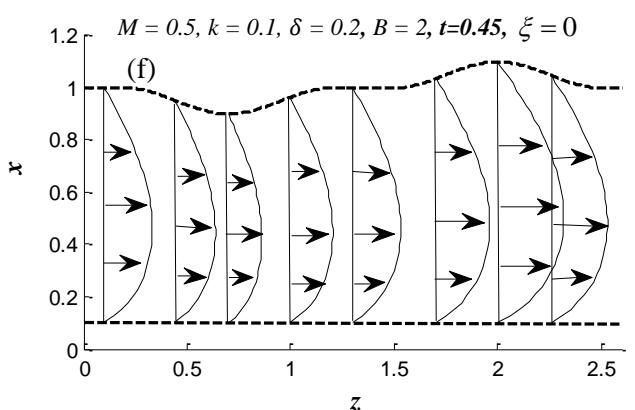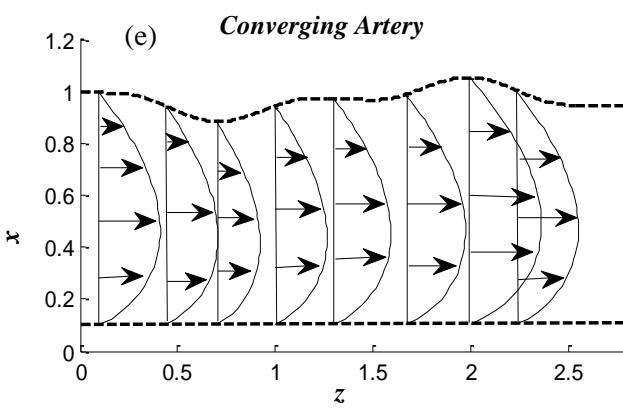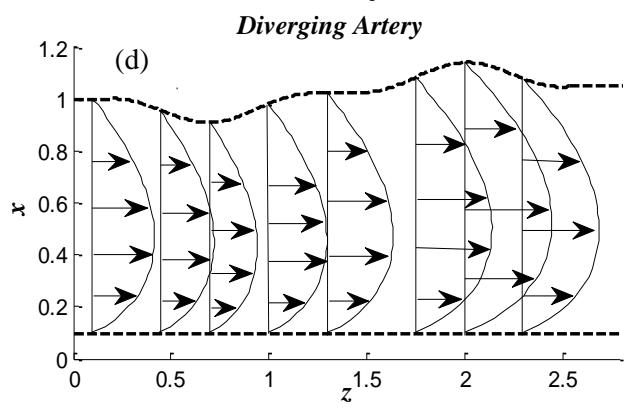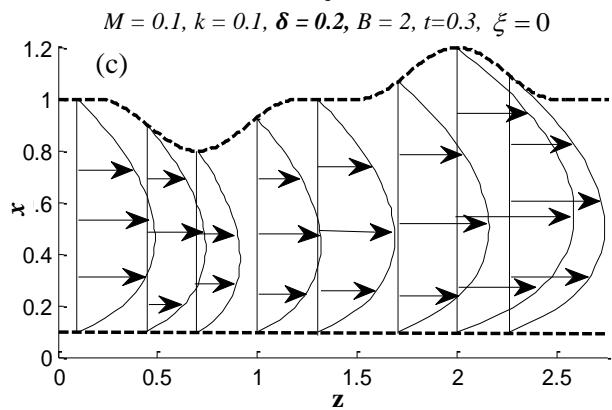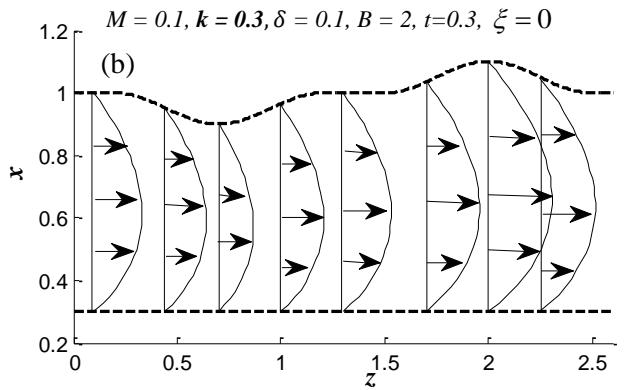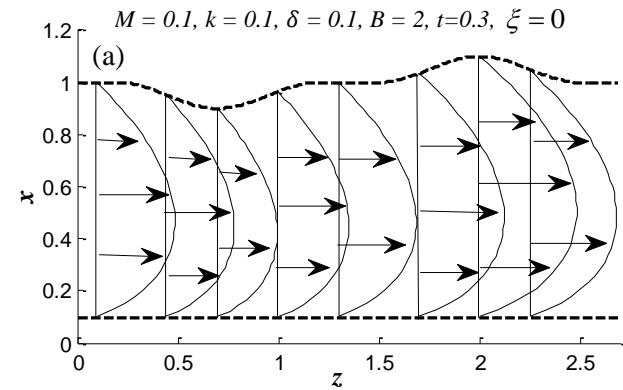
Fig. 6.2. Velocity profiles at different cross sections of the artery.

The blood velocity is also found to be influenced by the tapering of the artery. Computations are conducted for the *axial velocity* for two possible cases i.e. *negative tapering* (converging artery, $\xi < 0$) and *positive tapering* (diverging artery, $\xi > 0$). A comparison of panel (d) and panel (a) reveals that the blood velocity in a non-tapered artery attains lower values than in an artery with positive tapering. However, as is evident by comparing panel (a) and panel (e) the negative tapering in an artery suppresses the magnitude of axial velocity of blood *i.e. induces axial deceleration*. The velocity profiles over the whole arterial segment in the *diastolic phase* are shown in panel (f). A comparison of panel (a) and panel (f) shows a decrease in the magnitude of axial velocity in the diastolic phase. The rheological parameter i.e. micropolar parameter (*M*) also bears the potential to affect the magnitude of axial velocity. In fact it is evident from comparing panels (a) and (h) that the magnitude of axial velocity of blood decreases by increasing *M*. A general observation from Fig. 6.2 is that the rheological parameter (*M*) of blood and the catheter radius alter the magnitude of velocity *over the whole arterial segment*. However, the geometric parameter δ affect the velocity profile *only* in the stenotic and post-stenotic dilated regions. These observations further confirm the findings of Kang and Eringen [96]. They further highlight the intrinsic sophistication inherent to the micropolar constitutive model which simply is absent in other haemo-rheological formulations.

The time-series of flow rate at *z = 0.7* (where the maximum height of the stenosis is observed) for various values of emerging parameters is shown in **Fig. 6.3**. The solid line curve corresponds to a specific set of parameters i.e. *M = 0.1, k = 0.1, δ = 0.1, B = 2*. Each parameter from this set is varied to produce all the other curves in Fig. 6.3. For instance the dashed curve is generated by changing the value of δ. It is noticed that due to the pulsatile nature of flow (an inevitable result of the human heart beat), the flow rate also oscillates with time. For initial times flow rate behavior is *not periodic*. However, it is *strongly periodic* after *t = 1.2sec.* The amplitude of oscillations shows quantitative variations by changing *k*, δ and *M*. In fact it is seen by examining the other curves that *flow rate decreases* by increasing *M*, δ and *k*, while it exhibits an even faster descent by increasing the magnitude of δ. The solid line with open circles corresponds to

flow rate curve at $z = 2$ (where the critical height of the aneurysm is observed). This curve when compared with the solid line curve indicates higher values of flow rate in the post-stenotic dilated region.

The variation of wall shear stress over entire arterial length for some specific values of M, k, δ, and ξ is shown through solid line curve in **Fig. 6.4**. Various curves in Fig. 6.4 are compared according to the same rule used in Fig. 6.3. It is observed from this figure that wall shear stress (WSS) *increases* by increasing critical height of stenosis, radius of catheter *and* micropolar parameter, M. It is hypothesized that the acceleration in flow associated with increasing WSS is intimately linked to the decrease in viscosity of the blood with greater micropolar effect, an observation emphasized by Kang and Eringen [96]. Further details of viscosity variation with micropolarity are provided in Bég *et al.* [83] and Chaturani and Palanisamy [100]. The wall shear stress profiles for converging and diverging arteries are also included in this plot. It is noted that the *WSS* for the converging artery attains higher values as compared to the *WSS* for a diverging artery. This is most likely associated with the alteration in momentum with geometry- a diverging artery is associated with deceleration and a converging artery with acceleration. Moreover, a plummet in *WSS* is observed in the *post-stenotic* dilated region.
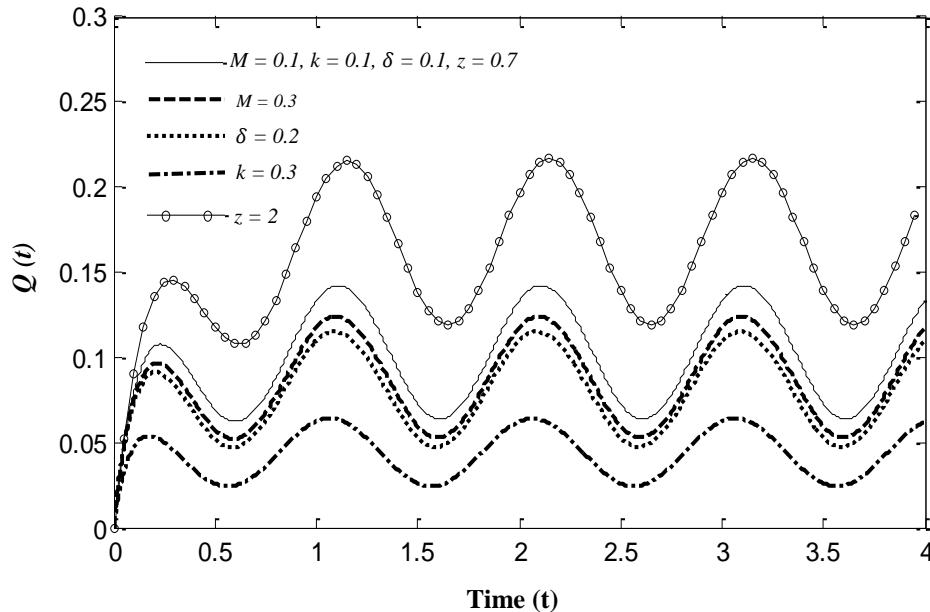

**Fig. 6.3**. Dimensionless flow rate profiles.
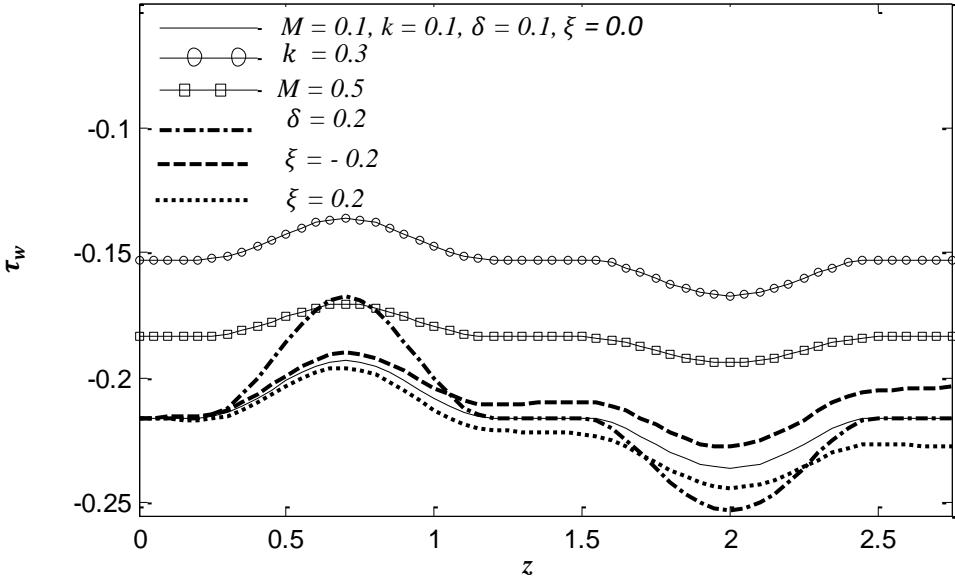
Fig. 6.4. Dimensionless wall shear stress (WSS) profiles.

The time-series of resistive impedance at $z = 0.7$ corresponding to the critical height of stenosis is calculated using Eqn. (6.37) and shown in **Fig. 6.5** for various values of the flow parameters. A comparison of solid line curve with others curves predicts that resistance to flow or impedance increases by elevating the catheter radius, critical height of stenosis and also the micropolar parameter. However, magnitudes considerably decrease at the location corresponding to the critical height of the post-stenotic dilated region. Thus it may be concluded that the overall value of impedance for a diseased arterial segment with a combination of stenosis and aneurysm is *less* than the overall value of impedance for a diseased arterial segment with stenosis only.

The blood flow patterns for different values of the hemodynamic and geometric parameters are shown in **Fig. 6.6.** Panel (a) shows the flow pattern for specific values of *k, M, δ,* and *t*. This panel confirms the appearance of a circulating bolus of fluid in the post-stenotic dilated region. The effects of critical height of stenosis/aneurysm on flow patterns can be understood by comparing panel (a) and panel (b). It is seen that the strength of the circulating region increases by increasing the critical height parameter ($δ$). A comparison of flow patterns in panel (a) and panel (c) indicates that the circulating region extends from the post-stenotic dilated region to the stenotic region in the case of a converging artery. On the contrary, the

strength of the circulating region in the post-stenotic dilated region reduces from the *non-tapered artery* scenario to the *diverging artery* scenario, as illustrated in panel (d). However, a small eddy materializes in the upstream region for a diverging artery which is not present for a non-tapered artery. The strength of the circulating bolus of fluid also varies with the passage of time. In fact the bolus size *decreases in the systolic phase* while in the *diastolic phase its behavior is reversed* (panel (e)). Similarly it is observed from panel (f) that the increase in size and circulation of bolus in post-stenotic dilated region is largely attributable to the larger values of the radius of catheter. The effect of non-Newtonian (micropolar) parameter on flow patterns is depicted in panel (g). It is evident that the strength of the circulating bolus of fluid decreases by increasing the micropolar parameter.
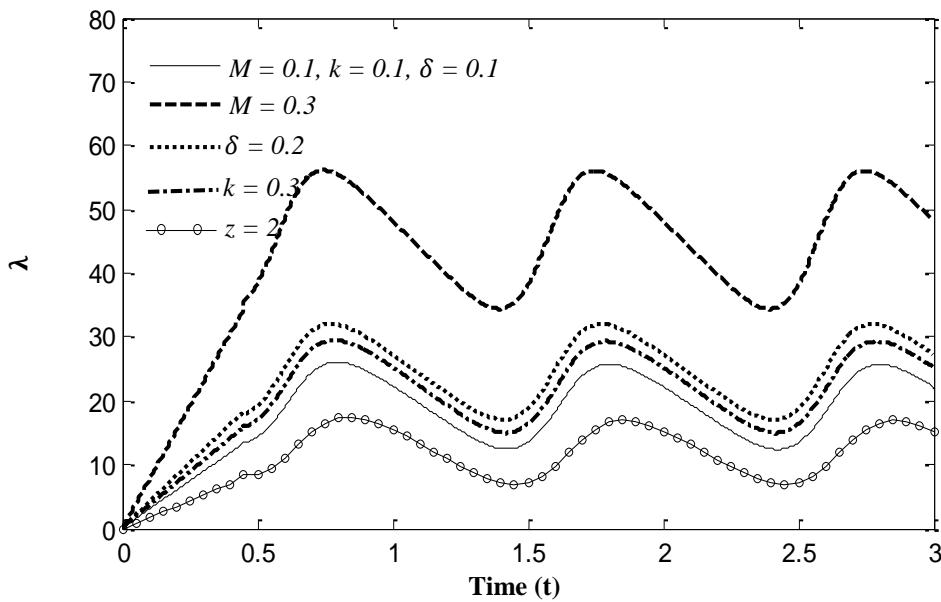

Fig. 6.5. Dimensionless impedance\resistance to flow profiles.

(a) *M = 0.1, k = 0.1, δ = 0.1, t = 0.3, ξ = 0* (b) *M = 0.1, k = 0.1, δ = 0.2, t = 0.3, ξ = 0*
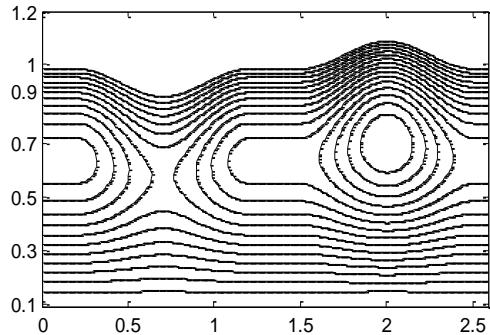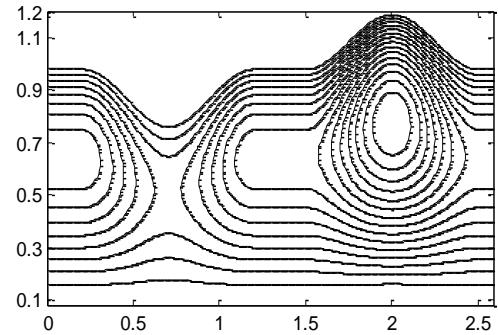
(c) *Converging Artery* (d) *Diverging Artery*

(e) *M = 0.1, k = 0.1, δ = 0.,1 t = 0.45, ξ = 0* (f) *M = 0.1, k = 0.3, δ = 0.1, t = 0.3, ξ = 0*
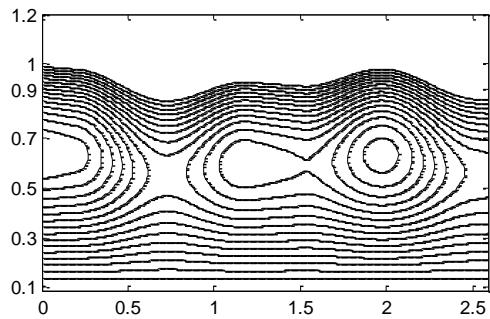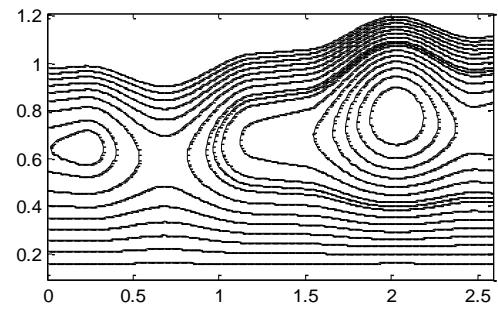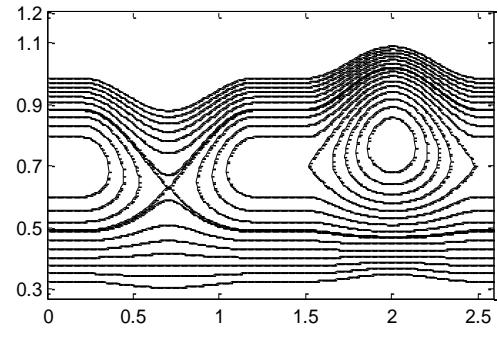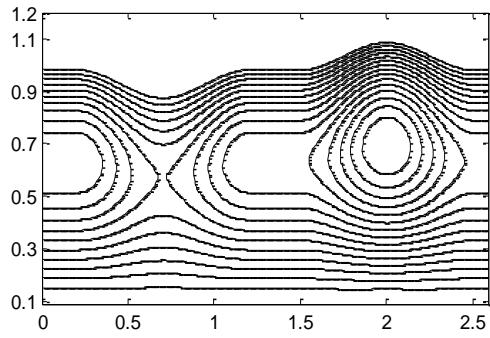
(g) *M = 0.8, k = 0.1, δ = 0., t = 0.3, ξ = 0*
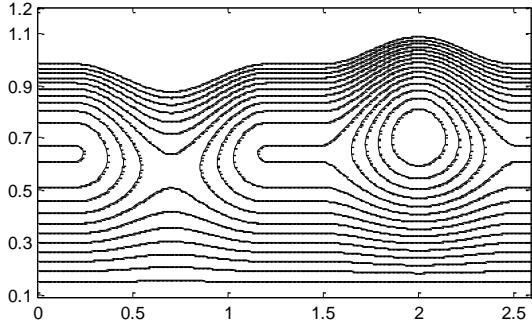
Fig. 6.6. Instantaneous flow patterns of streaming blood.

6.6   Discussion

Generally, it is observed that flow velocity attains higher values in the *post-stenotic dilated* region as compared to the *stenotic* region. The results further indicate that axial velocity of the blood decreases substantially by increasing the catheter size and rheological parameter of the micropolar fluid in *both* stenotic and post-stenotic dilated region. This decrease in flow velocity simultaneously modifies the other operating variables such as wall shear stress, volumetric flow rate and resistance to flow. In fact, it is found that volumetric flow decreases at the stenotic throat and at the critical height of the post-stenotic dilated region by *increasing* catheter radius and micropolar parameter. As an implication of the general observation of higher values of flow velocity in the post-stenotic dialateral region, the wall shear stress (WSS) also attains higher values in that region. However, WSS substantially descends by increasing catheter radius and rheological parameter of the blood. The impedance to flow at the stenotic throat is found to increase by increasing catheter radius and rheological parameter of the blood. On the contrary, it decreases at a critical height of the post-stenotic dilated region.

The previous studies [39-41] report the results for impedance and the other variable without taking into account the *pulsatile* nature of the flow. The rheology of the blood in these simulations is captured by Bingham, Casson and power-law models. The current study differs from previous studies in three ways. Firstly, we have computed the flow quantities by taking pulsatile pressure gradient, secondly the rheology of the blood is characterized by the constitutive equations of micropolar fluid and lastly the whole analysis

93

is carried out in presence of an inserted catheter. In contrast to the results presented in [39-41], our results indicate that for fixed values of geometrical and rheological parameters of the model, the flow quantities vary periodically at each arterial cross-section after the steady state condition has been reached. Initially these quantities fluctuate and increase and finally reaches the steady state condition as time increases. The presumed steady state condition imposed in previous studies does not delineate such situations.

Previous available studies also reveal that a dilatation near the stenosis causes an amelioration in the increase of the resistance to flow ratio that would occur were the stenosis isolated. Our results also comply well with such observations. However, improvement in the increase of resistance to flow ratio due to the presence of dilatation is *deteriorated* by inserting a catheter. This deterioration can be controlled by tuning the rheology of the blood which is not possible with a Newtonian fluid. According to Eringen's micropolar theory, the rheology of blood is a concentrated suspension of neutrally-buoyant deformable particles in a viscous fluid. The deformability of these particles, in particular erythrocytes (red blood cells) have a pronounced effects on the apparent viscosity. For instance at normal concentration, hardened cells will exhibit a viscosity ten times higher than normal blood. The dimensionless parameter M employed in the current study successfully captures this increase in the viscosity of the blood. Our study shows that the increase in the resistance to flow either due to the presence of the stenosis or due to insertion of catheter can be reduced by choosing M to be smaller. This observation suggests the possibility of tuning the rheology of the blood to control the reduction in blood flow rate and increase in the resistance to flow. The present study also indicates an increased wall shear stress arises at the throat of the post-stenotic dilated region for a *Newtonian* fluid in comparison with *micropolar* fluid. The increased wall shear stress at the throat of the post-stenotic dilated region may be of some concern to clinicians. Again Newtonian theory does not suggest any remedy to control this increase in wall shear stress. However, as disclosed by our computations, micropolar theory suggests that such an increase in WSS at the throat of the post-stenotic dilated region can be reduced by adjusting the rheology of the blood.

6.7   Conclusions

A mathematical model is presented to analyze the unsteady flow characteristics of blood through a diseased catheterized artery with a combination of stenosis and post-stenotic dilated regions. The constitutive equation of Eringen micropolar fluids has been implemented to simulate non-Newtonian micro-structural blood characteristics. A numerical method based on explicit finite difference scheme has been used to obtain the solution of the governing initial-boundary value problem. The velocity, volumetric flow rate of blood, arterial wall shear stress, impedance and streamlines of flow are analyzed quantitatively for geometrical parameter of stenosis, rheological parameters of blood and catheter radius. The computations reveal that blood velocity and flow rate both decrease while impedance increases by enhancing the size of catheter radius, critical height parameter and micropolar parameter in the stenotic region. However, these quantities demonstrate the contrary trend in the post-stenotic dilated region. Moreover, the strength of recirculating zones appearing in the *post-stenotic* region is also an increasing function of catheter radius, critical height parameter and micropolar parameter. These observations may have practical implications regarding treatment/diagnosis of atherosclerosis where it is desired to avoid the reduction of flow rate and to decrease the impedance (resistance to flow) due to insertion of a catheter in surgical procedures. The micropolar hameo-rheological model demonstrates some elegant features which warrant further investigations. It is envisaged that subsequent investigations will employ computational fluid dynamics (CFD) simulations to extend the two-dimensional computations to three dimensions. Efforts in this regard are being made with the ADINA-F finite element code [88] and other numerical approaches e.g. discrete particle dynamics (DPD) [89] which have demonstrated exceptional ability in stenotic hemodynamics.

Chapter 7

Time-dependent non-Newtonian blood flow through a tapered time-variant stenosed artery

In this chapter, a two-dimensional model is used to analyze the unsteady pulsatile flow of blood through a tapered artery with stenosis. The rheology of the flowing blood is captured by the constitutive equation of Carreau model. The time-variant nature of the stenotic artery has been incorporated in the present analysis. The flow equations are set up under the long wavelength assumption which states that the lumen radius is small in comparison to the wavelength of the pulsatile pressure wave. The effects of the vessel wall are immobilized by using a radial coordinate transformation. The resulting partial differential equations along with the boundary and initial conditions are solved using finite difference method. The important hemodynamical variables are analyzed for normal and diseased arteries with particular focus on their variation with non-Newtonian parameters.

7.1 Geometry of the problem

Let us consider flow of an incompressible Carreau fluid through a tapered artery with a single stenosis. We employ a cylindrical co-ordinate (r, θ, z) system for the purpose of flow analysis with r along the radial

direction and z along the axis of the tube (artery). The mathematical model of the time-variant stenosed arterial segment (see **Fig. 7.1**) is
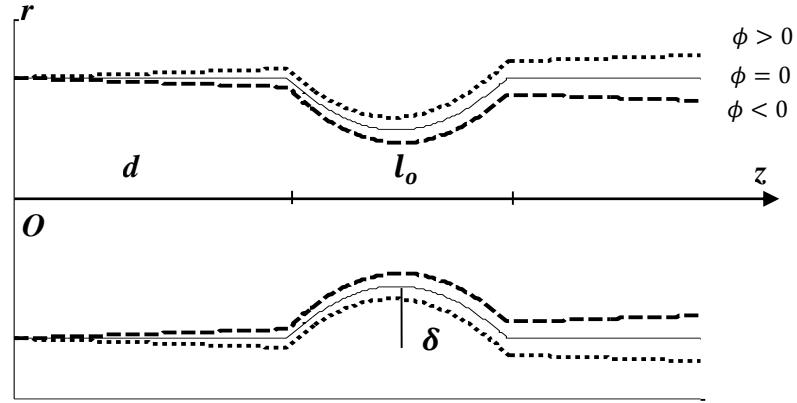

Fig. 7.1. Geometry of the stenotic artery with different tapering angles.

$$R(z,t)=\begin{cases}\left[(\xi z+a)-\dfrac{\delta^*\sec\phi(z-d)}{\delta^{*2}\sin\phi^2-\dfrac{l_0^2}{4}}\{l_0-(z-d)\}\right]a_1(t), & d\leq z\leq d+l_0 \\ (\xi z+a)a_1(t), & otherwise.\end{cases}$$ (7.1)

In above expression $R(z,t)$ denotes the radius of the tapered stenotic artery , ϕ is the angle of the tapering, a is the radius of the non-tapered artery in the non-stenotic region, l_0 is the stenotic length of an artery, d is the location of the stenosis and $\delta^*\sec\phi$ is taken to be the height of the stenosis for the tapered stenosed artery appearing at $z=d+\dfrac{l_0}{2}+\delta^*\sin\phi$ and $\xi=\tan\phi$ represents the slope of the tapered vessel and in our case $\delta^*=0.4a$. The time-variant parameter $a_1(t)$ is given by the following expression

$$a_1(t)=1-b_1\left(\cos\omega_p t-1\right)e^{-b_1\omega t},$$ (7.2)

where ω represents the angular frequency with $\omega=2\pi f_p$, f_p being the pulse frequency and b_1 is a constant. The length of the arterial segment is L. Note that the model given by (7.1) bears the possibility to

explore the case of non-tapered artery $(\phi = 0)$, converging tapering $(\phi < 0)$ and the diverging tapering artery $(\phi > 0)$ as evident from **Fig. 7.1**.

7.2 Problem formulation

Consider two-dimensional time-dependent flow of a Carreau fluid through a diseased arterial segment. The geometry of the present problem is given in **Fig. 7.1**. The velocity field for two-dimensional flow is given by:

$$V = \left[u(r,z,t), 0, w(r,z,t) \right].$$

(7.3)

In view of (7.3) the continuity equation (1.2) reduces to

$$\frac{\partial u}{\partial r} + \frac{u}{r} + \frac{\partial w}{\partial z} = 0.$$

(7.4)

Similarly, the momentum equation (1.3) take the following form:

$$\rho \left(\frac{\partial u}{\partial t} + u \frac{\partial u}{\partial r} + w \frac{\partial w}{\partial z} \right) = -\frac{\partial p}{\partial r} + \left(\frac{1}{r} \frac{\partial}{\partial r} \left(r S_{rr} \right) + \frac{\partial}{\partial z} \left(S_{rz} \right) \right),$$

(7.5)

$$\rho \left(\frac{\partial w}{\partial t} + u \frac{\partial w}{\partial r} + w \frac{\partial w}{\partial z} \right) = -\frac{\partial p}{\partial z} + \left(\frac{1}{r} \frac{\partial}{\partial r} \left(r S_{rz} \right) + \frac{\partial}{\partial z} \left(S_{zz} \right) \right),$$

(7.6)

where S_{rr}, S_{zz} and S_{rz} are defined in Eqns. (5.12).

Our current analysis is based on the assumption that the lumen radius R is taken sufficiently smaller than wavelength λ, of the pressure wave. i.e. $R/\lambda \ll 1$ [90]. On the basis of this assumption the radial momentum equation simply reduces to $\partial p/\partial r = 0$, which gives that pressure has no variation along the radial coordinate.

The boundary and initial conditions for the problem under consideration are [26]

$$u(r,z,t) = 0, \quad \frac{\partial w(r,z,t)}{\partial r} = 0 \text{ and } S_{rz} = 0, \text{ on } r = 0, \tag{7.7}$$

$$u(r,z,t) = \frac{\partial R}{\partial t}, \quad w(r,z,t) = 0, \quad on \ r = R(z,t), \tag{7.8}$$

$$u(r,z,0) = w(r,z,0) = 0. \tag{7.9}$$

7.3 Dimensionless formulation of the problem

We are interested in numerical solution of Eqns. (7.5) and (7.6) subject to conditions (7.7)-(7.9). To this end, we first normalize these equations by defining the new variables

$$\overline{r} = \frac{r}{a}; \overline{w} = \frac{w}{a\omega}; \overline{u} = \frac{u}{a\omega}; \overline{t} = \omega t; \overline{z} = \frac{z}{a}; \overline{p} = \frac{p}{\mu\omega}, \overline{d} = \frac{d}{a}; \overline{l_0} = \frac{l_0}{a}; \delta = \frac{\delta^*}{a}. \tag{7.10}$$

In terms of new variables Eqns. (7.5), (7.6) and (5.12) after dropping the bars read

$$\frac{\partial u}{\partial r} + \frac{u}{r} + \frac{\partial w}{\partial z} = 0, \tag{7.11}$$

$$\alpha \left(\frac{\partial w}{\partial t} + u\frac{\partial w}{\partial r} + w\frac{\partial w}{\partial z} \right) = -\frac{\partial p}{\partial z} + \left(\frac{1}{r}\frac{\partial}{\partial r}(rS_{rz}) + \frac{\partial}{\partial z}(S_{zz}) \right), \tag{7.12}$$

$$S_{rz} = \left[\frac{\mu_\infty}{\mu_0} + \left(1 - \frac{\mu_\infty}{\mu_0}\right)\left\{ 1 + We^2 \left[2\left(\left(\frac{\partial u}{\partial r}\right)^2 + \left(\frac{u}{r}\right)^2 + \left(\frac{\partial w}{\partial z}\right)^2 \right) + \left(\frac{\partial u}{\partial z} + \frac{\partial w}{\partial r}\right)^2 \right] \right\}^{\frac{n-1}{2}} \right]$$
$$\times \left(\frac{\partial w}{\partial r} + \frac{\partial u}{\partial z} \right), \tag{7.13}$$

$$S_{zz} = 2\left[\frac{\mu_\infty}{\mu_0} + \left(1 - \frac{\mu_\infty}{\mu_0}\right)\left\{ 1 + We^2 \left[2\left(\left(\frac{\partial u}{\partial r}\right)^2 + \left(\frac{u}{r}\right)^2 + \left(\frac{\partial w}{\partial z}\right)^2 \right) + \left(\frac{\partial u}{\partial z} + \frac{\partial w}{\partial r}\right)^2 \right] \right\}^{\frac{n-1}{2}} \right]\left(\frac{\partial w}{\partial z} \right). \tag{7.14}$$

The *Womersley number* and *Weissenberg number* in above equation are given as $\alpha\left(=\dfrac{a^2\omega\rho}{\mu_0}\right)$ and *We*

$\left(=\Gamma\left(\dfrac{\omega}{a}\right)\right)$, respectively. The dimensionless boundary and initial conditions are:

$$u(r,z,t)=0,\quad \frac{\partial w(r,z,t)}{\partial r}=0 \text{ and } S_{rz}=0,\ on\ r=0,\tag{7.15}$$

$$u(r,z,t)=\frac{\partial R}{\partial t},\quad w(r,z,t)=0,\ \ on\ r=R(z,t),\tag{7.16}$$

$$u(r,z,0)=w(r,z,0)=0.\tag{7.17}$$

Similarly as a consequence of (7.10), the geometry of the stenosis takes the following form:

$$R(z,t)=\begin{cases}\left[(\xi z+1)-\dfrac{\delta\sec\phi(z-d)}{\delta^2\sin\phi^2-\dfrac{l_0^2}{4}}\{l_0-(z-d)\}\right]a_1(t), & d\le z\le d+l_0,\\[4mm] (\xi z+1)a_1(t), & otherwise.\end{cases}\tag{7.18}$$

7.4   Transformation of the Problem

Employing the radial coordinate transformation [75]

$$x=\frac{r}{R(z,t)}\ ,\tag{7.19}$$

Eqs. (7.11) - (7.14) can be casted in the following form

$$\frac{\partial w}{\partial t}=\left\{\frac{x}{R}\frac{\partial R}{\partial t}-\frac{u}{R}+\frac{x}{R}\frac{\partial R}{\partial z}w\right\}\frac{\partial w}{\partial x}-\frac{1}{\alpha}\frac{\partial p}{\partial z}-w\frac{\partial w}{\partial z}-\frac{1}{\alpha}\left\{\frac{1}{xR}S_{xz}+\frac{1}{R}\frac{\partial S_{xz}}{\partial x}-\frac{\partial S_{zz}}{\partial z}+\frac{x}{R}\frac{\partial R}{\partial z}\frac{\partial S_{zz}}{\partial x}\right\},\tag{7.20}$$

$$\frac{1}{R}\frac{\partial u}{\partial x}+\frac{u}{xR}+\frac{\partial w}{\partial z}-\frac{x}{R}\frac{\partial R}{\partial z}\frac{\partial w}{\partial x}=0\ ,\tag{7.21}$$

100

$$S_{xz} = -\left[\frac{\mu_\infty}{\mu_0} + \left(1 - \frac{\mu_\infty}{\mu_0}\right)\left\{1 + We^2\left[\begin{array}{c} 2\left(\left(\frac{1}{R}\frac{\partial u}{\partial x}\right)^2 + \left(\frac{u}{xR}\right)^2 + \left(\frac{\partial w}{\partial z} - \frac{x}{R}\frac{\partial R}{\partial z}\frac{\partial w}{\partial x}\right)^2\right) \\ + \left(\frac{\partial u}{\partial z} - \frac{x}{R}\frac{\partial R}{\partial z}\frac{\partial u}{\partial x} + \frac{1}{R}\frac{\partial w}{\partial x}\right)^2 \end{array}\right]^{\frac{n-1}{2}}\right\}\right]$$
$$\times \left(\frac{\partial u}{\partial z} - \frac{x}{R}\frac{\partial R}{\partial z}\frac{\partial u}{\partial x} + \frac{1}{R}\frac{\partial w}{\partial x}\right),$$

$$\hspace{12cm} (7.22)$$

$$S_{zz} = -2\left[\cdots\cdots\cdots\right] \times \left(\frac{\partial w}{\partial z} - \frac{x}{R}\frac{\partial R}{\partial z}\frac{\partial w}{\partial x}\right). \hspace{3cm} (7.23)$$

Similarly we can write the boundary and initial conditions as

$$u(x,z,t) = 0, \frac{\partial w(x,z,t)}{\partial x} = 0, S_{xz} = 0, \hspace{1.5cm} on\ x = 0, \hspace{1.5cm} (7.24)$$

$$u(x,z,t) = \frac{\partial R}{\partial t}, \ w(x,z,t) = 0, \hspace{2.5cm} on\ x = 1, \hspace{1.5cm} (7.25)$$

$$u(x,z,0) = w(x,z,0) = 0. \hspace{6cm} (7.26)$$

An explicit expression for $u(x,z,t)$ can be obtained as follows: Multiplying Eq. (7.21) by xR and integrating with respect to x from 0 to x, we get

$$u(x,z,t) = x\frac{\partial R}{\partial z}w - \frac{R}{x}\int_0^x x\frac{\partial w}{\partial z}dx - \frac{2}{x}\frac{\partial R}{\partial z}\int_0^x xwdx, \hspace{2cm} (7.27)$$

Eq. (7.27) takes the following form by making use of the boundary condition (7.25)

$$-\int_0^1 x\frac{\partial w}{\partial \xi}dx = \int_0^1 x\left[\frac{2}{R}\frac{\partial R}{\partial z}w + \frac{1}{R}\frac{\partial R}{\partial t}f(x)\right]dx, \hspace{2cm} (7.28)$$

where $f(x)$ is an arbitrary function. Let us choose $f(x)$ of the form

$$f(x) = -4(x^2 - 1) \text{ satisfying } \int_0^1 x f(x) = 1. \tag{7.29}$$

Equating the integrands on both sides of (7.28), we find

$$\frac{\partial w}{\partial z} = -\frac{2}{R}\frac{\partial R}{\partial z} w + \frac{4}{R}(x^2 - 1)\frac{\partial R}{\partial t}, \tag{7.30}$$

utilizing (7.30) in (7.27), we finally arrive at

$$u(x, z, t) = x\left[\frac{\partial R}{\partial z} w + \frac{\partial R}{\partial t}(2 - x^2)\right]. \tag{7.31}$$

7.5   Numerical solution

The numerical method employed for solution of Eqs. (7.20)-(7.23) subject to boundary conditions (7.24)-(7.26) is forward in time and central in space and is already implemented in previous chapters for solutions of one-dimensional time-dependent equations. Here our system of equations is two-dimensional and time dependent. Due to this fact, we present a somewhat detailed procedure of discretization. The value of w at (x_j, z_i, t_k) is denoted by $w_{i,j}^k$. Thus, we approximate the space derivative as

$$\frac{\partial w}{\partial x} \cong \frac{w_{i,j+1}^k - w_{i,j-1}^k}{2\Delta x} = w_x, \tag{7.32}$$

$$\frac{\partial w}{\partial z} \cong \frac{w_{i+1,j}^k - w_{i-1,j}^k}{2\Delta z} = w_z, \tag{7.33}$$

$$\frac{\partial^2 w}{\partial x^2} \cong \frac{w_{i,j+1}^k - 2w_{i,j}^k + w_{i,j-1}^k}{(\Delta x)^2} = w_{xx}, \tag{7.34}$$

$$\frac{\partial^2 w}{\partial z^2} \cong \frac{w_{i+1,j}^k - 2 w_{i,j}^k + w_{i-1,j}^k}{(\Delta z)^2} = w_{zz}. \tag{7.35}$$

In a similar manner we write following expression for the time derivative,

$$\frac{\partial w}{\partial t} = \frac{w_{i,j}^{k+1} - w_{i,j}^{k}}{\Delta t}. \tag{7.36}$$

The discrete points in radial and axial directions are given as $x = (j-1)\Delta x, \ (j = 1, 2, \ldots N+1)$ such that $x_{(N+1)} = 1.0, z = (i-1)\Delta z, \ (i = 1, 2, \ldots M+1)$, which are uniformly distributed. Similar approach is used for the time step and is defined as $t_k = (k-1)\Delta t, \ (k = 1, 2, \ldots)$, where Δt is the time increment. Using (7.32)-(7.36), Eq. (7.20) may be transformed to the following difference equation

$$w_{i,j}^{k+1} = w_{i,j}^{k} + dt \left[\left\{ \frac{x_j}{R_i^k} \left(\frac{\partial R}{\partial t} \right)_i^k - \frac{u_{i,j}^k}{R_i^k} + \frac{x_j}{R_i^k} \left(\frac{\partial R}{\partial z} \right)_i^k w_{i,j}^k \right\} (w_x)_{i,j}^k - w_{i,j}^k (w_z)_{i,j}^k \right.$$

$$\left. - \frac{1}{\alpha} \left\{ -\left(\frac{\partial p}{\partial z} \right)^{k+1} + \frac{1}{x_j R_i^k} (S_{xz})_{i,j}^k + \frac{1}{R_i^k} \left[(S_{xz})_x \right]_{i,j}^k - \left[(S_{zz})_z \right]_{i,j}^k + \frac{x_j}{R_i^k} \left(\frac{\partial R}{\partial t} \right)_i^k \left[(S_{zz})_x \right]_{i,j}^k \right\} \right]. \tag{7.37}$$

Similarly, Eqns. (7.22) - (7.23) have the following discretized form

$$\left[(S_{zz})_z \right]_{i,j}^k = -2 \left[\left[\frac{\mu_\infty}{\mu_0} + \left(1 + \frac{\mu_\infty}{\mu_0} \right) \times \right. \right.$$
$$\left\{ 1 + We^2 \left[2 \left(\left(\frac{1}{R_i^k} (u_x)_{i,j}^k \right)^2 + \left(\frac{u_{i,j}^k}{x_j R_i^k} \right)^2 + \left((w_z)_{i,j}^k - \frac{x_j}{R_i^k} \left(\frac{\partial R}{\partial z} \right)_i^k (w_x)_{i,j}^k \right)^2 \right) \right. \right.$$
$$\left. \left. + \left((u_z)_{i,j}^k - \frac{x_j}{R_i^k} \left(\frac{\partial R}{\partial z} \right)_i^k (u_x)_{i,j}^k + \frac{1}{R_i^k} (w_x)_{i,j}^k \right)^2 \right] \right\}^{\frac{n-1}{2}} \right]$$
$$\times \left[(w_z)_{i,j}^k - \frac{x_j}{R_i^k} \left(\frac{\partial R}{\partial z} \right)_i^k (w_x)_{i,j}^k \right], \tag{7.38}$$

$$\left[(S_{xz})_z \right]_{i,j}^k = -\left[\cdots \cdots \cdots \right] \left[(u_z)_{i,j}^k - \frac{x_j}{R_i^k} \left(\frac{\partial R}{\partial z} \right)_i^k (u_x)_{i,j}^k + \frac{1}{R_i^k} (w_x)_{i,j}^k \right]. \tag{7.39}$$

The boundary and initial conditions can be written in the discretized form as:

$$u_{i,j}^k = 0, w_{i,1}^k = w_{i,2}^k, (S_{xz})_{i,1}^k = 0, \tag{7.40}$$

$$w_{i,N+1}^k = 0, u_{i,j}^k = \left(\frac{\partial R}{\partial t} \right)_i^k, \tag{7.41}$$

$$u^1_{(i,j)} = w^1_{(i,j)} = 0. \tag{7.42}$$

The volumetric flow rate (Q) and the wall shear stress (τ_w) are given by [26, 27]

$$Q^k_i = 2\pi \left(R^k_i\right)^2 \int_0^1 x_j w^k_{i,j} dx_j , \tag{7.43}$$

$$(\tau_w)^k_i = \left[\left(S_{xz}\right)_z\right]^k_{i,N+1} . \tag{7.44}$$

7.6   Results and Discussion

In this section graphical results are displayed for the following set of parameters [91-93]: $\mu_0 = 0.56$, $\mu_\infty =$ 0.0345, L = 50, *a = 1, d= 20, l_0=16, A_0 = 7, A_1 = 0.2A_0, δ = 0.4, Δx = 0.025, Δz = 0.01*. The accuracy of the numerical solution is maintained up to *10^{-7}* by choosing the time step *0.0001*.

The dimensionless axial velocity graphs of streaming blood in normal and stenotic artery for different values of tapering angles are shown in **Fig. 7.2a**. One can see from Fig. 7.2(a) that the magnitude of velocity is greater in the normal artery as compared with the stenotic artery. It is also observed that the velocity profile achieves higher values for diverging tapering as compared with the converging tapering. The graph of non-tapered artery lies in between. This observation is true for both normal and constricted artery. However, the shape of profile in considered artery for converging tapering is flat near the centre. This flat shape indicates a plug-flow like region in the centre of the artery. The existence of flat velocity profile in the constricted artery for converging tapering is because of the fact that near the artery wall the viscous and inertial forces are of the same order. However, near the centre of the artery the inertial forces dominate, thus compelling the axial velocity profile to attain a flat shape. The dimensionless radial velocity graphs of the flowing blood in normal and constricted artery for different taper angles are shown in **Fig. 7.2b**. All the graphs are taken at specific location *z = 28* and for time instant *t = 0.45*. This figure reveals that radial velocity is negative over the whole cross-section. All the curves start from zero and approach a constant value at wall due to the presence of wall movement in the stenosis geometry. It is further observed from this figure that the effects of vessel tapering on radial velocity are prominent for constricted artery compared

with the normal artery. The maximum deviation in the curves of radial velocity occurs near the wall both of the stenotic and normal artery.
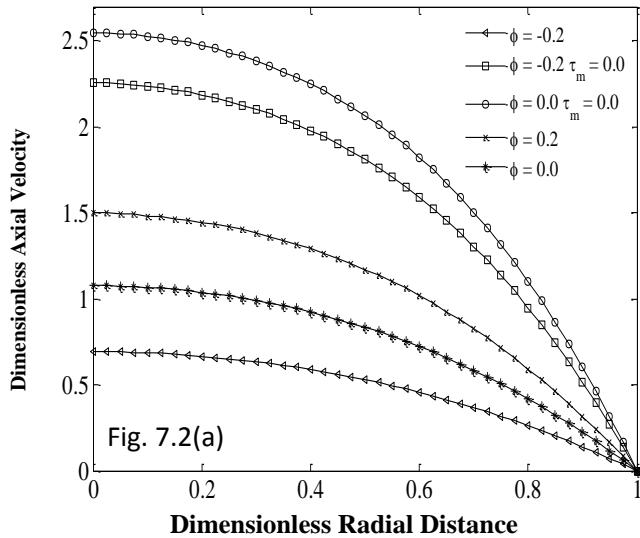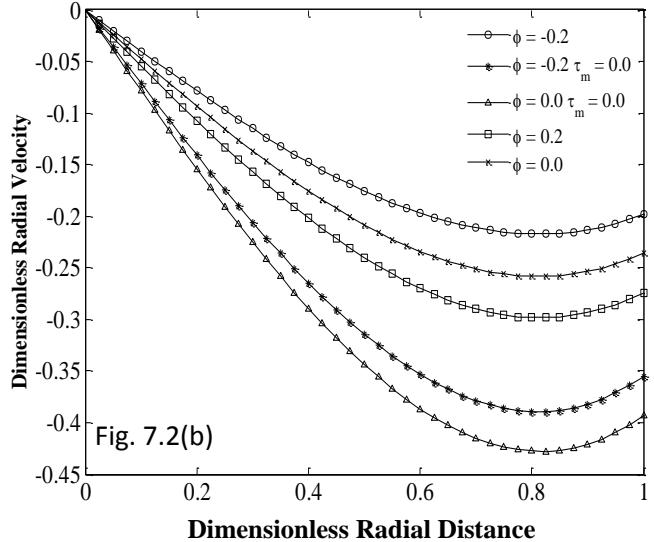

Fig. 7.2: Dimensionless Axial (Fig. 7.2(a)) and radial (Fig. 7.2(b)) velocity graphs for different tapering angles. Calculation is based on the following data: ($z = 28, t = 0.45,\ d = 20, l_0 = 16, We = 2, \alpha = 1, n = 0.639$).
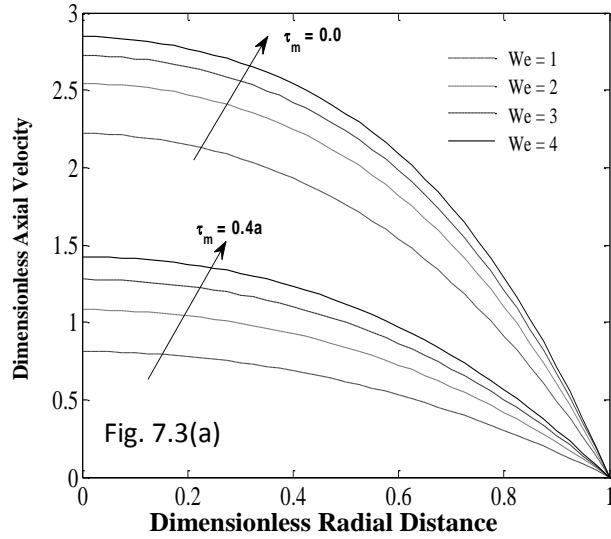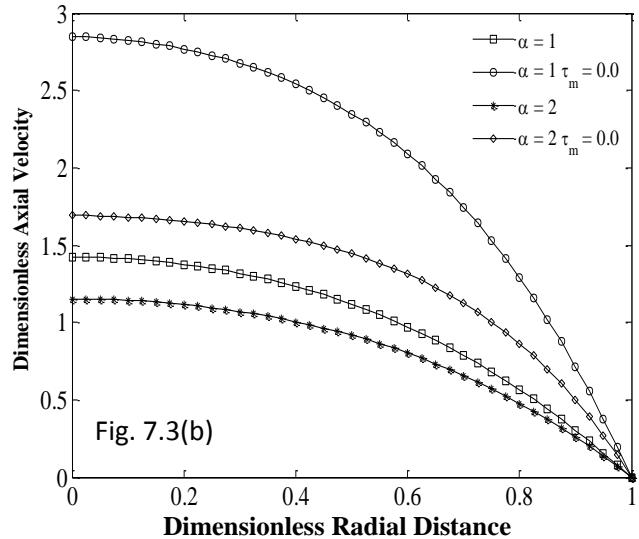

Fig. 7.3: Dimensionless Axial (Fig. 7.3(a) & 7.3.(b)) velocity graphs for different We (Weissenberg numbers) and α (Womersley numbers). Calculation is based on the following data: ($z = 28, t = 0.45, \delta = 0.4a, d = 20,$ $l_0 = 16, We = 3, n = 0.639$).

Fig. 7.3. (a) depicts the profiles of dimensionless axial velocity for different values of *We* (*Weissenberg numbers*) at a specific location at *z = 28.* These graphs indicate an increase in axial velocity with an increase in *We* both for normal and constricted artery. Thus *Carreau fluid* model predicts higher axial flow speed of blood in comparison with Newtonians fluid model. The effects of *Wormsley number* α on axial velocity of blood at a specific location *z =28* and time instant *t = 0.45* are illustrated in Fig. 7.3(b). These profiles show that an increase in α decrease the axial velocity of blood.
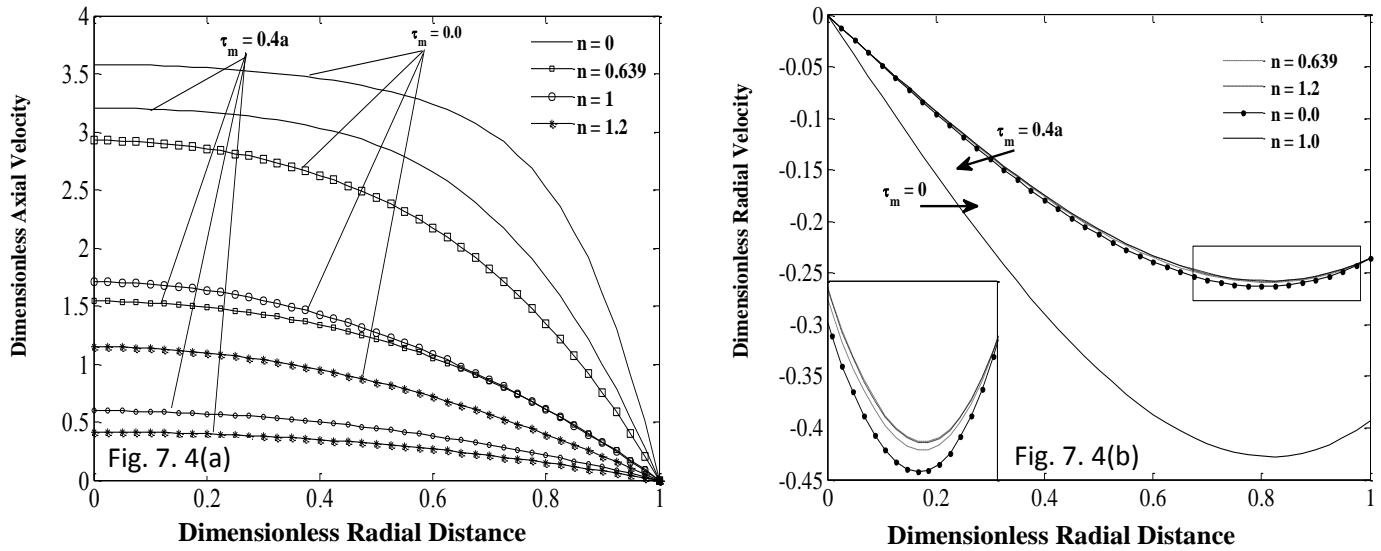

Fig. 7.4: Dimensionless Axial (Fig. 7.4(a)) and radial (Fig. 7.4(b)) velocity graphs for different *n* (Power law constant). Calculation is based on the following data: $(t = 0.45, \delta = 0.4, d = 20, l_0 = 16, We = 2, \alpha = 1)$.

The plots of dimensionless axial velocity of the flowing blood characterized by the Carreau fluid for different values power law parameter *n* at *t = 0.45* and *z = 28* are illustrated in Fig. **7.4 (a)**. One can see that the axial velocity decreases in going from shear-thinning *(n = 0.0, 0.639)* to shear-thickening *(n = 1, 1.2)* fluid. The profile of axial velocity for Newtonian fluid *(n=1)* lies in between shear-thinning and shear-thickening profiles. It is further observed that for shear-thinning fluid *(n = 0)* the profile tend to become flatter predicting a thin boundary layer near the wall. The behavior of radial velocity for different values of power law parameter *n* is depicted in **Fig. 7.4 (b)**. One can see that radial velocity in a normal artery is

independent of power law parameter n. However, it is slightly affected by n in the constricted artery. i.e. magnitude of radial velocity increases in going from shear-thinning to shear-thickening fluid.

The graphical illustrations of axial velocity profile of streaming blood characterized by the Carreau fluid for different values of τ_m are shown in **Fig. 7.5(a).** Fig. 7.5 (a) comprises of the three distinct curves showing different arteries with different stenotic height. The top most profile is for normal artery while the second and third curve correspond to the stenotic artery. One can see that the magnitude of the axial velocity decreases rapidly with an increase in the severity of the stenosis. **Fig. 7.5(b)** shows the profile of radial velocity for arteries with different severity level of stenosis at a specific location $z = 28$ and time instant $t = 0.45$. These profiles indicate that the magnitude of the radial velocity decreases with an increase in the severity level of stenosis.
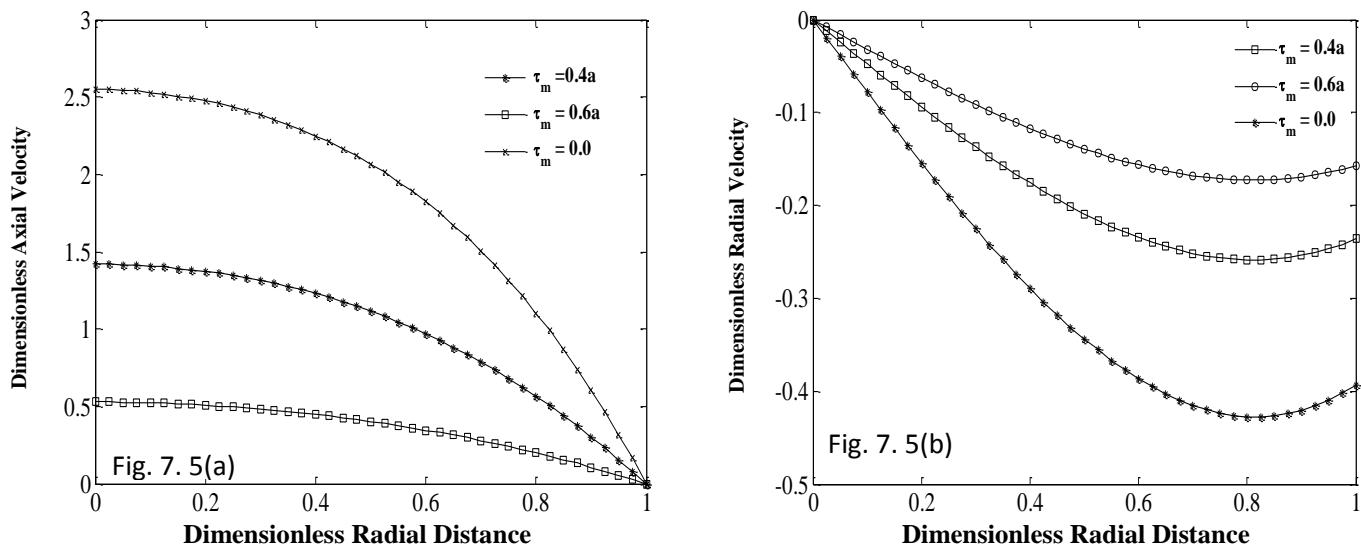

Fig. 7.5: Dimensionless Axial (Fig. 7.5(a)) and radial (Fig. 7.5(b)) velocity graphs for different values of τ_m. Calculation is based on the following data: $(t = 0.45, \delta = 0.4, d = 20, l_o = 16, We = 2, \alpha = 1)$.

The graphical illustrations of time series of dimensionless flow rate of streaming blood characterized by the Carreau fluid for a different tapering angles and different material parameters are presented **Fig. 7.6(a)** and (b), respectively. Fig. 7.6 (a) comprises of the five distinct curves of flow rate. The top most curve is for normal non-tapered artery while below it is the curve for diverging normal artery. The variation of flow

rate with time for diverging stenotic artery is shown in third curve. The fourth curve from the top corresponds to non-tapered stenotic artery. The last curve depicts the case of flow rate for a converging artery. We may conclude from Fig. 7.6 (a) that flow rate attain higher value in normal artery with wall movement as compared with stenotic artery. The positive values of taper angle further enhance the flow rate while the presence of stenosis reduces it significantly. **Fig 7.6 (b)** indicates an increase in the flow rate with increasing the material parameter *We* both in normal and constricted arteries. It is interesting to note that flow rate does not become periodic in the first four cardiac cycles.
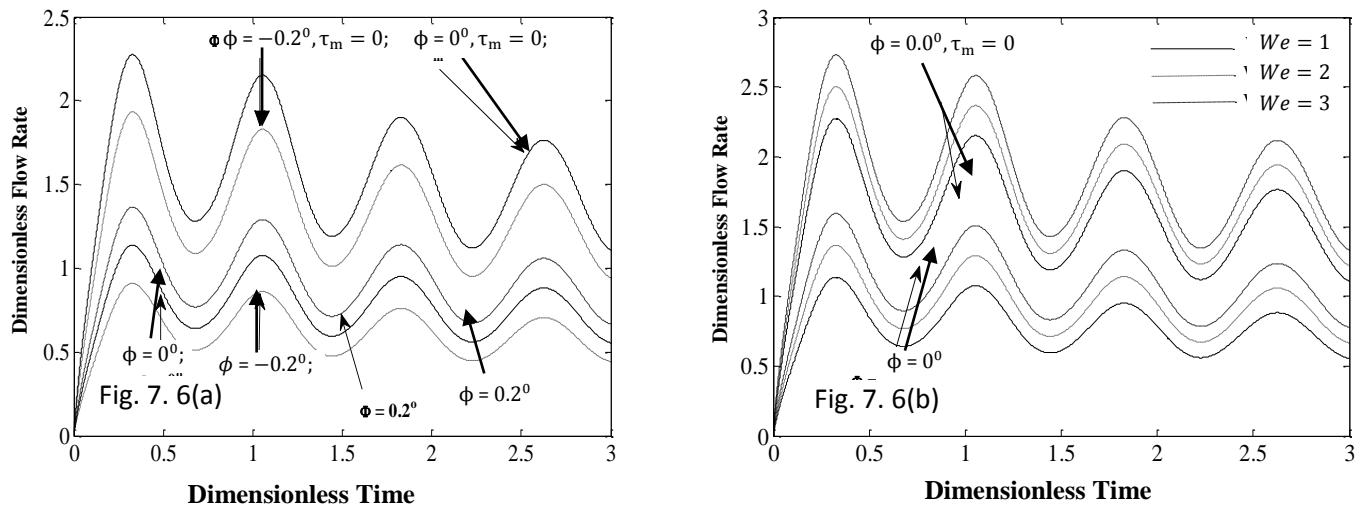

Fig. 7.6: Dimensionless flow rate for different values of tapering angles ϕ (Fig.7.6(a)) and for different *We* (Weissenberg numbers) (Fig. 7.6(b)) at $z = 28$. Calculation is based on the following data: $(t = 0.45, \delta = 0.4,$

$d = 20, l_0 = 16, We = 2, \alpha = 1)$.

The time series of wall shear stress for four cardiac cycles at a specific location $z = 28$ for different taper angles and different values of material parameter *We* are shown in **Fig. 7.7 (a) and (b)**, respectively. We note from Fig. 7.7 (a) that the value of shear stress in the stenotic region for a diverging constricted artery is higher than those of non-tapered and converging artery. We further note from Fig. 7.7 (a) that the profile of wall shear stress for a normal artery lies below of all other curves. This indicates that the presence of stenosis significantly enhances the wall shear stress. The influence of *We* (Weissenberg numbers) on wall shear is depicted in Fig. 7.7 (b). This figure predicts a reduction in wall shear stress by increasing *We*. This

result can also be anticipated from the profiles of flow rate in Fig. 7.6 (b) where the flow is found to be an increasing function of *We*. It is also evident from both the figures 7.7 (a) and (b) that wall shear stress become periodic immediately after the start of the flow.
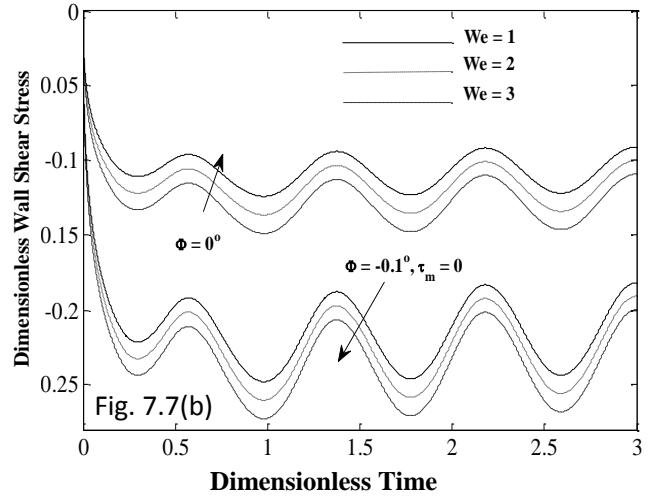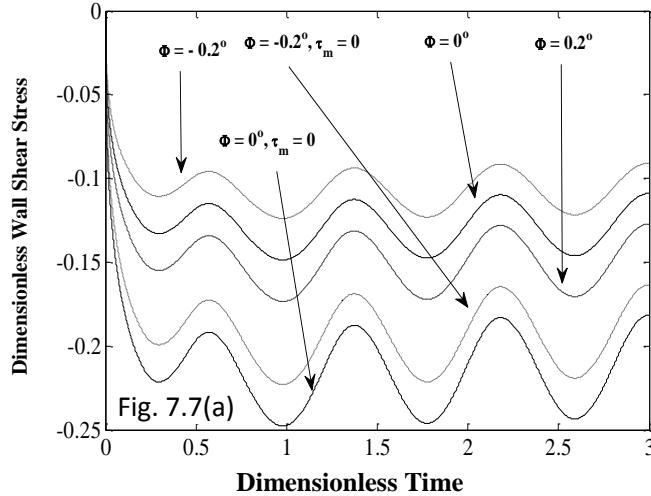

Fig. 7.7: Dimensionless Wall shear stress for different values of tapering angles ϕ (Fig. 7.7(a)) and for different *We* (W*eissenberg numbers*) (Fig. 7.7(b)) at $z = 28mm$. Calculation is based on the following data: $(t = 0.45, \delta = 0.4, d = 20, l_o = 16, We = 2, \alpha = 1)$.

Figs. 7.8(a) and (b) are plotted to see the time series of resistance impedance at a specific location $z = 28$ for different taper angles and different values of *We* (*Weissenberg numbers*). It is observed that these profiles follow a reverse trend in contrast to the flow rate profiles as expected from the formula of the resistance to flow given by expression (7.56). Contrary to flow rate profiles, one may observe that the resistance to flow in a stenotic region decreases as tapering angle increase from -0.2 to 0.2. A further decrease is observed in the absence of the stenotic region. Fig. 7.8 (b) reveals that the resistance to flow is a decreasing function of the *We* (*Weissenberg numbers*). Moreover, Fig. 7.8 (a) and (b) also indicate that like flow rate, the periodicity in the resistance to flow is not achieved within the first four cardiac cycles.
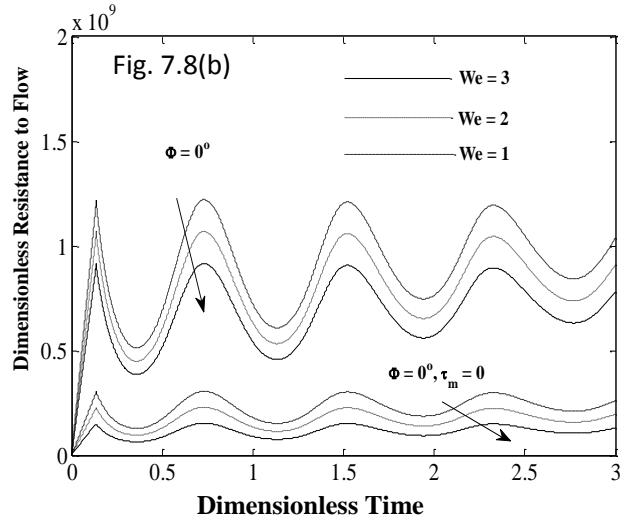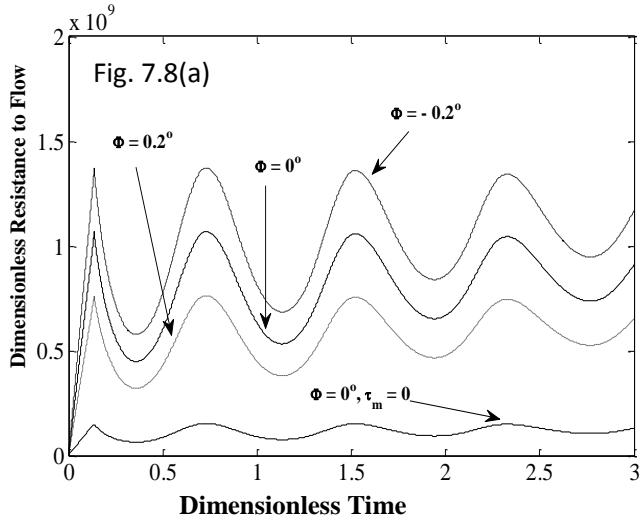
Fig. 7.8: Dimensionless variation of resistance to flow for different values of tapering angles ϕ (Fig. 7.8(a)) and for different *We* (*Weissenberg* numbers) (Fig. 7.8(b)) at $z = 28$. Calculation is based on the following data: $(t = 0.45, \delta = 0.4, d = 20, l_0 = 16, We = 2, \alpha = 1)$.

7.7   Conclusions

A theoretical model is presented for unsteady pulsatile flow of blood through a time-variant stenotic artery using the constitutive equation of a Carreau fluid. The equations governing are modeled under long wavelength assumption and then solved numerically using an explicit finite difference scheme. The present theoretical model is capable of exploring the effects of shear-thinning/thickening and viscoelastic nature of blood on various characteristics of blood. In addition to that the model also incorporates the effects of tapering and time-variant geometry of stenosis. The major findings of the present study are:

❖ The presence of stenosis reduces the magnitude of axial and radial velocity of blood.

❖ Axial velocity is an increasing function of Weissenberg number while it decreases by increasing Womersley number.

❖ Axial velocity decreases in going from shear-thinning to shear-thickening fluid.

❖ Radial velocity is not affected to an appreciable amount by increasing Weissenberg number.

❖ Flow rate increases while shear stress decreases by increasing Weissenberg number.

110

❖ Resistance to flow is found to be a decreasing function of Weissenberg number.

Chapter 8

Two-dimensional and two-layered pulsatile flow of blood in a stenotic artery

In this chapter, a theoretical study has been carried out to investigate the unsteady two-phase flow of blood through a flexible artery under stenotic conditions. The Newtonian and Herschel–Bulkley constitutive relations are used to model the core and peripheral regions, respectively. The present analysis treats the wall of the artery to be elastic. An explicit finite difference algorithm is implemented for the solution of the governing unsteady partial differential equations along with the given boundary and initial conditions. The radial and axial velocities of the streaming blood are computed for several values of the emerging parameters. The volumetric flow rate, resistance impedance and wall shear stress are also shown graphically and discussed in detail.

8.1   Geometry of the two layer stenotic artery

Let us consider two-dimensional flow of blood through a stenotic artery. It is assumed that due to aggregation of red blood cells, core and peripheral regions are developed in the centre and near the boundary of the artery, respectively. The flow is analyzed using cylindrical co-ordinate system *(r, θ, z)*. A schematic diagram is illustrated in **Fig. 8.1.**
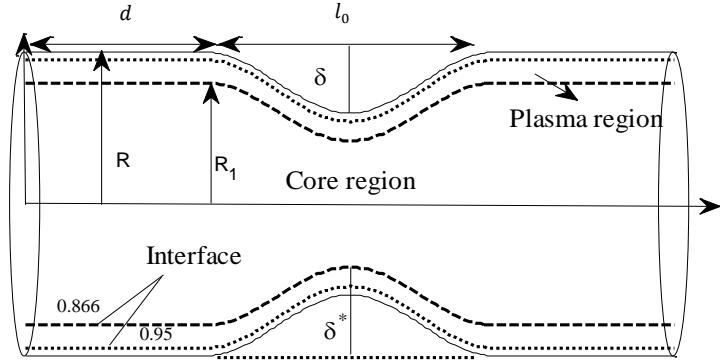
Fig. 8.1. Geometry of the stenotic artery with peripheral layer

The mathematical model of the time-variant stenosed arterial segment is

$$(R,R_1)(z,t) = \begin{cases} \left[\left(a,\ a^*\right) - \dfrac{\left(\delta,\delta^*\right)}{2} \left\{ 1 + \cos\dfrac{2\pi}{l_0}\left(z - d - \dfrac{l_0}{2}\right) \right\} \right] a_1(t), & d \le z \le d + l_0, \\ \left(a,\ a^*\right) a_1(t), & otherwise. \end{cases} \tag{8.1}$$

In above expression $R(z,t)$ denotes the radius of the arterial segment with stenosis, δ is the maximum height of the stenosis, a is the constant radius of the artery in the non-stenotic region, a^* is the constant radius of interface in the non-stenotic region, l_0 is the length of the stenosis, d is the length of the pre-stenotic region, δ^* is the bulging of interface and $R_1(z,t)$ denotes the radius of the central core layer. The time-variant parameter $a_1(t)$ is given by the following expression

$$a_1(t) = 1 - k_r\left(cos\omega_p t - \theta\right), \tag{8.2}$$

where ω_p represents the angular frequency with $\omega_p = 2\pi f_p$, f_p being the pulse frequency, k_r represents the amplitude constant and θ is the phase angle.

8.2   Mathematical formulation

Let $\left(V_i,\ \rho_i,\ T_i\right),\ i = 1,2$ denote the velocity vector, density and stress field in the core and peripheral regions, respectively. The governing laws of mass and momentum conservation in core and peripheral region becomes:

Law of conservation of mass:
$$\nabla \cdot \boldsymbol{V}_i = 0, i = 1, 2. \tag{8.3}$$

Law of conservation of Momentum:
$$\rho_i \frac{d\boldsymbol{V}_i}{dt} = \nabla \cdot \boldsymbol{T}_i, \ i = 1, 2, \tag{8.4}$$

where
$$\boldsymbol{T}_i = -p\boldsymbol{I} + \boldsymbol{S}_i, i = 1, 2. \tag{8.5}$$

The blood in the core region is characterized by the constitutive equation of Herschel–Bulkley model. According to Yilmaz and Gundogdu [22], the extra stress for Herschel Bulkley model is

$$\boldsymbol{S}_1 = \left(\mu_1 \, \Pi^{n-1} + \frac{\tau_y}{\Pi} \right) \boldsymbol{A}_1^{*}, \tag{8.6}$$

where τ_y is the yield stress, $\boldsymbol{A}_1^{*} = \nabla \bar{\boldsymbol{V}}_2 + \nabla \bar{\boldsymbol{V}}_2^{T}$ and $\Pi = \sqrt{\frac{1}{2} \mathrm{tr}\left(\boldsymbol{A}_1^{*} \cdot \boldsymbol{A}_1^{*T} \right)^2}$.

The stress tensor in the peripheral region is given by:

$$\boldsymbol{S}_2 = \mu_2 \left(\nabla \bar{\boldsymbol{V}}_2 + \nabla \bar{\boldsymbol{V}}_2^{T} \right). \tag{8.7}$$

The velocity field for two-dimensional flow in the core and peripheral regions is given by:

$$\boldsymbol{V}_i = \left[u_i(r, z, t), 0, w_i(r, z, t) \right], i = 1, 2. \tag{8.8}$$

In view of (8.8), the continuity equation (8.3) in core and periphery region reduces to

$$\frac{\partial u_i}{\partial r} + \frac{u_i}{r} + \frac{\partial w_i}{\partial z} = 0, \ i = 1, 2. \tag{8.9}$$

The momentum equation (8.4) in the core region takes the following form:

$$\rho_1 \left(\frac{\partial u_1}{\partial t} + u_1 \frac{\partial u_1}{\partial r} + w_1 \frac{\partial u_1}{\partial z} \right) = -\frac{\partial p}{\partial r} + \left(\frac{1}{r} \frac{\partial}{\partial r}(rS_{rr}) + \frac{\partial}{\partial z}(S_{rz}) \right), \tag{8.10}$$

$$\rho_1 \left(\frac{\partial w_1}{\partial t} + u_1 \frac{\partial w_1}{\partial r} + w_1 \frac{\partial w_1}{\partial z} \right) = -\frac{\partial p}{\partial z} + \left(\frac{1}{r} \frac{\partial}{\partial r}(rS_{rz}) + \frac{\partial}{\partial z}(S_{zz}) \right), \tag{8.11}$$

114

$$S_{rr} = 2\left[\left\{\mu_1\left[2\left(\left(\frac{\partial u_1}{\partial r}\right)^2 + \left(\frac{u_1}{r}\right)^2 + \left(\frac{\partial w_1}{\partial z}\right)^2\right) + \left(\frac{\partial u_1}{\partial z} + \frac{\partial w_1}{\partial r}\right)^2\right]^{\frac{n-1}{2}} + \tau_y\left[2\left(\left(\frac{\partial u_1}{\partial r}\right)^2 + \left(\frac{u_1}{r}\right)^2 + \left(\frac{\partial w_1}{\partial z}\right)^2\right)\right.\right.$$

$$\left.\left.+ \left(\frac{\partial u_1}{\partial z} + \frac{\partial w_1}{\partial r}\right)^2\right]^{-1/2}\right\}\right] \times \left(\frac{\partial u_1}{\partial r}\right), \tag{8.12}$$

$$S_{zz} = 2[\cdots\cdots\cdots] \times \left(\frac{\partial w_1}{\partial z}\right), \tag{8.13}$$

$$S_{rz} = [\cdots\cdots\cdots] \times \left(\frac{\partial w_1}{\partial r} + \frac{\partial u_1}{\partial z}\right). \tag{8.14}$$

Similarly the momentum equations for the peripheral region are defined as:

$$\rho\left(\frac{\partial u_2}{\partial t} + u_2\frac{\partial u_2}{\partial r} + w_2\frac{\partial u_2}{\partial z}\right) = -\frac{\partial p}{\partial r} + \mu_2\left(\frac{\partial^2 u_2}{\partial r^2} + \frac{1}{r}\frac{\partial u_2}{\partial r} + \frac{\partial^2 u_2}{\partial z^2} - \frac{u_2}{r^2}\right), \tag{8.15}$$

$$\rho\left(\frac{\partial w_2}{\partial t} + u_2\frac{\partial w_2}{\partial r} + w_2\frac{\partial w_2}{\partial z}\right) = -\frac{\partial p}{\partial z} + \mu_2\left(\frac{\partial^2 w_2}{\partial r^2} + \frac{1}{r}\frac{\partial w_2}{\partial r} + \frac{\partial^2 w_2}{\partial z^2}\right). \tag{8.16}$$

The subsequent analysis is based on the assumption that the lumen radius R is taken sufficiently smaller than wavelength λ, of the pressure wave in our current analysis. i.e. R/λ, $\lambda \ll 1$ [90]. On the basis of this assumption the radial Navier-Stokes equation simply reduces to $\partial p/\partial r = 0$ which gives that pressure is independent of radial coordinate.

The boundary and initial conditions for the problem under consideration are [26]

$$u_1(r,z,t) = 0, \frac{\partial w_1(r,z,t)}{\partial r} = 0 \text{ and } S_{rz} = 0, \text{ on } r = 0, \tag{8.17}$$

$$u_2(r,z,t) = \frac{\partial R}{\partial t}, \quad w_2(r,z,t) = 0, \text{ on } r = R, \tag{8.18}$$

$$u_i(r,z,0) = w_i(r,z,0) = 0, \ i = 1, \ 2. \tag{8.19}$$

115

At the interface, it is assumed that both the axial and radial velocities are continuous i.e.

$$w_1(r,z,t) = w_2(r,z,t), \quad on \ r = R_1,$$

$$u_1(r,z,t) = u_2(r,z,t). \quad on \ r = R_1. \tag{8.20}$$

8.3   Non-dimensionalization of the problem

We are interested in numerical solution of Eqns. (8.10) and (8.11) subject to conditions (8.17)-(8.19). We first normalize these equations by defining given in Eq. (7.10). In terms of new variables Eqns. (8.10), (8.15), (8.13)-(8.14) after dropping the bars read

$$\frac{\partial u_i}{\partial r} + \frac{u_i}{r} + \frac{\partial w_i}{\partial z} = 0, \ i = 1, \ 2, \tag{8.21}$$

$$\alpha\left(\frac{\partial w_1}{\partial t} + u_1 \frac{\partial w_1}{\partial r} + w_1 \frac{\partial w_1}{\partial z}\right) = -\frac{\partial p}{\partial z} + \left(\frac{1}{r}\frac{\partial}{\partial r}(rS_{rz}) + \frac{\partial}{\partial z}(S_{zz})\right), \tag{8.22}$$

and the Newtonian equation in the periphery region

$$\alpha\left(\frac{\partial w_2}{\partial t} + u_1 \frac{\partial w_2}{\partial r} + w_1 \frac{\partial w_2}{\partial z}\right) = -\frac{\partial p}{\partial z} + \left(\frac{\partial^2 w_2}{\partial r^2} + \frac{1}{r}\frac{\partial w_2}{\partial r} + \frac{\partial^2 w_2}{\partial z^2}\right), \tag{8.23}$$

where

$$S_{rz} = \left[\left\{\left[\left[2\left(\left(\frac{\partial u_1}{\partial r}\right)^2 + \left(\frac{u_1}{r}\right)^2 + \left(\frac{\partial w_1}{\partial z}\right)^2\right) + \left(\frac{\partial u_1}{\partial z} + \frac{\partial w_1}{\partial r}\right)^2\right]\right]^{\frac{n-1}{2}} + \tau\left[2\left(\left(\frac{\partial u_1}{\partial r}\right)^2 + \left(\frac{u_1}{r}\right)^2 + \left(\frac{\partial w_1}{\partial z}\right)^2\right)\right.\right.$$

$$\left.\left.+ \left(\frac{\partial u_1}{\partial z} + \frac{\partial w_1}{\partial r}\right)^2\right]^{-\frac{1}{2}}\right\}\right] \times \left(\frac{\partial w_1}{\partial r} + \frac{\partial u_1}{\partial z}\right), \tag{8.24}$$

$$S_{zz} = \left[\cdots\cdots\cdots\right] \times \left(\frac{\partial w}{\partial z}\right), \tag{8.25}$$

$\tau \left(= {\tau_y}\big/{\rho \omega^n} \right)$ is the dimensionless yield stress and where $\mu = \mu_1 \omega^n$ is the average viscosity. The

dimensionless boundary and initial conditions are:

$$u_1(r,z,t) = 0, \quad \frac{\partial w_1(r,z,t)}{\partial r} = 0 \text{ and } S_{rz} = 0, \text{ on } r = 0, \tag{8.26}$$

$$u_2(r,z,t) = \frac{\partial R}{\partial t}, \quad w_2(r,z,t) = 0, \quad \text{on } r = R, \tag{8.27}$$

$$u_i(r,z,0) = w_i(r,z,0) = 0, \quad i = 1,2. \tag{8.28}$$

The boundary condition at the interface becomes

$$w_1(r,z,t) = w_2(r,z,t),$$

$$u_1(r,z,t) = u_2(r,z,t) \qquad on \ r = R_1. \tag{8.29}$$

In above equations

$$(R,R_1)(z,t) = \begin{cases} \left[(1,\beta) - \frac{(\delta,\delta^*)}{2a} \left\{ 1 + \cos\frac{2\pi}{l_0}\left(z - d - \frac{l_0}{2} \right) \right\} \right] a_1(t), & d \le z \le d + 2z_0, \\ (1,\beta) a_1(t), & otherwise. \end{cases} \tag{8.30}$$

where $\delta^* = \beta \delta$, where $\beta \left(= \dfrac{a^*}{a} \right)$ is a geometric parameter.

8.4 Problem transformation

Now we introduce a radial coordinate transformation [75]

$$x = \frac{r}{R(z,t)}, \tag{8.31}$$

to map the constricted domain into a rectangular one. Using this transformation, Eqns. (8.22)-(8.29) can be

rewritten in the following form

$$\frac{\partial w_1}{\partial t} = \left\{ \frac{x}{R}\frac{\partial R}{\partial t} - \frac{u_1}{R} + \frac{x}{R}\frac{\partial R}{\partial z}w_1 \right\}\frac{\partial w_1}{\partial x} - \frac{1}{\alpha}\frac{\partial p}{\partial z} - w_1\frac{\partial w_1}{\partial z} - \frac{1}{\alpha}\left\{ \frac{1}{xR}S_{xz} + \frac{1}{R}\frac{\partial S_{xz}}{\partial x} - \frac{\partial S_{zz}}{\partial z} + \frac{x}{R}\frac{\partial R}{\partial z}\frac{\partial S_{zz}}{\partial x} \right\}, \qquad (8.32)$$

$$\frac{\partial w_2}{\partial t} = \left\{ \frac{x}{R}\frac{\partial R}{\partial t} - \frac{u_2}{R} + \frac{x}{R}\frac{\partial R}{\partial z}w_2 \right\}\frac{\partial w_2}{\partial x} - \frac{1}{\alpha}\frac{\partial p}{\partial z} - w_2\frac{\partial w_2}{\partial z} - \frac{1}{\alpha}\left[\frac{1}{R^2}\left\{ 1 + \left(x\frac{\partial R}{\partial z} \right)^2 \right\}\frac{\partial^2 w_2}{\partial x^2} + \right.$$
$$\left. \frac{1}{xR^2}\left\{ 1 + 2\left(x\frac{\partial R}{\partial z} \right)^2 - x^2 R\frac{\partial^2 R}{\partial z^2} \right\}\frac{\partial w_2}{\partial x} + \frac{\partial^2 w_2}{\partial z^2} \right], \qquad (8.33)$$

$$\frac{1}{R}\frac{\partial u_i}{\partial x} + \frac{u_i}{xR} + \frac{\partial w_i}{\partial z} - \frac{x}{R}\frac{\partial R}{\partial z}\frac{\partial w_i}{\partial x} = 0, \; i = 1,\; 2, \qquad (8.34)$$

$$S_{xz} = \left[\left\{ \left[2\left(\left(\frac{1}{R}\frac{\partial u_1}{\partial x} \right)^2 + \left(\frac{u_1}{xR} \right)^2 + \left(\frac{\partial w_1}{\partial z} - \frac{x}{R}\frac{\partial R}{\partial z}\frac{\partial w_1}{\partial x} \right)^2 \right) + \left(\frac{\partial u_1}{\partial z} - \frac{x}{R}\frac{\partial R}{\partial z}\frac{\partial u_1}{\partial x} + \frac{1}{R}\frac{\partial w_1}{\partial x} \right)^2 \right]^{\frac{n-1}{2}} \right. \right.$$
$$\left. + \tau \left[2\left(\left(\frac{1}{R}\frac{\partial u_1}{\partial x} \right)^2 + \left(\frac{u_1}{xR} \right)^2 + \left(\frac{\partial w_1}{\partial z} - \frac{x}{R}\frac{\partial R}{\partial z}\frac{\partial w_1}{\partial x} \right)^2 \right) + \left(\frac{\partial u_1}{\partial z} - \frac{x}{R}\frac{\partial R}{\partial z}\frac{\partial u_1}{\partial x} + \frac{1}{R}\frac{\partial w_1}{\partial x} \right)^2 \right]^{-\frac{1}{2}} \right\} \right]$$
$$\times \left(\frac{\partial u_1}{\partial z} - \frac{x}{R}\frac{\partial R}{\partial z}\frac{\partial u_1}{\partial x} + \frac{1}{R}\frac{\partial w_1}{\partial x} \right), \qquad (8.35)$$

$$S_{zz} = 2[\cdots\cdots\cdots\cdots] \times \left(\frac{\partial w_1}{\partial z} - \frac{x}{R}\frac{\partial R}{\partial z}\frac{\partial w_1}{\partial x} \right). \qquad (8.36)$$

Similarly, we can write the boundary and initial conditions as

$$u_1(x,z,t) = 0, \frac{\partial w_1(x,z,t)}{\partial x} = 0, \; S_{xz} = 0, \qquad on \; x = 0, \qquad (8.37)$$

$$u_2(x,z,t) = \frac{\partial R}{\partial t}, \; w_2(x,z,t) = 0, \qquad on \; x = 1, \qquad (8.38)$$

$$u_i(x,z,0) = w_i(x,z,0) = 0, \; i = 1,\; 2. \qquad (8.39)$$

The interface boundary condition becomes

$$w_1(x,z,t) = w_2(x,z,t),$$

$$u_1(x,z,t) = u_2(x,z,t), \qquad on \ x = \beta, \tag{8.40}$$

An explicit expression for $u_1(x, z, t)$ can be obtained as follows: Multiplying Eq. (8.34) by xR and integrating with respect to x from 0 to x, we get

$$u_1(x,z,t) = \frac{\partial R}{\partial z}\left[xw_1 - \frac{2}{x}\int_0^x xw_1 dx \right] - \frac{R}{x}\int_0^x x\frac{\partial w_1}{\partial z} dx, \tag{8.41}$$

Eq. (8.41) takes the following form by making use of the boundary condition (8.40)

$$\int_0^\beta x\frac{\partial w_1}{\partial z} dx = \int_0^\beta x\left[\frac{2}{R}\frac{\partial R}{\partial z}w + \frac{\beta}{R}\left(\beta\frac{\partial R}{\partial z}w_{1\beta} - u_{1\beta}\right) f(x) \right] dx, \tag{8.42}$$

where

$$u_{1\beta} = u_1(x,z,t)\big|_{x=\beta} = u_2(x,z,t)\big|_{x=\beta},$$

$$w_{1\beta} = w_1(x,z,t)\big|_{x=\beta} = w_2(x,z,t)\big|_{x=\beta}. \tag{8.43}$$

Since the choice of $f(x)$ is arbitrary therefore we take $f(x) = \dfrac{4(x^2 - 1)}{a^{*2}(a^{*2} - 2)}$ which satisfies the condition

$\int_0^x xf(x) dx = 1$. The equality of integrands in Eq. (8.42) gives

$$\frac{\partial w_1}{\partial z} = -\frac{2}{R}\frac{\partial R}{\partial z}w_1 + \frac{\beta}{R}\left(\beta\frac{\partial R}{\partial z}w_{1\beta} - u_{1\beta}\right)\frac{4(x^2 - 1)}{\beta^2(\beta^2 - 2)}. \tag{8.44}$$

Utilizing (8.44) in (8.41), we finally arrive at

$$u_1(x,z,t) = x\left[\frac{\partial R}{\partial z}w_1 - \frac{\left(\beta\frac{\partial R}{\partial z}w_{1\beta} - u_{1\beta}\right)(x^2 - 2)}{\beta^2(\beta^2 - 2)} \right]. \tag{8.45}$$

In a similar manner, for the plasma region $(\beta \le x \le 1)$, multiplying (8.36) by xR and integrating with respect to x between the limits β and x $(\beta \le x \le 1)$, and exploiting the boundary conditions (8.43), one finds

$$\frac{\partial w_2}{\partial z} = -\frac{2}{R}\frac{\partial R}{\partial z}w_2 - \frac{1}{R}\left(\beta u_{2\beta} - \beta^2 \frac{\partial R}{\partial z}w_{2\beta} - \frac{\partial R}{\partial t}\right)\frac{4\left(x^2-1\right)}{\left(\beta^2-1\right)^2}, \qquad (8.46)$$

and finally

$$u_2\left(x,z,t\right) = x\left[\frac{\partial R}{\partial z}w_2 - \frac{1}{x^2}\left(\beta u_{2\beta} - \beta^2 \frac{\partial R}{\partial z}w_{2\beta} - \frac{\partial R}{\partial t}\right)\frac{\left(x^2-\beta^2\right)\left(x^2+\beta^2-2\right)}{\left(\beta^2-1\right)^2} + \frac{\beta}{x^2}\left(u_{2\beta} - \beta\frac{\partial R}{\partial z}w_{2\beta}\right)\right], \qquad (8.47)$$

now from Eqns (8.46) and (8.47) one can obtain

$$u_2\left(x,z,t\right) = \frac{x^2+1}{2x}\left[\frac{\partial R}{\partial z}w_2 - \frac{\left(x^2-1\right)}{\left(\beta^2+1\right)^2}\frac{\partial w_2}{\partial z} + \frac{2}{x^2+1}\frac{\partial R}{\partial t}\right]. \qquad (8.48)$$

8.5   Finite difference technique

Following Mandal [26] and Mandal et al. [27], we use the central difference formula for the approximation of space derivatives and forward difference formula for the approximation of time derivative. The discrete points in radial directions are given as $x_j = \left(j-1\right)\Delta x$, $\left(j=1,2,\ldots N_c+1\right)$, such that $x_{\left(N_c+1\right)} = \beta$ and $x_j = \left(j-\left(N_c+1\right)\right)\Delta x$, $j = \left(N_c+1, N_c+2, \ldots, N+1\right)$, such that $x_{\left(N+1\right)} = 1$ where Δx is the increment in the radial direction. Similarly, we define $z_i = \left(i-1\right)\Delta z$, $\left(i=1,2,\ldots M+1\right)$, where Δz the increment is in the axial direction, as uniformly distributed points in axial direction. Similar approach is used to define time step as $t_k = \left(k-1\right)\Delta t$, $\left(k=1,2,\ldots\right)$, where Δt is the time increment. Using (7.32) and (7.34), Eqs. (8.32) and (8.33) may be transformed to the following difference equations

$$w_{1i,j}^{k+1} = w_{1i,j}^k + dt\left[\left\{\frac{x_j}{R_i^k}\left(\frac{\partial R}{\partial t}\right)_i^k - \frac{u_{1i,j}^k}{R_i^k} + \frac{x_j}{R_i^k}\left(\frac{\partial R}{\partial z}\right)_i^k w_{1i,j}^k\right\}\left(w_{1x}\right)_{i,j}^k - w_{1i,j}^k\left(w_{1z}\right)_{i,j}^k - \right.$$

$$\left. + \frac{1}{\alpha}\left\{-\left(\frac{\partial p}{\partial z}\right)^{k+1} + \frac{1}{x_j R_i^k}\left(S_{xz}\right)_{i,j}^k + \frac{1}{R_i^k}\left[\left(S_{xz}\right)_x\right]_{i,j}^k - \left[\left(S_{zz}\right)_z\right]_{i,j}^k + \frac{x_j}{R_i^k}\left(\frac{\partial R}{\partial t}\right)_i^k\left[\left(S_{zz}\right)_x\right]_{i,j}^k\right\}\right], \qquad (8.49)$$

$$w_{2i,j}^{k+1} = w_{2i,j}^k + dt\left[\left\{\frac{x_j}{R_i^k}\left(\frac{\partial R}{\partial t}\right)_i^k - \frac{u_{2i,j}^k}{R_i^k} + \frac{x_j}{R_i^k}\left(\frac{\partial R}{\partial z}\right)_i^k w_{2i,j}^k\right\}\left(w_{2x}\right)_{i,j}^k - w_{2i,j}^k\left(w_{2x}\right)_{i,j}^k + \right.$$

$$\left. + \frac{1}{\alpha}\left\{-\left(\frac{\partial p}{\partial z}\right)^{k+1} + \left(w_{2x}\right)_{i,j}^k + \frac{1}{x_j R_i^k}\left(w_{2x}\right)_{i,j}^k + \left(w_{2z}\right)_{i,j}^k\right\}\right], \qquad (8.50)$$

where

$$\left[\left(S_{zz}\right)\right]_{i,j}^k = 2\left[\left[2\left(\left(\frac{1}{R_i^k}\left(u_x\right)_{i,j}^k\right)^2 + \left(\frac{u_{i,j}^k}{x_j R_i^k}\right)^2 + \left(\left(w_z\right)_{i,j}^k - \frac{x_j}{R_i^k}\left(\frac{\partial R}{\partial z}\right)_i^k\left(w_x\right)_{i,j}^k\right)^2\right) + \left(-\frac{x_j}{R_i^k}\left(\frac{\partial R}{\partial z}\right)_i^k\left(u_x\right)_{i,j}^k\right.\right.\right.$$

$$\left.+\left(u_z\right)_{i,j}^k + \frac{1}{R_i^k}\left(w_x\right)_{i,j}^k\right)^2\right]^{\frac{n-1}{2}} + \frac{\tau}{2}\left(\left(\left(\frac{1}{R_i^k}\left(u_\xi\right)_{i,j}^k\right)^2 + \left(\frac{u_{i,j}^k}{x_j R_i^k}\right)^2 + \left(\left(w_z\right)_{i,j}^k - \frac{x_j}{R_i^k}\left(\frac{\partial R}{\partial z}\right)_i^k\left(w_\xi\right)_{i,j}^k\right)^2\right)\right.$$

$$\left.\left.+\left(\left(u_z\right)_{i,j}^k - \frac{x_j}{R_i^k}\left(\frac{\partial R}{\partial z}\right)_i^k\left(u_x\right)_{i,j}^k + \frac{1}{R_i^k}\left(w_x\right)_{i,j}^k\right)^2\right)\right]^{-1}\right]\times\left[\left(w_z\right)_{i,j}^k - \frac{x_j}{R_i^k}\left(\frac{\partial R}{\partial z}\right)_i^k\left(w_x\right)_{i,j}^k\right], \quad (8.51)$$

$$\left[\left(S_{xz}\right)\right]_{i,j}^k = \left[\cdots\cdots\cdots\cdots\right]\times\left[\left(u_{fz}\right)_{i,j}^k - \frac{x_j}{R_i^k}\left(\frac{\partial R}{\partial z}\right)_i^k\left(u_x\right)_{i,j}^k + \frac{1}{R_i^k}\left(w_x\right)_{i,j}^k\right]. \qquad (8.52)$$

The boundary and initial conditions can be written in the discretized form as:

$$u_{1i,j}^k = 0, w_{1i,1}^k = w_{1i,2}^k, \left(S_{xz}\right)_{i,1}^k = 0, \qquad (8.53)$$

$$w_{2i,N+1}^k = 0, u_{2i,j}^k = \left(\frac{\partial R}{\partial t}\right)_i^k, \qquad (8.54)$$

$$u_{m(i,j)}^1 = w_{m(i,j)}^1 = 0, \ m = 1, \ 2. \qquad (8.55)$$

The discretized form of interface conditions read

$$\left(w_1\right)^k_{i,N_c+1} = \left(w_2\right)^k_{i,N_c+1}, \left(u_1\right)^k_{i,N_c+1} = \left(u_2\right)^k_{i,N_c+1}. \tag{8.56}$$

The volumetric flow rate (Q) and the wall shear stress (τ_w) and the resistance impedance Λ are given by Mekheimer and Mohamed [94]

$$Q^k_i = 2\pi\left(R^k_i\right)^2\left(\int_0^\beta x_j w^k_{1i,j}dx_j + \int_\beta^1 x_j w^k_{2i,j}dx_j\right), \tag{8.57}$$

$$\Lambda^k_i = \frac{\left|L\left(\partial p / \partial z\right)^k\right|}{Q^k_i}, \tag{8.58}$$

$$\left(\tau_w\right)^k_i = \left[\left(S_{xz}\right)_{fz}\right]^k_{i,N+1}. \tag{8.59}$$

The expression for normalized flux (Q'), resistance to flow (Λ') and the wall shear stress (τ') are obtained as

$$Q'^k_i = \frac{Q^k_i}{\left(Q_n\right)^k_i}, \quad \Lambda^\kappa_t = \frac{\Lambda^\kappa_t}{\left(\Lambda_v\right)^\kappa_t} \quad and \quad \tau'^k_i = \frac{\tau^k_i}{\left(\tau_n\right)^k_i}. \tag{8.60}$$

where Q_n, Λ_v and τ_n are the flux, the resistance to flow and the wall shear stress respectively for the normal artery in the absence of peripheral layer.

8.6   Numerical results and discussion

In this section graphical results are displayed for the following set of parameters in Mandal [26]: Numerical computations have been carried out using the following parameter values: $\mu_0 = 0.56$, $L = 18$, $a = 1$, $d= 5$, $l_0= 8$, $A_0 = 7$, $A_1 = 0.2A_0$, $\delta = 0.3$. To obtain a convergent and stable solution, the temporal and spatial step sizes are chosen as: $\Delta x = 0.025$, $\Delta z = 0.1$, $\Delta t = 0.0001$. These values are also in accordance with the criteria for the convergent and stability of such method proposed by Hoffmann and Chiang [71]. Test computations show that the proposed method with the indicated restrictions is convergent up to 10^{-5}.

Fig. 8.2 shows the results of the axial velocity profile of the two-layered fluid model characterized by the Herschel Bulkley fluid in the core region and Newtonian fluid in the plasma region for various time instants and different peripheral layer thickness at a specific location *(z = 9)* of the artery. It is observed that velocity profile increases with time in both peripheral and core regions. Since the thickness of the peripheral region is small therefore the profiles in this region are found to be linear. However, in the core region the curves become parabolic. For a fixed value of time the effects of increasing peripheral layer thickness on velocity in peripheral region are negligible. Interestingly the velocity profile in the core region is found to increase by increasing peripheral layer thickness for a fixed value of time *t*. Such results are also reported by Ikbal et al. [70] in their analysis where the blood in the core region is modeled as a micropolar fluid. For a comparative study, the experimental results of Bugliarello [95] are also included in Figure 8.2. In addition to that the plots of steady state solutions obtained by Kang and Eringen [96] and Akay and Kaye [97] (both used Micropolar model to describe blood rheology) have also been shown in this figure. It is observed that the velocity profile predicted by our model (for $t = 8, \beta = 0.95$) approximates the experimental data relatively closer than the velocity profiles obtained through the models given in references [96] and [97]. It is pointed out that the value of yield stress taken in Fig. 8.2 is chosen from the data given by Valencia et al. [98]. However, it is expected that if we increase the yield stress parameter, the velocity profile shifts toward the origin and in this case it better fits the experimental results of Bugliarello and Sevilla [95]. This shift of velocity toward the origin by increasing yield stress parameter is shown in Fig. 4(b).
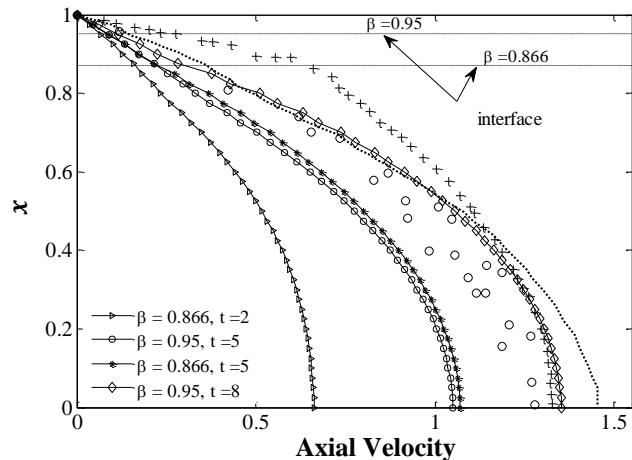
Fig. 8.2: Dimensionless axial velocity profiles at various dimensionless times; (o), experimental results of Bugliarello and Sevilla for blood containing 40% RBC (-), prediction of Kang and Eringen's model for blood with 40% RBC ;(+), prediction of Akay and Kaye for $\beta = 0.866$. Calculation is based on the following data: $\left(z = 9, n = 0.7, d = 5, \right.$

$\left. l_0 = 8, \ \alpha = 1.5, \ \tau = 0.0175 \right).$

The profiles of dimensionless radial velocity of the flowing blood in constricted artery at different time instants are shown in **Fig. 8.3**. All the graphs are taken at specific location $z = 9$. All the curves start from zero at the centre and approach a constant value at the interface thereby indicating the presence of wall movement. It is also noted from Fig. 8.3 that for a fixed value of time the magnitude of flow velocity diminishes as the peripheral layer thickness decreases. Moreover, in the systolic phase *(t=2)* the radial velocity assumes positive values while in the diastolic phase *(t = 5, 8)* it continues with negative values only.
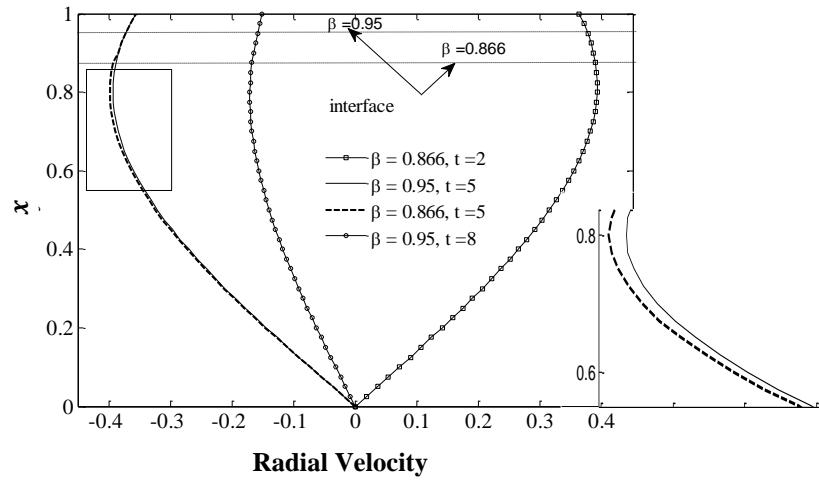

Fig. 8.3: Dimensionless radial velocity profiles at various dimensionless times. Calculation is based on the following data: ($z = 9, \ n = 0.7, \ d = 5, \ l_0 = 8, \ \alpha = 1.5$).

The plots of dimensionless axial velocity of the flowing blood characterized by the Herschel Bulkley fluid for different values of power law parameter *n* at *t = 5* and *z = 9* are illustrated in **Fig. 8.4a**. One can see that the axial velocity decreases in going from shear thinning *(n = 0.7)* to shear thickening *(n = 1, 1.3)* fluid. The profile of axial velocity for *n=1* lies in between shear thinning and shear thickening profiles. As expected it is observed that trend of axial velocity does not change with *n* in the plasma region near the

wall. The plots of dimensionless axial velocity for different values of yield stress are shown in Fig. **8.4b**. This figure indicates that the trend of axial velocity is strongly influenced by the values of yield stress. It is found that the magnitude of the velocity profile decreases by increasing the value of yield stress.
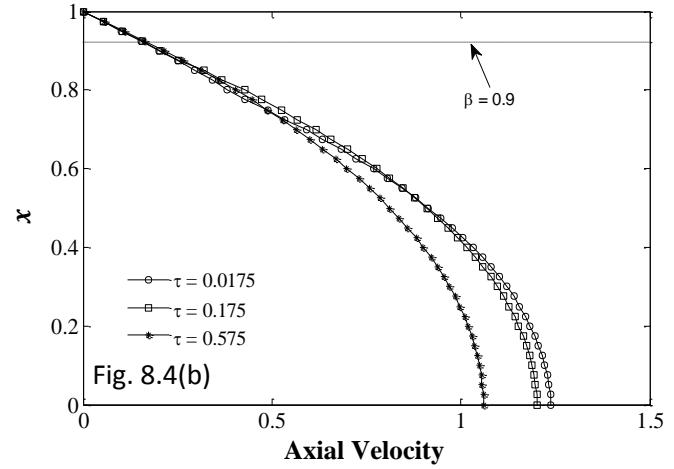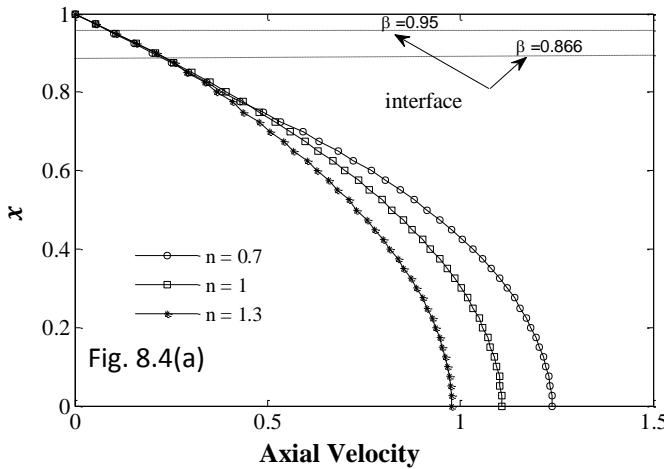

Fig. 8.4: Dimensionless Axial (Fig. 8.4(a) & 8.4. (b)) velocity graphs for different n and τ (yield stress). Calculation is based on the following data: ($z = 9$, $t = 5$, $\delta = 0.3$, $d = 5$, $l_0 = 8$, $\tau = 0.0175$, $n = 0.7$).

Fig. 8.5. (a) shows a comparison among three different models namely: single layer Newtonian model, single layer non-Newtonian model and two layer non-Newtonian model. One can observe that the profile of axial velocity for single layer Newtonian model coincides with that two-layered non-Newtonian model in plasma region while it predicts lower values of axial velocity in core region. Moreover, the values of axial velocity predicted by single layer non-Newtonian model are in excess of the values predicted by the other two models. Fig. 8.5 (b) shows the profiles of dimensionless axial velocity for different stenotic heights at a specific instant of time $t = 5$. It can be deduced that in these profile the magnitude of velocity decreases with an increase in the stenotic height.

Fig. 8.6 shows the curves of the flow rate over whole arterial length for three instants of time. It is evident from these curves that qualitative behavior of flow rate is same at different time instants. However, there do arise a qualitative difference i.e. the flow rate increases with time. Furthermore, at a fixed instant of time the flow rate is found to increase by increasing peripheral layer thickness.
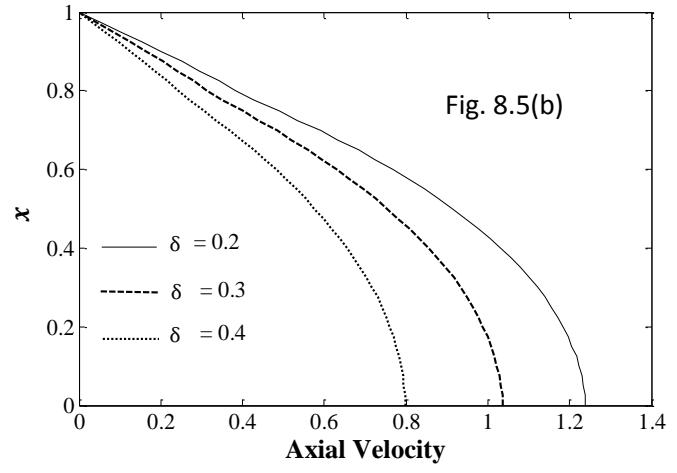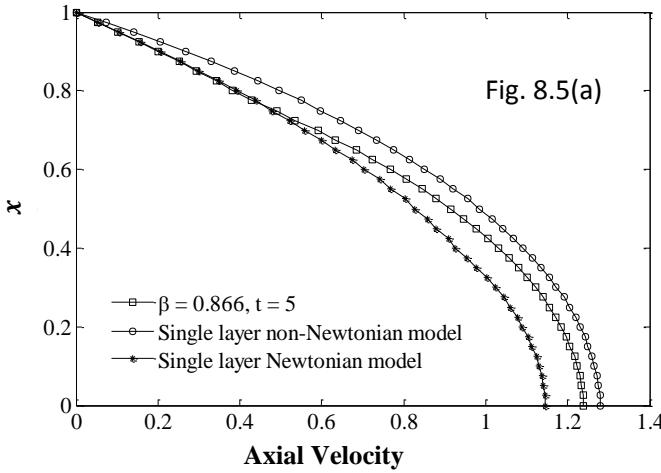
Fig. 8.5: Dimensionless Axial (Fig. 8.5(a) & 8.5.(b)) velocity graphs for different peripheral layer thickness and δ (stenotic length). Calculation is based on the following data: ($z = 9,\ t = 5\,, d = 5, l_0 = 8, \tau = 0.0175, n = 0.7$).
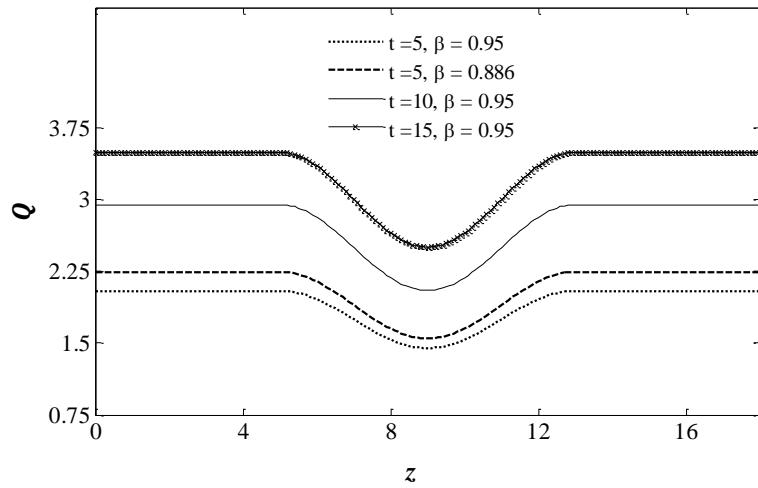

Fig. 8.6: Distribution of flow rate for different dimensionless time (t). Calculation is based on the following data: ($\delta = 0.3, d = 5, l_0 = 8, n = 0.7, \alpha = 1.5$) .

The curves of **Fig. 8.7** illustrate the distribution of the normalized resistive impedances $\left(\Lambda'\right)$ at the same critical location of stenosis $z = 9$ at t = 5. These curves indicate that on one hand resistance to flow increases by increasing the height of stenosis while on other hand it decreases by increasing the peripheral layer thickness. The profile of impedance based on the existing study performed by Young [1] is also shown in

Fig. 8.7. It is found that our results are qualitatively similar to those given by Young [1]. However, quantitative differences are observed which may be attributed to unsteadiness and nonlinear model of the blood used in the present study.
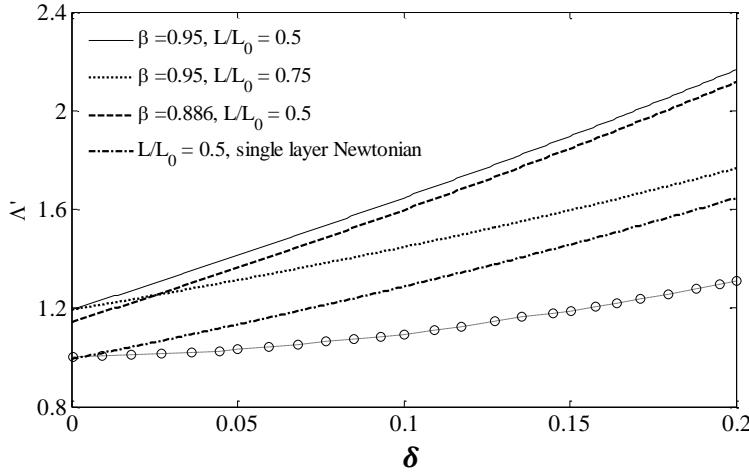

Fig. 8.7: Distribution of normalized resistance to flow for $t = 5$ at $z = 0$; (o-o), Young results (1968). Calculation is based on the following data: ($d = 5, l_0 = 8, \alpha = 1.5, \text{n} = 0.7$).
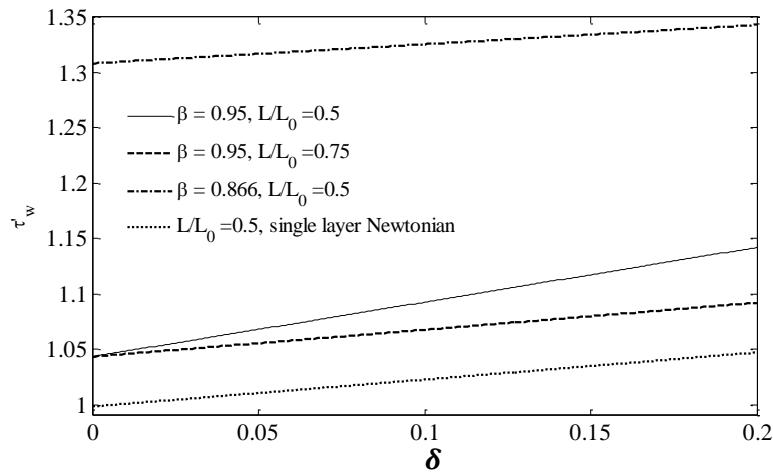

Fig. 8.8: Distribution of normalized wall shear stress at $z = 9$ at $t = 5$. Calculation is based on the following data: ($d = 5, l_0 = 8, \alpha = 1.5, \text{n} = 0.7$).

Fig. 8.8 illustrates the plots of normalized wall shear stress $\left(\tau'_w \right)$ versus stenotic height corresponding to the critical location $z = 9$ at $t = 5$ with different peripheral layer thickness. The increasing trend of the curves indicates the development of the stress due to the increase of the severity of the stenosis from *0.0 to*

0.2. Interestingly, the single layer Newtonian model predicts lower values of wall shear stress than that of two layer model. Further the wall shear stress predicted by two layer model is quite sensitive to the thickness of the peripheral layer. In fact, it increases by increasing peripheral layer thickness.

The time series of wall shear stress at a specific location $z = 14$ of the constricted arterial segment for different Womersley number is shown in **Fig. 8.9**. It is inferred from this figure that the wall shear stress is compressive in nature and its magnitude increases with Womersley number.
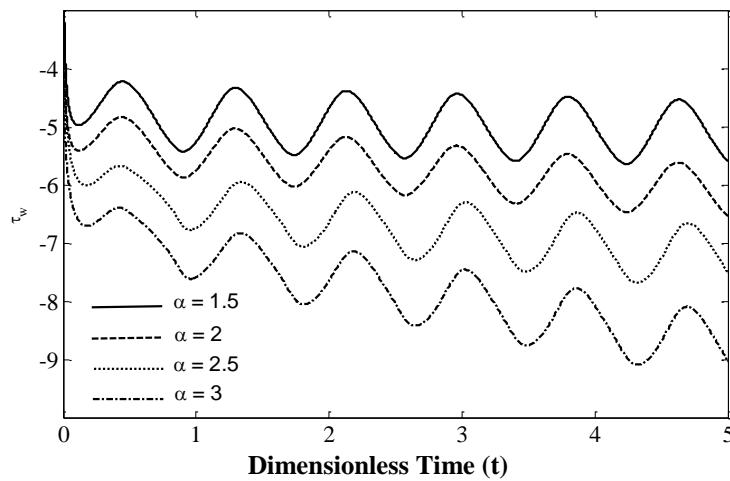

Fig. 8.9: Variation of wall shear stress for different Womersley number (α) with dimensionless time. Calculation is based on the following data: $\left(\delta = 0.3, d = 5, l_0 = 8, z = 9, n = 0.7 \right)$.

8.7   Conclusion

The analysis of pulsatile flow of blood through a diseased artery exhibiting the importance of peripheral layer thickness is carried out in the present study. The important findings of the study can be summarized as:

- The magnitude of the velocity profile increases by increasing the peripheral layer thickness and decreases with the increase of height of the stenosis.
- Wall shear stress increases with the increase of yield stress and height of the stenosis.
- The flow rate is found to increase by increasing the peripheral layer thickness.

- Resistance to flow increases by increasing the height of stenosis while on other hand it decreases by increasing the peripheral layer thickness.

- Resistance to flow increases with the increase in the size of stenosis.

Chapter 9

Unsteady blood flow through a tapered stenotic artery using Sisko model

This chapter explores the simultaneous effects of unsteadiness and non-Newtonian characteristics on flow of blood through a tapered stenosed artery. The rheology of blood is characterized by the constitutive equation of Sisko model. The time-variant nature of the stenosed artery is integrated in the geometry. The flow equations are derived for the scenario when the lumen radius is small than the wavelength of the pulsatile pressure wave. Employing radial coordinate transformation, the governing equations are integrated numerically along with the initial and boundary data over the whole arterial domain. Some important observations regarding the radial and axial velocities, volumetric flow rate and resistance impedance are made through graphical results.

9.1   Geometry of the problem

The model of the tapered artery with stenosis in its lumen is considered as a thin elastic tube with circular cross-section containing non-Newtonian fluid characterized by Sisko fluid model. A cylindrical polar co-ordinate (r, θ, z) system is employed for the purpose of flow analysis with r along the radial direction, while θ, z are taken along axial and circumferential directions respectively. A schematic diagram of stenosed

arterial segment is already shown in Fig. 7. 1. The expression defining the shape of this segment is reported in Eq. (7.1).

9.2   Problem formulation

The geometry and under lying assumption of the flow problem under consideration are similar as given in chapter 7. However, the rheological behavior of the streaming blood through the artery is characterized by the constitutive equation of Sisko model which is already given in (2.3) i.e.

$$S = \left[\varepsilon_1 + \varepsilon_2 \left(\left| \sqrt{\Pi} \right| \right)^{n-1} \right] A_1^*. \tag{9.1}$$

Assuming the flow to be two-dimensional, it is appropriate to choose a velocity field defined through Eq. (7.3) for the present flow situation. The continuity and momentum equations governing the flow under consideration are given by Eqs. (7.4) and (7.5)-(7.6).

Since the Sisko model (2.3) is employed to capture the rheology of the blood. Therefore, the components of extra stress arising in momentum equations (7.5) and (7.6) can be written as

$$S_{rr} = -2 \left[\varepsilon_1 + \varepsilon_2 \left\{ \left| \left[\left(\frac{\partial u}{\partial r} \right)^2 + \left(\frac{u}{r} \right)^2 + \left(\frac{\partial w}{\partial z} \right)^2 + \left(\frac{\partial u}{\partial z} + \frac{\partial w}{\partial r} \right)^2 \right]^{1/2} \right|^{n-1} \right\} \right] \left(\frac{\partial u}{\partial r} \right), \tag{9.2}$$

$$S_{zz} = -2 \left[\varepsilon_1 + \varepsilon_2 \left\{ \left| \left[\left(\frac{\partial u}{\partial r} \right)^2 + \left(\frac{u}{r} \right)^2 + \left(\frac{\partial w}{\partial z} \right)^2 + \left(\frac{\partial u}{\partial z} + \frac{\partial w}{\partial r} \right)^2 \right]^{1/2} \right|^{n-1} \right\} \right] \left(\frac{\partial w}{\partial z} \right), \tag{9.3}$$

$$S_{rz} = - \left[\varepsilon_1 + \varepsilon_2 \left\{ \left| \left[\left(\frac{\partial u}{\partial r} \right)^2 + \left(\frac{u}{r} \right)^2 + \left(\frac{\partial w}{\partial z} \right)^2 + \left(\frac{\partial u}{\partial z} + \frac{\partial w}{\partial r} \right)^2 \right]^{1/2} \right|^{n-1} \right\} \right] \left(\frac{\partial w}{\partial r} + \frac{\partial u}{\partial z} \right). \tag{9.4}$$

With a similar argument based on evidence that the lumen radius R is sufficiently smaller than wavelength λ, of the pressure wave. i.e. $R / \lambda \ll 1$ [90], the radial Navier-Stokes equation simply reduces to $\partial p/\partial r = 0$ which implies that pressure is independent of the radial coordinate [90].

The problem defined through Eqs. (7.4)-(7.6) and (9.2)-(9.4) is subject to the boundary and initial conditions given through (7.7)-(7.9).

9.3   Transformation of the Problem

In order to immobilize the effects of vessel wall the following radial coordinate transformation is obtained [75]

$$x = \frac{r}{R(z,t)}.$$

(9.5)

In terms of new variable x, Eqns. (7.4), (9.2)-(9.4) read

$$\frac{\partial w}{\partial t} = \left\{ \frac{x}{R}\frac{\partial R}{\partial t} - \frac{u}{R} + \frac{x}{R}\frac{\partial R}{\partial z}w \right\}\frac{\partial w}{\partial x} - \frac{1}{\rho}\frac{\partial p}{\partial z} - w\frac{\partial w}{\partial z} + \frac{1}{\rho}\left\{ \frac{1}{xR}S_{xz} + \frac{1}{R}\frac{\partial S_{xz}}{\partial x} + \frac{\partial S_{zz}}{\partial z} - \frac{x}{R}\frac{\partial R}{\partial z}\frac{\partial S_{zz}}{\partial x} \right\},$$

(9.6)

$$\frac{1}{R}\frac{\partial u}{\partial x} + \frac{u}{xR} + \frac{\partial w}{\partial z} - \frac{x}{R}\frac{\partial R}{\partial z}\frac{\partial w}{\partial x} = 0,$$

(9.7)

$$S_{xz} = -\left[\varepsilon_1 + \varepsilon_2 \left\{ \left[\left[\left(\frac{1}{R}\frac{\partial u}{\partial x}\right)^2 + \left(\frac{u}{xR}\right)^2 + \left(\frac{\partial w}{\partial z} - \frac{x}{R}\frac{\partial R}{\partial z}\frac{\partial w}{\partial x}\right)^2 + \left(\frac{\partial u}{\partial z} - \frac{x}{R}\frac{\partial R}{\partial z}\frac{\partial u}{\partial x} + \frac{1}{R}\frac{\partial w}{\partial x}\right) \right]^{1/2} \right|^{n-1} \right\} \right]$$
$$\times \left(\frac{\partial u}{\partial z} - \frac{x}{R}\frac{\partial R}{\partial z}\frac{\partial u}{\partial x} + \frac{1}{R}\frac{\partial w}{\partial x} \right),$$

(9.8)

Similarly

$$S_{zz} = -2\left[\cdots\cdots\cdots\cdots \right]\times\left(\frac{\partial w}{\partial z} - \frac{x}{R}\frac{\partial R}{\partial z}\frac{\partial w}{\partial x} \right),$$

(9.9)

and

$$S_{xx} = -2\left[\cdots\cdots\cdots\cdots \right]\times\left(\frac{1}{R}\frac{\partial u}{\partial x} \right).$$

(9.10)

132

The boundary conditions are

$$u(x,z,t)=0, \ \frac{\partial w(x,z,t)}{\partial x}=0, \ S_{xz}=0 \qquad on \ x=0, \qquad (9.11)$$

$$u(x,z,t)=\frac{\partial R}{\partial t}, \ w(x,z,t)=0 \qquad on \ x=1, \qquad (9.12)$$

and
$$u(x,z,0)=w(x,z,0)=0. \qquad (9.13)$$

As explicit expression for $u(x,z,t)$ can be obtained as follows: Multiplying Eq. (9.7) by xR and integrating with respect to x from 0 to x, we get

$$u(x,z,t)=x\frac{\partial R}{\partial z}w-\frac{R}{x}\int_0^x x\frac{\partial w}{\partial z}dx-\frac{2}{x}\frac{\partial R}{\partial z}\int_0^x xwdx. \qquad (9.14)$$

Eq. (9.14) takes the following form by making use of the boundary condition (9.12)

$$-\int_0^1 x\frac{\partial w}{\partial x}dx=\int_0^1 x\left[\frac{2}{R}\frac{\partial R}{\partial z}w+\frac{1}{R}\frac{\partial R}{\partial t}f(x)\right]dx. \qquad (9.15)$$

where $f(x)$ is an arbitrary function. Let us choose $f(x)$ of the form

$$f(x)=-4(x^2-1) \ \text{satisfying} \ \int_0^1 xf(x)=1. \qquad (9.16)$$

Equating the integrands on both sides of (9.14) yields

$$\frac{\partial w}{\partial z}=-\frac{2}{R}\frac{\partial R}{\partial z}w+\frac{4}{R}(x^2-1)\frac{\partial R}{\partial t}. \qquad (9.17)$$

Utilizing (9.17) in (9.14), we finally arrive at

133

$$u(x,z,t)=x\left[\frac{\partial R}{\partial z}w+\frac{\partial R}{\partial t}\left(2-x^2\right)\right].$$

(9.18)

9.4 Numerical solution using finite difference method

Due to their nonlinear nature, it is difficult to obtain a closed form solution of Eqns. (9.6) and (9.8) subject to the boundary and initial conditions (9.11)-(9.13). For further analysis, these equations are integrated numerically using an explicit finite difference method. This method is based on the approximation of partial derivatives with their finite difference counterparts. The formulae of various derivatives appearing in (9.6) are already provided in chapter 7 through (7.32)-(7.34).

Using (7.32)-(7.35), Eq. (9.6) may be transformed to the following difference equation

$$
\begin{aligned}
w_{i,j}^{k+1} &= w_{i,j}^k + \Delta t\left[-\frac{1}{\rho}\left(\frac{\partial p}{\partial z}\right)^{k+1} + \left\{\frac{x_j}{R_i^k}\left(\frac{\partial R}{\partial t}\right)_i - \frac{u_{i,j}^k}{R_i^k} + \frac{x_j}{R_i^k}\left(\frac{\partial R}{\partial z}\right)_i w_{i,j}^k\right\}\left(w_x\right)_{i,j}^k - w_{i,j}^k\left(w_z\right)_{i,j}^k\right. \\
&\quad \left. -\frac{1}{\rho}\left\{\frac{1}{x_j R_i^k}\left(S_{xz}\right)_{i,j}^k + \frac{1}{R_i^k}\left[\left(S_{xz}\right)_x\right]_{i,j}^k - \left[\left(S_{zz}\right)_{fz}\right]_{i,j}^k + \frac{x_j}{R_i^k}\left(\frac{\partial R}{\partial t}\right)_i\left[\left(S_{zz}\right)_x\right]_{i,j}^k\right\}\right].
\end{aligned}
$$

(9.19)

and Eqns. (9.8)-(9.10) have the following discretized form

$$
\begin{aligned}
\left[\left(S_{zz}\right)_{fz}\right]_{i,j}^k &= -2\left[\varepsilon_1 + \varepsilon_2\left\{\left|\left[\left(\frac{1}{R_i^k}\left(u_x\right)_{i,j}^k\right)^2 + \left(\frac{u_{i,j}^k}{x_j R_i^k}\right)^2 + \left(\left(w_z\right)_{i,j}^k - \frac{x_j}{R_i^k}\left(\frac{\partial R}{\partial z}\right)_i\left(w_x\right)_{i,j}^k\right)^2 + \left(\left(u_z\right)_{i,j}^k - \frac{x_j}{R_i^k}\left(\frac{\partial R}{\partial z}\right)_i\left(u_x\right)_{i,j}^k + \frac{1}{R_i^k}\left(w_x\right)_{i,j}^k\right)^2\right]^{1/2}\right|\right\}^{n-1}\right] \\
&\quad \times\left[\left(w_z\right)_{i,j}^k - \frac{x_j}{R_i^k}\left(\frac{\partial R}{\partial z}\right)_i\left(w_x\right)_{i,j}^k\right],
\end{aligned}
$$

(9.20)

$$\left[\left(S_{xx}\right)_z\right]_{i,j}^k = -2\left[\cdots\cdots\cdots\cdots\right]\times\left[\frac{1}{R_i^k}\left(u_x\right)_{i,j}^k\right],$$

(9.21)

$$\left[\left(S_{xz}\right)_z\right]_{i,j}^k = -\left[\cdots\cdots\cdots\cdots\right]\times\left[\left(u_z\right)_{i,j}^k - \frac{x_j}{R_i^k}\left(\frac{\partial R}{\partial z}\right)_i\left(u_x\right)_{i,j}^k + \frac{1}{R_i^k}\left(w_x\right)_{i,j}^k\right].$$

(9.22)

The boundary and initial conditions can be written in the discretized form as:

$$u_{i,j}^{k} = 0, w_{i,1}^{k} = w_{i,2}^{k}, \left(S_{xz}\right)_{i,1}^{k} = 0, \tag{9.23}$$

$$w_{i,N+1}^{k} = 0, u_{i,j}^{k} = \left(\frac{\partial R}{\partial t}\right)_{i}^{k} \tag{9.24}$$

$$u_{i,j}^{1} = w_{i,j}^{1} = 0. \tag{9.25}$$

The wall shear stress $\left(\tau_w\right)$ is given by

$$(\tau_w)_i^k = \left[\varepsilon_1 + \varepsilon_2 \left\{ \left[\left[\left(\frac{1}{R_i^k}(u_x)_{i,j}^k\right)^2 + \left(\frac{u_{i,j}^k}{x_j R_i^k}\right)^2 + \left((w_z)_{i,j}^k - \frac{x_j}{R_i^k}\left(\frac{\partial R}{\partial z}\right)_i^k (w_x)_{i,j}^k\right)^2 \right. \right. \right. \right. \left. \left. \left. + \left((u_z)_{i,j}^k - \frac{x_j}{R_i^k}\left(\frac{\partial R}{\partial z}\right)_i^k (u_x)_{i,j}^k + \frac{1}{R_i^k}(w_x)_{i,j}^k\right)^2 \right]^{1/2} \right]^{n-1} \right\} \right] \left[\frac{1}{R_i^k}(w_x)_{i,j}^k + (u_z)_{i,j}^k - \frac{x_j}{R_i^k}\left(\frac{\partial R}{\partial z}\right)_i^k (u_x)_{i,j}^k\right]_{x=1}. \tag{9.26}$$

The resistance to flow or impedance experienced by flowing blood at any cross-section is given by [26]

$$\Lambda_i^k = \frac{\left|L\left(\partial p / \partial z\right)^k\right|}{Q_i^k}. \tag{9.27}$$

9.5   Results and Discussion

The computations presented in this section are carried out for the following physiologically relevant values of parameters [26, 91-93]: $a = 0.8$mm, $n = 0.639$, $\rho = 1.06 \times 10^3$ kg m^{-3}, $f_p = 1.2$ H$_z$, $A_0 = 100$ kg m^{-2} s^{-2}, $A_1 = 0.2A_0$, $\delta = 0.4a$. In fact the parameters chosen here correspond to flow of blood in a coronary stenosed artery. The step sizes are taken [26] $\Delta x = 0.025$, $\Delta z = 0.01$. Since no data is available about the value of $\bar{a}$, therefore for the calculation purpose we have chosen it equal to $0.035P$. The accuracy of the numerical solution is maintained up to 10^{-7} by choosing the time step 0.0001. Test computations show that if we decrease the spatial step size then simulations will take more time and accuracy will be slightly improved.

Thus we can say that numerical solution is nearly independent of spatial step size for $\Delta x < 0.025$ and $\Delta z < 0.1$.

The profiles of the axial velocity of streaming blood in normal and stenotic artery for different values of tapering angles are shown in **Fig. 9.1a**. We can observe from Fig.9.1a that the magnitude of velocity is greater in the normal artery as compared with the stenotic artery. Further velocity profile attains higher values for diverging tapering as compared with the converging tapering. The profile of non-tapered artery lies in between. This observation is true for both normal and constricted artery. However, the profile in constricted artery for converging tapering is flatter over whole cross-section except near the wall. For such case, except the thin boundary layer the flow in the interior region is similar to a plug flow. The existence of flat velocity profile in the constricted region for converging tapering is because of the fact that near the artery wall the viscous and inertial forces are of the same order. However, near the centre of the artery the inertial forces dominate, thus compelling the axial velocity profile to attain a flat shape. The profiles of radial velocity of the flowing blood in normal and constricted artery for different taper angles are illustrated in Fig. 9.1b. All the profiles are taken at specific location $z = 28mm$ and at time instant $t = 0.45\ s$. This figure reveals that radial velocity is negative over the whole cross-section. All the curves start from zero and approach a constant value at wall due to the presence of wall movement in the stenosis geometry. It is further observed from this figure that the effects of vessel tapering on radial velocity are prominent for constricted artery as compared with the normal artery. The maximum deviation in the shape of curves of radial velocity occurs near the wall for both stenotic and normal artery.

Fig. 9.2. (a) depicts the profiles of axial velocity for different instants of time t within single cardiac period at a specific location $z = 28mm$ in the stenotic region. These profiles indicate a decreasing trend of the axial velocity when t increases from 0.1 to $0.45\ s$. However opposite trend is observed at $t = 0.7\ s$ i.e., axial velocity starts to rise again. Such a trend is clearly due to the pulsatile pressure gradient produced by the imposed boundary condition. The time instants $0.1,\ 0.3$ and $0.45\ s$ belong to systolic phase while time instant $0.7\ s$ belongs to diastolic phase. The plots of radial velocity for different instants of t over a single cardiac cycle at a location $z = 28mm$ in the stenotic region are shown in **Fig. 9.2b**. It is noted from this

figure that radial velocity assumes positive values in the time period *0.1* to *0.3 s* while as time increases further from *0.3 s* it decreases and become negative for $t = 0.45s$. It further continues with negative values for $t = 0.7s$. The shift in the values of radial velocity from positive to negative is due to the pulsatile pressure gradient while its non-symmetric shape owes due to the arterial wall movement.

The results for the axial velocity profile of the flowing blood characterized by the Sisko fluid at different axial positions for $t = 0.45 s$ are illustrated in **Fig. 9.3a**. One can see that the shape of velocity profile at cross-section $z = 15mm$ is parabolic. However, as one moves downstream toward the stenotic region a flattening trend is observed. The change in the velocity profile is confined in a thin layer near the wall at $z = 28mm$ and outside this layer there is no appreciable change in it. At the offset of the stenosis i.e $z = 34mm$ the velocity profile gets back to its original parabolic form. **Fig. 9.3b** exhibits the profiles of radial velocity at different axial stations for $\phi = -0.1^o$ and $t=0.45s$. We can observe that the behavior of all curves is similar except the curve for $z = 34 mm$ i.e. they get concave near the wall. However, at the location $z = 34 mm$ the radial velocity changes its sign from positive to negative. The change of sign in the radial velocity at the downstream stenosis is an indicator of separation in the flow field.

Figs.9. 4(a) and (b) show the axial and radial velocity plots for different tapering angles at $t= 0.45 s$. It is observed from both panels that when the tapered angle increases from -0.2° to -0.4°, the velocity profiles do shifts toward the origin. Similarly it shows opposite behavior when taper angle assumes positive values from $\phi = 0^o$ to $\phi = 0.2^o$ i.e the magnitude of the velocity increases or shift away from the origin. From these graphs one may conclude that there are significant effects of the tapering angle on the flow field of blood.

Figs.9. 5(a) and (b) show the axial and radial velocity profiles for different values of the material parameter ε_2 at $z = 28mm$ and $t = 0.45 s$. It is observed from both panels that with an increase in value of ε_2 from 0.1735 to 0.5735, the velocity profiles do shift away from the origin. A comparison of axial and radial velocity for power law and Sisko fluid is shown in **Fig. 9.6(a) and (b)**. This figure predicts higher values of axial velocity both in stenotic and normal artery for power-law fluid in comparison with Sisko fluid.

The graphical illustrations of time series of flow rate of streaming blood is characterized by the Sisko fluid for a different tapering angles and different material parameters are presented in **Fig. 9.7(a) and (b)**, respectively. Fig.9.7 (a) comprises of the five distinct curves of flow rate. The top most curve is for normal converging artery with wall movement. Below it lays the curve for diverging stenotic artery. The third curve from the top corresponds to non-tapered stenotic artery. The variation of flow rate with time for diverging stenotic artery is shown in fourth curve. The last curve depicts the case of flow rate for artery with rigid wall. We may conclude from Fig. 9.7(a) that flow rate attain higher value in normal artery with wall movement as compared with stenotic artery. The positive values of taper angle further enhance the flow rate while the presence of stenosis reduces it significantly. Moreover, the flow rate fluctuates in the first two cardiac cycles and after that the periodic behavior prevails. This is because of the arterial wall movement included in the geometry of stenosis through the factor $a_1(t)$ given by Eq. (7.2). Now with the increase of time the factor $a_1(t)$ goes to unity due to its dependence on e^{-t} and thus the profiles of flow rate becomes periodic. This is also evident from the curve for rigid wall where the flow rate is periodic for all times. Fig 9.7(b) indicates an increase in the flow rate with increasing the material parameter ε_2.

The time series of wall shear stress for four cardiac cycles at a location $z = 28mm$ for different taper angles and different values of material parameter ε_2 are shown in **Fig. 9.8 (a) and (b)** respectively. We note from Fig. 9.8 (a) that the value of shear stress value in the stenotic region for a diverging constricted artery is higher than those of non-tapered and converging artery. We further note from Fig. 9.8 (a) that the profile of wall shear stress for a normal artery lies below of all other curves indicating how significantly the presence of stenosis can affect the wall shear stress. The material parameter of Sisko fluid ε_2 also affects the wall shear in the sense that wall shear stress reduces with an increase in ε_2. Thus the non-Newtonian characteristics of blood also bear the potential to influence the wall shear stress. It is also evident from both the figures 9.8(a) and (b) that wall shear stress become periodic immediately after the start of the flow.

Figs. 9. 9 (a) and (b) are plotted to see the time series of resistance impedance at a specific location $z = 28mm$ for different taper angles and different values of material parameter ε_2. It is observed that these

profiles follow a reverse trend in contrast to the flow rate profiles as expected from the formula of the resistance to flow given by expression (9.31). Contrary to flow rate profiles, one may observe that the resistance to flow in a stenotic region decreases as tapering angle increase from -0.1 to 0.1. A further decrease is observed in the absence of the stenotic region. Fig. 9.9 (b) reveals that the resistance to flow is a decreasing function of the material parameter ε_2. Moreover Fig. 9.9 (a) and (b) also indicate that like flow rate, the periodicity in the resistance to flow is not attained within the first four cardiac cycles.

9.6   Conclusion

A mathematical model based on Sisko constitutive relation is developed to study the unsteady pulsatile flow of blood through a time variant stenotic artery. The analysis carried out here is general and includes the results for Newtonian and power law fluids as limiting cases. The present model is also capable of predicting the effects of vessel tapering and severity of the stenosis on the important variables associated with the blood flow. The study reveals that the axial velocity of blood, resistance to flow, flow rate and wall shear stress are greatly influenced by the blood rheology, wall movement, presence of stenosis and degree of taperness of the artery. The study further gives a motivation to incorporate more realistic constitutive equations in the present model to represent the blood rheology.
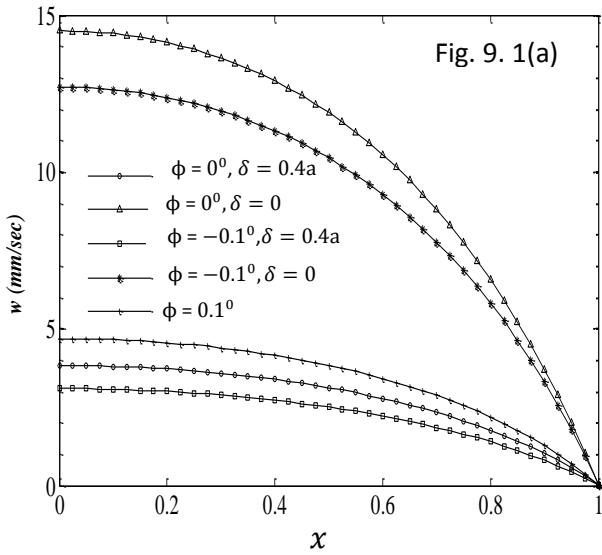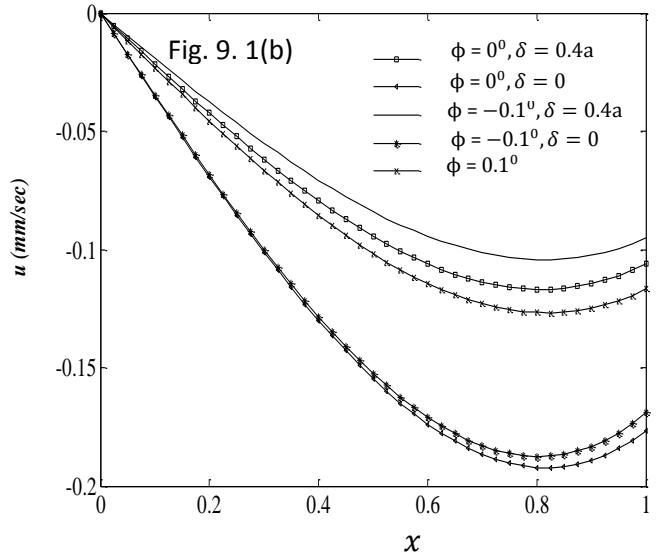
Fig. 9.1: Axial (panel (a)) and radial (panel (b)) velocity profiles for different values of ϕ. The others parameters are

($z = 28mm$, $t = 0.45\,s$, $\delta = 0.4a$, $d = 20mm$, $l_0 = 16mm$, $\varepsilon_2 = 0.1735 Pa.s^n$).
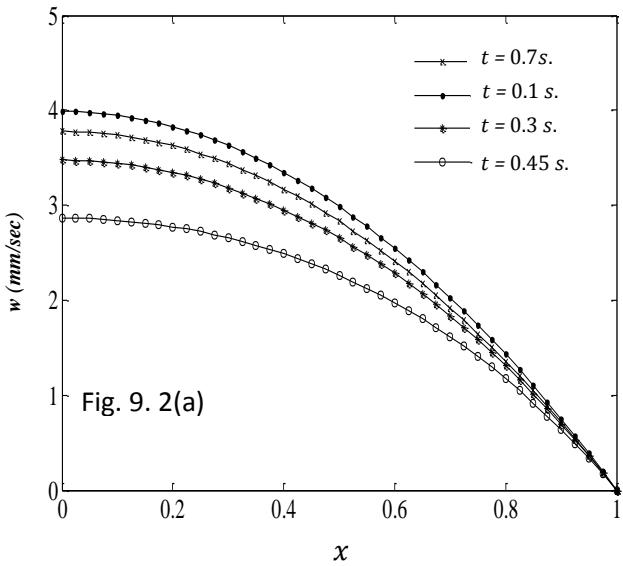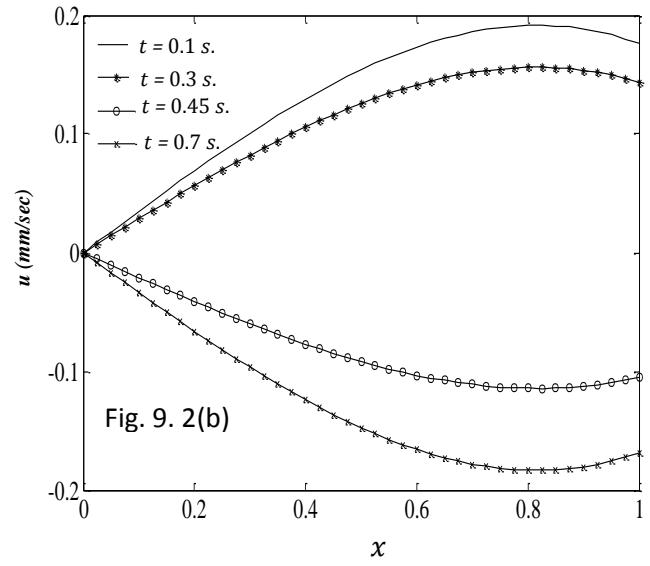
Fig. 9.2: Axial (panel (a)) and radial (panel (b)) velocity profiles at different time instants. The others parameters are

($z = 28mm$, $t = 0.45\,s$, $\delta = 0.4a$, $d = 20mm$, $l_0 = 16mm$, $\varepsilon_2 = 0.1735 Pa.s^n$).
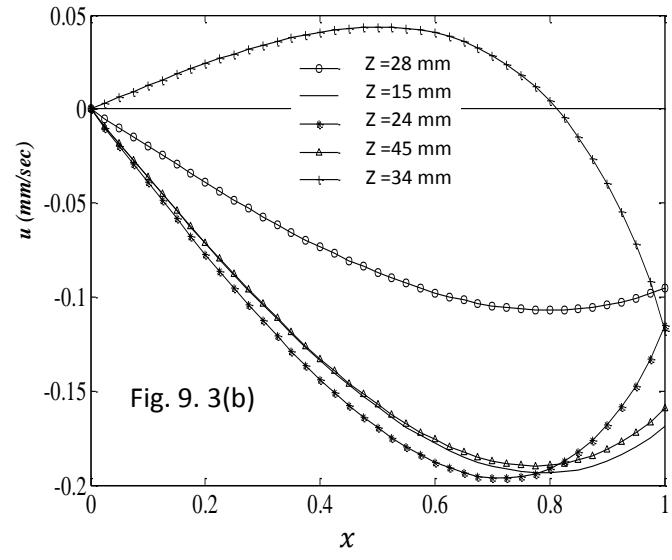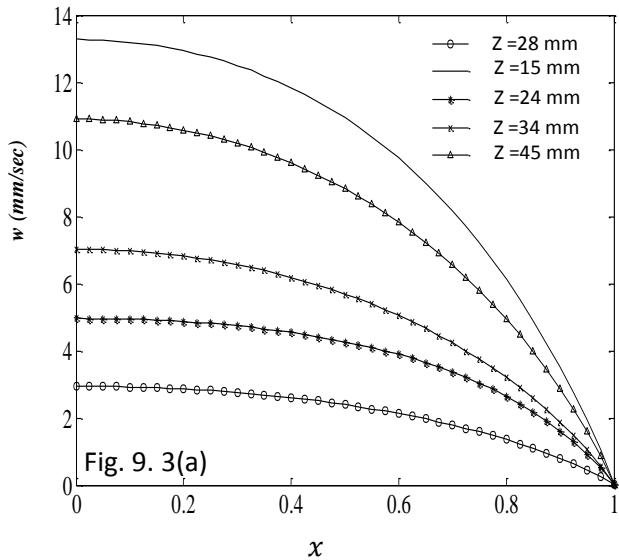
Fig. 9.3: Axial (panel (a)) and radial (panel (b)) velocity profiles for different axial stations. The others parameters are ($t = 0.45\,s, \delta = 0.4a, d = 20mm, l_0 = 16mm, \varepsilon_2 = 0.1735\,Pa.s^n$).
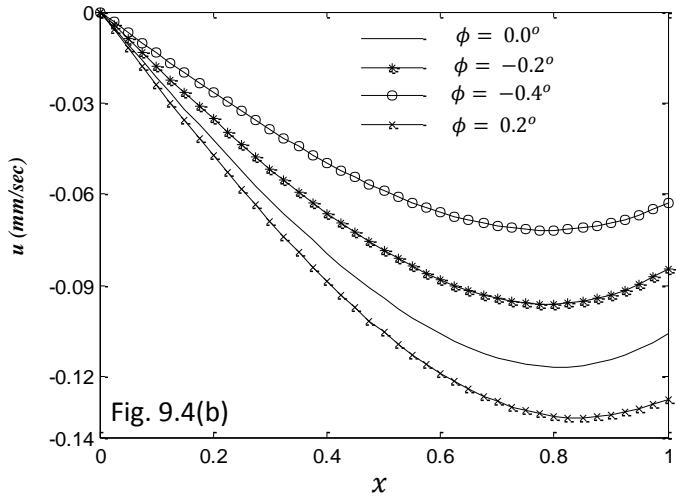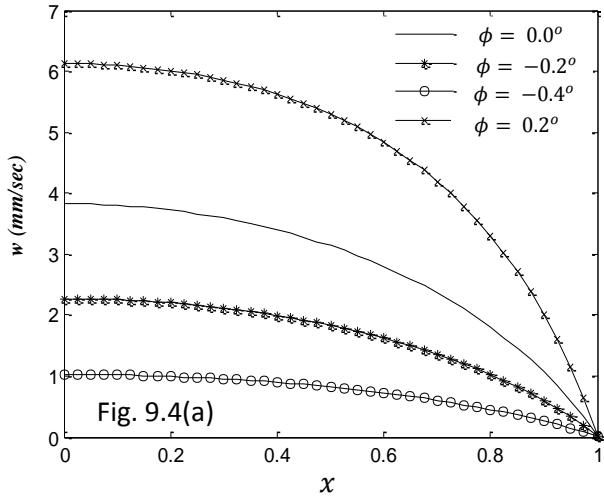

Fig. 9.4: Axial (panel (a)) and radial (panel (b)) velocity profiles for different values of ϕ. The others parameters are ($z = 28mm, t = 0.45\,s, \delta = 0.4a, d = 20mm, l_0 = 16mm, \varepsilon_2 = 0.1735\,Pa.s^n$).

141
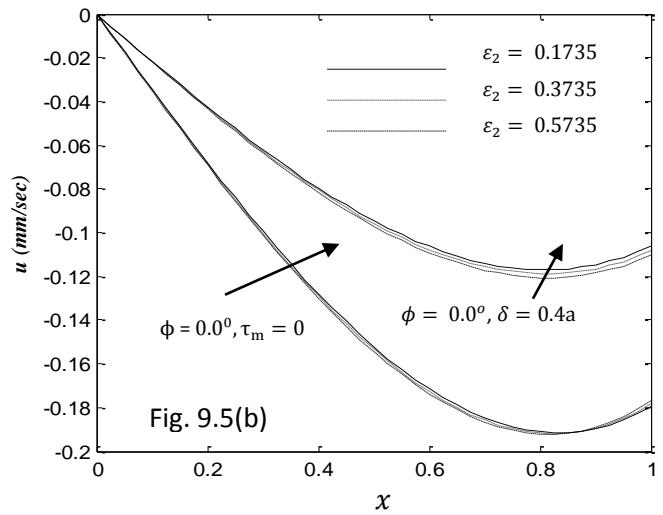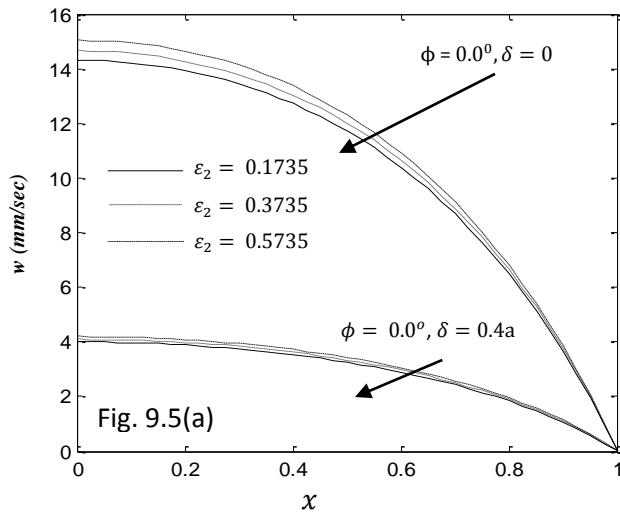
Fig. 9.5: Axial (panel (a)) and radial (panel (b)) velocity profiles for different values of ε_2. The others parameters are

($z = 28mm$, $t = 0.45\,s$, $\delta = 0.4a$, $d = 20mm$, $l_0 = 16mm$).
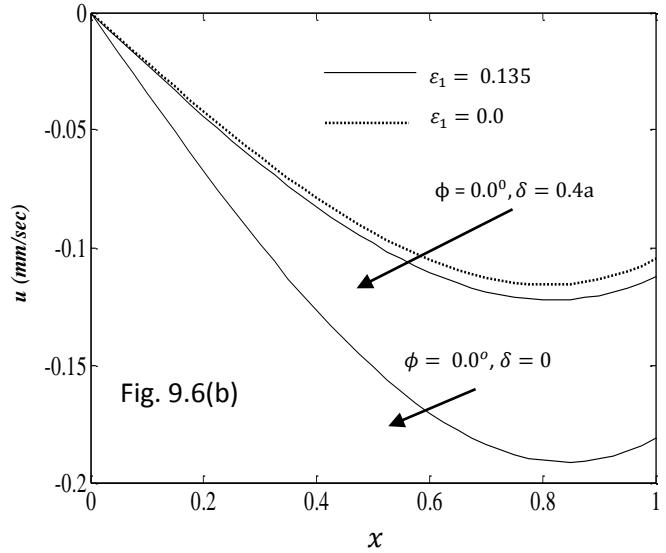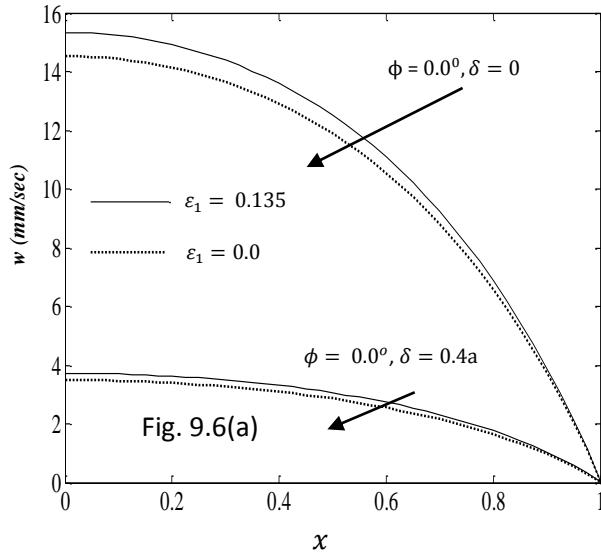
Fig. 9.6: Axial (panel (a)) and radial (panel (b)) velocity profiles for different values of $\bar{a}$. The others parameters are

($z = 28mm$, $t = 0.45\,s$, $\delta = 0.4a$, $d = 20mm$, $l_0 = 16mm$, $\varepsilon_2 = 0.1735 Pa.s^n$).
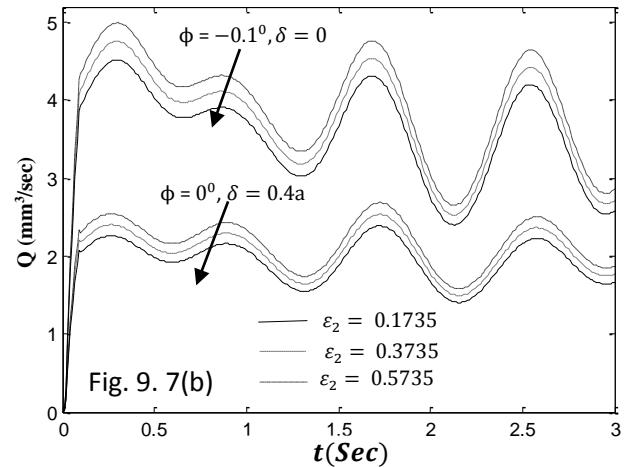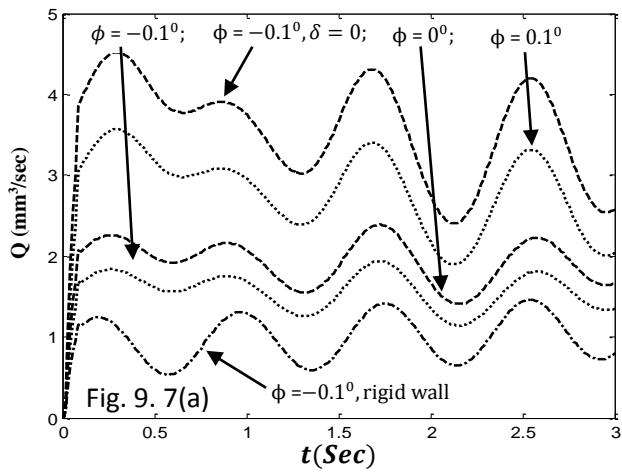
Fig. 9.7: Time series of flow rate for different values of tapering angles ϕ (panel (a)) and different material parameter

values (panel (b)) at $z = 28mm$. The others parameters are ($\tau_m = 0.4a$, $d = 20mm, l_0 = 16mm, \varepsilon_2 = 0.1735 Pa.s^n$).
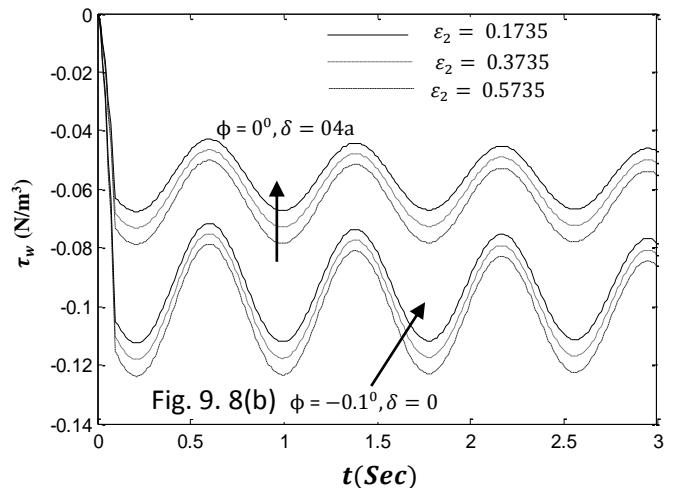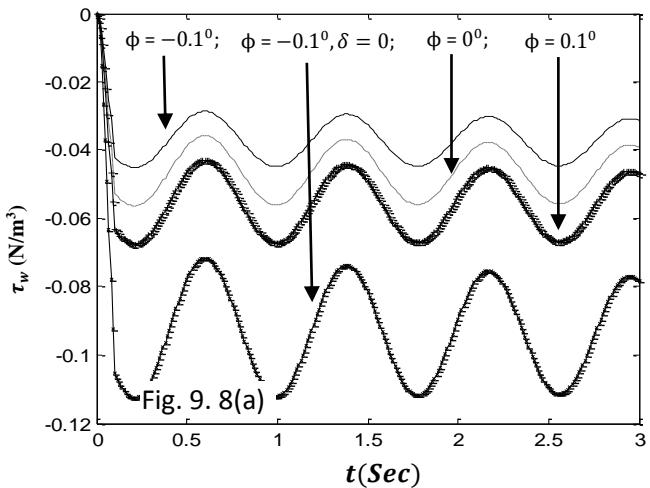
Fig. 9.8: Time series of Wall shear stress for different values of tapering angles ϕ (panel(a)) and different material

parameter values (panel(b)) at $z = 28mm$. The others parameters are ($\delta = 0.4a$,

$d = 20mm, l_0 = 16mm, \varepsilon_2 = 0.1735 Pa.s^n$).
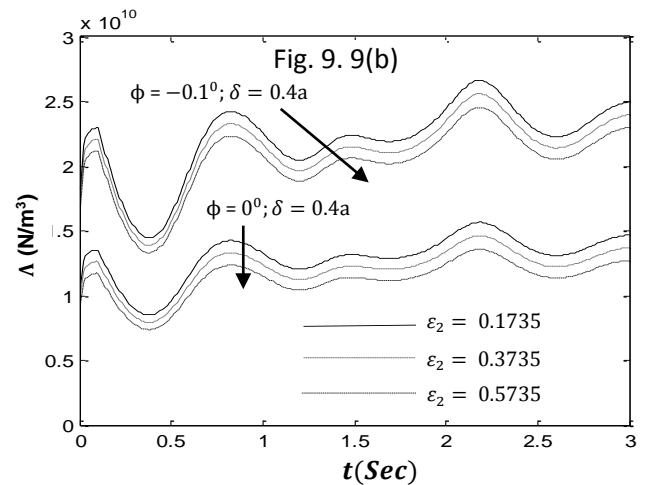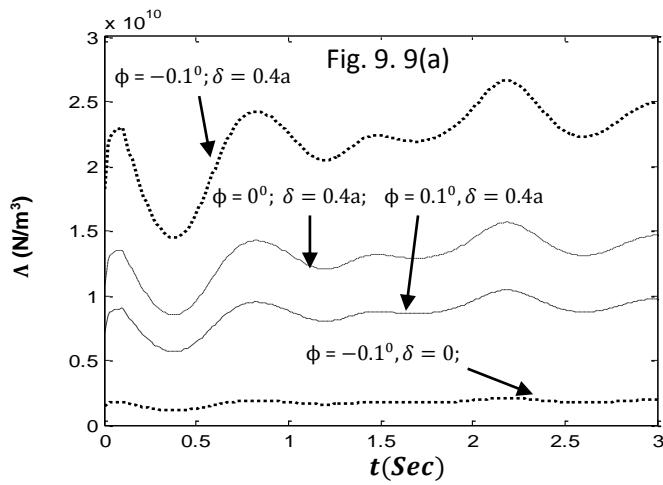
Fig. 9.9: Time series of variation of resistance to flow for different values of tapering angles ϕ (panel (a)) and different material parameter values (panel (b)) at $z = 28mm$. The others parameters are ($\delta = 0.4a$, $d = 20mm, l_0 = 16mm, \varepsilon_2 = 0.1735 Pa.s^n$).

# Bibliography

[1]. D. F. Young, Effect of a time-dependent stenosis on flow through a tube, J. Eng. Ind. 90 **(1968)** 248-254.

[2]. D. A. MacDonald, On steady flow through modeled vascular stenosis, J. Biomechanics 12 **(1979)** 13-30.

[3]. W. Youngchareon and D. F. Young, Initiation of turbulence in models of arterial stenosis, J. Biomechanics 12 **(1979)** 185-196.

[4]. J. Doffin and F. Chagneau, Oscillating flow between a clot model and a stenosis, J. Biomechanics 14 **(1981)** 143-148.

[5]. R. J. Liou, M. E. Clark, J. M. Robertson, and L. C. Cheng, Three-dimensional simulation of steady past a partial stenosis, J. Biomechanics 14 **(1981)** 325-338.

[6]. A. Pollard, A contribution on the effects of inlet conditions when modeling stenosis using sudden expansions, J. Biomechanics 14 **(1981)** 349-356.

[7]. P. Chaturani, V. Palanisamy, Pulsatile flow of blood with periodic body acceleration, Int. J. Eng. Sci. 29 (**1991**) 113–121.

[8]. S. Chakravarty, P. K. Mandal, A. Mandal, Mathematical model of pulsatile blood flow in a distensibleaortic bifurcation subject to body acceleration, Int. J. Eng. Sci. 38 (**2000**) 215–238.

[9]. S. Chakravarty, P. K. Mandal, Two-dimensional blood flow through tapered arteries under stenotic conditions, Int. J. Nonlinear Mech. 35 **(2000)** 779-793.

[10]. M. El-Shahed, Pulsatile flow of blood through a stenosed porous medium under periodic body acceleration, Appl. Math. Comput. 138 **(2003)** 479–488.

[11]. K. Halder, Application of adomian's approximation to blood flow through arteries in the presence of a magnetic field, J. Appl. Math. Comput. 1 **(2009)** 17-28.

[12]. E. E. Tzirtzilakis, Biomagnetic fluid flow in a channel with stenosis, Physica D 237 (**2008**) 66-81.

[13]. O. U. Mehmood, · N. Mustapha, ·S. Shafie, Unsteady two-dimensional blood flow in porous artery with multi-irregular stenoses, Transp. Porous. Med. 92 (**2012**) 259–275.

[14]. M. K. Sharma, K. Bansal, S. Bansal, Pulsatile unsteady flow of blood through porous medium in a stenotic artery under the influence of transverse magnetic field, Kor. Aust. Rheo. J. 24 (**2012**) 181-189.

[15]. I. M. Eldesoky, M. H. Kamel, R. M. Hussien, R. M. Abumandour, Numerical study of unsteady MHD pulsatile flow through porous medium in an artery using Generalized Differential Quadrature Method (GDQM), Int. J. Mat. Mech. Manuf. 1 (**2013**) 200-206.

[16]. A. R. Haghighi, M. S. Asl, M. Kiyasatfar, Mathematical modeling of unsteady blood flow through elastic tapered artery with overlapping stenosis, J. Brazil. Soc. Mech. Sci. Eng. 37 (**2015**) 571-578.

[17]. Y. I. Cho and K.R. Kensey, Effects of the non-Newtonian viscosity of blood on hemodynamics of diseased arterial flows: Part 1, steady flows, Biorheo. 28 (**1991**)241-262.

[18]. C. T. Leondes, Biomechanical systems: techniques and applications, volume IV: biofluid methods in vascular and pulmonary systems: techniques and applications: 4 CRC Press. (**2000**).

[19]. D. S. Long, M. L. Smith, A.R. Pries, K. Ley and E. R. Damiano, Microviscometry reveals reduced blood viscosity and altered shear rate and shear stress profiles in microvessels after hemodilution, PNAS 101, (**2004**) 10060-10065.

[20]. W. Y. Chan, Y. Ding and J. Y. Tu, Modeling of non-Newtonian blood flow through a stenosed artery incorporating fluid structure interaction, ANZIAM J. 47 (**2007**) C507-C523.

[21]. T. A. Crowley, and V. Pizziconi, Isolation of plasma from whole blood using planer microfilters for lab-on- a chip applications, Lab. Chip. 5 (**2005**) 922-929.

[22]. F. Yilmaz, and M. Y. Gundogdu, A critical review on blood flow in large arteries; relevance to blood rheology, viscosity models, and physiologic conditions, Korea-Australia Rheo. J. 20 **(2008)** 197-211.

[23]. L. M. Srivastava, flow of couple stress fluid through stenotic blood vessels, J. Biomech. Vol. 18. (**1985**) 479-485.

[24]. S. N. Majhi, V. R. Nair, Pulsatile flow of third grade fluids under body acceleration—Modeling blood flow, Int. J. Eng. Sci. 32 (**1994**) 839–846.

[25]. J. C. Misra, B. Pal, Mathematical model for the study of the pulsatile flow of blood under an externally imposed body acceleration, Math. Comp. Model. 29 (**1999**) 89-106.

[26]. P. K. Mandal, An unsteady analysis of non-Newtonian blood through tapered arteries with a stenosis, Int. J. Nonlinear Mech. 40 **(2005)** 151–164.

[27]. P. K. Mandal, S. Chakravarty, A. Mandal, N. Amin, Effect of body acceleration on unsteady pulsatile flow of non-Newtonian fluid through a stenosed artery, Appl. Math. Comp. 189 **(2007)** 766–779.

[28]. Z. Ismail, I. Abdullah, N. Mustapha, N. Amin, The power law model of blood flow through a tapered overlapping stenosedartery, Appl. Math. Comput.195 (**2008**) 669–680.

[29]. Kh. S. Mekheimer, M. A. El Kot, The micropolar fluid model for blood flow through a tapered artery with a stenosis, Acta. Mech. Sin. 24 (**2008**) 637–644.

[30]. S.U. Siddiqui, N. K. Verma, S. Mishra, R. S. Gupta, Mathematical modelling of pulsatile flow of Casson's fluid in arterial stenosis, Appl. Math. Comput. 210 (**2009**) 1–10.

[31]. V. P. Srivastava and Shailesh Mishra, Non-Newtonian Arterial Blood Flow through an Overlapping Stenosis, Applicat. Appl. Math. 5 (**2010**) 225 - 238.

[32]. I. Abdullaha and N. Amin, A micropolar fluid model of blood flow through a tapered artery with a stenosis. Math. Meth. Appl. Sci. 33 (**2010**) 1910–1923.

[33]. I. Abdullah, N. Amin and T. Hayat, Magnetohydrodynamic effects on blood flow through an irregular stenosis, Int. J. Num. Meth. Fluid 67 (**2011**)1624–1636.

[34]. Md. A. Ikbal, S. Chakravarty, Sarifuddin and P. K. Mandal, unsteady analysis of viscoelastic blood flow through arterial stenosis, Chem. Eng. Comm., 199 (**2012**) 40–62.

[35]. Kh. S. Mekheimer and M. A. Elkot, Mathematical modeling of unsteady flow of a Sisko fluid through an anisotropically tapered elastic arteries with time –variant overlapping stenosis, Appl. Math. Model 36 (**2012**) 5393-5407.

[36]. Sarifuddin, S. Chakravarty and P. K. Mandal, Numerical simulation of Casson fluid flow through differently shaped arterial stenoses, Z. Angew. Math. Phys. 65 (**2014**) 767-782.

[37]. N. S. Akbar and S. Nadeem, Carreau fluid model for blood flow through a tapered artery with a stenosis, A. Shams Eng. J. 5 (**2014**) 1307–1316.

[38]. K. L. Moore, Clinically Oriented Anatomy. Williams and Wilkins, Baltimore MD (**1990**).

[39]. B. Pincombe and J. N. Mazumdar, The effects of post-stenotic dilatations on the flow of a blood analogue through stenosed coronary arteries. Math. Comput. Mod 25 (**1997**) 57-70.

[40]. B. Pincombe, J. Mazumdar, I. Hamilton-Craig, Effects of multiple stenoses and post- stenotic dilatation on non-Newtonian blood flow in small arteries, Med. Bioi. Eng. Comput. 37 (**1999**) 595-599.

[41]. K. Wong, J. Tu, J. Mazumdar, D. Abbott, Modelling of blood flow resistance for an atherosclerotic artery with multiple stenosis and post-stenotic dilations, ANZIAM. J. 51 (**2010**) 66-82.

[42]. M. Dabagh, P. Vasava, P. Jalah, Effects of severity and location of stenosis on the hemodynamics in human aorta and its branches, Med. Biol. Eng. Comp. 53 (**2015**) 463-476.

[43]. K. Wang, J. Mazumdar, B. Pincombe, S. G. Worthley, P. Sanders, D. Abbot, Theoretical modeling of micro-scale biological phenomena in human coronary arteries, Med. Biol. Eng. Comp*.,* 44 (**2006**) 971-982.

[44]. H. Kanai, M. Iizuka, K. Sakamoto, One of the problems in the measurement of blood pressure by catheter-insertion: Wave reflection at the tip of the catheter, Med. Bio. Eng. 8 (**1970**) 483-496.

[45]. L. H. Back, T. A. Denton, Some arterial wall shear stress estimates in coronary angioplasty, Adv. Bio. Eng, 22 (**1992**) 337–340.

[46]. L. H. Back, Estimated mean flow resistance increase during coronary artery catheterization, J. Biomech., 27 (**1994**) 169–175.

[47]. L. H. Back, E.Y. Kwack, M. R. Back, Flow rate–pressure drop relation in coronary angioplasty: catheter obstruction effect, J. Biomech. Eng. Trans., 118 (**1996**) 83–89.

[48]. A. Sarkar, G. Jayaraman, Correction to flow rate–pressure drop relation in coronary angioplasty: steady streaming effect, J. Biomech. 31 (**1998**) 781.

[49]. R. K. Dash, G. Jayaraman, K.N. Mehta, Flow in a catheterized curved artery with stenosis, J. Biomech. 32 (**1999**) 49-61.

[50]. N. Filipovic, D. Nikolic, I. Saveljic, Z. Milosevic, T. Exarchos, G. Pelosi, O. Parodi, Computer simulation of three-dimensional plaque formation and progression in the coronary artery, Compu. Fluids 88 (**2013**) 826-833.

[51]. S. Nikolov, S. Stoytchev, A. Torres, J.J. Nieto, Biomathematical modeling and analysis of blood flow in an intracranial aneurysm, Neurol. Res. 25 (**2003**) 497-504.

[52]. W. Ruan, A coupled system of ODEs and quasilinear hyperbolic PDEs arising in a multiscale blood flow model, J. Math. Anal. Appl. 343 (**2008**) 778-798.

[53]. C. M. Rodkiewicz, P. Sinha, J. S. Kennedy, On the application of a constitutive equation for whole human blood, J. Eng. Math. 42 (**2002**) 1–22.

[54]. A. M. Gambaruto, J. Janela, A. Moura, A. Sequeira, Sensitivity of hemodynamics in a patient specific cerebral aneurysm to vascular geometry and blood rheology, Math. Biosci. Eng. 42 (**2011**) 1–22.

[55]. R. K. Dash, G. Jayaraman, K. N. Metha, Estimation of increased flow resistance in a narrow catheterized artery – A theoretical model, J. Biomech. 29 (**1996**) 917–930.

[56]. D. S. Sankar, K. Hemalatha, Pulsatile flow of Herschel–Bulkley fluid through catheterized arteries – A mathematical model, Appl Math. Mod. 31 (**2007**) 1497–1517.

[57]. J. V. R. Reddy, D. Srikanth , S.V.S.S.N.V.G. K. Murthy, Mathematical modelling of pulsatile flow of blood through catheterized unsymmetric stenosed artery—Effects of tapering angle and slip velocity, Eur. J. of Mech. B/Fluids, 48 (**2014**) 236–244.

[58]. V. P. Srivastava, R. Rastogi, Blood flow through a stenosed catheterized artery: Effects of hematocrit and stenosis shape, Comp. Math. Appl., 59 (**2010**) 1377-1385.

[59]. S. Nadeem, S. Ijaz, Nanoparticles analysis on the blood flow through a tapered catheterized elastic artery with overlapping stenosis. Eur. Phys. J. Plus. 129 (**2014**) 249.

[60]. D. S. Sankar, K. Hemalatha, A non-Newtonian fluid flow model for blood flow through a catheterized artery—Steady flow. Appl. Math. Model. 31 (**2007**) 1847-1864.

[61]. R. Fahraeus, T. Lindqvist, The viscosity of blood in narrow capillary tubes, Amer. J. Physiol., 96 (**1931**) 562–568.

[62]. J. M. Lighthill, Physical fluid dynamics a survey, J. Fluid. Mech., 52 (**1972**) 475.

[63]. G. Segre, A. Silberberg, Behavior of macroscopic rigid spheres in Poiseuille flow. Part 1, J. Fluid Mech., 14 (**1962**) 115–135.

[64]. S. N. Majhi, L. Usha, Modeling the Fahraeus–Lindqvist effect through fluids of differential type, Int. J. Engng. Sci., 26 (**1988**) 503–508.

[65]. S. N. Majhi, V.R. Nair, Pulsatile flow of third grade fluids under body acceleration—Modeling blood flow, Int. J. Engng. Sci., 32 (**1994**) 839–846.

[66]. K. Haldar, H. I. Andresson, Two-layered model of blood flow through stenosed arteries, Acta Mech., 117 (**1996**) 221–228.

[67]. R. Usha, K. Prema, Pulsatile flow of a particle–fluid suspension model of blood under periodic body acceleration, Z. Angew. Math. Phys. (ZAMP), 50 (**1999**) 175–192.

[68]. M. Massoudi, T. X. Phuoc, Pulsatile Flow of a blood using second grade fluid model, Comp. and Math. Appl., 16 (**2008**) 199–211.

[69]. D. S. Sankar, Two-phase non-linear model for blood flow in asymmetric and axi-symmetric stenosed arteries, Int. J of Non-Linear Mech., 46 (**2011**) 296–305.

[70]. Md. A. Ikbal, S. Chakravarty, and P. K. Mandal, Two-layered micropolar fluid flow through stenosed artery: Effect of peripheral layer thickness, Comput and Math. with Appl. 230 (**2009**), 243–259.

[71]. K. A. Hoffmann, S. T. Chiang, Computational Fluid Dynamics, A Publication of Engineering Edition System, Wichita, Kansas USA. 1 (**2000**) 67208-1078.

[72]. H. A. Branes, J. F. Hutton and K. Walter, An introduction to rheology, Elsevier, Amsterdam (**1989**).

[73]. J. G. Oldroyd, On the Formulation of Rheological Equations of State. Proceedings of the Royal Society of London. Series A, Mathematical and Physical Sciences, 200 (**1950**) 523-541.

[74]. T. Tosco, D. L. Marchisio, F. Lince, R. Sethi, Extension of the Darcy–Forchheimerlawfor shear-thinning fluids and validation viapore-scale flow simulations, Transp. Porous. Med, 96 (**2013**) 1–20.

[75]. S. C. Ling, H. B. Atabek, A nonlinear analysis of pulsatile flow in arteries, J Fluid Mech. 55 (**1972**) 493–511.

[76]. A. M. Gambaruto, J. Janela, A. Moura, A. Sequeira, Sensitivity of hemodynamics in a patient specific cerebral aneurysm to vascular geometry and blood rheology, Math. Biosci. Eng. 42 (**2011**) 1–22.

[77]. E. E. Tzirtzilakis, Biomagnetic fluid flow in a channel with stenosis, Physica D. 237 (**2008**) 66-81.

[78]. J. S. Lee and Y. C. Fung, Flow in locally constricted tubes at low Reynolds number, J. Appl. Mech. 37 (**1970**) 9-16.

[79]. T. Guerra, J. Tiago, A. Sequeira, Optimal control in blood flow simulations, Int. J. of Non-Linear Mech., 64 (**2014**) 57-59.

[80]. M. D'. Elia, M. Perego, A. Veneziani, A variational Data Assimilation procedure for the incompressible Navier-Stokes equations in hemodynamics, J. Sci. Comput. 52 (**2011**) 340-359.

[81]. A. C. Eringen, Theory of micropolar fluids. J. Math. Mech, 16 (**1966**) 1–18.

[82]. K. J. Bathe, Finite Element Procedures. Addison Welsey, USA (**1996**).

[83]. O. A. Bég, R. Bhargava, S. Rawat, H. S. Takhar, M. K. Halim, Computational modeling of biomagnetic micropolar blood flow and heat transfer in a two-dimensional non-Darcian porous medium. Meccanica 43 (**2008**) 391-410.

[84]. R. Bhargava, S. Sharma, O. A. Bég and J. Zueco, Finite element study of nonlinear two-dimensional deoxygenated biomagnetic micropolar flow, Comm. in Nonlin. Sci. Num. Simu. 15 (**2010**) 1210-1233.

[85]. O. A. Bég, T. A. Bég, R. Bhargava, S. Rawat and D. Tripathi, Finite element study of pulsatile magneto-hemodynamic non-Newtonian flow and drug diffusion in a porous medium channel. J. Mech. Med. and Bio. 12 (**2012**) 1250081.1 – 1250081.26.

[86]. P. Rana, R. Bhargava and O. A. Beg, Finite element simulation of unsteady MHD transport phenomena on a stretching sheet in a rotating nanofluid. Proc. IMECHE- Part N; J. Nanoeng. and Nanosys. 227 (**2013**) 77-99.

[87]. P. Rana and O. A. Bég, Mixed convection flow along an inclined permeable plate: effect of magnetic field, nanolayer conductivity and nanoparticle diameter. Appl. Nanosci. (**2014**) DOI 10.1007/s :13204-014-0352-z.

[88]. M. Bathe, R. D. Kamm, A fluid-structure interaction finite element analysis of pulsatile blood flow through a compliant stenotic artery, ASME J. Biomech. Eng. 121(**1999**) 361–369.

[89]. R. Feng, M. Xenos, G. Girdhar, W. Kang, J. W. Davenport and Y. Deng, Danny Bluestein Viscous flow simulation in a stenosis model using discrete particle dynamics: a comparison between DPD and CFD. Biomech. Model. Mechanobiol. (**2011**) DOI 10.1007/s10237-011-0297.

[90]. T. J. Pedley, The fluid mechanics of large blood vessels, Cambridge University Press, London, (**1980**).

[91]. C. E. Huckaba and A.W. Hahn, A generalised approach to the modeling of arterial blood flow, Bull. Math. Biophys. 30 (**1968**) 645–662.

[92]. D. A. McDonald, Blood Flow in Arteries, Edward, (**1974**).

[93]. W. R. Milnor, Hemodynamics, Williams and Williams, Baltimore, (**1982**).

[94]. Kh. S. Mekheimer, M. S. Mohamed, Interaction of pulsatile flow on the peristaltic motion of a magneto-micropolar fluid through porous medium in a flexible channel: blood flow model, Int. J. of Pure and Appl. Math. 94 (**2014**) 323-339.

[95]. G. Bugliarello, J. Sevilla, Velocity distribution and other characteristics of steady and pulsatile blood flow in fine glass tubes, Biorheol. 7 (**1970**) 85-107.

[96]. C. K. Kang, A. C. Eringen, The effect of microstructure on the rheological properties of blood, Bull. Math. Biol. 38 (**1976**) 135-158.

[97]. G. Akay, A. Kaye, Numerical solution of time dependent stratified two-phase flow of micropolar fluids and its application to flow of blood through fine capillaries, Int. J. Eng. Sci. 23 (**1985**) 265-276.

[98]. A. Valencia, A. Zarate, M. Galvez and L. Badilla, Non- Newtonian blood flow dynamics in a right internal carotid artery with a saccular aneurysm, Int. J. Numer. Meth. Fluid. 50 (**2006**) 751-764.

[99]. A. C. Burton, Physiology and Biophysics of the Circulation, Introductory Text, Year Book Medical Publisher Chicago, (**1966**).

[100]. P. Chaturani and V. Palanisamy, Micro-continuum model for pulsatile blood flow through a stenosed tube. *Biorheo.* 26 (**1989**) 835-846.